



## AN ABSTRACT OF THE THESIS OF

Christopher O'Day for the degree of Master of Science in Civil Engineering presented on September 2, 2021.

Title: Evaluation of Stereoscopic Camera Systems for Non-Intrusive Spatial Free Surface Measurement in Coastal Research Laboratories

Abstract approved: \_\_\_\_\_

Pedro Lomónaco

Physical modelling is instrumental to the progression of coastal engineering research and our understanding of the offshore and nearshore environments. Scaled models are designed and built to be tested in coastal research laboratories, where a wave basin or flume generates the desired wave conditions for experimentation. The surrounding hydrodynamics of the research specimen are measured by deployed wave gauges that collect high-quality water surface elevation data. These instruments are constrained to measuring a single, stationary location and often require arrays of multiple gauges when it is necessary to collect surface elevation data at a high spatial resolution. Hydrodynamic disruption of the support framing and gauges can be significant, and the complete spatial variability in the wave field is still unknown regardless of the array size. When several reflective contours are introduced to a wave system, such as in port basins or with multiple specimen, spatial variability can be amplified and characterizing wave height with a single value is inadequate. The need for a non-intrusive spatial free surface measurement system that is capable of capturing this variability arises. This thesis evaluates two stereoscopic video measurement systems through multiple experiments in the Directional Wave Basin at the O.H. Hinsdale Wave Research Laboratory at Oregon State University. Both systems are tested in a variety of wave conditions and validated using traditional point measurement instruments such as resistive and ultrasonic wave gauges. Their ability to measure a 6 m by 6 m area in the basin is confirmed and further results are discussed.

Stereoscopic measurement requires the matching of pixels from multiple calibrated and synchronized video frames through image processing techniques. The positional difference

between objects in each frame can then be used to calculate depth and obtain a three-dimensional point cloud of the cameras' overlapping views. Stereo matching algorithms can have difficulty recognizing smooth, translucent water surfaces, therefore texturization or the addition of seeding material is often required for wave measurement within a laboratory. Seeding can disrupt instrumentation and wave propagation and may not always be feasible for use, so a system capable of non-intrusive free surface measurement was prioritized. Two existing stereo measurement systems were selected for this study: the Wave Acquisition Stereo System (WASS), and the Intel® RealSense™ D455 Depth Camera. WASS is an open-source video post-processing pipeline which utilizes stereo matching algorithms developed for use in the open ocean. Multiple GoPro® camera pairs were calibrated and used for video collection for WASS. The Intel® RealSense™ is a consumer grade active infrared stereo camera that internally processes and displays sensor data in real-time. It is a stand-alone system that provides hardware and software to the user so no additional equipment was needed. Methodologies were developed for both systems' calibration, data synchronization, and post-processing. The camera positioning, lighting, and wave conditions were optimized in a series of preliminary experiments before each system was thoroughly tested in a variety of regular and irregular waves.

It was found that WASS heavily relied on wave breaking for water surface recognition and much of the data associated with unbroken waves was unusable. The Intel® system was capable of reliably capturing the water surface regardless of wave breaking. Both systems could not easily differentiate between objects and the water surface, hence instrumentation in view greatly affected data quality. Both datasets contained high frequency noise, but WASS produced lower quality data than that of the Intel® system. Therefore, the Intel® system's dataset was selected for a more extensive spatial time and frequency domain analysis. Wave gauges in frame of the camera were used for measurement validation and the average error across all wave cases was 6.81% and 5.21% for mean and significant wave heights respectively. More importantly, the camera successfully captured a high spatial resolution of wave height variability that the array of point gauges were not able to measure. A BDM directionality analysis was completed on both the gauge and Intel® camera measurements to output directional wave spectra, which showed good agreement.

Both systems were able to spatially reconstruct the water surface of the basin without the need for seeding material. The Intel® system was easily deployed and more versatile in wave

conditions without breaking, but its measurement distance is constrained to the geometries of the sensor housing. The WASS system was more difficult to use but its customizability allowed for hardware selection and the potential to measure a larger water surface area.

©Copyright by Christopher O'Day

September 2, 2021

All Rights Reserved

Evaluation of Stereoscopic Camera Systems for Non-Intrusive Spatial Free Surface  
Measurement in Coastal Research Laboratories

by

Christopher O'Day

A THESIS

submitted to

Oregon State University

in partial fulfillment of  
the requirements for the  
degree of

Master of Science

Presented September 2, 2021  
Commencement June 2022

Master of Science thesis of Christopher O'Day presented on September 2, 2021

APPROVED:

---

Major Professor, representing Civil Engineering

---

Head of the School of Civil and Construction Engineering

---

Dean of the Graduate School

I understand that my thesis will become part of the permanent collection of Oregon State University libraries. My signature below authorizes release of my thesis to any reader upon request.

---

Christopher O'Day, Author

## ACKNOWLEDGEMENTS

I would like to thank the National Science Foundation for funding this project through the Natural Hazards Engineering Research Infrastructure program. I would also like to thank the following list of people:

- Pedro Lomónaco for being an amazing advisor and inspiring this project, never allowing the conversation to get dull, sharing your endless knowledge of coastal engineering with me, and all the other help you gave me along the way.
- Rebecca Miller, Tim Maddux, Bret Bosma, and all of the other workers of the wave lab for helping me set up instrumentation, running waves while I ran around with cameras, and welcoming me into the lab with smiles.
- The professors and faculty of OSU for being great teachers and always leaving your doors open to our questions.
- My committee for reviewing my work and giving me feedback.
- Filippo Bergamasco and Alvis Benetazzo for the help with WASS and sending me Matlab processing codes
- Daniel Piedrahita for being my part-time advisor and answering all the low-level robotics questions I had.
- Matt Leary for always being down for an adventure and a laugh, giving me advice on navigating the bureaucracy of the academic system, and reminding me to not take things too seriously.
- Kiernan Kelty for showing me pure determination in the ocean regardless of your experience level, giving me a second opinion on my workings as “camera guy”, and sharing in relentless spray downs at the lab.
- Nick Mathews and Paige Hovenga for the constant laughs, accents, turning almost any situation into something hysterical, and introducing me into an amazing friend group here.
- All the friends and colleagues at OSU for the support along the way. Everyone here has challenged me inside and out of the classroom and made me a better student/person.
- All of my friends from Cal Poly, Charleston, and where ever else for constant good times and reminding me of the world that exists outside of grad school.



- Julie and Andy Russell for opening your beautiful home to us over quarantine and turning a terrible situation into a positive, memorable experience with lots of laughs, movies, puzzles, and bike rides.
- My mom, dad, and sister for constant love and support, even if you still don't really understand what coastal engineering is. You guys are always there for me and encouraged me to follow my passions, which I appreciate more than I can put into words.
- My girlfriend Hannah, for being there for me through the thick and thin, making every weekend the best adventure ever whether we're getting blown off of Mt. Shasta or just taking over the farmer's market on our knee scooters, and being a truly amazing girlfriend, friend, and adventure buddy.

# TABLE OF CONTENTS

	<u>Page</u>
Chapter 1 Introduction .....	1
1.1 Research Goals and Objectives .....	3
1.2 Document Overview .....	4
Chapter 2 Surface Elevation Reconstruction Methods .....	5
2.1 Review of Literature.....	5
2.1.1 Radar Scanners.....	6
2.1.2 Shape from Shading.....	6
2.1.3 Edge Detection.....	6
2.1.4 Structured Light Methods .....	7
2.1.5 Stereo Photogrammetry .....	7
2.1.6 Combined Stereo Methods.....	8
2.2 System Selection .....	9
2.3 Wave Acquisition Stereo System (WASS).....	10
2.3.1 Software Architecture .....	10
2.3.2 Uncertainties .....	12
2.3.3 Applications .....	13
2.4 Intel® RealSense™ .....	14
2.4.1 Hardware.....	14
2.4.2 Software .....	16
2.4.3 Uncertainties .....	16
2.4.4 Applications .....	16
2.5 Chapter Conclusions .....	17
Chapter 3 Experimental Setup & Procedure .....	18
3.1 Experimental Setup .....	18
3.1.1 Wave Basin .....	18
3.1.2 Instrumentation .....	20
3.1.2.1 Instrumentation Frame.....	20

## TABLE OF CONTENTS (Continued)

	<u>Page</u>
3.1.2.2 Surface-piercing Resistive Wave Gauges.....	21
3.1.2.3 Acoustic Wave Gauges.....	21
3.1.2.4 Camera Equipment .....	21
3.1.2.5 LED Synchronization .....	24
3.1.2.6 Lighting .....	25
3.1.3 Data Acquisition System.....	25
3.1.4 Instrumentation Layout.....	25
3.1.5 Wave Conditions.....	27
3.1.5.1 Regular Waves.....	27
3.1.5.2 Regular Bidirectional Waves.....	29
3.1.5.3 Focusing Waves.....	30
3.1.5.4 Irregular Waves .....	31
3.1.5.5 Wave Generation .....	32
3.2 Experimental Procedure .....	32
3.2.1 Preliminary Tests .....	33
3.2.1.1 Basin Views.....	33
3.2.1.2 Airy Validation .....	34
3.2.1.3 Circular Polarizing Lens (CPL) Filter .....	34
3.2.2 Final Tests.....	35
3.2.2.1 Two WASS Stereo Pairs and Intel® Camera: Frame.....	36
3.2.2.2 Two WASS Stereo Pairs and Intel® Camera: Beach.....	36
3.3 Chapter Conclusions .....	37
Chapter 4 Stereo Data Processing Methodology .....	38
4.1 WASS.....	38

## TABLE OF CONTENTS (Continued)

	<u>Page</u>
4.1.1 Camera Calibration .....	39
4.1.2 Frame and Data Synchronization.....	44
4.1.3 WASS Processing .....	48
4.1.4 NetCDF Generation and Data Visualization.....	49
4.2 Intel® RealSense™ .....	51
4.2.1 Intel® RealSense™ Viewer .....	52
4.2.2 LED Signal Extraction .....	53
4.2.3 Coordinate Adjustment .....	54
4.2.4 Spatial Data Filtering .....	56
4.2.5 Mesh Generation.....	57
4.3 System Comparisons .....	58
4.4 Chapter Conclusions .....	60
Chapter 5 Data Analysis.....	61
5.1 Basin Views.....	61
5.1.1 Camera Angles.....	62
5.1.2 Camera Settings .....	64
5.1.3 Lighting.....	65
5.2 Airy Validation.....	66
5.2.1 Un-broken Waves .....	66
5.2.2 Broken Waves.....	67
5.3 CPL Filter.....	69
5.4 Two WASS Stereo Pairs and Intel® Camera.....	71
5.4.1 Data Filtering .....	78
5.4.2 Time Domain Analysis .....	79
5.4.3 Frequency Domain Analysis.....	80
5.4.4 Directional Analysis.....	81
5.5 Chapter Conclusions .....	84
Chapter 6 Results .....	86

## TABLE OF CONTENTS (Continued)

	<u>Page</u>
6.1 Regular Waves .....	87
6.1.1 Shore Normal (H = 0.5 m, T = 1.8 s, $\theta$ = 0 deg, h = 1 m) .....	88
6.1.2 Directional (H = 0.56 m, T = 5 s, $\theta$ = 15 deg, h = 1 m) .....	92
6.1.3 Bidirectional (H = 0.3 m, 0.3 m, T = 2 s, 2 s, $\theta$ = 15 deg, -15 deg., h = 1 m) .....	97
6.2 Irregular Waves (JONSWAP spectra, $H_s$ = 0.51 m, $T_p$ = 4 s, $\theta$ = $\pm 20$ deg, h = 1 m) ....	99
6.3 Focusing Waves .....	103
6.4 Discussion .....	107
Chapter 7 Conclusion .....	112
7.1 WASS Findings .....	112
7.2 Intel <sup>®</sup> Findings .....	115
7.3 Future Considerations .....	117
References .....	121

## LIST OF FIGURES

<u>Figure</u>	<u>Page</u>
2.1	Example of stereo image rectification. Source:[22]. ..... 12
2.2	Elevation error with respect to horizontal field of view in a field application. Stereo cameras located at the origin. Source:[7]..... 13
2.3	Internal sensor housing of the Intel® D455 Depth Camera with sensor labels. Source: [37]..... 14
2.4	RGB (left) and IR (right) images from the Intel® D455 camera showing the projected IR random pattern that assists with stereo matching. .... 15
3.1	Image of the DWB generating breaking long-crested waves looking toward the wave-maker..... 19
3.2	DWB layout with wave-maker position, coordinate system, and instrumentation frame labeled. Top shows the plan view of the basin and bottom shows a section view. .... 20
3.3	A pair of GoPros® (Pair 1) with their Unistrut mount attached to a movable tripod for preliminary testing. .... 22
3.4	GoPro® stereo pair mounted to instrumentation frame..... 23
3.5	Intel® RealSense™ D455 camera system..... 24
3.6	Instrumentation layout for the preliminary tests. .... 26
3.7	Instrumentation layout for the final tests. .... 26
3.8	A schematic of regular waves labeling the wave amplitude (a), wave height (H), and wave length (L) over a sloped bathymetry $h(x)$ . Source: [16]..... 28
3.9	Regular, shore normal waves generated in the DWB at Oregon State. .... 29
3.10	Schematic of a wave basin generating directional regular waves and the diffraction and reflection affects that occur. Source:[45]..... 29
3.11	Regular bidirectional waves in a wave basin. .... 30
3.12	A focusing wave being generated in the DWB..... 31
3.13	An example of long-crested (left) and short-crested (right) irregular waves. Source:[2]. 32

## LIST OF FIGURES (Continued)

<u>Figure</u>	<u>Page</u>
3.14 GoPro <sup>®</sup> camera layout and approximate reconstructed area for Two Stereo Pairs and Intel <sup>®</sup> Camera: Frame experiment. ....	36
3.15 GoPro <sup>®</sup> camera layout and approximate reconstructed area for Two Stereo Pairs and Intel <sup>®</sup> Camera: Beach experiment. The Intel <sup>®</sup> camera was located at various positions along the basin beach and South side of the basin. ....	37
4.1 Example of calibration picture within Camera Calibration Toolbox for Matlab with user selected image points on each corner and the reprojected grid points with their associated error (blue arrows). ....	40
4.2 Reprojection error in pixels calculated by the Camera Calibration Toolbox for Matlab [9] with each point representing a checkerboard grid point and each color representing a particular image. ....	41
4.3 Tangential (top left), radial (top right), and complete (bottom) distortion models for one of the GoPro <sup>®</sup> Hero 6s used in this study output by Camera Calibration Toolbox for Matlab [7]. X and Y are pixel location in the camera frame and the arrow magnitude and direction are the pixel displacement in number of pixels. Other important calibration parameters listed at the bottom. ....	42
4.4 Extrinsic parameters for a stereo setup of two GoPro <sup>®</sup> cameras with each calibration image's position shown using Camera Calibration Toolbox for Matlab. The axes signify location in space (cm) with the origin at the center of the camera pair. ....	43
4.5 Video frame showing camera's field of view of the DWB with blinking LED. The blue box zooms in on where the LED is mounted and the red box is the selection of LED pixel used to generate an output signal. ....	45
4.6 Output LED signals from both videos in a stereo set before synchronization. The right camera (blue) leads the left camera (red) by an average of 1.93 frames, which is calculated from the zero-crossings (x's) from the signals. ....	46
4.7 Video synchronization Matlab program command prompt output displaying the steps of the synchronization process. ....	46
4.8 Frame difference for each zero crossing over the length of an entire WASS video pair including mean frame difference and standard deviation of the dataset. ....	47
4.9 LED signals from the DAQ (red) and a GoPro <sup>®</sup> (blue) synchronized in time using Wavelab. ....	47

## LIST OF FIGURES (Continued)

<u>Figure</u>	<u>Page</u>
4.10	WASS debugging command prompt window initially shown when "launch_wassjs.bat" is run..... 48
4.11	WASS monitor displaying the overall progress of the run at hand, any failures that may have occurred, and the directories WASS is working from..... 49
4.12	WASS spatial data overlaid on its respective video frame with red being higher surface elevations (crests) and blue being lower elevations (troughs). ..... 50
4.13	Gridded spatial data from the scene in Figure 4.12 showing both wave crests and spikes where instrumentation features disrupted the surface elevation data. .... 51
4.14	Screenshot of Intel® RealSense™ Viewer showing spatial data of the DWB water surface with a breaking wave crest in the main right panel. The left panel shows the camera setting controls with the three main tabs: Stereo Module, RGB Camera, and Motion Module with the stereo tab open to show its settings. The red, blue, and green coordinate origin in the right panel represents the position and orientation of the Intel® camera. .... 53
4.15	The LED signals from both the Intel® camera (blue) and DAQ (red) synchronized in Wavelab. .... 54
4.16	(Top) Schematic of idealized water surface mesh with wave crests and direction of propagation (red) and calculated mean water level plane (green), including camera location and orientation with its localized axes. (Bottom) Actual time-averaged point cloud and camera location with model plane (green) of mean water level that was calculated using the RANSAC method..... 56
4.17	Intel® point cloud before (top) and after (bottom) data filtering with data points associated with instrumentation indicated by red shapes. .... 57
4.18	Gridded Intel® data with a focusing wave crest propagating in the positive y direction. The five lines of higher elevation starting around y=6 m are created from the wave gauges and frame supports shadowing these regions from the camera's perspective. .... 58
5.1	Layout of DWB and numbered GoPro® camera angles used in Basin Views experiment. Camera angles: 1. Instrumentation frame high, 2. Instrumentation frame low, 3. Instrumentation bridge towards beach, 4. Instrumentation bridge towards wavemaker, 5. DWB side, 6. Beach corner, 7. Beach center. .... 63
5.2	Screenshot of the output video from Basin Views experiment during regular waves viewed from the beach center (position 7)..... 64



## LIST OF FIGURES (Continued)

<u>Figure</u>	<u>Page</u>
5.3	Screenshots of GoPro <sup>®</sup> videos with Protune on and off from the Basin Views experiment from the instrumentation bridge facing the wavemaker. Top shows GoPro <sup>®</sup> with Protune on with an ISO of 400 and a shutter speed of 1/60. Bottom shows GoPro <sup>®</sup> with Protune off in Auto setting..... 65
5.4	Screenshot of an output video highlighting WASS' ability to reconstruct the foamy trail left by a broken wave crest in the Airy Validation experiment. .... 67
5.5	Signal comparison of WG 11 (red) and WASS (blue) during the trial shown in Figure 5.4. Areas with sharp downward spikes within the WASS data signify an absence of data. .... 68
5.6	Signal comparison of WG 13 (red) and WASS (blue) during the trial shown in Figure 5.4. Areas with sharp downward spikes within the WASS data signify an absence of data. .... 68
5.7	Measured wave gauge data vs. camera data from all broken wave trials in Airy Validation. Linear regression model (grey line) equation shown. .... 69
5.8	Wavelab signal comparison of wave gauge 13 (red) and WASS data (blue) from this location during the beginning of a focusing wave trial..... 70
5.9	Camera vs. WG 13 data for regular (left) and focusing (right) wave cases and their associated linear regression fit and $R^2$ values. .... 71
5.10	Wave gauge measurements vs. WASS measurements for two different NetCDF grid sizes: $dxy = 0.1$ m and $0.5$ m for focusing waves. .... 73
5.11	Linear regression fits and associated $R^2$ values for WASS vs. wave gauge measurements for each gauge locations comparing two different NetCDF grid sizes ( $dxy = 0.1$ m and $0.5$ m) and the onshore (red) and offshore (green) facing camera sets. 74
5.12	Spectral ( $H_{mo}$ ), significant ( $H_s$ ), and mean ( $H_{mean}$ ) wave height values for WASS and Intel <sup>®</sup> vs. wave gauge for the focusing wave case. The blue lines signify a perfect correlation. .... 75
5.13	Peak ( $T_p$ ) and mean ( $T_{mean}$ ) wave periods for WASS and Intel <sup>®</sup> vs. wave gauge for focusing wave case. The blue lines signify a perfect correlation. .... 76
5.14	Intel <sup>®</sup> (top) and WASS (bottom) timeseries vs. WG 13 for regular wave case..... 76

## LIST OF FIGURES (Continued)

<u>Figure</u>	<u>Page</u>
5.15 Time series comparison of Intel <sup>®</sup> (blue) vs wave gauge (red) data for an irregular wave case.....	77
5.16 Wave gauge vs. Intel <sup>®</sup> data with linear regression fit and R <sup>2</sup> value for USWG 1 during an irregular wave case.....	77
5.17 Intel <sup>®</sup> vs. WG data before (top) and after (bottom) filtering. ....	78
5.18 Irregular wave surface elevation time series with individual wave heights (H <sub>n</sub> ) and periods (T <sub>n</sub> ) labeled.....	79
5.19 Relationship between frequency and time domain of an irregular wave time series. Source:[21].....	80
5.20 WG (red) and extracted Intel <sup>®</sup> data node (blue) locations for the irregular wave CERC array. Intel <sup>®</sup> camera location denoted by the camera icon. Both camera and wave propagation direction in the positive x direction. ....	83
5.21 WG (red) and extracted Intel <sup>®</sup> data node (blue) locations for regular (top) and checkered (bottom) directional analysis grid arrays. Intel <sup>®</sup> camera location denoted by the camera icon. Both camera and wave propagation direction in the positive x direction. ....	83
5.22 Crest detection tool output for focusing wave case with measured surface elevation, local crest maxima (black), and wave crest lines (red) represented by polynomial curve fits. ....	84
6.1 Normalized mean wave height (k) for the shore normal regular wave case in the basin coordinate system with direction of wave propagation in the positive x direction. WG and USWG measurements normalized and relative error (ε) between the camera and gauge measurement are also displayed for each wave gauge. ....	89
6.2 Normalized spectral significant wave height (k) for the shore normal regular wave case in the basin coordinate system with direction of wave propagation in the positive x direction. WG and USWG measurements normalized and relative error (ε) between the camera and gauge measurement are also displayed for each wave gauge.....	90
6.3 GoPro <sup>®</sup> screenshots of shore normal regular wave case from (a) instrumentation frame looking offshore (b) instrumentation frame looking onshore (c) basin beach looking offshore. Red arrows indicate areas with larger wave crests. ....	91

## LIST OF FIGURES (Continued)

<u>Figure</u>	<u>Page</u>
6.4	Normalized mean wave period ( $k$ ) for the shore normal regular wave case in the basin coordinate system with direction of wave propagation in the positive $x$ direction. WG and USWG measurements normalized and relative error ( $\epsilon$ ) between the camera and gauge measurement are also displayed for each wave gauge. .... 92
6.5	Average wave profiles for the wave gauges (black) and Intel <sup>®</sup> camera (blue) at WG 13 (left) and WG 10 (right). Shaded regions indicate the standard deviation in wave profiles. .... 94
6.6	Average wave profile height ( $H_{avg}$ ) for the directional regular wave case in the basin coordinate system. WG and USWG measurements are displayed along with relative error ( $\epsilon$ ) between the camera and gauge. .... 95
6.7	Directional wave spectra output from BDM analysis using data from: (a) shortened WG timeseries, (b) Intel <sup>®</sup> 3 by 5 grid array, and (c) Intel <sup>®</sup> CERC array from the directional regular wave case. .... 96
6.8	Directional wave spectrum output from BDM analysis calculated using: (a) extended Intel <sup>®</sup> CERC array timeseries and (b) complete WG timeseries. .... 96
6.9	Normalized mean wave height ( $H_{mean}$ ) for the bidirectional regular wave case in the basin coordinate system. WG and USWG measurements are displayed along with relative error ( $\epsilon$ ) between the camera and gauge. .... 97
6.10	Normalized spectral significant wave height ( $H_{m0}$ ) for the bidirectional regular wave case in the basin coordinate system. WG and USWG measurements are displayed along with relative error ( $\epsilon$ ) between the camera and gauge. .... 98
6.11	GoPro <sup>®</sup> snapshot of waves under the instrumentation frame taken from basin beach during the bidirectional regular wave case. .... 99
6.12	Normalized significant wave height ( $H_s$ ) for the directionally spread irregular wave case in the basin coordinate system. WG and USWG measurements are displayed along with relative error ( $\epsilon$ ) between the camera and gauge. .... 100
6.13	Normalized spectral significant wave height ( $H_{m0}$ ) for the directionally spread irregular wave case in the basin coordinate system. WG and USWG measurements are displayed along with relative error ( $\epsilon$ ) between the camera and gauge. .... 101
6.14	Directional wave spectra output from BDM analysis using data from: (a) WGs, (b) Intel <sup>®</sup> CERC array, and (c) Intel <sup>®</sup> 3 by 5 grid array from the directionally spread irregular wave case. .... 102

## LIST OF FIGURES (Continued)

<u>Figure</u>	<u>Page</u>
6.15	3D polar directional wave spectra from BDM analysis for the Intel <sup>®</sup> CERC array. The radial axis is the frequency [Hz], azimuthal axis is the wave direction [deg], and z axis is the spectral density ( $S(f(\theta))$ )..... 103
6.16	Snapshot from a GoPro <sup>®</sup> video of the focusing wave case viewed the instrumentation frame looking (a) offshore and (b) onshore. .... 104
6.17	Normalized mean wave height ( $H_{\text{mean}}$ ) for the focusing wave cases in the basin coordinate system. The top shows results for a shorter duration video (15 s) taken from a location near WG 8 and the bottom shows a longer duration video (80 s) taken between WG 5 and 6. WG and USWG measurements are displayed along with relative error ( $\epsilon$ ) between the camera and gauge. .... 105
6.18	Normalized spectral significant wave height ( $H_{\text{mo}}$ ) for the focusing wave cases in the basin coordinate system. The top shows results for a shorter duration video (15 s) taken from a location near WG 8 and the bottom shows a longer duration video (80 s) taken between WG 5 and 6. WG and USWG measurements are displayed along with relative error ( $\epsilon$ ) between the camera and gauge. .... 107
6.19	Comparison of (a) predicted spectral significant wave height ( $H_{\text{mo}} \text{ WG}_{\text{interp}}$ ) interpolated from wave gauge measurements and (b) Intel <sup>®</sup> measured spectral significant wave height ( $H_{\text{mo}} \text{ camera}$ ) from the regular shore normal wave case. (c) Difference between each ( $H_{\text{mo}} \text{ camera} - H_{\text{mo}} \text{ WG}_{\text{interp}}$ ) also displayed. WG and USWG locations labelled on each plot as black squares. .... 109
7.1	Example of both RGB (left) and point cloud (right) data collected by the Intel <sup>®</sup> camera of a model mangrove forest. Traditional wave gauges could not be placed in many areas of the flume where they could potentially collide with the lower “root” section of the model trees. .... 119
7.2	Example of RGB (top) and point cloud (bottom) data collected by the Intel <sup>®</sup> camera of the nearshore environment in the DWB..... 120

## LIST OF TABLES

<u>Table</u>		<u>Page</u>
3.1	Test wave conditions for all experiments and trials.....	27
6.1	Average relative camera error for each wave type and statistical analysis method.....	108

## LIST OF APPENDICES

<u>Appendix</u>	<u>Page</u>
A Test Sheets .....	126
B Output Video Screenshots .....	130
B.1 Basin Views Experiment.....	130
B.2 Airy Validation Experiment.....	138
B.3 CPL Filter Experiment.....	140
C WASS Camera Pairs Comparisons.....	142
D Camera Distortion Models.....	144
E Average Wave Gauge Values .....	148
F Intel® RealSense™ D455 Depth Camera Mechanical Drawing .....	149

## LIST OF APPENDIX FIGURES

<u>Figure</u>	<u>Page</u>
B.1 Basin Views WASS auto snapshot for regular wave case from beach center. ....	130
B.2 Basin Views WASS auto snapshot for regular wave case from beach side. ....	130
B.3 Basin Views WASS auto snapshot for regular wave case from instrumentation bridge side toward beach.....	131
B.4 Basin Views WASS auto snapshot for regular wave case from instrumentation bridge side toward wavemaker.....	131
B.5 Basin Views WASS auto lights on snapshot for regular wave case from instrumentation frame high. ....	132
B.6 Basin Views WASS auto lights on snapshot for regular wave case from instrumentation frame low. ....	132
B.7 Basin Views WASS auto snapshot for regular wave case from basin side. ....	133
B.8 Basin Views WASS auto snapshot for focusing wave case from basin beach center. ...	133
B.9 Basin Views WASS auto snapshot for focusing wave case from basin beach side. ....	134
B.10 Basin Views WASS auto snapshot for focusing wave case from instrumentation bridge side toward beach.....	134
B.11 Basin Views WASS auto snapshot for focusing wave case from instrumentation bridge side toward wavemaker.....	135
B.12 Basin Views WASS auto lights off snapshot for focusing wave case from instrumentation frame high. ....	135
B.13 Basin Views WASS auto lights on snapshot for focusing wave case from instrumentation frame high. ....	136
B.14 Basin Views WASS auto lights off snapshot for focusing wave case from instrumentation frame low. ....	136
B.15 Basin Views WASS auto lights on snapshot for focusing wave case from instrumentation frame low. ....	137
B.16 Basin Views WASS protune lights off snapshot for focusing wave case from instrumentation frame low. ....	137

## LIST OF APPENDIX FIGURES (Continued)

<u>Figure</u>	<u>Page</u>
B.17 Basin Views WASS auto snapshot for focusing wave case from basin side.....	138
B.18 Airy Validation WASS snapshot non-breaking regular wave case instrumentation frame toward North.....	138
B.19 Airy Validation WASS snapshot breaking regular wave case instrumentation frame toward North. ....	139
B.20 Airy Validation WASS snapshot breaking regular wave case instrumentation frame toward South. ....	139
B.21 CPL Filter WASS backlit snapshot non-breaking regular wave case instrumentation frame center. ....	140
B.22 CPL Filter WASS fully-lit snapshot breaking regular wave case instrumentation frame center.....	140
B.23 CPL Filter WASS backlit snapshot focusing wave case instrumentation frame center.	141
C.1 WASS spatial/grid spacing study. Wave propagation direction and gauge/camera locations labelled. Linear regression fit equations $R^2$ values shown at each wave gauge locations with red associated with onshore facing camera (Pair 2) and green associated with offshore facing (Pair 1). Table containing linear regression slope, intercept, and $R^2$ values for each grid spacing, wave gauge, and camera pair. ....	142
C.2 WG vs. WASS data comparison plots in plan view of gauge locations for 0.1 m grid spacing with green plots for offshore facing camera pair and red plots for onshore camera pair.....	143
D.1 GoPro <sup>®</sup> Hero 6 R25 (Pair 1) distortion models. ....	144
D.2 GoPro <sup>®</sup> Hero 6 L48 (Pair 1) distortion models.....	145
D.3 GoPro <sup>®</sup> Hero 6 3433 (Pair 2) distortion models. ....	146
D.4 GoPro <sup>®</sup> Hero 8 1885 (Pair 2) distortion models. ....	147
F.1 Mechanical drawing of Intel <sup>®</sup> RealSense <sup>™</sup> D455 external housing. Source: [37]. ....	149
F.2 Mechanical drawing of D4Vission Processor board. Source: [37].....	150



## LIST OF APPENDIX TABLES

<u>Table</u>		<u>Page</u>
A.1	Basin Views experiment test sheet .....	126
A.2	Airy Validation experiment test sheet.....	127
A.3	CPL Filter experiment test sheet.....	127
A.4	Two Stereo Pairs, Intel® Cam, Frame experiment test sheet. ....	128
A.5	Two Stereo Pairs, Intel® Cam, Beach experiment test sheet. ....	129
E.1	Average measured wave gauge values for trials discussed in Chapter 6.....	148

## **Chapter 1 Introduction**

Understanding the coastal environment is a fundamental task for any coastal scientist or engineer. It is essential to the longevity of the many communities bordering our oceans, and requires an assortment of research tools to continually advance our current knowledge. Scientists often utilize physical and numerical modelling to investigate a research question. Physical models are simplified material representations of the object or process being studied, while numerical models are computational simulations that use mathematical equations to estimate physical outcomes. In the realm of coastal and ocean engineering research, physical modelling plays a vital role in investigating and understanding scientific questions that have yet to be answered. Although numerical and analytical models continue to advance what scientists are able to explore, the dynamic and complex nature of the marine environment often requires the use of scaled physical models within a wave research facility to accurately analyze a structure design or theoretical research question.

Hydrodynamic testing on newly designed coastal and offshore infrastructure is an important aspect of the engineering process and requires precise, repeatable wave and current forcing that simulate the extreme conditions these structures may see in a natural coastal environment. Wave research flumes, basins, and tanks provide a facility where scientists can control these variables and design experiments without concern for the randomness and unpredictability of the ocean. Modern wavemakers are capable of generating similar conditions to what are seen in the ocean, called irregular waves, or further simplify the forcing by generating a chain of identical waves, called regular waves. Researchers can input the desired wave conditions into computer software and the wavemaker's electronic control system will produce the waves in a repeatable manner. Once generated, the physics and mechanics of wave propagation can no longer be controlled by the facility though. A wave may be generated in a certain shape or amplitude and evolve due to wave transformation processes such as reflection, refraction, shoaling, and diffraction or other more complicated processes such as bottom friction, viscous effects, wave breaking, and non-linear particle interactions. This makes data collection a very important aspect of research so that precise hydrodynamic measurements can be taken in the area of interest.

One of the most important and commonly collected data measured within a wave laboratory is the elevation of the water surface, or free surface. The free surface is defined as the interface between two homogenous fluids [44]. In the case of a water surface within a wave research lab, these fluids are the air and water within the basin or flume. It is referred to as the free surface because it is only constrained by gravity and the physical rules of our universe, allowing it to move in a limitless variety of complex three-dimensional motions in reaction to whatever energy may be input. In an attempt to understand these motions, different instruments are used to measure its elevation over time. Water surface elevation is typically measured in a single, stationary point in space, therefore called a point measurement. These generally require a high time resolution, or sampling rate, to adequately capture variations of the free surface, which can often change quite fast in a coastal laboratory. A series of point measurements can be taken throughout the length of the wave flume or basin so that wave characteristics can be quantified in multiple areas where the researcher deems necessary. Although these methods are highly accurate at collecting two-dimensional surface elevation data, they require spatial interpolation to estimate wave conditions in any area where a point measurement is not taken. As previously mentioned, the motion of the water surface and the evolution of waves over space and time is not always straightforward, so inferring what is happening in one area based off of measurements from another can lead to errors. The current theoretical understanding of wave physics allow relatively accurate assumptions to be made about the propagation and transformation of laboratory waves. It is generally expected that waves will remain spatially and temporally identical unless disruptions such as changes to water depth and obstructing specimen are included, but this is strictly theoretical and other processes may introduce unpredictable variability. Analytical and numerical models that utilize our current knowledge of wave mechanics can greatly increase spatial prediction accuracy, but still assumptions must be made and the chance of error persists. Wave conditions can vary in a small amount of space, especially once research specimens and structures are introduced, so the need for surface elevation instruments with high spatial resolution arises. This need is ubiquitous across coastal engineering applications, as spatial measurements are often required for field work and numerical modelling as well.

Obtaining a dataset with high spatial resolution using point measurements often requires a number of gauges and support framing that may be infeasible within the spatial limitations of a

laboratory. Surface elevation instrumentation and their supportive framing generally penetrate into the water or is even secured to the bottom of the basin or flume, disrupting the surrounding hydrodynamics. This can be an issue in the case of a single instrument, so when a large array of instruments must be deployed the problem greatly increases. Not only is this hydrodynamically disruptive, it can also be very difficult and time intensive to deploy. For these reasons a single instrument, or instrumentation system, is sought out that is capable of three-dimensionally reconstructing a significant spatial extent of the free surface within a laboratory setting.

### *1.1 Research Goals and Objectives*

The scope of this Master's thesis is to research the cutting edge in instrumentation that is potentially capable of spatially measuring the free surface in a variety of wave conditions, selecting and implementing one or more of these systems into the wave research lab at Oregon State University, and analyzing their ability to accurately measure the water surface in comparison to traditional point gauges. Multiple wave conditions and instrumentation layouts will be used to understand the limitations of these systems and optimize their performance for use in future research. A methodology is developed to incorporate the instrument(s) into the lab's preexisting data acquisition procedures. Calibration and post-processing routines are developed to analyze spatial data using traditional and non-traditional wave analysis techniques.

Measurements are compared to conventional point measurement surface elevation instruments for validation and spatial resolution comparison. Wave characteristics such as average wave height, period, and directionality are calculated with a variety of techniques to explore the capabilities of the systems.

The objective of this study is not to replace conventional point measurement techniques, but rather compliment them with a system that can expand the capabilities of data collection within the lab. This will potentially increase our spatial understanding and awareness of the free surface during testing while decreasing the number of instruments required to do so. Existing technology will be utilized for the advancement of coastal engineering and wave laboratory data collection. This project is not intended to develop new instrumentation, but unique methodologies may be required to implement the selected instruments.

## 1.2 *Document Overview*

This chapter introduced the project's scope and discussed the relevance of the research problem at hand. The general research goals and objectives were stated. Chapter 2 contains a review of literature discussing any potential instruments for this application along with their limitations. Past research studies are reviewed and pertinent findings are summarized before two instrumentation systems are selected. These systems are then described and their functionalities are detailed. Chapter 3 describes the experimental setup and procedure used for each experiment in this study. The facility, instrumentation, wave conditions, and experiments are all thoroughly described. Chapter 4 outlines the data processing methodology that was developed for each system's setup, use, and post-processing. Chapter 5 describes the data analysis techniques applied to each experiment and discusses the preliminary findings. Both systems are compared and one is selected for further analysis based on overall performance. Chapter 6 displays the results of an in-depth spatial analysis from the selected system. The results are organized by wave case and findings are discussed. Chapter 7 offers concluding remarks for both systems, research considerations, and suggestions for future use.

## Chapter 2 Surface Elevation Reconstruction Methods

This study intends to research, select, implement, and analyze instrumentation that is capable of three-dimensionally reconstructing the water surface within a wave research laboratory. A number of systems will be investigated in the literature so that the most feasible can be selected for testing. It will be implemented into an indoor facility and its ability to spatially measure a variety of wave conditions will be assessed. This chapter contains a review of literature that states the instrumentation options available for this application and briefly discusses their use in previous studies and the pertinent findings. Then the two most feasible systems are selected and their functionalities are further discussed. The hardware and software required for each is described along with their expected uncertainties.

### 2.1 *Review of Literature*

The most common method for measuring water surface elevation in a laboratory environment is using fixed point measurement instrumentation such as surface piercing wire wave gauges. The direct measurement of wave characteristics using these instruments can supply reliable, highly accurate data that is easily validated, but it has its limitations. This instrumentation is spatially constrained to one location and generally requires supportive framing that may disrupt the surrounding hydrodynamics. New non-intrusive methods of measuring the water surface profile are currently being explored that can instantaneously measure the water surface elevation at a high spatial resolution without affecting the hydrodynamics of the experiment. There are several different techniques that utilize a variety of instrumentation types with this capability. The aim of this review of literature is to discuss several of these methods along with their limitations, then select two systems that are deemed most feasible for implementation within the wave research lab at Oregon State University.

Emec et al. [19] reviews a variety of non-intrusive wave measurement techniques that are used in both the lab and field. They categorize these instruments into optical and acoustic sensors, radar, video, and combined video hybrid systems. These methods may require certain lighting and water qualities to be accurate and cost often varies from system to system. The systems that fall within the spatial and budgetary constraints of this project are discussed and their application within the literature is reviewed.

### 2.1.1 *Radar Scanners*

Radar scanners have the ability to take three-dimensional point data at very fine resolutions in space and time. Terrestrial laser scanner (TLS) have previously been used for wave flume water surface measurements [28]. The measurements were validated with traditional point measurement wave gauges and proved to be accurate, but the reflectivity of the water proved to be an issue. The water was intermittently seeded with clay and foam particles to decrease reflectivity. The Leica TLS system used is very expensive and requires a large amount of data post-processing. Adding seeding material to the water is not always desirable either. It can interfere with instruments and in certain wave conditions it tends to concentrate in small areas, which requires the experiment to be stopped and the material redispersed. This may be feasible for certain projects but does not have the potential to be applied to a variety of projects in the future.

### 2.1.2 *Shape from Shading*

Shape from shading is a lower cost method that is often used for visual animation purposes and visual effects. It uses a single video camera and a visual algorithm that recognizes surfaces based on the lighting and shading of the image. Liu et al. [41] used shape from shading to reconstruct the water surface geometry while focusing on simplicity, cheapness, and efficiency but disregarding accuracy. This method relies on shallow water physical wave assumptions to recreate the water surface being filmed. Although it is cheaper and less time intensive, its accuracy would not be appropriate for most academic research.

### 2.1.3 *Edge Detection*

Edge detection is another single video method that uses feature detection algorithms to differentiate the water surface from its contact point with the side of the wave flume wall. The transparency of the water surface makes it difficult to differentiate between the water surface and the surrounding air environment so a line detection method is utilized at the water-to-air interface at the edge of the flume. Although not necessarily required, many experiments that have utilized this method in the past were in a glass walled wave flume with the camera filming through the glass wall [40][59]. Others painted stripes inside of the wave flume wall to assist the algorithm in differentiating between the water surface and the wall [54]. This method could work well but the spatial extent of the measurements is only a single line along the wall of the flume or basin and

the area in the center must be interpolated. This may be feasible for a narrow flume or non-directional waves, but greatly limits the capacity of this technique.

#### 2.1.4 *Structured Light Methods*

Other fields of study use structured light-based methods, which project known patterns of light onto an object in order to three-dimensionally reconstruct its surface. The deflection of the light pattern can be used to calculate surface slope and then derive surface elevation. Liu et al. [42] projected a laser dot matrix onto a cylinder to calculate the surface shape and Deetjen et al. [17] projected a grid of horizontal and vertical laser strips onto a moving bird to reconstruct the wing surface at a high temporal resolution with small error (0.31 mm). This method proves more difficult when measuring a water surface due to the transmission of light through the water, but may still be applied if light refraction is considered.

Dabiri et al. [14] projected a series of colored beams onto the water surface and used each beam's refraction through the water to calculate the free surface slope. The slope was then used to derive the surface elevation in high accuracy but was spatially limited to a 200 by 140 mm region and may not be as applicable in a larger region. Grant et al. [25] suggested a similar approach, instead using a laser dot matrix, and concluded that this approach could be scaled. These approaches generally require a very specific ambient lighting, which may prove problematic in a laboratory with windows. Gomit et al. [23] used this method in combination with stereography and particle image velocimetry to measure water particle velocity and surface elevation, but this method requires extra thermal imaging equipment which can be expensive. The laser pattern generally needs to be reflected by the free surface, which may not be the case without seeding material or wave breaking.

#### 2.1.5 *Stereo Photogrammetry*

Stereo photogrammetry, also known as stereoscopic or stereo imaging, uses two or more cameras to view the same surface, then triangulate a point cloud out of the matched pixels from each view. If the exact location of each camera is known along with how each lens distorts the scene being filmed, the images can be rectified into a common image plane and used to measure desired characteristics of the view in real-world coordinates. This technique has long since been proven to be useful for wave and ocean research. Holthuijsen [35] introduced the basics of stereo photogrammetry to the oceanographic field by mounting two cameras on a helicopter to collect



images of the open ocean and measure characteristics of the sea state. In the past this method was too computationally intensive, but it is now feasible with the computing power available.

Many studies have shown its validity in field research [4][51][53] where the water surface is texturized and light reflection and refraction are not an issue. De Vries et al. [15] compared the method in both a laboratory and field scenario and proved that the clarity of the water inside the lab is an issue with surface detection. Several solutions to this problem have been attempted to create a less transparent water surface. De Vries et al. [15] and Perelman et al. [49] both used diffuse ambient lighting and a fine mist sprayed over the water surface to create contrast in their pictures. Perelman et al. [49] also texturized the water surface by blowing wind across it to create small capillary waves and seeded it with floating particles to homogeneously cover the surface. Douxchamps et al. [18] seeded floating wood particles but found that after some time the particles formed groups within the wave-breaking zone and no longer homogeneously covered the water surface. Tsubaki and Fujita [56] dyed the water with a white opaque tint and Harry et al. [28] dispersed clay within the water. These methods are simple solutions to the laboratory water reflectivity issue, but each have their limitations. Several of these techniques were applied to the facility of interest [3], but modifications were needed for success. A combination of instruments, including stereo cameras and a laser scanner, was used to measure the surface elevation and velocity field of the nearshore region in a wave basin, which showed the potential for a combined system. The water was seeded with plastic beads, flakes, and surfactant in an attempt to find the best method.

#### *2.1.6 Combined Stereo Methods*

In some cases, a combination of instruments is utilized to increase system accuracy and the number of attributes that can be measured. Particle Image Velocimetry (PIV) methods use infrared cameras to track water particles that are heated with a pulsed laser pattern [34]. These water particles become passive tracers that are tracked by the infrared camera so that water column velocities can be derived. This method has been combined with stereo photogrammetry methods in order to reconstruct the water surface [32][52]. Another technique called laser-induced-fluorescent imagery uses a laser sheet to illuminate the water surface with the aid of fluorescein dye to be measured by high-speed cameras [11]. The issue of water reflectivity is

solved but these methods require infrared camera equipment and powerful lasers which can be expensive.

Other methods include the use of structured light to enhance the accuracy of their stereo system. When a pattern is projected onto the object being measured, the cameras can use them to assist in matching the pixels from each view, an essential process to stereo measurement. The addition of a light projection adds texture to the scene and can make image matching unambiguous. Bung et al. [10] utilized a consumer grade system like this to accurately measure a hydraulic jump in a laboratory setting. These systems have a wide variety of applications within robotics, health care, and virtual reality making them openly available to the commercial and scientific community for further development. Stereo matching using infrared cameras has also been applied in both laboratory and field applications for wave measurement [32][55]. The use of infrared imaging decreases the reflectivity problem associated with imaging the water surface, but may introduce its own set of limitations.

## 2.2 *System Selection*

Each of these techniques have their advantages and disadvantages in a laboratory setting, but stereo and combined stereo methods seem the most feasible considering the budgetary and spatial constraints of this project. Benetazzo [4] presented an open-source software called the Wave Acquisition Stereo System (WASS) that is a free code pipeline that analyzes user input stereo images of ocean waves specifically. The system was implemented on offshore ocean platforms to analyze wave conditions. An open-source dataset collected from multiple field locations was analyzed using WASS and presented [27]. Root-mean-squared (RMS) error values ranged from 1-9 cm and large spatial extents were able to be measured dependent on the camera setup. Although 9 cm is large when considering laboratory waves, it is much smaller relative to the open ocean waves it was calculated from. WASS was designed for field applications such as this, but has also been successfully implemented in a laboratory setting [61]. Due to its past success, open-source availability, and the ability to customize hardware and their orientation, WASS is the first system selected for implementation.

The second method selected for implementation is a combined stereo structured light method. Past studies have customized their own systems by using specific hardware and developing

matching algorithms that are adapted to a specific setting, but this is out of the scope of this project so a preexisting system was selected for use. The Intel® RealSense™ D455 depth camera [37] was selected based on its low price and previous application to free surface measurements in a laboratory setting [10]. Both systems that were selected are thoroughly described in the following sub-sections.

### 2.3 Wave Acquisition Stereo System (WASS)

As previously mentioned, WASS was the first free surface measurement system selected for implementation in this study. To review, it is an open-source software pipeline that requires user input stereo images that are analyzed by WASS to output a reconstructed three-dimensional point cloud of the scene in frame. Cameras are not provided, so the user is given the flexibility of selecting hardware within their budgetary limits and orienting the stereo pair specific to their needs. This is especially important when deciding upon the size of the target measurement area and adjusting the distance between each camera, also known as the stereo baseline. Typically, a larger stereo baseline allows one to measure a larger area and vice versa. With the research goal of measuring waves in a laboratory setting, the stereo baseline will be much smaller when compared to field applications. The downside to hardware customization is that camera calibration is required. WASS requires the input of intrinsic parameters, which define the camera's lens distortion and focal length, for each camera in use. These are calculated through the individual calibration of each camera, further described in Section 4.1.1. Hardware selection and orientation are also important and will be discussed in Chapter 3. This section, however, focuses on the internal workings of the WASS software, overviewing the software architecture and its functions, the uncertainty involved, and several examples of previous system applications. It is noted that stereoscopic measurement and the development of a customized matching algorithm are very involved and complicated processes. This section by no means details the more complex aspects of WASS, but merely offers a brief overview to give readers a general understanding of basic stereoscopic methods.

#### 2.3.1 Software Architecture

There are four main components within the WASS software pipeline: *wass\_prepare*, *wass\_match*, *wass\_autocalibrate*, and *wass\_stereo* [7]. Together, these allow the user to advance from a directory of synchronized video frames and intrinsic camera parameters, to a dataset of

filtered three-dimensional point clouds reconstructed for each video frame. This section describes the basic functions of each component and how they collaborate within WASS.

The first function, *wass\_prepare*, initializes the working directories for each image pair. The user must first allocate a single directory for each camera being input, save individual video frames as images with a specific file naming system, and create a configuration directory containing each camera's intrinsic parameters. Once the appropriate directory architecture is setup, *wass\_prepare* can then recognize image pairs, create the correct output file structure for each, and undistort the images based upon the input camera intrinsics. The data is then prepared for the next functions to complete stereo matching and extrinsic calibration.

The *wass\_match* function randomly selects a set of calibration image pairs to use for the extrinsic calibration processes. The extrinsic parameters of a stereo pair are the position and orientation of one camera relative to the other. Generally, extrinsic parameters would need to be measured for the stereo pair, but the autocalibration feature of WASS automatically calculates this using the input stereo images. Once the calibration images are selected, *wass\_match* matches features in the image pairs using the framework from Albarelli et al. [1]. Erroneous matches are removed using RANSAC-based epipolar filtering [7]. Now the extrinsic parameters of the stereo pair are ready to be calculated.

The *wass\_autocalibrate* function utilizes the results from *wass\_match* to automatically calibrate the extrinsics of the stereo pair. It assumes that the cameras remain stationary during the duration of each input video so that only a single set of extrinsic parameters must be calculated. Once calculated, the parameters are input into the configuration directory in two separate files containing the translation and rotation matrix. These matrices numerically define the geometric transformation of one camera's location from the others. If desired, *wass\_autocalibrate* can be turned off and the camera pair can be manually calibrated.

Finally, the *wass\_stereo* function outputs a dense three-dimensional point cloud of each image pair. Images are rectified using the intrinsic and extrinsic parameters of the cameras. Image rectification is the transformation of two or more stereo images into a common image plane. This results in two geometrically corrected images that align with one another, as seen in Figure 2.1. Disparity, or the horizontal distance between objects in the left and right images, is then calculated for each frame using a semi-global dense stereo method [33]. This is a feature matching method that combines techniques from both local matching, where pixels from either

image are matched within a specific window, and global matching, where pixels from either image are matched from the entire image. The semi-global technique increases the accuracy of the local technique while decreasing the computational time required from the global technique. The resulting disparity map is then partially filtered to decrease any holes within the dataset. Because this system was specifically designed for use in the open ocean, any data points not associated with the sea surface are also filtered. The water surface is assumed to be continuous and relatively smooth, therefore any data point with an abrupt elevation change relative to its neighbor is removed. Finally, the cleaned point cloud is rotated into a gravitational coordinate system by estimating the mean sea plane and using it as the x-y plane. Each image pair's resulting point cloud is saved within their specific output directory for further analysis.

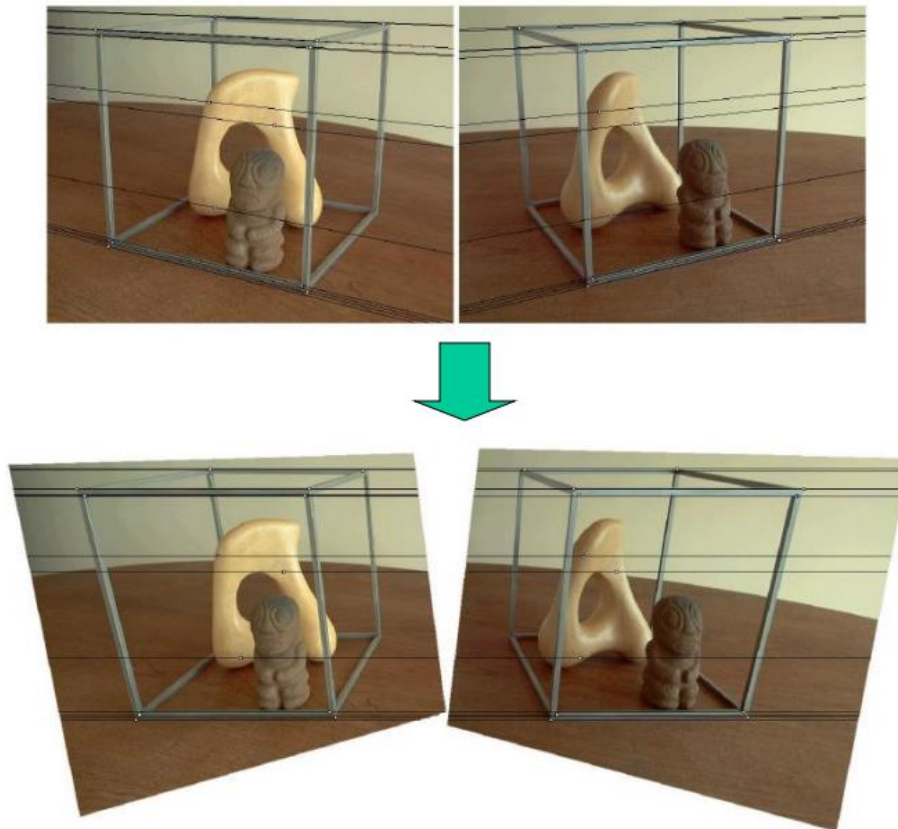


*Figure 2.1: Example of stereo image rectification. Source:[22].*

### 2.3.2 Uncertainties

Uncertainties from these processes originate from four main components: intrinsic and extrinsic calibration, pixel matching, recovery of three-dimensional coordinates, and mean sea level

estimation [7]. These uncertainties eventually propagate into water surface elevation error, which is dependent on the location of the data point within the camera frame. Figure 2.2 shows the calculated elevation error from a field application, with an increase in elevation error as distance from the cameras increases. Guimarães et al. [27] offers validation of the WASS system in comparison to in-situ wave gauges at several different open ocean sites. Four separate root-mean-square error values were parameterized in this study: error in  $x$ ,  $y$ , and  $z$  and frequency. These errors were quantified from a variety of locations and the expected error values for each were displayed. Errors ranged from 1-9 cm and 0.5-1.4 Hz for  $z$  and frequency respectively.

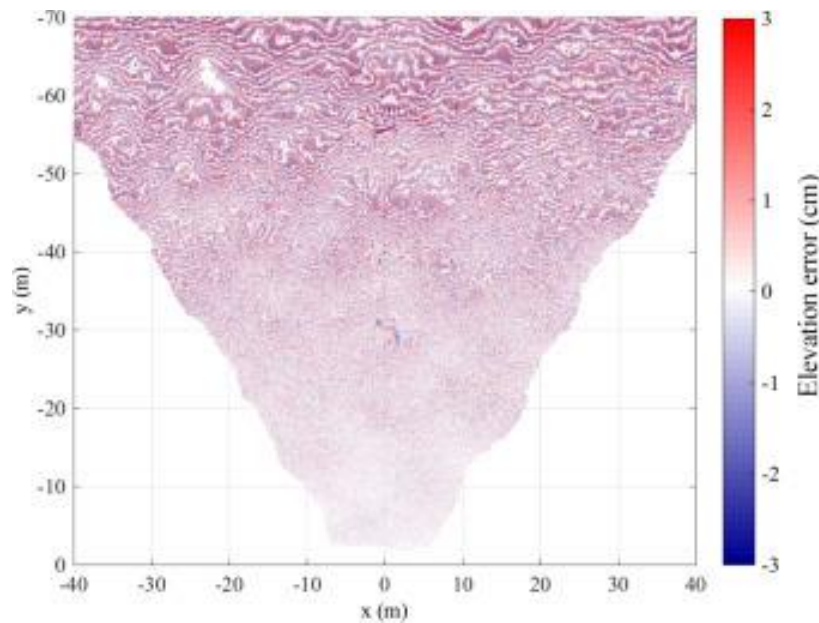


*Figure 2.2: Elevation error with respect to horizontal field of view in a field application. Stereo cameras located at the origin. Source:[7].*

### 2.3.3 Applications

Along with the aforementioned studies, WASS has been applied to numerous applications in both the field and laboratory. The majority of these studies consisted of data collection on oceanographic platforms [4][5][7][27], but others have also applied similar systems on moving vessels at sea [53]. WASS' validity has also been proven using low cost smart phone cameras in a smaller measurement [58]. This technique has also been applied in laboratory settings for three-dimensional wave analysis in a wave flume [60], but much less frequently than in the field due to lighting and reflectivity issues.

## 2.4 Intel® RealSense™

The second spatial free surface measurement system selected for implementation in this study is an infrared structured light stereo camera developed by Intel®. Unlike WASS, the Intel® RealSense™ system is based around a hardware product, the D455 depth camera. This is an off-the-shelf, consumer grade sensor that uses infrared (IR) projected light structure to aid the stereo reconstruction of two onboard IR depth cameras. A traditional RGB camera is also included to assign color values to each reconstructed data point. A software package is included that allows the user to control the camera settings and view real-time two and three-dimensional data while recording from a computer. Numerous open-source tools have also been built by different communities in a variety of code languages. Both the hardware and software provided with this system are detailed in this sub-section along with expected uncertainties and various application examples.

### 2.4.1 Hardware

Two main components of the D455's hardware system are described herein: the depth module and the processing module. The depth module houses the camera system's sensors and the processing module consists of a chip that processes sensor data in real-time among other functions. Mechanical drawings of both components can be found in Appendix F.

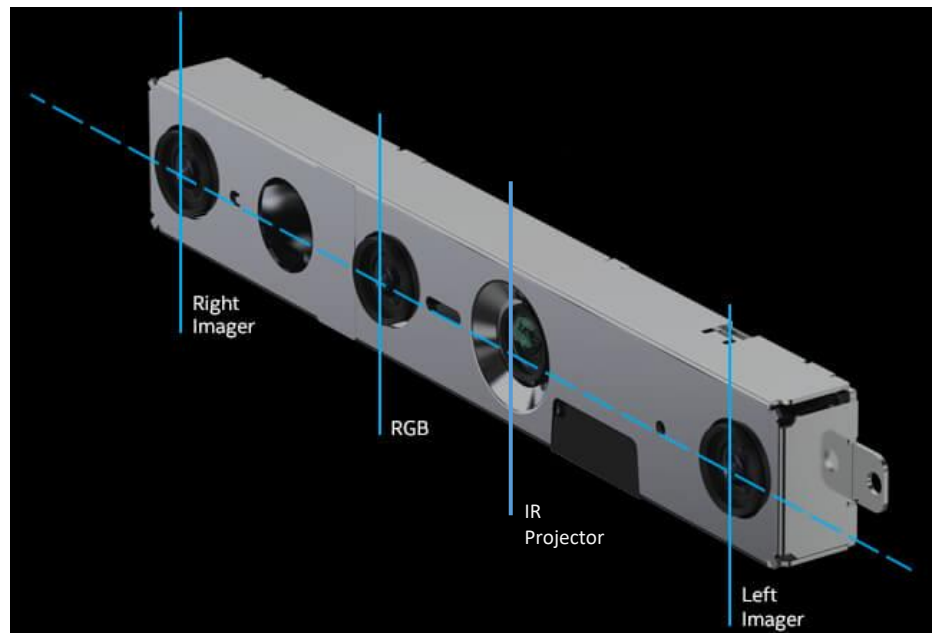
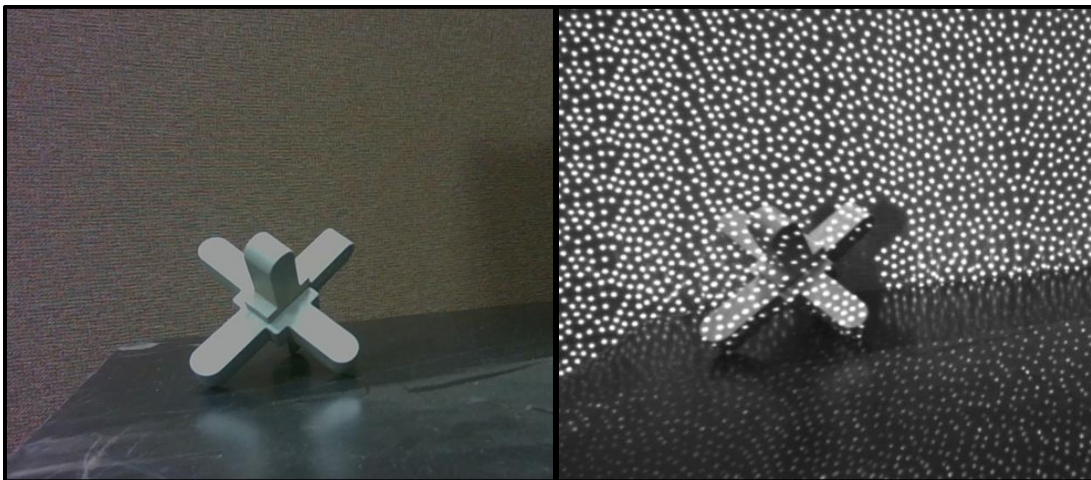


Figure 2.3: Internal sensor housing of the Intel® D455 Depth Camera with sensor labels. Source: [37].

The internal housing of the depth module is displayed in Figure 2.3 with each sensor labeled, excluding the internal motion unit (IMU). There are four components that make up the depth module: the stereo imagers, an IR projector, RGB camera, and the IMU. There are two stereo imagers that are identical IR cameras with a stereo baseline of 95 mm. These sensors collaborate with the IR projector to calculate stereo depth. The IR projector is a class 1 laser that projects a static, random IR dot matrix on the scene to provide the recorded scene with more texture. The randomness of the pattern assures unambiguous stereo matching which increases accuracy. Figure 2.4 shows an example of an RGB and IR image taken from the Intel<sup>®</sup> camera showcasing the projected random IR pattern. The RGB camera records high definition video and assigns each spatial data point with a color value, making the visual appearance of the dataset more realistic. Finally, the IMU tracks the motion and orientation of the camera system while recording. All of these systems are synchronized either by hardware triggers or internal post-processing.



*Figure 2.4: RGB (left) and IR (right) images from the Intel<sup>®</sup> D455 camera showing the projected IR random pattern that assists with stereo matching.*

The processing module is comprised of a D4 image processor that internally completes real-time stereo reconstruction of the recorded scene. It rectifies video frames and controls the IR projector and sensor settings. The stereo imager synchronization is controlled within this unit as well and RGB image data is integrated into the spatial data. A high precision internal clock is used to timestamp each individual RGB and stereo frame accordingly. Power delivery and USB data connection port are also located within this module.



### 2.4.2 *Software*

Intel<sup>®</sup> offers image processing software with this product which includes the stereo reconstruction firmware contained within the D4 processor. This firmware consists of similar stereo matching algorithms as described for WASS that utilize factory calibrations and in-house developed computational techniques for stereo reconstruction. Unlike WASS this system was not developed for sea surface measurement, rather for a wide variety of applications. Many of the filtering techniques described for WASS are thus not used within the Intel<sup>®</sup> system, but others must be applied.

Intel<sup>®</sup> offers a Software Developer Kit (SDK), which includes a desktop application called the Intel<sup>®</sup> RealSense™ Viewer. This program allows the user to control the camera system and adjust its settings as needed before recording data. It displays real-time two and three-dimensional data while the camera is recording. This can be useful for data visualization and inspection during experimentation. The program includes a self-calibration process that can recalibrate the camera system if needed. Data filters and post-processing routines can be controlled from this application as well. The SDK and its use in this study is further described in Section 4.2.1.

### 2.4.3 *Uncertainties*

Similar to the WASS system, uncertainties are present in the stereo reconstruction methods used in the Intel<sup>®</sup> system. The R200, a predecessor product to the D455, was analyzed to understand the RMS error in depth related to distance from the camera [38]. At approximately 5 m from the camera, a depth error of 6 cm could be expected. The technology within the D455, however, has progressed since the R200 and the camera system has become more accurate overall. Wang and Shih [60] analyzed the D455's ability to measure small elevation differences at different distances and the noise output by the camera when measuring static, flat surfaces. Millimeter accuracy was achieved in near range, but this project will likely implement the camera at a greater distance to the desired measurement surface, leaving expected uncertainty undefined.

### 2.4.4 *Applications*

As previously mentioned, this system has been used in a variety of applications including but not limited to robotics, 3D scanning, object tracking and measurement, facial authentication, cinema,

and video game development (<https://www.intelrealsense.com/use-cases/>). The most similar application reported in the literature was the use of the Intel® D455 to measure a hydraulic jump in a laboratory setting [10]. Similar to the scope of this project, their research goal was to spatially measure the dynamic free surface of a hydraulic jump, a phenomenon common in high velocity riverine flows. The camera measurements were then validated with traditional point gauges. Although successful, a hydraulic jump is more aerated and static when compared to water waves, so different conclusions are expected.

## 2.5 *Chapter Conclusions*

This chapter contained a review of literature of the state-of-the-art instrumentation and techniques that could potentially be implemented to spatially measure the water surface within a laboratory setting. Stereo and combined stereo techniques were deemed the most feasible for their low cost, and previous success in three-dimensional measurement and two systems were selected for implementation: WASS and an Intel® RealSense™ Depth Camera. WASS, or Wave Acquisition Stereo System, is an open-source stereo image processing pipeline developed for the specific purpose of measuring the sea surface. The Intel® RealSense™ system is a consumer grade stereo camera that utilizes infrared active stereo techniques to three-dimensionally measure the scene recorded. Expected uncertainties and previous applications were discussed for each. The following chapter will introduce the facility used throughout experimentation. Experimental setup and procedures are described.

## Chapter 3 Experimental Setup & Procedure

This study aims to implement and assess two stereo-video free surface measurement systems in a wave research laboratory at Oregon State University. Two separate systems, described in detail in Chapter 2, will be tested in various wave conditions and validated using more classical point measurement instruments such as surface-piercing resistive wave gauges and acoustic wave gauges. This chapter describes the facilities at Oregon State that were used for testing along with the experimental setup of instrumentation, cameras, and data acquisition system. The experimental procedure, the progression of tests completed, and the numerous test wave conditions used for validating the stereo-video measurement systems are also described.

### 3.1 Experimental Setup

#### 3.1.1 Wave Basin

These experiments took place in the Directional Wave Basin (DWB) which is located in the O.H. Hinsdale Wave Research Laboratory (HWRL) at Oregon State University in Corvallis, Oregon. It is a 48.9 m long, 26.5 m wide, and 2.1 m deep wave basin designed for tsunami research, testing of coastal infrastructure, as well as nearshore processes and wave hydrodynamic research [20]. The basin is equipped with a snake-type, wet-backed wave-maker developed by MTS Corporation for generating regular, irregular, solitary, and directional waves. There are 29 waveboards in total, each is 2.0 m tall and driven by two servomotor actuation points on either side of the board for a total of 30 actuators. The maximum board stroke is 2.1 m and the maximum velocity is 2 m/s [31]. The wavemaker is controlled by an MTS wave generation software that allows the user to input wave characteristics such as wave type, wave height, wave period, and direction to achieve the desired wave field. Waveboard displacement files generated by third party sources can also be loaded into the system to run. This allows the user to generate repeatable wave conditions for testing within the physical limitations of the system. The system is limited by the basin dimensions (water depth, wave height) and the limitations of the wave-maker (board velocity, acceleration, displacement, force exerted on each board). The maximum water depth is 1.84 m, but no waves can be generated at this depth. The maximum wave height is 0.85 m which can be generated for depths from 1.15 to 1.35 m and the wave period can range from 0.5 to 10 s [20]. The DWB is pictured in Figure 3.1.



*Figure 3.1: Image of the DWB generating breaking long-crested waves looking toward the wave-maker.*

The DWB has a 1:10 sloped removable steel beach that was left in place for testing in this study. Unistrut floor attachment points span the floor of the basin in the alongshore direction every 1.22 m for specimen and instrument installation. A 7.5-ton bridge crane above the DWB assisted in positioning heavier objects throughout the basin. A movable instrumentation bridge that spans the width of the basin was positioned to support data acquisition equipment and instrumentation over the center of the basin during testing. The coordinate system for the DWB is defined with the origin located at the center of the base of the wave-maker when its stroke is in neutral position. For reference, the DWB runs East-West within the HWRL facility with the wave-maker at the East end of the basin. Positive x-direction is therefore defined to the West along the direction of wave propagation. Positive y-direction is defined South along the wave-maker and positive z-direction is upwards. The DWB layout and coordinate system is shown in Figure 3.2.

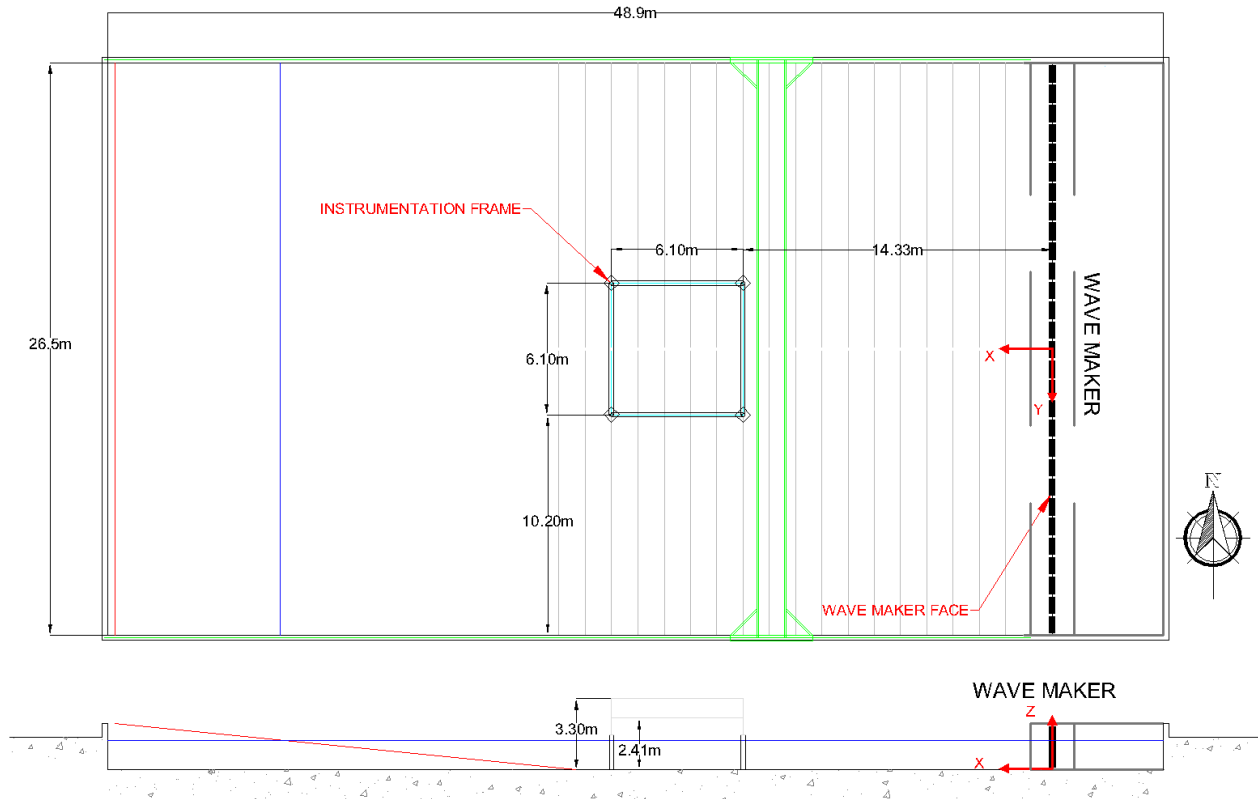


Figure 3.2: DWB layout with wave-maker position, coordinate system, and instrumentation frame labeled. Top shows the plan view of the basin and bottom shows a section view.

### 3.1.2 Instrumentation

There were two main sets of instrumentation used for this study: the camera equipment along with its required lighting and accessories, and the HWRL point measurement instruments with their required support frame and acquisition system. These instrumentation systems are described in this subsection.

#### 3.1.2.1 Instrumentation Frame

The instrumentation frame used to position and support the HWRL instrumentation over the water surface was re-utilized from a previous project in the DWB for convenience. The frame's perimeter was a 6.10 m by 6.10 m square whose center point was located 17.38 m away from the wavemaker face in the positive x-direction and centered in the width of the basin. Four large circular support columns were fixed to the Unistrut floor attachment points in the basin and acted as the base of the frame in the water. The body of the frame was constructed on top of these base

supports and secured in place. The frame body was constructed out of aluminum tubing and Unistrut cross supports, upon which most of the instrumentation was attached to. This simplified instrument deployment and relocation is necessary. To further support the frame and decrease its movement due to wave forces, guy wiring was attached and fed outward toward the basin floor. The frame measured 3.30 m high from the basin floor with the additional Unistrut cross supports at 2.41 m, as seen in the cross-sectional view in Figure 3.2.

#### *3.1.2.2 Surface-piercing Resistive Wave Gauges*

Surface-piercing resistive wave gauges (WG) were the primary free surface elevation point measurement used for the validation of the camera systems. These consist of two vertical, parallel steel rods spaced slightly apart that penetrate the water surface. They are fixed in place and measure the free surface elevation at the point where the wires come in contact with the water. A current is run through the wires and the resistance is measured, which is correlated to the water surface elevation through a calibration process when the basin is filling or draining. Ten resistive wave gauges were fixed to the Unistrut cross members of the support frame to measure water surface elevation in locations along the perimeter of the frame. Details on their location can be found in Section 3.1.4.

#### *3.1.2.3 Acoustic Wave Gauges*

Acoustic wave gauges, also known as ultrasonic wave gauges (USWG), were the secondary free surface elevation point measurement used for the validation of the camera systems. USWG's measure the free surface elevation by directing sound waves down towards the surface of the water and recording the time it takes for them to reflect back to the gauge. Unlike WGs, they are nondisruptive and do not need to penetrate into the water to measure its elevation, but they have range limitations and difficulty measuring steep or broken waves. Details on the USWG locations can be found in Section 3.1.4.

#### *3.1.2.4 Camera Equipment*

Two different camera systems were used in this study: WASS and an Intel® RealSense™ Depth Camera. Details on these camera systems are described in Chapter 2. The cameras selected for use with the WASS system consisted of four GoPro® cameras. In preliminary tests, a single pair (Pair 1) of GoPros® was used and in the final tests a second pair (Pair 2) was added. Pair 1

consisted of two GoPro® Hero6 Blacks and Pair 2 was a GoPro® Hero6 Black and a GoPro® Hero8 Black. Telesin® Circular Polarizing Lens (CPL) were attached to the GoPro® lenses to reduce reflection and glare from the water surface. These camera pairs were mounted on 0.6 m Unistrut lengths using original, stick-on GoPro® mounts and assorted nuts and bolts. Once attached, the cameras' horizontal spacing was not further adjusted after camera calibration to ensure each stereo pair had consistent extrinsic parameters. Pair 1 and 2 were spaced 0.49 m and 0.51 m respectively from the center of the left camera to the center of the right camera and both pairs were mounted horizontally. During preliminary tests, Pair 1 was mounted onto an adjustable tripod so that different views of the basin could be tested. The GoPros®, Unistrut mount, and tripod setup are shown in Figure 3.3.



*Figure 3.3: A pair of GoPros® (Pair 1) with their Unistrut mount attached to a movable tripod for preliminary testing.*



*Figure 3.4: GoPro® stereo pair mounted to instrumentation frame.*

During later experiments, the Unistrut mount was disconnected from the tripod and attached to the instrumentation frame, as shown in Figure 3.4. In the final tests, Pair 2 was added to the opposite side of the frame facing toward the wavemaker. For more information on the specific location of the cameras during each test, refer to Appendix A.

To remotely start all the cameras, the Multi Camera Control for GoPro® app [46] was used on an iPhone 11. Further video post processing was required to synchronize the video data and is described in Chapter 4. In later tests where the cameras were not accessible for some time, power was constantly being supplied to the cameras from extension cords running along the top of the frame. Camera settings and frame rate were adjusted throughout different tests as needed.





*Figure 3.5: Intel® RealSense™ D455 camera system.*

The second camera system used in this study was an Intel® RealSense™ depth-camera. The Intel® RealSense™ D455 is an off-the-shelf stereo camera that has its sensors built into a single housing. For more information on this camera system, see Section 2.4. The camera was either mounted to the small tripod provided by Intel®, shown in Figure 3.5, or on the instrumentation frame using Unistrut connection hardware. During testing, the camera was connected to a Windows laptop using a USB-C cable. The Intel® RealSense™ SDK 2.0 was used for camera control and real time post processing of the video data during testing. Camera settings were adjusted throughout testing and are listed in further detail in Appendix A.

#### *3.1.2.5 LED Synchronization*

In order to synchronize the video data with the wave gauge data, a blinking LED was placed in view of the cameras. The LED was controlled by a random digital pulse generator whose signal is recorded by the data acquisition system and stored for future use. This signal could then be

used to synchronize a signal retrieved from the pixels of the LED in each individual video. This process is described in further detail in Chapter 4.

#### 3.1.2.6 *Lighting*

Lighting is an important factor to consider when recording video data of a highly reflective water surface. To properly light the scene being recorded with minimal reflection and glare affects, diffuse photography lighting structures were used. Four Fovitec 1575 W fluorescent lighting kits (<https://www.fovitec.com/products/2-light-classic-softbox-kit>) were used for lighting in this study. These lighting kits come with an inner and outer diffuser to minimize shadowing and glare and a tripod stand to mount them on. Depending on the experiment, the fixtures were either adjusted to the desired location or mounted in place on the top corners of the instrumentation frame. The overhead lights in the DWB facility were also adjusted as needed to reduce surface reflections.

#### 3.1.3 *Data Acquisition System*

The data acquisition system (DAQ) used for this study was a previously in-place system at the HWRL facility. All resistive wave gauges, USWG's, the LED signal, as well as the DWB wavemaker system gauges were recorded through the DAQ and displayed on a central computer system in the control room of the HWRL. This computer saved raw data under the user-specified experiment name, trial number, trial description, and file name for each test in the HWRL shared server drive. Duration of each trial was adjusted as necessary and sampling frequency remained 100 Hz for all instruments attached to the DAQ.

#### 3.1.4 *Instrumentation Layout*

During the course of this study the support frame and instrumentation bridge were kept in place, but the instrumentation layout was adjusted throughout different stages of the project. For preliminary testing, the instrumentation layout followed that of the Sandia FOSWEC wave energy study [13], which had already been constructed in the DWB (Figure 3.6). For the final experiments, the instruments were rearranged in a more ideal layout with any obstructions removed from the cameras' fields of view and the USWG's extended further toward the center of the instrumentation frame (Figure 3.7). The layouts were designed to measure a large spatial extent in the center of the DWB where the walls and beach were not obstructing any view the

cameras may have. This way the camera systems could be validated from a variety of locations and the traditional gauges could measure the wave height variability in a large, open area.

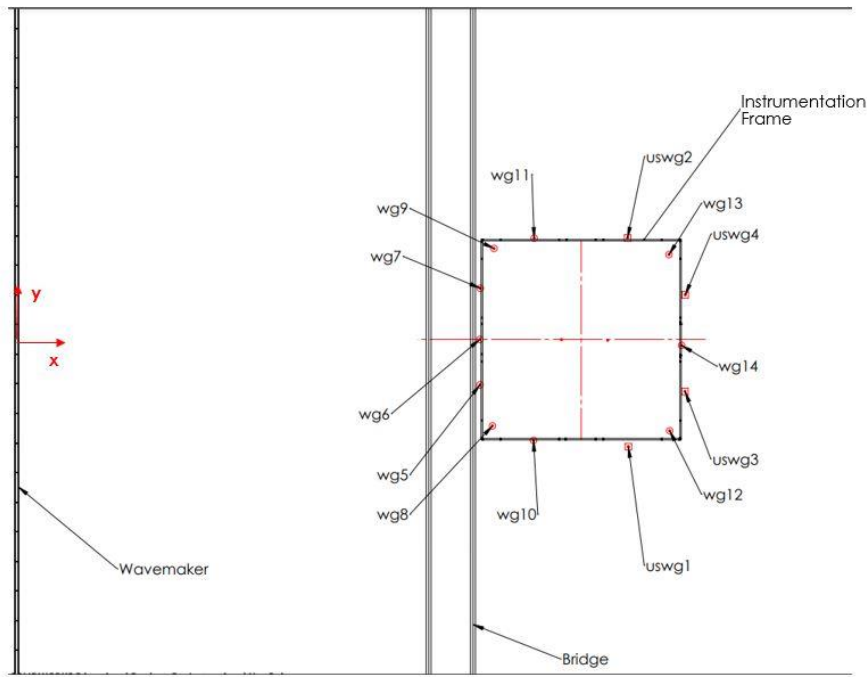


Figure 3.6: Instrumentation layout for the preliminary tests.

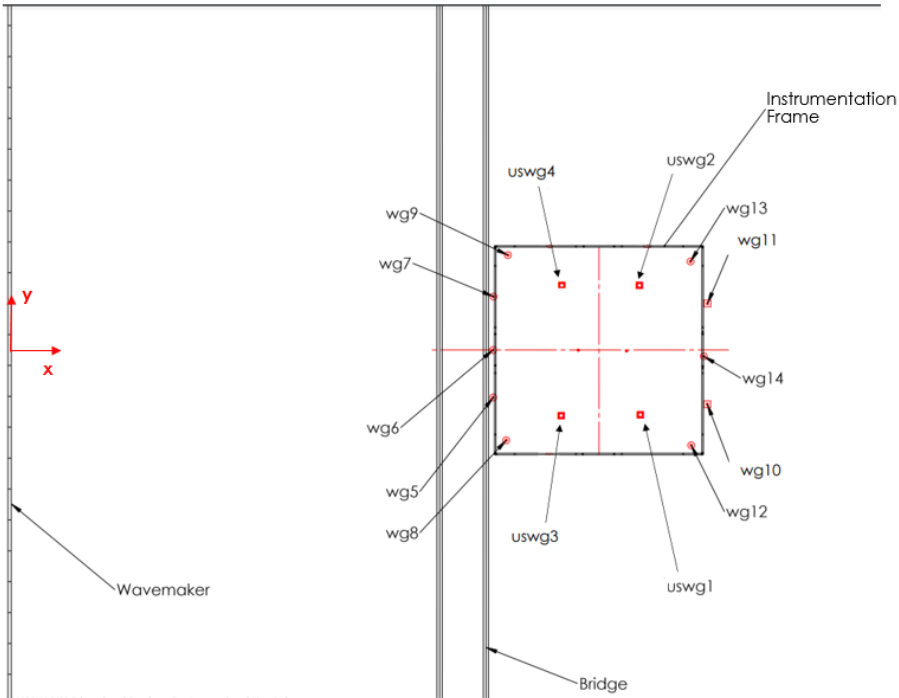


Figure 3.7: Instrumentation layout for the final tests.

### 3.1.5 Wave Conditions

Table 3.1 shows each experiments' test wave conditions. Each were selected based upon the specific goals and objectives of the experiment, but in general a large variety was used to thoroughly understand the cameras' abilities and limitations. The wave types within this study are further described in the following sub-sections.

Table 3.1: Test wave conditions for all experiments and trials.

Trial #	Wave Type	Generation	Wave Height	Wave Period	Wave Direction	Water Depth	Duration
			H (m)	T (s)	$\theta$ ( $^{\circ}$ )	h (m)	(s)
<b>Basin Views</b>							
1	Focusing	AwaSys		1.8		1.0	600
2	Regular	MTS	0.5	2.0	0	1.0	600
<b>Airy Validation</b>							
1	Regular	MTS	0.5	2.0	0	1.0	180
2	Regular	MTS	0.4	2.0	0	1.0	120
3	Regular	MTS	0.5	2.0	0	1.0	120
4	Regular	MTS	0.4	2.0	0	1.0	120
<b>CPL Filter</b>							
1	Regular	MTS	0.5	2.0	0	1.08	60
2	Regular	MTS	0.54	2.0	0	1.08	60
3	Regular	MTS	0.54	2.0	0	1.07	60
4	Focusing	AwaSys		1.8		1.07	60
5	Focusing	AwaSys		1.8		1.07	60
6	Regular	MTS	0.54	2.0	0	1.07	60
<b>Two Stereo Pairs and Intel<sup>®</sup> Cam: Frame</b>							
1	Focusing	AwaSys				1.0	120
2	Regular	MTS	0.5	1.8	0	1.0	120
3	Regular	MTS	0.55	3.0	15	1.0	120
4	Regular	MTS	0.56	5.0	15	1.0	120
5	Irregular	Matlab	0.51	4.0	20	1.0	340
6	Regular Bi-Dir	AwaSys	0.3, 0.3	2.0, 2.0	15, -15	1.0	100
7	Regular Bi-Dir	AwaSys	0.15, 0.12	2.0, 1.5	25, 0	1.0	100
8	Focusing	AwaSys				1.0	60
<b>Two Stereo Pairs and Intel<sup>®</sup> Cam: Beach</b>							
1	Focusing	AwaSys				1.0	120
2	Regular	MTS	0.5	1.8	0	1.0	120
3	Regular	MTS	0.55	3.0	15	1.0	120
4	Regular Bi-Dir	AwaSys	0.3, 0.3	2.0, 2.0	15, -15	1.0	100
5	Regular	MTS	0.56	5.0	15	1.0	120
6	Irregular	Matlab	0.5	4.0	0	1.0	340
7	Irregular	Matlab	0.51	4.0	20	1.0	340

#### 3.1.5.1 Regular Waves

Waves can be defined as “regular” when they have an identical amplitude and frequency. In their simplest form, they can be mathematically interpreted as a single sine or cosine wave oscillating about the mean water level. More complicated wave profiles, such as a superposition

of various sine waves or cnoidal waves, can also be defined as regular presuming their frequency and amplitude remain equal. Figure 3.8 shows a schematic of a regular wave with important wave characteristics labeled. For regular waves, each wave's wavelength ( $L$ ), or the horizontal distance between two successive wave crests, and wave height ( $H$ ), the vertical distance between the wave trough and crest, must be precisely the same value for each wave.

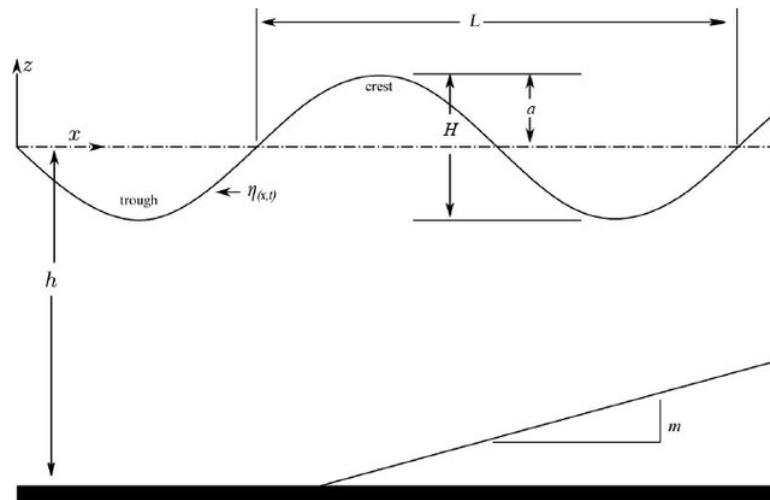


Figure 3.8: A schematic of regular waves labeling the wave amplitude ( $a$ ), wave height ( $H$ ), and wave length ( $L$ ) over a sloped bathymetry  $h(x)$ . Source: [16].

Regular waves are almost never found in nature but can be used in laboratory settings to simplify the forcing of an experiment to further understand a system's response to a specific frequency or amplitude of wave. Although the wave maker in the DWB has the ability to generate regular waves, it is very difficult to generate regular waves that spatially and temporally maintain precisely the same amplitude and frequency over the entire basin, especially when instrumentation and research specimens are placed throughout.

The directionality of regular waves can be defined as the angle at which each wave crest approaches the shoreline. When the wave direction is equal to zero the waves are described as shore normal, similar to the waves seen in Figure 3.9. When the directionality is nonzero, the waves approach the shoreline at an angle and become affected by wave propagation processes such as refraction. When directional regular waves are generated within a basin, refraction and other processes create an environment that is not spatially uniform. This can create unwanted areas of wave height variability, as seen in Figure 3.10.



Figure 3.9: Regular, shore normal waves generated in the DWB at Oregon State.

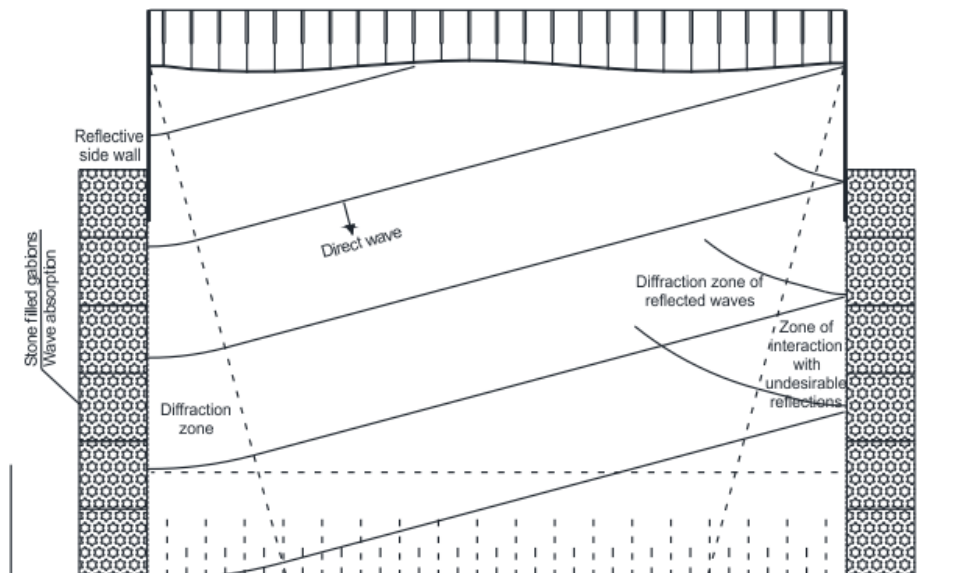
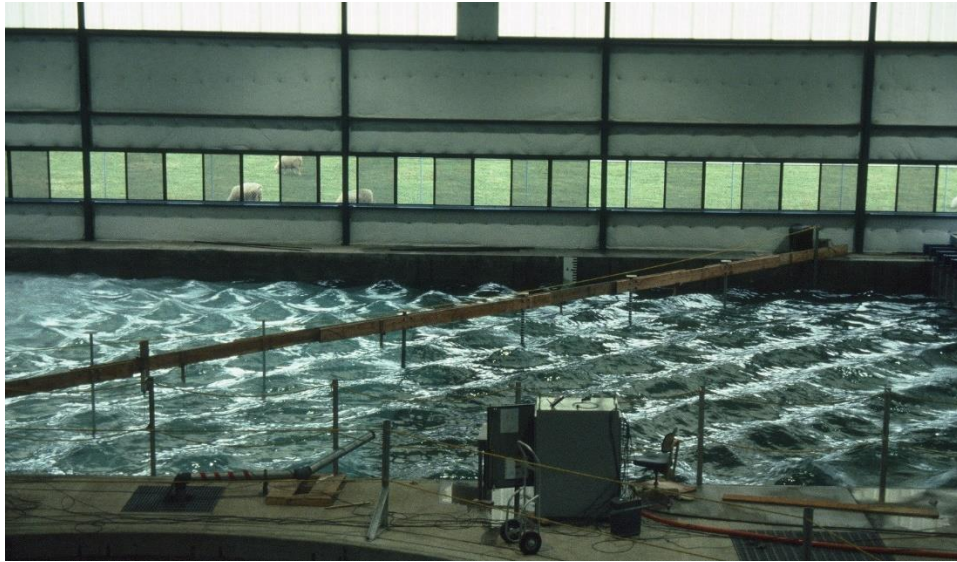


Figure 3.10: Schematic of a wave basin generating directional regular waves and the diffraction and reflection affects that occur. Source:[45].

### 3.1.5.2 Regular Bidirectional Waves

Regular bidirectional waves refer to the superposition of two sets of regular waves with differing wave directions. The difference in directionality creates a regular pattern of waves crossing through one another. At locations where two wave crests intersect, the wave heights are added and the local water surface elevation increases. Figure 3.11 shows regular bidirectional waves in a wave basin that emphasizes the spatial variability of wave height. Table 3.1 states the wave height and period of each regular wave set for the bidirectional cases in this study.

Due to the regularity in wave fields such as this, crest intersections can be linearly traced along the water surface and will consistently occur in the same location. When spatially analyzed over time, these intersection lines can be expected to have several times the average wave height when compared to other areas. This average wave height variability is therefore ideal for testing the capabilities of the camera systems.



*Figure 3.11: Regular bidirectional waves in a wave basin.*

### *3.1.5.3 Focusing Waves*

Focusing waves are a type of regular wave with a curved wave crest such that energy is focused at a point along the center of the crest. This is the result of superimposing several waves with different directions that coincide at a given point. If the phase of each of these waves is symmetric relative to the wavemaker, the resulting shape is a curved crest with the maximum amplitude occurring at the center. The wave often breaks first at this point if the depth is shallow enough or the wave becomes steep enough. These waves are often called “bullseye” waves due to the manner that they focus toward a single target point.

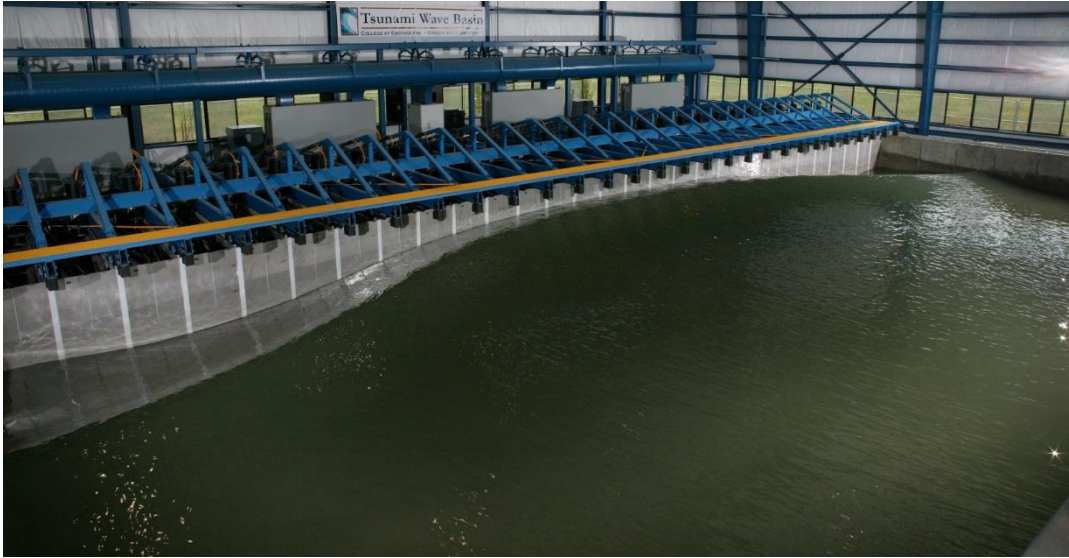


Figure 3.12: A focusing wave being generated in the DWB.

#### 3.1.5.4 Irregular Waves

Irregular waves are generally what is found in nature and can be defined as the superposition of a number of regular waves, or wave components, with different amplitudes, frequencies, and directions. They can be either short-crested or long-crested, as shown in Figure 3.13, which is dependent on their directionality. Long-crested waves are unidirectional, or all propagating in the same direction, and have long, continuous crest lines. In contrast, short-crested waves contain waves with differing wave directions, creating short, peaky wave crests. The directional spreading of short-crested irregular waves refers to the range of directions contained within them.

Each individual wave is unique within irregular waves so they must be described statistically, generally using significant wave height ( $H_s$ ) and peak wave period ( $T_p$ ).  $H_s$  refers to the mean of the highest one third of the waves, while  $T_p$  is the wave period with the highest energy associated with it. These are calculated using a time or frequency domain analysis, which are further described in Section 5.4.2 and 5.4.3. A frequency domain analysis outputs a wave spectrum, or how energy is distributed throughout different frequencies, for any given set of irregular waves. There are several different theoretical wave spectrums commonly used to represent irregular waves, one of the most common being the JONSWAP spectrum [29]. This model allows one to predict the energy distribution in a developing sea state using only local wind parameters and a



peak enhancement factor ( $\gamma$ ). It was later parametrized and defined with significant wave height and peak period to output the model spectra, which was utilized in the generation of the irregular wave time series for this study. Table 3.1 states the significant wave height, peak period, and directional spreading of each irregular wave case.

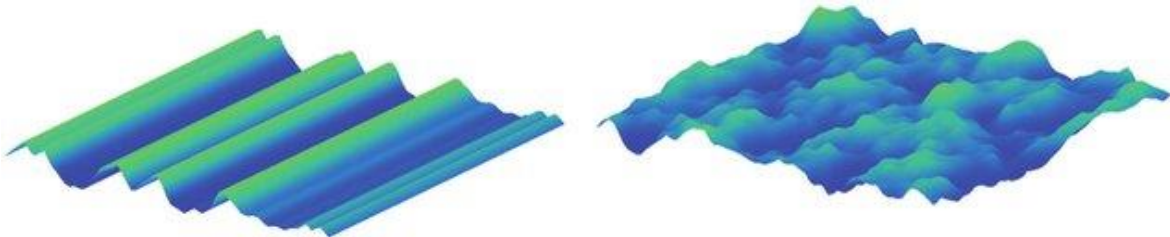


Figure 3.13: An example of long-crested (left) and short-crested (right) irregular waves. Source:[2].

#### 3.1.5.5 Wave Generation

Three different wave generation softwares were used to produce control files, called wavemaker input files, that precisely control the wavemaker's movement during testing. These allow the user to generate the desired wave conditions in the basin. Regular wave conditions were generated using the MTS wavemaker control software where wave height, period, and direction can be specified by the user directly before wave generation. For irregular wave cases, Matlab routines obtained from HWRL were used to generate a representative water surface elevation time series for a JONSWAP spectra. In order to increase the concentration of waves surrounding the peak period and significant wave height, a peak enhancement factor of 6 was used as opposed to the default value of 3.3. Through testing it was found that this ensured several instances of breaking wave groups throughout the duration of the trial, which was an important aspect when selecting wave conditions. The output time series could then be converted into a wavemaker input file using the MTS software. The MTS software was not capable of generating bidirectional or focusing waves and Matlab routines were not in-place, so a third party wavemaker controller software called AwaSys [45] was used to generate these wavemaker input files.

### 3.2 Experimental Procedure

In order to establish a proper experimental procedure for the camera systems, a series of preliminary tests needed to be designed to further understand the ideal camera orientation and

lighting required to accurately measure the water surface. Once these parameters were understood, final tests could be designed with adequate wave conditions, lighting, and camera angles to investigate the research questions at hand. Tests were run in a series of five experiments, the first three being the preliminary tests and the last two being the final tests.

Preliminary tests focused on camera settings, positioning, and lighting while keeping wave conditions relatively the same and are described in further detail in the following section. During testing, the DAQ would begin recording 30 seconds before the start of the wavemaker to ensure thorough gauge measurements. To limit video data file size, the cameras began recording following wavemaker startup or shortly after once the wave field was fully developed. The GoPro® cameras were controlled remotely using a mobile app while the Intel® system was controlled using a laptop connected to the camera both by a person on the lab floor. The wavemaker was controlled by a certified wavemaker operator in the HWRL control room. Once the test was complete, the wavemaker would ramp-down to ensure a smooth shutdown. Instrumentation data was saved, and 15 minutes were allowed for the basin to settle before the next test. Lighting and camera positions were adjusted between tests when needed.

### *3.2.1 Preliminary Tests*

This series of three experiments (Basin Views, Airy Validation, and CPL Filter) included the WASS system with a single pair of GoPros® and excluded the Intel® RealSense™ system. The tests were designed to understand the ideal positioning and angle for the cameras over the water, which light setting reduced glare most efficiently, and what wave conditions were most easily handled by the WASS software. They also gave the opportunity for the stereo data post processing methodology to be developed that is described in Chapter 4. The objectives and details of each experiment are described in the following sub-sections.

#### *3.2.1.1 Basin Views*

The first preliminary test, named Basin Views, was designed to test the WASS camera system in two sets of wave conditions while changing the camera angle, setting, and lighting. For this experiment it was not necessary for the DAQ to collect data. The first wave case was run for ten minutes while the camera operator moved to seven different positions around the basin and collected video data with the GoPros® spaced 0.49 m apart on the tripod stand seen in Figure 3.3. In each location, three different camera settings and two lighting settings were tested in thirty

second videos. The process was then repeated for the second wave condition. In total, 36 videos were taken and processed through the WASS software. For more details on each video and their results in WASS, see the Basin Views test sheet in Appendix A.

The first wave case tested were focusing waves designed to break due to wave steepness directly under the instrumentation frame. The next were regular waves whose crests spanned the width of the basin. Due to the wave height selected and hydrodynamic conditions created in the basin, the wave crests broke in certain areas but not others, giving a variety of breaking and non-breaking waves over the entirety of the basin which was ideal for investigating WASS's ability to distinguish between the two. For more detail on the wave conditions and water levels for this test, see Table 3.1.

#### *3.2.1.2 Airy Validation*

Once ideal camera positioning, camera settings, and lighting of the water surface were established, the Airy Validation test was run to compare WASS and wave gauge measurements. For these tests, the pair of GoPros<sup>®</sup> were spaced 0.49 m apart and mounted on the instrumentation frame facing onshore approximately 2.5 m above the water surface. The diffuse lighting fixtures were mounted on the top corners of the instrumentation frame pointing inward and turned on while the overhead HWRL basin lighting was turned off to reduce overhead light reflection on the water surface. Two wave cases of regular "Airy" waves were each run twice for this experiment for a total of four trials. The first case was the same regular wave conditions run for the Basin Views experiment. The next case had a slightly smaller wave height so they did not break until reaching the beach where depth-limited breaking occurred. The data from this experiment was post-processed and camera measurements were compared to wave gauge measurements to quickly test the validity of the WASS system in this setting before carrying on with further experiments.

#### *3.2.1.3 Circular Polarizing Lens (CPL) Filter*

The Airy Validation experiment revealed that there were still reflectivity issues occurring that WASS could not process well. To further reduce reflectivity, Telesin<sup>®</sup> CPL GoPro<sup>®</sup> lenses were attached to the cameras and a final series of preliminary experiments were carried out. This was similar to the Airy Validation experiment, but lighting was adjusted so that the scene was either

fully-lit or back-lit by the diffuse lighting fixtures. Focusing waves were added to this experiment for a more three-dimensional wave field.

### 3.2.2 *Final Tests*

Once the limitations of the WASS camera system were assessed, a set of final experiments were designed to test both the WASS camera system and the Intel<sup>®</sup> RealSense<sup>™</sup> system in a variety of wave conditions. The goals of these tests were as follows:

1. Increase quality/area of WASS measurements
2. Test Intel<sup>®</sup> camera
  - a. Camera range
  - b. Ideal wave conditions
3. Measure wave directionality, spectra, and wave height variability with both camera systems

To increase the quality and area of the WASS system measurements, another pair of GoPros<sup>®</sup> was added so that waves could be measured on either side of the crests at any given moment. This was intended to increase the measurement area and data quality.

According to Intel<sup>®</sup>'s factory specifications, the Intel<sup>®</sup> RealSense<sup>™</sup> D455 is rated for measurement from 0.6 to 6 m with a maximum range of 16 m [37]. These parameters were tested in this experiment as well as the system's ability to capture the water surface. During testing, camera positioning was optimized using the real-time data visualization capabilities of the Intel<sup>®</sup> system. Camera settings and control were adjusted from the laptop between trials as needed.

Wave conditions were selected based upon the experiment objectives. A variety of conditions were chosen that enabled the cameras to analyze directionality, spectra, and wave height variability and validate their measurements with the point gauges in view. In order to highlight the advantages of the high spatial resolution measurements from the camera systems as opposed to the point measurements from the wave gauges, multiple wave conditions with high wave three-dimensionality were selected: focusing waves, bidirectional regular waves, and directional regular waves that excited a cross-wave mode within the basin. These were intended to create systematic wave height variability under the instrumentation frame that could be measured by both the cameras and the wave gauges. Directional and non-directional irregular wave cases were selected to compare time and frequency domain analyses from the cameras and wave gauges as well as have a case with both broken and unbroken waves under the instrumentation frame.

Regular directional waves were also chosen to assess the camera systems' abilities to measure wave directionality.

### 3.2.2.1 Two WASS Stereo Pairs and Intel® Camera: Frame

The first experiment of the final tests focused on measuring waves within the instrumentation frame. The GoPros® were mounted on the East and West side of the frame so that an 8 m by 10 m area could be viewed from either side of the frame. Cameras were mounted facing inward on the top center of either side of the frame at approximately 3.5 m above the still water surface. A layout of the GoPro® cameras and their expected measurement area is seen in Figure 3.14. During this test, the Intel® camera was moved to different positions along the instrumentation bridge.

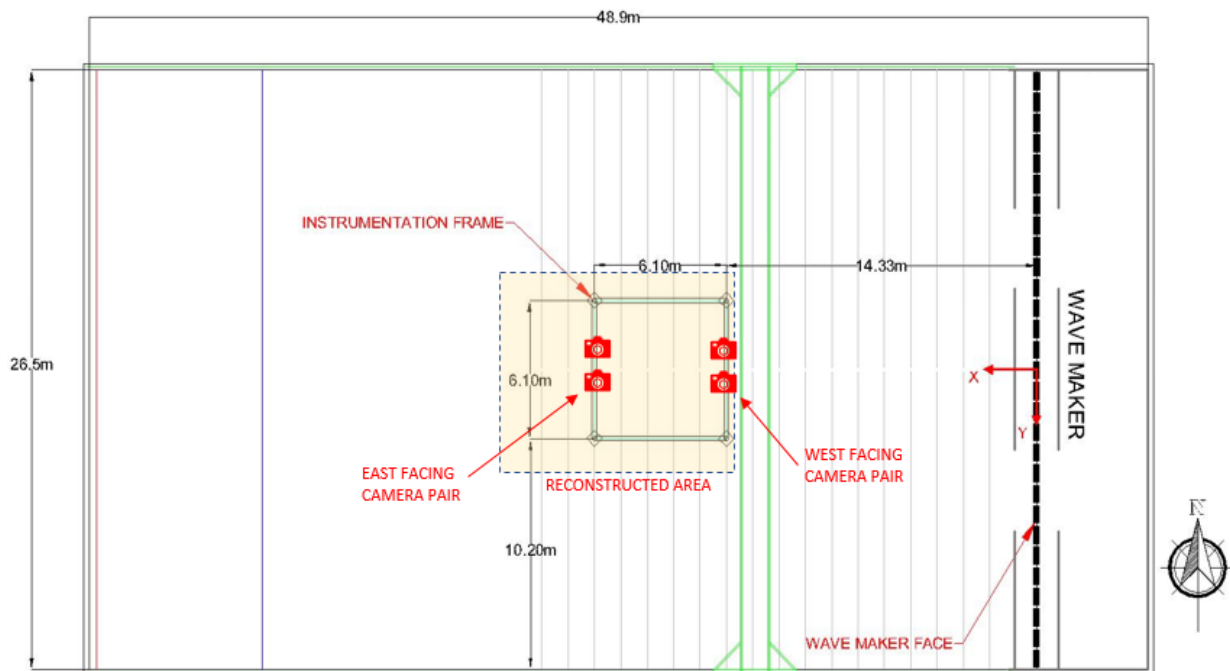


Figure 3.14: GoPro® camera layout and approximate reconstructed area for Two Stereo Pairs and Intel® Camera: Frame experiment.

### 3.2.2.2 Two WASS Stereo Pairs and Intel® Camera: Beach

The second experiment of the final tests intended to increase the area being measured by the WASS camera system to the entire width of the DWB. To achieve this, one of the GoPro® camera sets was removed from the instrumentation frame and moved to the DWB beach. To assist in measuring a larger area, the cameras were removed from their original mounting, and

each placed on a tripod so the stereo baseline (horizontal distance between the cameras) could be increased to 3 m. The cameras were placed 4.8 m up the slope of the beach from the still water level with a tripod height of 1.35 m, making the camera set 1.82 m above the still water elevation. In order to properly light the measurement area, two of the lighting fixtures were placed on the corners of the beach facing toward the wavemaker. During these trials, the Intel<sup>®</sup> camera was positioned in different areas along the beach and side of the basin to assess its ability to measure the surf and swash zone.

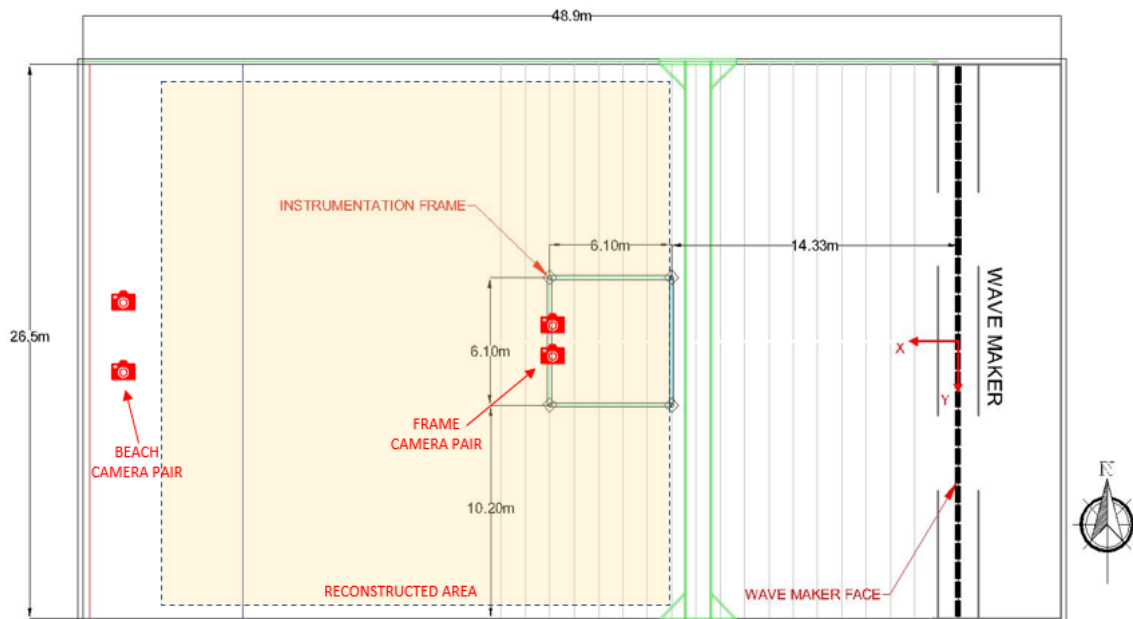


Figure 3.15: GoPro<sup>®</sup> camera layout and approximate reconstructed area for Two Stereo Pairs and Intel<sup>®</sup> Camera: Beach experiment. The Intel<sup>®</sup> camera was located at various positions along the basin beach and South side of the basin.

### 3.3 Chapter Conclusions

This chapter described the experimental setup and procedure of each experiment in this study. The wave basin and instrumentation were detailed. Each wave condition was tabulated and explained for a non-scientific audience. The progression of experiments, objectives, and the motivation behind wave condition selection was described. Chapter 4 explains the methodologies developed for both the WASS and Intel<sup>®</sup> camera systems to process raw video files into gridded spatial data including any calibration and synchronization techniques required.

## Chapter 4 Stereo Data Processing Methodology

This study examines the feasibility of using stereo reconstruction methods to spatially measure the free surface in a coastal laboratory environment, more specifically the DWB in the HWRL. Two different stereo measurement systems are assessed in several different wave conditions, lighting, and camera angles then compared to more classical free surface measurement instrumentation used in the HWRL, mainly surface-piercing resistive wave gauges and non-intrusive USWG's. Once video data was collected, it had to be post-processed to transform it from a series of images into spatio-temporal data where free surface elevation could be readily analyzed for its wave characteristics. Both video measurement systems, WASS and Intel<sup>®</sup> RealSense<sup>™</sup>, had a unique methodology for video post-processing that was necessary before any wave analyses could be completed. Video data was independently recorded, therefore needed to be synchronized with gauge data collected through the DAQ. Image processing routines were developed utilizing a randomly blinking LED in view of the cameras for data synchronization. The post-processing and synchronization methodologies are a conglomerate of standard practices defined for each system, methods from the literature, and original processes developed for this study. Chapter 4 describes the methodologies used for both the WASS and Intel<sup>®</sup> RealSense<sup>™</sup> systems.

### 4.1 WASS

The first stereo-video measurement system used during this study was the Wave Acquisition Stereo System (WASS) developed by Filippo Bergamasco [7], who was instrumental in the success of this project. WASS was designed for the measurement of open ocean waves and has been used extensively in the field [22]. For more detail on how this system works and the theory behind it, see Section 2.3. This system is an open-source code pipeline (<http://www.dais.unive.it/wass>) and not necessarily as “off-the-shelf” as the Intel<sup>®</sup> RealSense<sup>™</sup> system, so some amount of preparation work was required. No hardware is provided, so cameras must be selected by the user then individually calibrated and synchronized with one another. Once this is completed and data is collected, a specific file structure must be created for each video frame so that it will be recognized by the WASS pipeline. This file structure includes the user determined camera calibration parameters, the desired WASS software settings, and all video frames that need to be reconstructed into real world coordinates. The WASS software,

which is set up as a pipeline of four algorithms (Section 2.3.1), can then be run using a batch file called *launch\_wassjs.bat* and the video data will be spatially reconstructed. WASS outputs a spatial data file for each video frame's stereo reconstruction that contains a dense point cloud of each image pixel that is associated with the water surface. This point cloud must be further processed into a regular spatial grid for easier analysis, but before this it was desirable to visualize the raw data. To do this, it was overlaid on to its respective video frame and a .AVI movie file was created for the entire recording. Then, if the quality was deemed fit after visual inspection, a final NetCDF (Network Common Data Form) file was created which contained an interpolated spatial grid with the desired resolution. Further data visualization techniques were used to inspect the quality of the interpolation within these NetCDFs. The following sub-sections thoroughly describe these steps required to process video data through WASS and convert it to a gridded format.

#### 4.1.1 Camera Calibration

In order to perform an accurate three-dimensional surface reconstruction of video data, each camera within the stereo pair must be properly calibrated to understand their intrinsic and extrinsic parameters. The intrinsic parameters include the focal length, distortion, and individual cameras' digital sensor position while the extrinsic parameters refer to each cameras' position relative to the other camera within the stereo pair [50]. "Off-the-shelf" stereo pairs, such as the Intel<sup>®</sup> camera, often come factory calibrated but because WASS relies on the user to select the cameras and their positioning these calibration parameters must be calculated. To compute each cameras' intrinsic parameters, the open source Camera Calibration Toolbox for Matlab [9] was used due to its availability, ease of use, and common pairing with WASS [4][27][62]. The methodology provided in the first calibration example ([http://www.vision.caltech.edu/bouguetj/calib\\_doc/htmls/example.html](http://www.vision.caltech.edu/bouguetj/calib_doc/htmls/example.html)) provided by the toolbox was generally followed to determine each GoPro<sup>®</sup>'s intrinsic calibration parameters. To compute the extrinsic parameters, the *wass\_autocalibrate* feature was used within WASS and validated using the Camera Calibration Toolbox's stereo calibration feature.

In order to use the Camera Calibration Toolbox, a checkboard calibration pattern must be printed and pasted on to a flat surface. Two black and white checkered calibration patterns were printed and used to calibrate each camera. The first was printed on standard 11 by 17-inch paper and



contained a 9 by 13 square checkerboard matrix of 3 cm squares. The second was a larger 8 by 8 checkerboard matrix of 10 cm squares printed on 40 by 40-inch plotting paper, which is pictured in Figure 4.1. These patterns were glued flush to rigid, flat surfaces (plywood and clipboard) to ensure they were flat throughout the calibration process. A total of 20 to 30 calibration images were taken of the checkerboards at different distances, angles, and positions within the camera's field of view to avoid ambiguity in the calibration parameter estimates. The smaller checkerboard was used for calibration pictures closer to the camera (0.5-1 m) and the larger was used at greater distances (1-4 m) to increase image variety. These images were then loaded into the calibration toolbox and inspected to verify the entire checkerboard was visible in each. Then the four grid corners were extracted by selecting the pixel representing each corner of the pattern and entering the dimensions of the checkerboard (number and size of squares) into the toolbox. The software could then project the estimated checkerboard intersection locations on to the pattern and calculate the distortion of the camera based on the error of these estimations. Figure 4.1 shows an example of a calibration picture after the reprojection process with the blue arrows signifying the error associated with each grid point estimation. The magnitude of the error, shown by the size of the arrow, is amplified so that the user can visualize these small pixel errors which are usually in the order of a single pixel. The reprojection error is then correlated to its position within the camera's field of view so that a distortion model can be estimated for the entire frame of the camera.

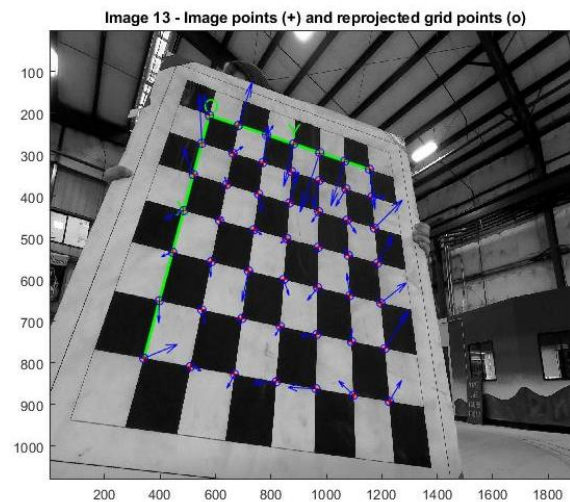


*Figure 4.1: Example of calibration picture within Camera Calibration Toolbox for Matlab with user selected image points on each corner and the reprojected grid points with their associated error (blue arrows).*

Once a mathematical distortion model is estimated for the camera, the grid corners are then reprojected on to each image using the distortion model instead of the original estimation. The reprojection error associated with every grid point is reanalyzed. Images with high associated error were discarded or reanalyzed. It was found that if the checkboard pattern was contorted in any way while the picture was being taken (paper folding, coming unglued, etc.), the image had higher error and had to be discarded from the calibration set. Figure 4.2 shows the reprojection error associated with an acceptable calibration image set. Each image is represented by a set of points with a particular color while each individual point represents a single grid corner's error. The x and y distance (in pixels) from the reprojected point to the actual location of the grid corner is calculated and shown on the x and y axes.

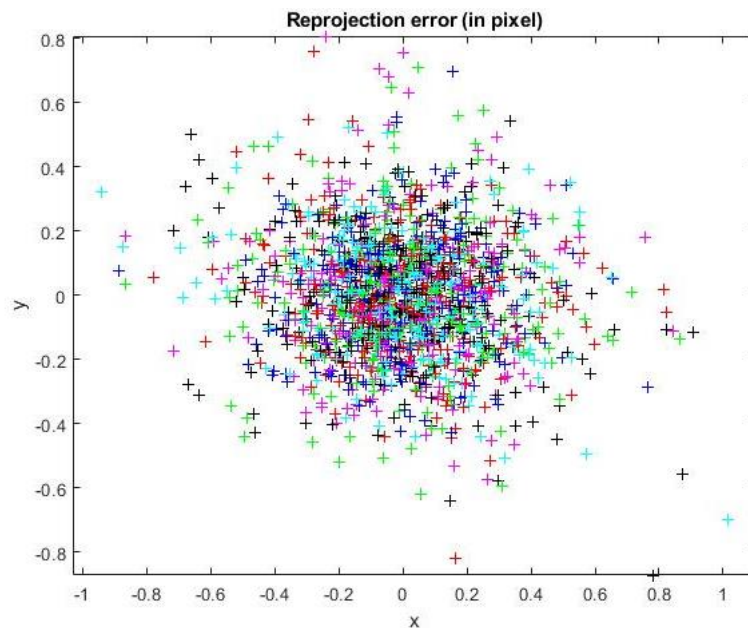


*Figure 4.2: Reprojection error in pixels calculated by the Camera Calibration Toolbox for Matlab [9] with each point representing a checkerboard grid point and each color representing a particular image.*

Once the reprojection error of a set of calibration images is deemed acceptable, the toolbox will recalculate the camera's distortion model. Radial and tangential distortion models are output, which can be combined for a complete distortion model of the camera, shown graphically in Figure 4.3. This figure is output by the Camera Calibration Toolbox so that the user can visualize each model and decide which to select when representing the camera's distortion. Both the tangential and radial models are mathematical representations of the lens distortion that can be used to approximate any camera's intrinsic parameters. Each model is represented by an  $n^{\text{th}}$  order

polar distortion function with coefficients estimated for each term. The coefficients along with their associated error are listed at the bottom of Figure 4.3. Each arrow in the figure represents the pixel displacement in this area of the camera frame due to lens distortion, with displacement magnitude contours labelled in units of pixels. At the center of the frame the distortion is zero, but as one moves away from center the distortion becomes greater which can be seen in the increasing arrow magnitude. Both tangential and radial models had effective pixel displacements of approximately 20 pixels towards the edge of the camera frame, so the complete distortion model was selected to represent the camera's distortion instead of solely the radial or tangential. The distortion coefficients as well as the camera's focal length and principal point listed under the figure and were saved in a specific .XML file for the configuration of WASS. The files are saved in each camera's *config* directory and used during WASS processing. To see each camera's distortion model used for this study, see Appendix D.

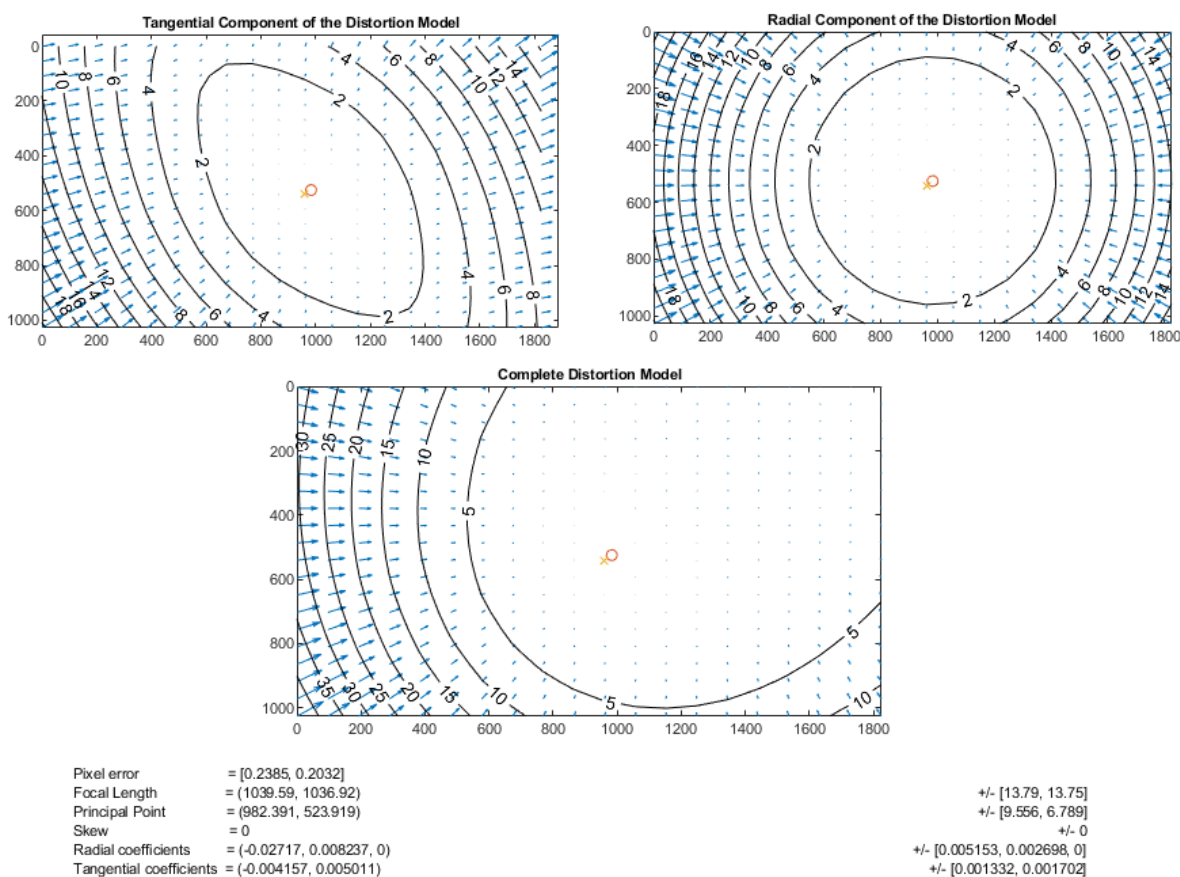


Figure 4.3: Tangential (top left), radial (top right), and complete (bottom) distortion models for one of the GoPro® Hero 6s used in this study output by Camera Calibration Toolbox for Matlab [7]. X and Y are pixel location in the camera frame and the arrow magnitude and direction are the pixel displacement in number of pixels. Other important calibration parameters listed at the bottom.

Extrinsic parameters were estimated using WASS' *auto-calibrate* feature so that camera positions did not have to be remeasured each time the cameras were adjusted before experimentation. This feature uses the frames inputted into WASS to estimate each camera's relative position to one another and does not require having a specific pattern in the images. This is convenient for use on the lab floor and eliminates the need for recalibration between testing. To validate the *auto-calibrate* feature, the Camera Calibration Toolbox's *stereo\_calib* feature was used on the same stereo camera set up to compare each system's estimated extrinsic parameters. The methodology provided in the fifth example by the Calibration Toolbox ([http://www.vision.caltech.edu/bouguetj/calib\\_doc/htmls/example5.html](http://www.vision.caltech.edu/bouguetj/calib_doc/htmls/example5.html)) was used, which is very similar to calibrating a single camera but synchronized images of the checkerboard pattern from two cameras are analyzed. The cameras are kept in place for the entirety of this process then their location relative to one another can be triangulated using the differing fields of view. Each cameras' precise location relative to one another along with the location and orientation of the checkerboard in each calibration image is shown graphically in Figure 4.4. WASS' *auto-calibrate* feature matched the extrinsic parameters from the Calibration Toolbox and was used for the remainder of this study.

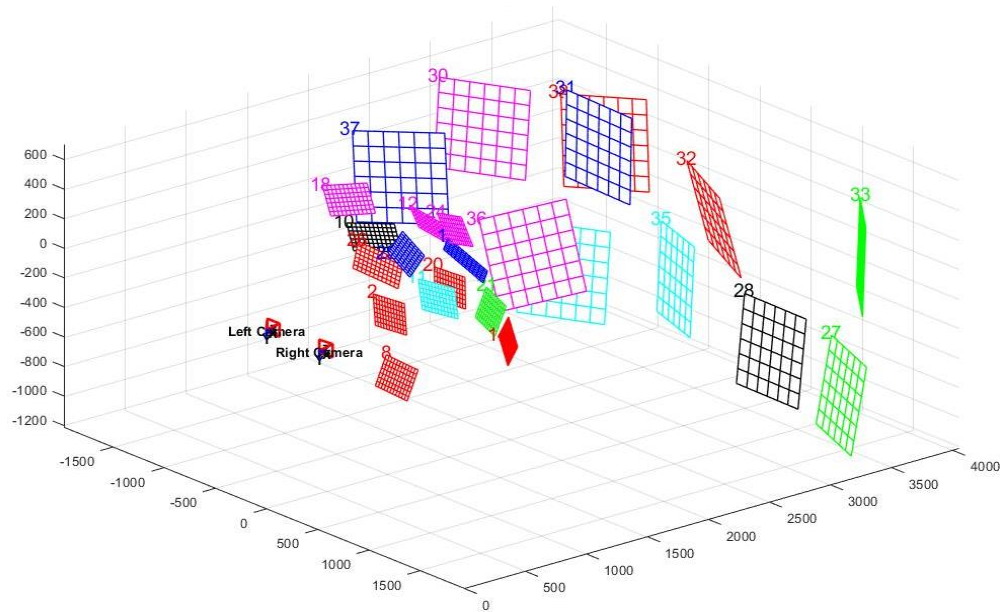


Figure 4.4: Extrinsic parameters for a stereo setup of two GoPro<sup>®</sup> cameras with each calibration image's position shown using Camera Calibration Toolbox for Matlab. The axes signify location in space (cm) with the origin at the center of the camera pair.

#### 4.1.2 *Frame and Data Synchronization*

After the GoPros<sup>®</sup> used for WASS were calibrated and ready to record video data, they needed to be temporally synchronized with one another as well as with the wave gauge data recorded by the DAQ. The Multi Camera Control app [46] was used to remotely start each GoPro<sup>®</sup> recording but was unable to start each camera at precisely the same time. It generally started the cameras 1 to 3 frames out of synch. Frames from each camera need to display precisely the same scene for WASS to accurately reconstruct the free surface, so this slight asynchronization would cause WASS to fail. Also, upon measuring each GoPro's<sup>®</sup> actual framerate, which is controlled internally, it was found that each camera's was slightly different. This could cause the synchronization of each camera to drift throughout the course of a recording, regardless of if they were initially synchronized. In order to ensure camera synchronization, a randomly blinking LED was placed in view of the cameras so that a signal could be output from each recorded video, synchronized with the other camera's, then aligned with the LED signal which was recorded by the DAQ. This sub-section describes this synchronization process.

An external camera hardware trigger is generally used to perfectly synchronize a set of stereo cameras with one another [7], but for simplicity and to stay within this project's budgetary constraints this hardware was not used. It is also not easily implemented to the GoPro<sup>®</sup> cameras selected for use. Instead, the video data can be aligned after recording using a pattern (visual or audio) that is captured by both cameras. In this project's case, a LED powered by a random digital pulse generator was connected to the DAQ and placed in view of the cameras to use for synchronization. The signal recorded by the DAQ was a 5-volt output when the LED was lit, and 0-volts when it was off. The LED would blink in random intervals to eliminate the ambiguity of a regular blinking pattern. Since cameras were kept in place for the entirety of each trial run, the LED's position within each camera's field of view remained constant. The pixels representing the LED could therefore be selected from a single video frame and analyzed over the duration of the video. An example of a frame used to locate the LED pixels is shown in Figure 4.5, where the blue box zooms in on the LED's general location and the red box selects the pixels which represent the LED. A black sheet of construction paper was used to outline the LED and reduce background noise. Total pixel intensity was calculated from the selected LED pixels for each video frame to output a blinking signal identical to the digital pulse generator recorded by the

DAQ. This pixel intensity was then normalized by the timeseries' maximum value so that the signal would oscillate about zero.

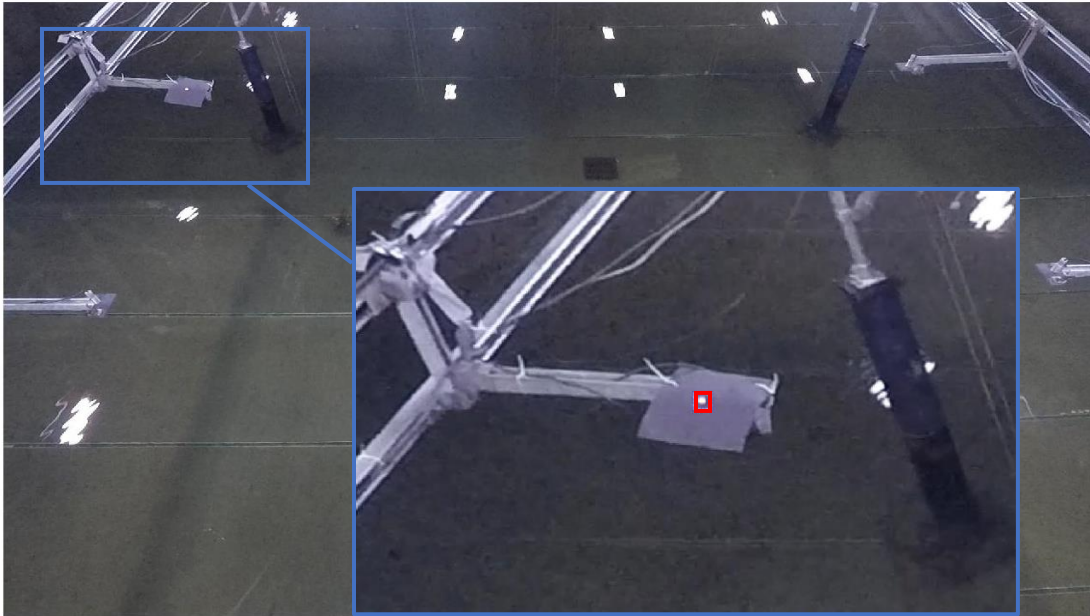


*Figure 4.5: Video frame showing camera's field of view of the DWB with blinking LED. The blue box zooms in on where the LED is mounted, and the red box is the selection of LED pixel used to generate an output signal.*

A zero-crossing analysis was then used to determine the average timing difference for each LED blink in either video from the stereo pair. Two unsynchronized LED signals from a set of stereo videos are shown in Figure 4.6 with an average timing difference of 1.93 frames. To ensure that the average framerate difference was an accurate measure from which to synchronize the videos, the timing difference for each blink was plotted for the duration of the video sets in Figure 4.8. This was used to confirm there was not significant drift throughout the videos caused by the difference in exact framerates between the two cameras. As seen in the figure, there was consistently a frame timing difference of two for each blink with only four exceptions, deeming the average frame difference of 1.93 feasible to use for synchronization. The rounded average frame difference was then used to determine the number of frames cropped from the leading video in pair. For Figure 4.6, the first two frames of the video from the left camera (red) were cropped so that the LED blinks were aligned from each video. Once cropped, the videos were then reanalyzed to ensure that they were properly synchronized. One of the output LED signals was saved for future use and the cropped videos were rewritten into a new directory. A user-

friendly Matlab routine was created so this methodology could be easily repeated during this project and future implementations of WASS. The Matlab command prompt output from this routine is shown in Figure 4.7 that highlights the steps followed.

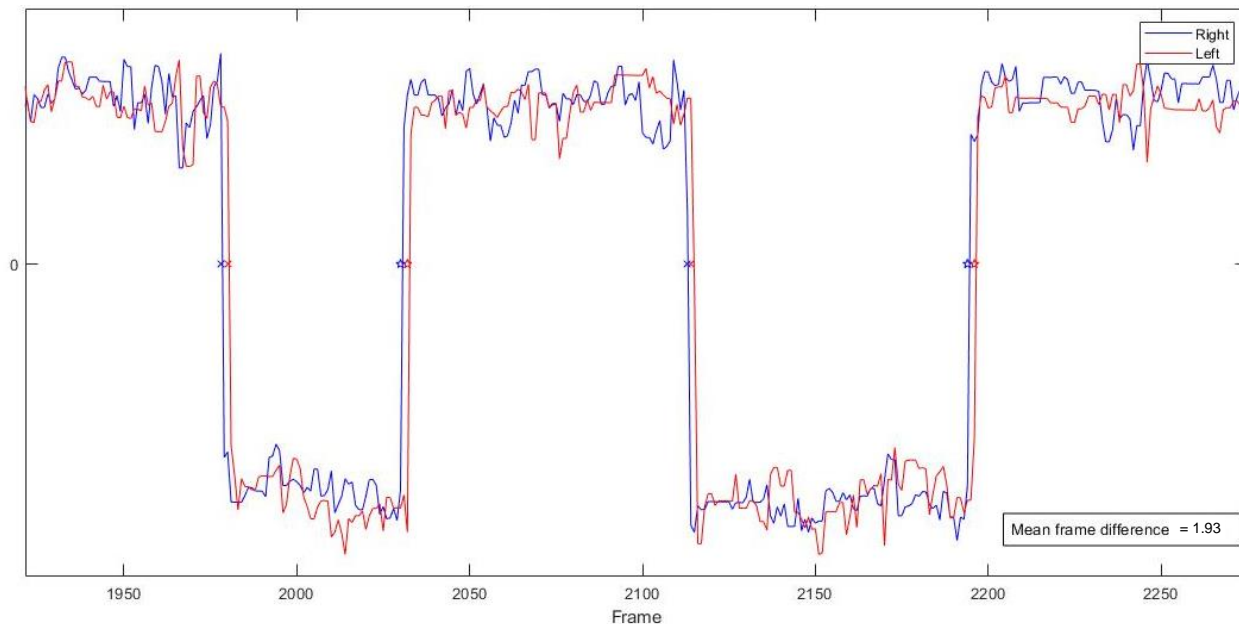


Figure 4.6: Output LED signals from both videos in a stereo set before synchronization. The right camera (blue) leads the left camera (red) by an average of 1.93 frames, which is calculated from the zero-crossings ( $x$ 's) from the signals.

```

Command Window
Opening videos for intial user LED crop...
Saving crops...
Analyzing LED signal in left video...
Analyzing LED signal in right video...
Cropping 2.000000 frames from left video to synchronize...
Writing left video: F:\OpticalWaveGauge\vids_synched\CPL_09_25_2020\L48_Beach_Trial01_synched.mp4
Left video complete!
Writing right video: F:\OpticalWaveGauge\vids_synched\CPL_09_25_2020\R25_Beach_Trial01_synched.mp4
Right video complete!
Analyzing LED signal in synched left video...
Analyzing LED signal in synched right video...
LED Signal saved as: F:\OpticalWaveGauge\vids_synched\CPL_09_25_2020\R25_Beach_Trial01_synched_LED.mat
fx >>

```

Figure 4.7: Video synchronization Matlab program command prompt output displaying the steps of the synchronization process.

The LED signal was saved in a .TXT file as a timeseries of pixel intensities with the timestep defined as the camera's framerate. Wavelab, a wave analysis desktop application used at HWRL, aligned this signal with the recorded LED signal from the DAQ using a signal matching algorithm. The time delay between both signals was output and used to synchronize the video data with the gauge data. This was done by adding the time delay to the time vector of the

trailing timeseries so that the time stamp of both signals match. Figure 4.9 shows a set of synchronized signals aligned in Wavelab. This methodology is only as accurate as the framerate of each video, which was generally 30 fps for this project.

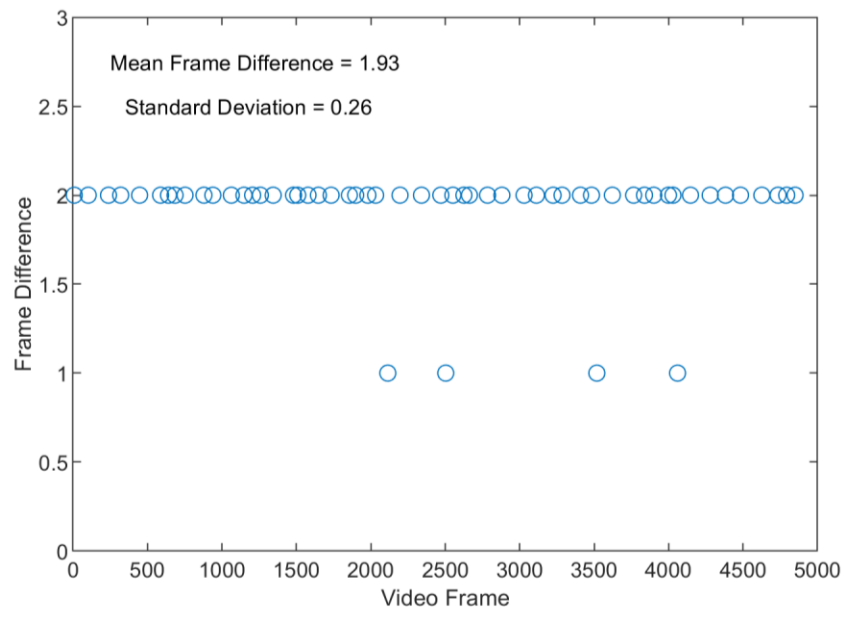


Figure 4.8: Frame difference for each zero crossing over the length of an entire WASS video pair including mean frame difference and standard deviation of the dataset.

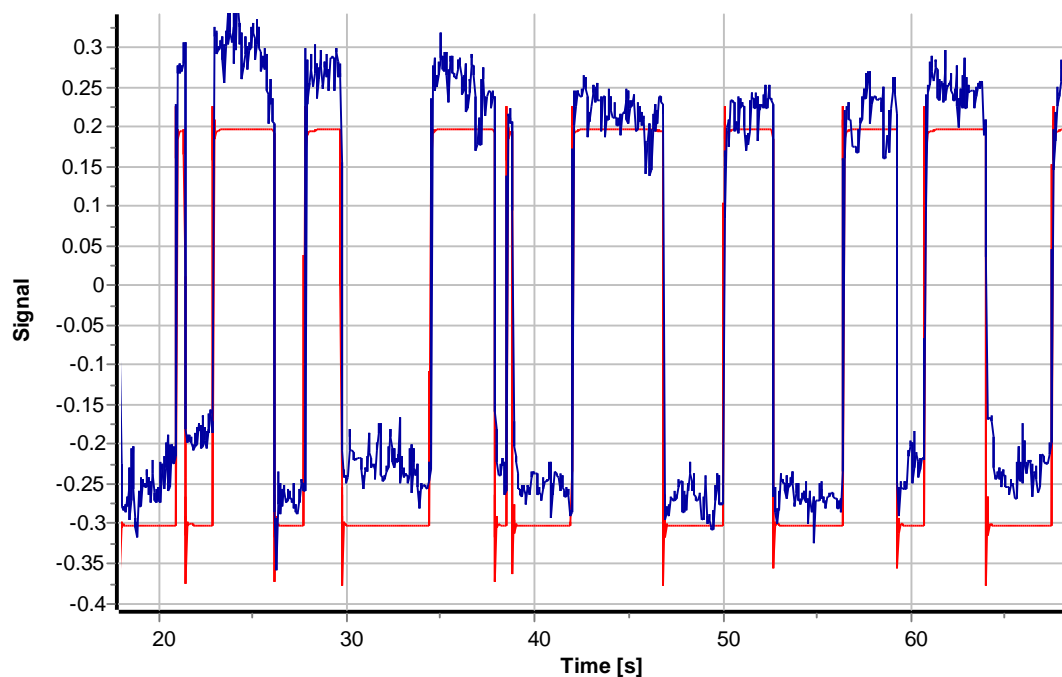
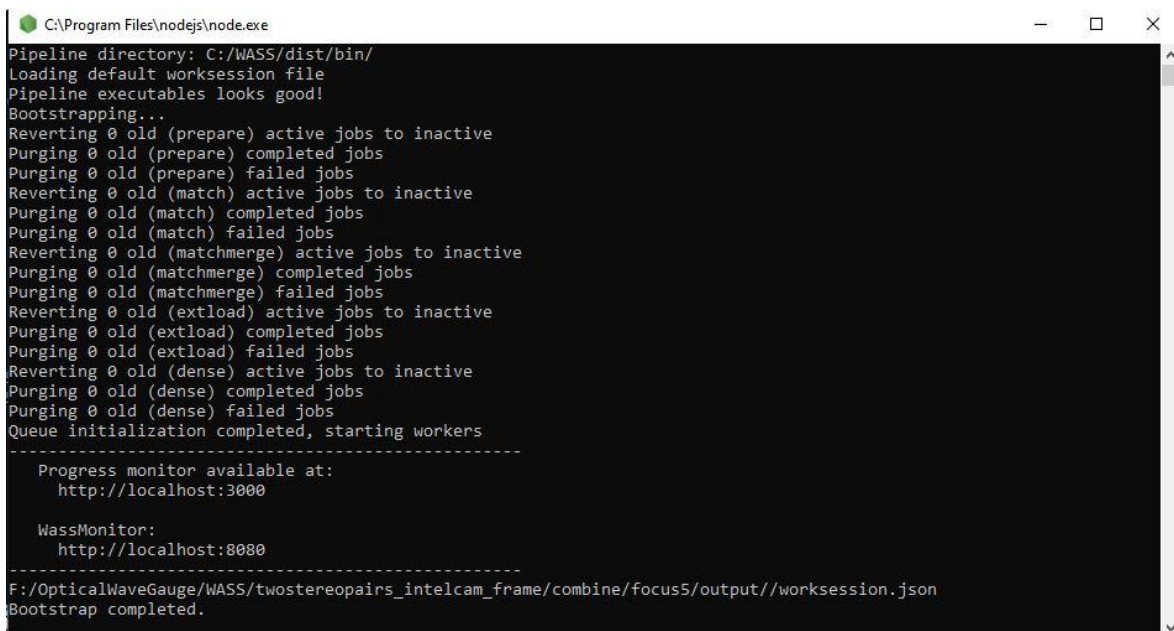


Figure 4.9: LED signals from the DAQ (red) and a GoPro<sup>®</sup> (blue) synchronized in time using Wavelab.



### 4.1.3 WASS Processing

Once the videos captured by the GoPros<sup>®</sup> were properly synchronized, they were analyzed using the WASS software pipeline. WASS can be installed on several different operating systems, but for this study it was built on a Microsoft Windows computer using Microsoft Visual Studio. The WASS software along with its dependent programs must be installed before stereo video analysis. Once built, a specific directory architecture must be followed for WASS to recognize video data. A Matlab routine was developed to take each frame from the synchronized GoPro<sup>®</sup> videos and place them in WASS directory folders following a specific naming format. The methodology laid out by the developers of WASS ([https://www.dais.unive.it/wass/documentation/getting\\_started.html](https://www.dais.unive.it/wass/documentation/getting_started.html)) was then followed to spatially reconstruct the data. WASS is started from a provided batch script, *launch\_wassjs.bat*, which runs WASS through the command prompt of a Windows computer. First, the system loads and debugs any issues from the previous WASS run on a command prompt window shown in Figure 4.10.



```

C:\Program Files\nodejs\node.exe
Pipeline directory: C:\WASS\dist\bin/
Loading default worksession file
Pipeline executables looks good!
Bootstrapping...
Reverting 0 old (prepare) active jobs to inactive
Purging 0 old (prepare) completed jobs
Purging 0 old (prepare) failed jobs
Reverting 0 old (match) active jobs to inactive
Purging 0 old (match) completed jobs
Purging 0 old (match) failed jobs
Reverting 0 old (matchmerge) active jobs to inactive
Purging 0 old (matchmerge) completed jobs
Purging 0 old (matchmerge) failed jobs
Reverting 0 old (extload) active jobs to inactive
Purging 0 old (extload) completed jobs
Purging 0 old (extload) failed jobs
Reverting 0 old (dense) active jobs to inactive
Purging 0 old (dense) completed jobs
Purging 0 old (dense) failed jobs
Queue initialization completed, starting workers
-----
Progress monitor available at:
  http://localhost:3000

WassMonitor:
  http://localhost:8080
-----
F:/OpticalWaveGauge/WASS/twostereopairs_intelcam_frame/combine/focus5/output//worksession.json
Bootstrap completed.

```

Figure 4.10: WASS debugging command prompt window initially shown when "launch\_wassjs.bat" is run.

Then four separate WASS features: *prepare*, *match*, *auto-calibrate*, and *dense stereo*, must be initiated by the user using the WASS monitor that can be accessed on the computer's internet browser at <http://localhost:8080>. The monitor displays the working directories, the progress of

the current task, the estimated time remaining, and any failures that may have occurred during processing. An example of the WASS monitor during a video analysis is seen in Figure 4.11.

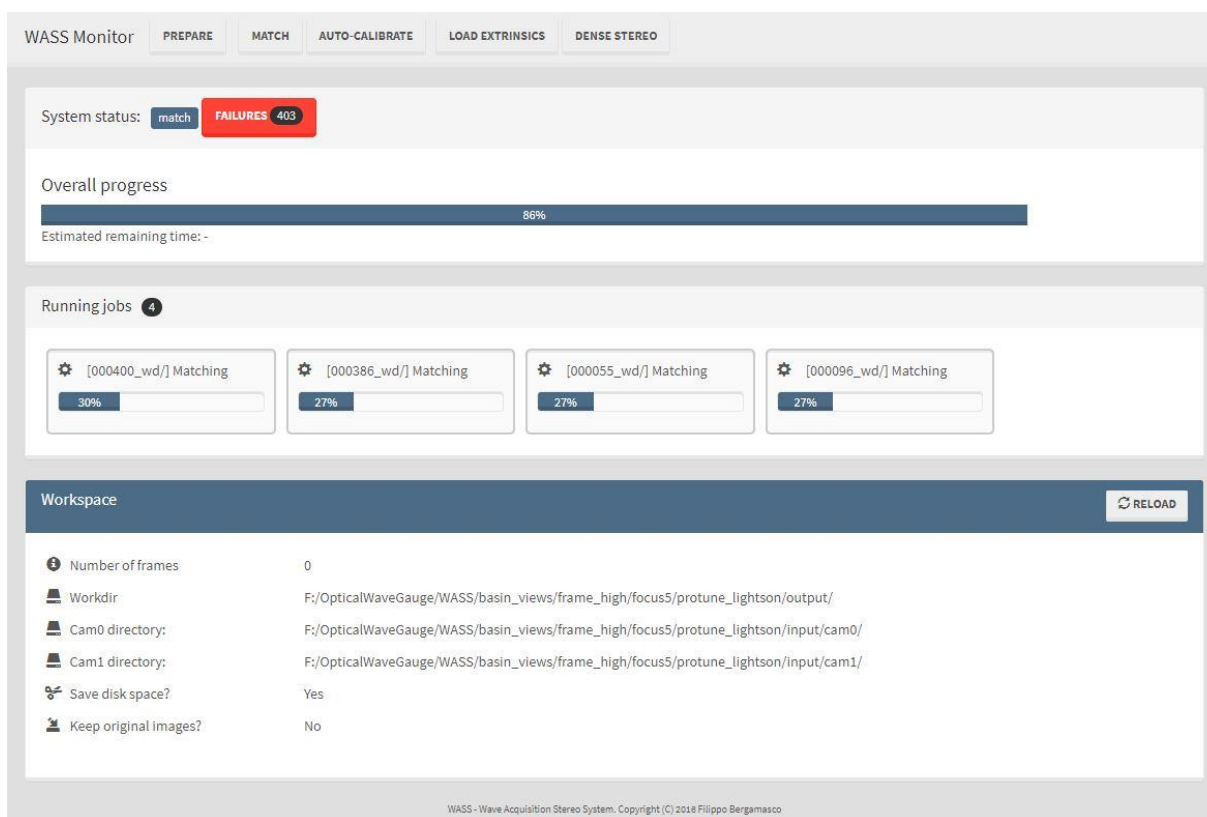


Figure 4.11: WASS monitor displaying the overall progress of the run at hand, any failures that may have occurred, and the directories WASS is working from.

The approximate run time, number of failures, and storage space required for each WASS run for this project was noted in an Excel spreadsheet. This information was later used for an overall system comparison to the Intel<sup>®</sup> system, which can be found in Section 4.3.

#### 4.1.4 NetCDF Generation and Data Visualization

WASS outputs spatial data for each video frame in a .XYZ and .PLY file that was converted into a format more easily recognized by Matlab. The .XYZ and .PLY files consist of data points from each image pixel that make up a point cloud of spatial points. WASS provides a Matlab routine that will load this raw spatial data and overlay it onto the input video frame so that the data can be quickly visualized after each WASS run without much further analysis. Often times, WASS could not reconstruct certain areas in the cameras' fields of view for various reasons, so visualizing the data in this way helped determine WASS' strengths and weaknesses. This process

was crucial in optimizing lighting, camera angles, and wave conditions. After each WASS run, this Matlab code was used to create a video showing the data output from WASS overlaid onto the original video frames. Figure 4.12 shows a single frame of a video taken during the Basin Views experiment. The color overlaid on the black and white video frame represents the water surface elevation estimated by WASS. Areas with no color were unable to be reconstructed.

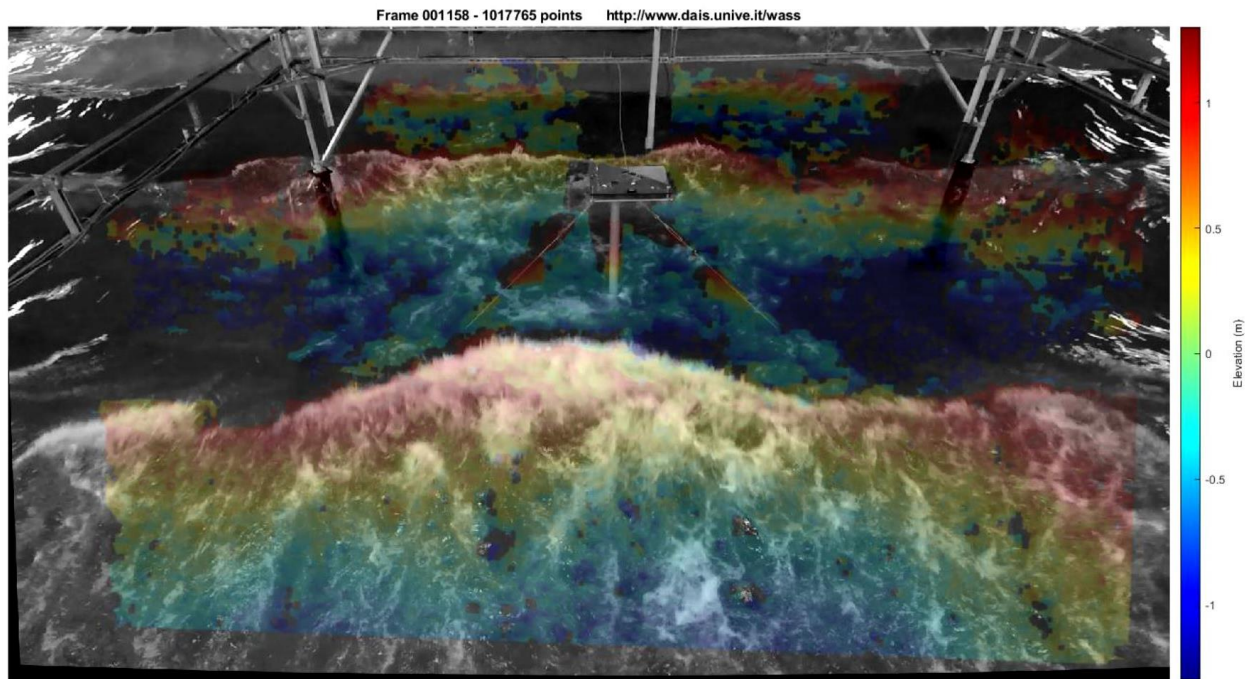
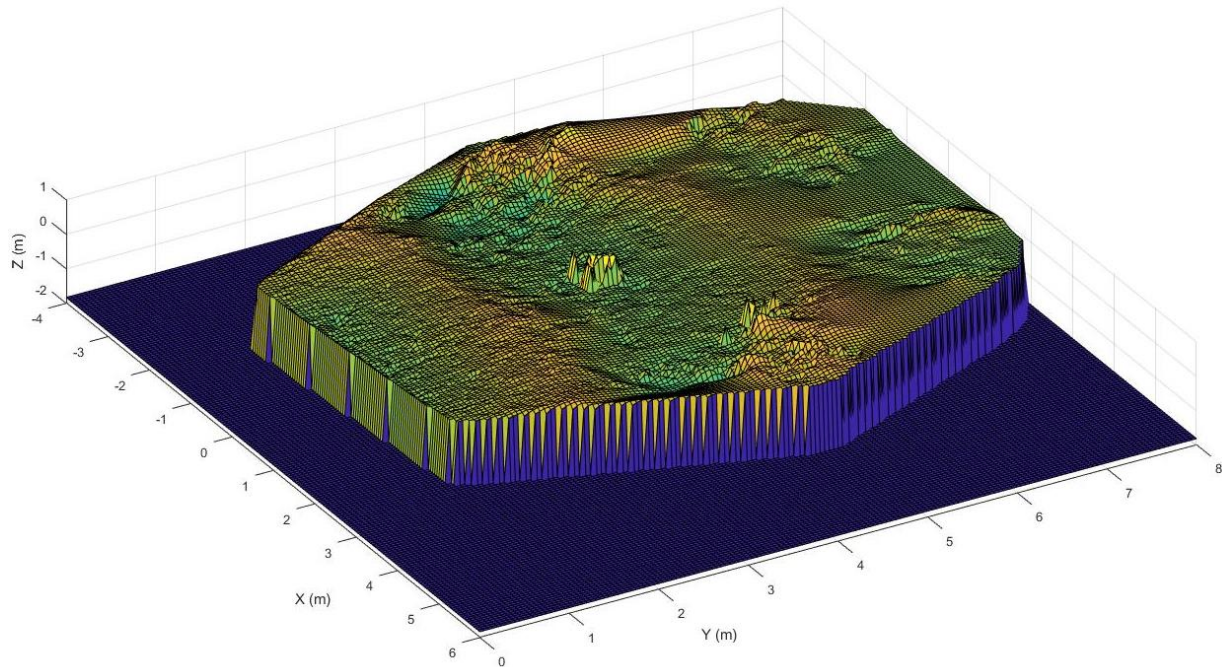


Figure 4.12: WASS spatial data overlaid on its respective video frame with red being higher surface elevations (crests) and blue being lower elevations (troughs).

The raw point cloud is difficult to analyze due to its non-uniformity and any gaps that may occur within the data, so it was interpolated into a gridded format that could be easily analyzed for wave properties. Filippo Bergamasco, the developer of WASS, personally provided a Matlab script that interpolates the raw WASS data into a user-defined grid surface, and then saves the data in a NetCDF file with all pertinent spatial information [8]. The x and y limits of the grid as well as the grid spacing are defined by the user, then a linear interpolation is applied to the dataset using the *TriScatteredInterp* function in Matlab. These NetCDF files, generally used by the oceanography community, can easily be loaded into Matlab for further analysis using the *ncread* function. The gridded spatial data that coincides with the scene in Figure 4.12 is shown in Figure 4.13, where both wave crests can be seen as well as spikes in the surface elevation where the instrumentation pictured disrupted the water surface reconstruction. The interpolation

smoothed over any gaps in the raw data and gridded areas with a high point density into one representative data point. In order to select the appropriate grid spacing, a grid sensitivity study was performed and outlined in Section 5.4. Once the spatial data was interpolated into a NetCDF file, it was ready for further wave analysis and validation using gauge measurements.



*Figure 4.13: Gridded spatial data from the scene in Figure 4.12 showing both wave crests and spikes where instrumentation features disrupted the surface elevation data.*

#### 4.2 Intel® RealSense™

The second stereo-video measurement system used in this study was the Intel® RealSense™ D455 depth camera. This is an “off-the-shelf”, consumer grade depth imaging system that uses active infrared stereoscopy for spatial measurements in applications such as robotics, 3D scanning, and object tracking [37]. Open source software is available for this system in the Intel® RealSense™ Software Developer Kit (SDK) 2.0

(<https://github.com/IntelRealSense/librealsense/releases/tag/v2.43.0>) that is composed of a variety of tools and software including the Intel® RealSense™ Viewer, which was the tool primarily used for camera visualization and control in this study. The Intel® RealSense™ Viewer can be run as a desktop application in Windows and used to control the camera settings, visualize data in real time, and start and stop camera recording. This was used on a Windows laptop to

record data from the Intel® system during testing. The data is recorded with its coordinate system defined about the camera's location and orientation, which was generally pointed downward toward the water surface. Hence, the coordinate system had to be adjusted so that the mean water level was the x-y plane and the water surface oscillated about  $z = 0$ . Once the coordinate system was rotated, the spatial data was filtered to discard any unwanted data points. Then, similar to the methodology for WASS, the data was synchronized to the gauge measurements using an in frame randomly blinking LED. The point cloud was finally interpolated into a grid array before final wave analysis. These processes are described in detail in the following sub-sections.

#### 4.2.1 Intel® RealSense™ Viewer

The aforementioned Intel® RealSense™ Viewer Windows desktop application was downloaded with the Intel® RealSense™ SDK 2.0 and used for controlling the Intel® camera and initial data visualization during this study. The program was downloaded on a Windows laptop so that it could be used on the lab floor for camera control. Several camera settings can be adjusted using this software, but the camera and stereo module resolution and frame rate along with the depth threshold filter under the stereo module's post-processing tab were predominantly adjusted. The resolution and frame rate were selected to closely match the settings used on the GoPros®. The threshold filter was adjusted so that the maximum distance recorded was 16 m instead of the factory default of 4 m. Once the camera settings were adjusted, the Viewer could be used to visualize spatial data before recording. This helped optimize the camera's positioning and distance to the water surface. The Viewer was used to start and stop camera recording and save each video in a user named .BAG file, a file format exclusively used by the robotics community. A screenshot of the Intel® RealSense™ Viewer displaying water surface spatial data of a breaking wave crest in the DWB is shown in Figure 4.14. The original camera coordinate system is shown on the righthand side of the figure and causes the water surface to be tilted upward. This is later adjusted to closer match the DWB coordinate system.

The Viewer saved each recording into a single .BAG file with both spatial and video data stored within. There are several methods for extracting data from a .BAG, but this study used the *rs-convert* tool from the RealSense™ SDK 2.0. This tool converted each frame of spatial data from the .BAG file into an individual .PLY file which could easily be read using Matlab's Point Cloud Processing Toolbox. These files only contain the spatial data from the .BAG file, but the RGB

video data was needed to extract an LED signal for data synchronization. This process is described in the next sub-section.

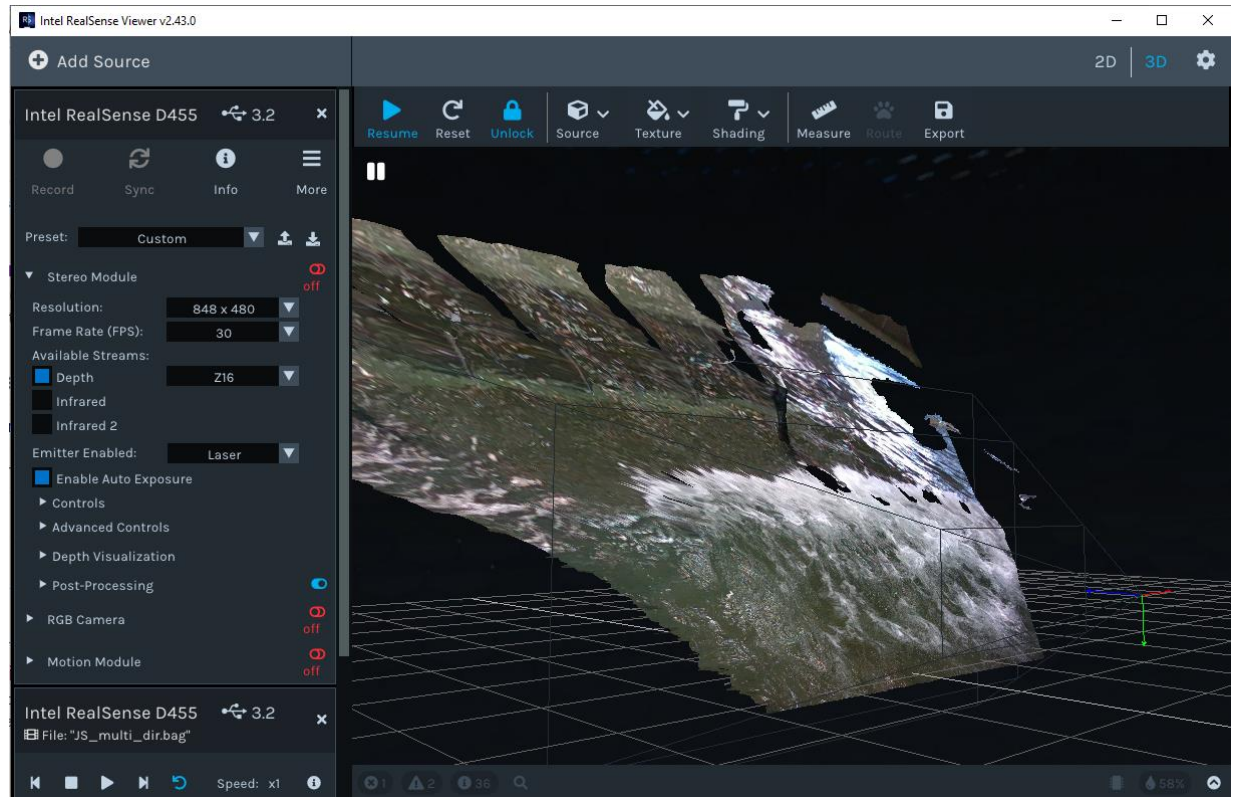


Figure 4.14: Screenshot of Intel<sup>®</sup> RealSense<sup>™</sup> Viewer showing spatial data of the DWB water surface with a breaking wave crest in the main right panel. The left panel shows the camera setting controls with the three main tabs: Stereo Module, RGB Camera, and Motion Module with the stereo tab open to show its settings. The red, blue, and green coordinate origin in the right panel represents the position and orientation of the Intel<sup>®</sup> camera.

#### 4.2.2 LED Signal Extraction

In order to synchronize the Intel<sup>®</sup> and DAQ data, a similar method used to synchronize WASS data (Section 4.1.2) was implemented. The blinking LED was placed in view of the Intel<sup>®</sup> camera in each trial so that video data could be used to output an LED signal. The same code structure developed for WASS synchronization was utilized for the Intel<sup>®</sup> data. The *rs-convert* tool first converted the .BAG file into individual .PNG image files for each video frame. The files were appropriately named with a timestamp that could be used to generate a time vector for the images, ensuring that signal drift did not occur during the duration of the video. Then the LED signal extraction Matlab code was used to output a LED signal from each video, which was used for data synchronization within Wavelab, as described in Section 4.1.2. An example of

synchronized LED signals from both the DAQ and Intel<sup>®</sup> camera is displayed in Figure 4.15. The time delay for the Intel<sup>®</sup> signal is calculated by Wavelab and this delay is added to the time vector of the signal to correct it. The period of the individual blinks from each signal were calculated and compared to understand the quality of the time synchronization completed by Wavelab. The average difference in wave periods between the two signals was 0.02 s with a standard deviation of 0.18 s for the particular timeseries displayed in Figure 4.15. Because the exact time of each video frame is recorded by the camera system video drift was not investigated as it was for the WASS system, but future work should include testing the synchronization quality after a longer duration of 10 minutes to ensure no drifting is present.

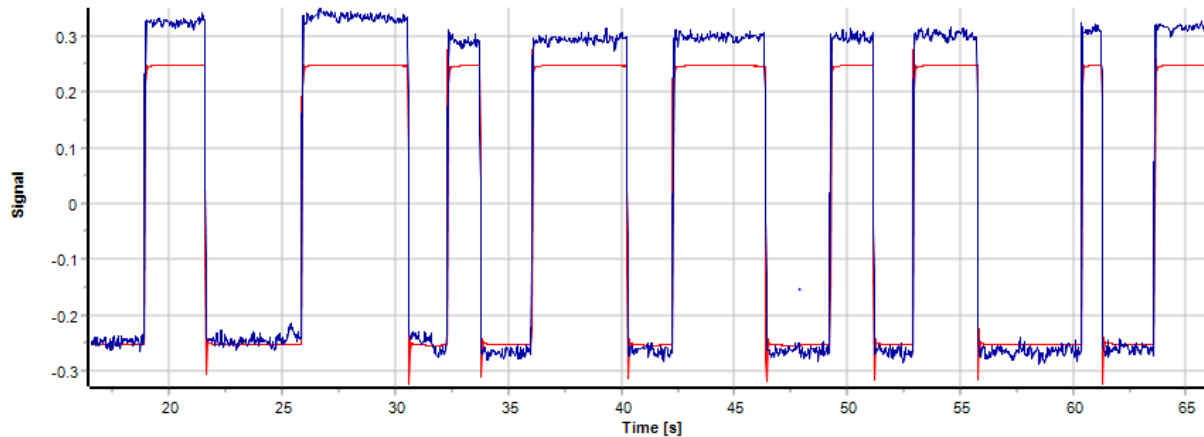


Figure 4.15: The LED signals from both the Intel<sup>®</sup> camera (blue) and DAQ (red) synchronized in Wavelab.

#### 4.2.3 Coordinate Adjustment

The Intel<sup>®</sup> RealSense<sup>™</sup> Viewer automatically sets the coordinate system origin about the position and rotation of the Intel<sup>®</sup> camera unit, defining positive x (blue) in the direction the lens is aimed, positive y (red) to the right of this, and positive z (green) downward, as seen in Figure 4.14. Typically, the camera was aimed downward causing the water surface to be rotated about the camera's y-axis. Before performing wave analyses on this data, the coordinate system had to be adjusted so that the mean water level was parallel to the x-y plane. To do this, either the camera's exact positioning in the real world must be known or a reference within the recorded data must be used to understand the camera's rotation.

Ideally, IMU data from the Intel<sup>®</sup> camera containing information on gravitational acceleration would be used as a reference, but this was an unforeseen problem and no IMU data was recorded during the study's trials. Instead, a point of reference within the spatial data was used to estimate the camera's positioning for each trial. The instrumentation frame in view was relatively level but due to its distance from the camera and the small size of the level plane on the Unistrut, this surface was not usable. At the beginning of each trial the water surface was flat and could ideally be used for a plane reference when adjusting the coordinates. The camera had difficulty recognizing the water surface at these moments though, and the data was unusable. Instead, the moving water surface, which was more easily recognized by the camera, was used to calculate a dynamic mean water level to use as a plane of reference. This could lead to inaccuracies dependent on the wave conditions of the particular trial, but it was the only consistent plane of reference. Thus, it was used to initially rotate the point cloud, then further adjustment was completed during two-dimensional data analysis to subtract the mean of each grid node's timeseries. Further information on this process can be found in Section 5.4.2.

To find the dynamic mean water level plane, point clouds from multiple timesteps spanning over a period of several waves were combined to average out the effect of individual waves. Then a mean water level could be extracted from this combined point cloud. There were several other objects in the camera's field of view that needed to be disregarded to accurately calculate mean water level. A three-dimensional random sampling consensus (RANSAC) method was applied in Matlab to estimate a mathematical model, in this case an average linear plane, of the time-averaged dataset without considering unwanted data points from instrumentation [7]. The RANSAC method disregards outlier points when determining the dataset's model so it could be used without further data filtering. The *pcfitplane* Matlab function was used to detect the water surface plane. This function allows one to define a maximum allowable distance for plane detection, outside of which the data points will be considered outliers and not affect the average plane. This distance was set as the trial's wave height to most accurately represent the span in which water surface data point may lie.

Once a good representative plane was found, its normal vector was used to calculate a rotation matrix from the unit vector of the original camera coordinate system. The rotation matrix was then mathematically applied to each data point and saved for future reference. Figure 4.16 shows



an example of both an idealized, schematic of this process and the mean water level plane calculated for an actual point cloud. Camera positions and their relative coordinate systems are labeled as well as wave propagation direction. Once rotated, the dataset also often required translation so that the free surface was oscillating about  $z = 0$ , but this process was trivial.

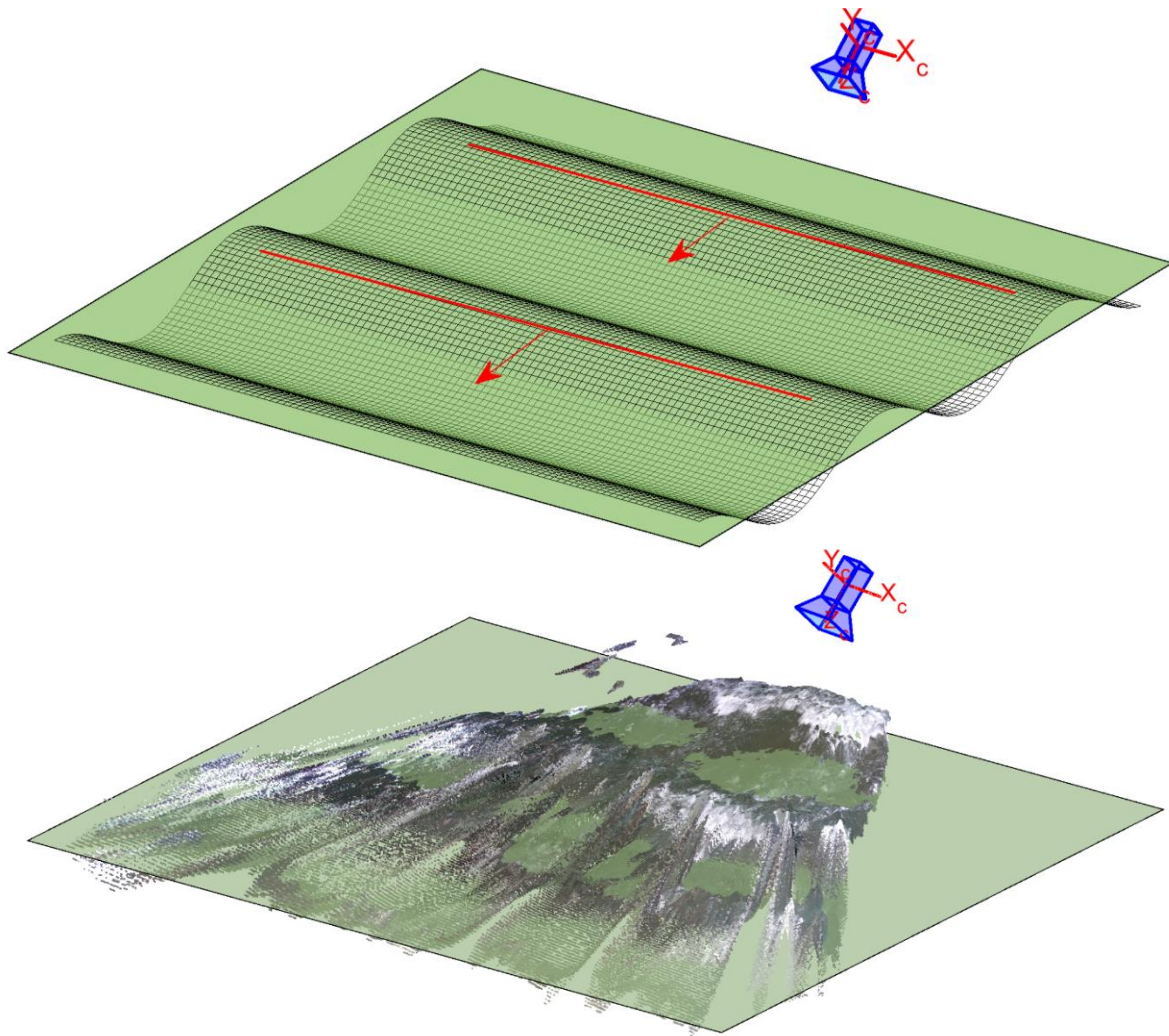


*Figure 4.16: (Top) Schematic of idealized water surface mesh with wave crests and direction of propagation (red) and calculated mean water level plane (green), including camera location and orientation with its localized axes. (Bottom) Actual time-averaged point cloud and camera location with model plane (green) of mean water level that was calculated using the RANSAC method.*

#### 4.2.4 Spatial Data Filtering

After each point cloud data was rotated into the correct coordinate system, any unwanted data points from the instrumentation and water surface noise was removed using a z-axis minimum

and maximum threshold filter. This was generally set to the wave height plus ~20% so that all wave crests and troughs were thoroughly captured. This technique resulted in retaining several unwanted points such as the base of any surface-piercing wave gauges or the instrumentation frame but filtered the majority of unwanted data. Figure 4.17 shows a point cloud before and after data filtering with unwanted data points associated with instrumentation highlighted. As seen in the figure, the majority of the points are removed but their bases remain. Other spatial data filtering techniques were considered, such as color filtering or manual removal of unwanted points, but the elevation filter was deemed more feasible after testing.

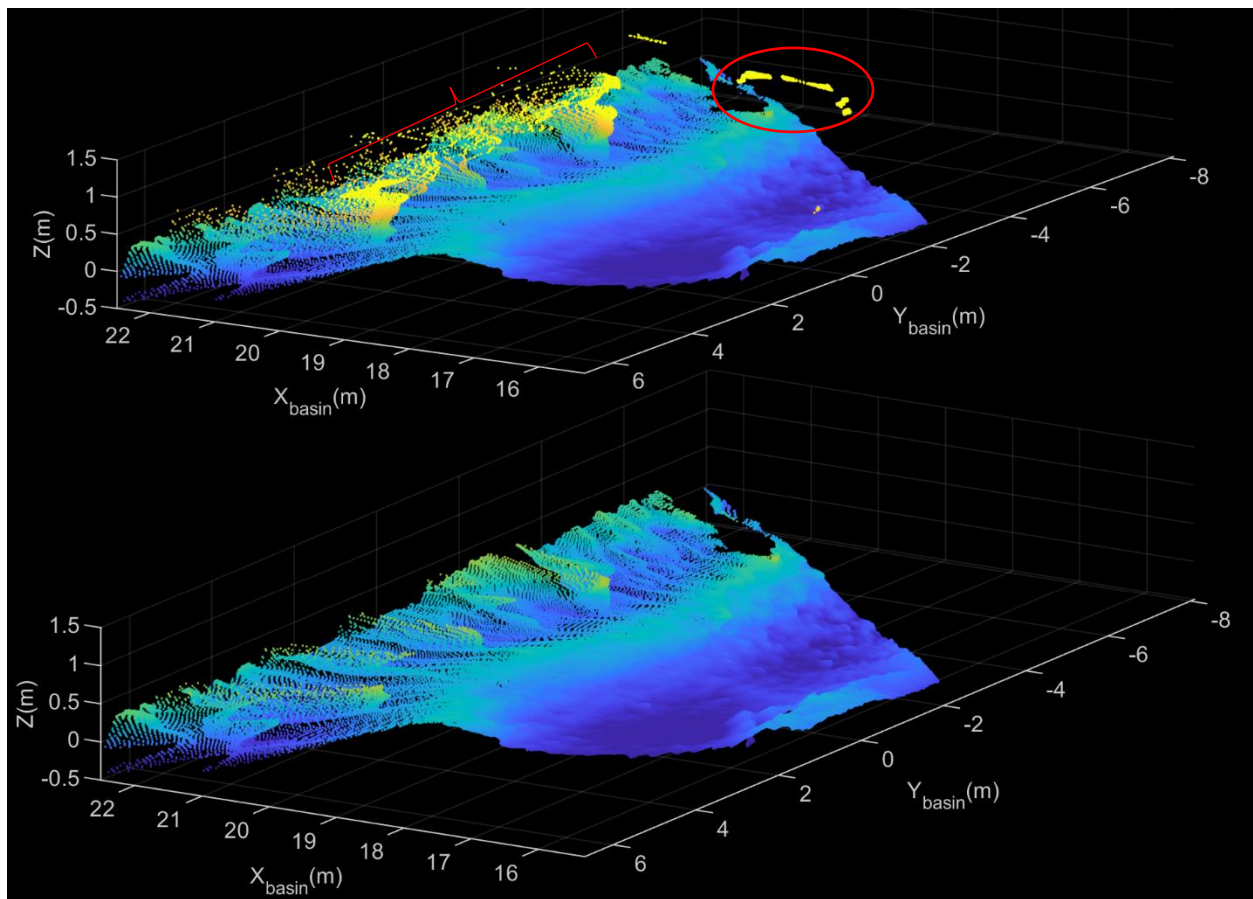
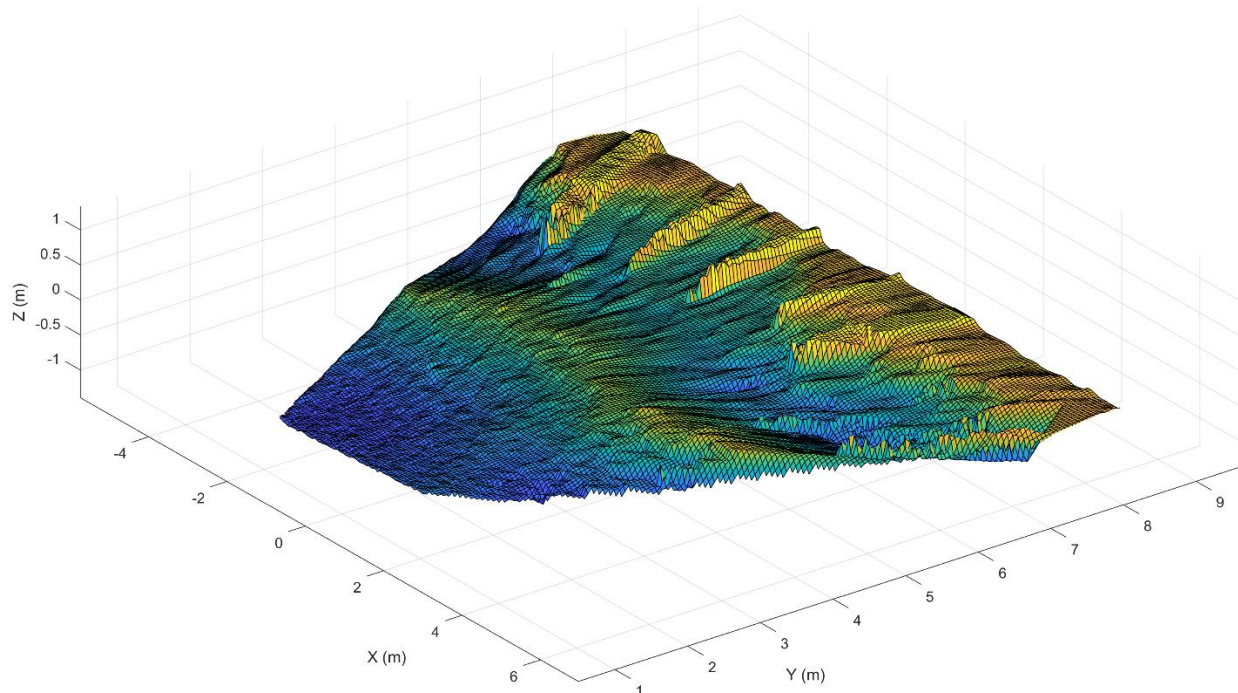


Figure 4.17: Intel® point cloud before (top) and after (bottom) data filtering with data points associated with instrumentation indicated by red shapes.

#### 4.2.5 Mesh Generation

Once datasets were rotated and gleaned of any unwanted points, a similar procedure used for the WASS data (Section 4.1.4) was utilized to interpolate each point cloud into an evenly gridded, three-dimensional surface. A triangulation-based three-dimensional linear interpolation method

was used with the Matlab *griddata* function. The area of interest would be selected using x and y bounds along with the appropriate grid spacing (dx, dy) based on the grid sensitivity study that is described in Section 5.4. Then each point cloud was interpolated into a gridded surface and saved into a structured array in Matlab with the data fields: x grid, y grid, elevations, and time. This was the final file format used before wave analyses were performed on the data. Figure 4.18 shows an example of gridded data from a focusing wave case. There are several “shadows” that are created behind the instrumentation frame supports and surface-piercing wave gauges that originally had no data present but were interpolated to be of higher elevation. These areas will be disregarded during analysis.



*Figure 4.18: Gridded Intel® data with a focusing wave crest propagating in the positive y direction. The five lines of higher elevation starting around  $y=6$  m are created from the wave gauges and frame supports shadowing these regions from the camera’s perspective.*

### 4.3 System Comparisons

The WASS and Intel® stereo video measurement systems have many differences in their hardware, user interface, intended application, processing time, and output file size. Chapter 5 and Chapter 6 discuss each system’s accuracy when measuring wave characteristics, but other attributes of the systems are important to consider when deciding whether they are appropriate

for use in a future research study. Processing time, file size, and ease of use of each system were noted while completing the stereo data post-processing steps and described in this section.

Post-processing time and data storage are important factors to consider when analyzing each system's feasibility for use in the lab. For many research studies in the HWRL, there are numerous trials per experiment and numerous experiments per study which can last up to several months. This can lead to hours of video data needing to be stored and processed, often deeming stereo video methods unfeasible. For each trial in this study, the file sizes for data from both systems was recorded and averaged to estimate the data storage requirements. Each WASS directory averaged 20.13 megabytes per frame of video while each Intel® directory averaged 2.75 megabytes per frame. The WASS system requires approximately 7.3 times the amount of data storage than the Intel® system requires. For a 2-minute video taken at 30 frames per second (the average trial length and camera setting for this study), this approximates to 72.5 gigabytes of storage for WASS and 9.9 gigabytes of storage for the Intel® system. This of course depends on the cameras selected for WASS, the area being measured, the camera settings selected for each system, and several other variables but it gives a good idea of what may be required for future projects.

The methodology for post-processing data from both systems was developed during the course of this study, so it is difficult to parameterize the computational time required for each. Both system's initial processing time is well known, however, and can easily be compared. The Intel® system processes data in real time and immediately saves the spatial and video data into the final .BAG file, so the time taken for stereo matching and spatial approximation is negligible. The duration required for each WASS run was recorded and averaged to 4.45 seconds of computational time per frame of video. This equates to 4 hours and 27 minutes to process a 2-minute video taken at 30 frames per second for reference.

Ease of use and set up are less important than accuracy when considering a system for scientific use, but are still important to consider especially for the HWRL. Faculty, staff, and students working on each project are constantly rotating at HWRL so a system that is easy to set up and understand is preferred if it is to be used for a wide variety of projects. While the WASS system gives some flexibility on hardware selection, the camera calibration needed, specific file directory set up, and the system's sensitivity to lighting and camera positioning make it a more

difficult system to deploy and use. Lead researchers on each project would need to understand this process and take the time to post-process all video data before doing any further data analysis. The Intel<sup>®</sup> system is much easier to deploy and troubleshoot because of the professionally developed software that it is provided with but is less customizable and may not be as easily applied in certain cases. Hence, both systems have advantages and disadvantages that should be thoroughly understood by a researcher before an informed selection can be made.

#### 4.4 *Chapter Conclusions*

This chapter discussed the methodology developed and used for both stereo measurement systems in this study. For WASS, the required camera calibration procedure was described and a data synchronization technique using an in-frame randomly blinking LED was presented. The WASS software interface was overviewed as well as the method used to interpolate the point cloud data into gridded NetCDF files. Data visualization techniques were also described. For the Intel<sup>®</sup> system, the RealSense<sup>™</sup> Viewer was used for camera control and data visualization. The blinking LED synchronization method was also used for the Intel<sup>®</sup> data. The coordinate system of the raw spatial data was adjusted using the estimated dynamic mean water level plane. This plane was calculated using a RANSAC based method. Once rotated, the point cloud data was then filtered using an elevation threshold and interpolated into a gridded mesh file for further analysis. The following chapter describes the data analysis techniques used for each experiment and the preliminary findings of each. Then a single system is selected based on performance and an in-depth spatial analysis is completed for each wave case whose results are presented and discussed in Chapter 6.

## Chapter 5 Data Analysis

This study aims to implement a stereo-video free surface measurement system into the DWB at the HWRL. A number of spatial water surface measurement techniques were explored for laboratory use and two systems were ultimately selected for testing: WASS, an open-source stereo image processing software designed for the measurement of ocean waves, and the Intel<sup>®</sup> D455 Depth Camera, a consumer grade active infrared stereo camera designed for a variety of applications. Multiple experiments were constructed to optimize these two systems for use in the lab and validate their measurements against traditional point gauges in numerous wave conditions. Video data was collected with the WASS and Intel<sup>®</sup> systems, post processed into gridded three-dimensional surface timeseries as described in Chapter 4, then further analyzed for its wave properties and abilities to recognize the water surface. This chapter describes the data analysis techniques used for each experiment and describes their preliminary findings. The Basin Views experiment utilizes data visualization techniques described in Section 4.1.4 to optimize the camera settings, positioning, and lighting for the WASS system. Then, in the Airy Validation experiment, this system is tested in both breaking and non-breaking regular wave conditions and the camera measurements are compared to measurements from traditional wave gauges. A polarized lens is added to the cameras in the CPL Filter experiment, and finally the Intel<sup>®</sup> system is included in the final set of experiments. In these experiments, both systems are tested in a variety of wave conditions and multiple data analysis techniques are applied to measure statistical wave height values and directionality. Finally, a system is selected based on performance and a more extensive spatial analysis is performed on data collected during the final experiments. The results are presented and discussed in Chapter 6.

### 5.1 Basin Views

The Basin Views experiment was the first preliminary experiment of this study with the objective of optimizing camera angle, settings, and lighting for the remainder of the project. Short 30 seconds videos were taken with GoPro<sup>®</sup> cameras of two different wave conditions in the basin. Several different camera angles, settings, and lighting were recorded then analyzed using WASS to determine which of these worked best within the software. Spatial data reconstructed by WASS was overlaid on to the GoPro<sup>®</sup> videos using the methodology described in Section 4.1.4 in order to visualize the quality of the data output. Each video was examined to

see whether WASS was reliably reconstructing the free surface, and the number of frame failures output by the WASS Monitor (described in Section 4.1.3) was recorded. This information helped determine the design and layout of subsequent experiments.

### *5.1.1 Camera Angles*

Seven different camera positions around the DWB were tested to determine which angle and camera height would render the best water surface reconstruction. The area of focus was under the instrumentation frame, where reliable surface elevation data was being collected by point wave gauges. Figure 5.1 shows the seven camera locations around the DWB. Each position had its own unique lighting issues, with glare and reflection from several different lighting sources. The artificial lighting and sunlight from the windows lining the North and South sides of the basin were the main sources of light. A balance between maximizing the lighting of the scene and minimizing surface reflections was crucial to WASS' success. WASS also had difficulties reconstructing the water surface when the cameras were able to see the bottom of the basin, so positioning the cameras at an oblique angle was important. This often required lowering the cameras significantly, which unfortunately resulted in a shadowing affect from the waves in view of the cameras. Shadowing occurred when any object obstructing the view of the cameras blocked the scene behind the object, creating an empty space in the spatial data. When the cameras were placed on the center of the beach (position 7 in Figure 5.1) they were able to capture a larger area of the basin, but due to the lower elevation of this position much of the instrumentation frame was shadowed by waves in the foreground. This can be seen in Figure 5.2 where the red areas of the wave crests are obstructing the view of the water surface directly behind them. To see screenshots of output videos from the other camera angles see Appendix B.

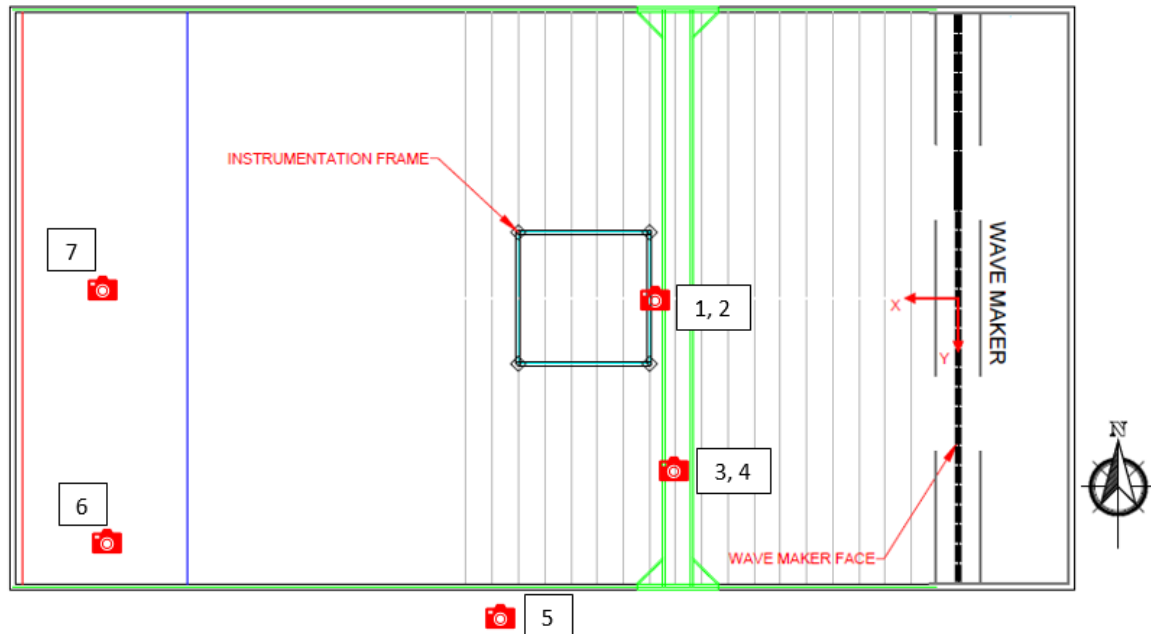


*Figure 5.1: Layout of DWB and numbered GoPro<sup>®</sup> camera angles used in Basin Views experiment. Camera angles: 1. Instrumentation frame high, 2. Instrumentation frame low, 3. Instrumentation bridge towards beach, 4. Instrumentation bridge towards wavemaker, 5. DWB side, 6. Beach corner, 7. Beach center.*

The output videos also proved that fixed objects, such as the instrumentation frame, would often be recognized by WASS and greatly affect the area of measurement surrounding their position. This created problems in data comparison when wave gauges were located directly next to a frame support or furthermore the gauge itself was present in the spatial data. Overall, positioning the cameras within the instrumentation frame at an elevation high enough to keep the majority of wave gauges in view but low enough to reduce surface reflections and the cameras' ability to see the bottom of the basin was ideal. This eliminated the obstruction from the frame supports while maintaining an oblique angle of the water surface being measured.



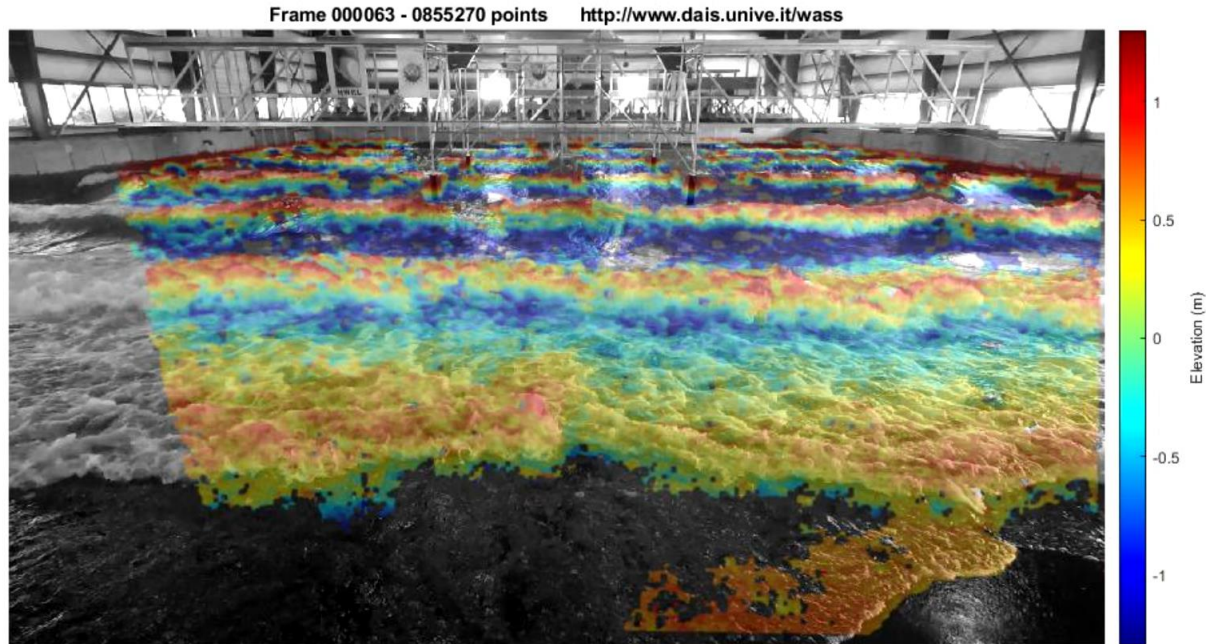
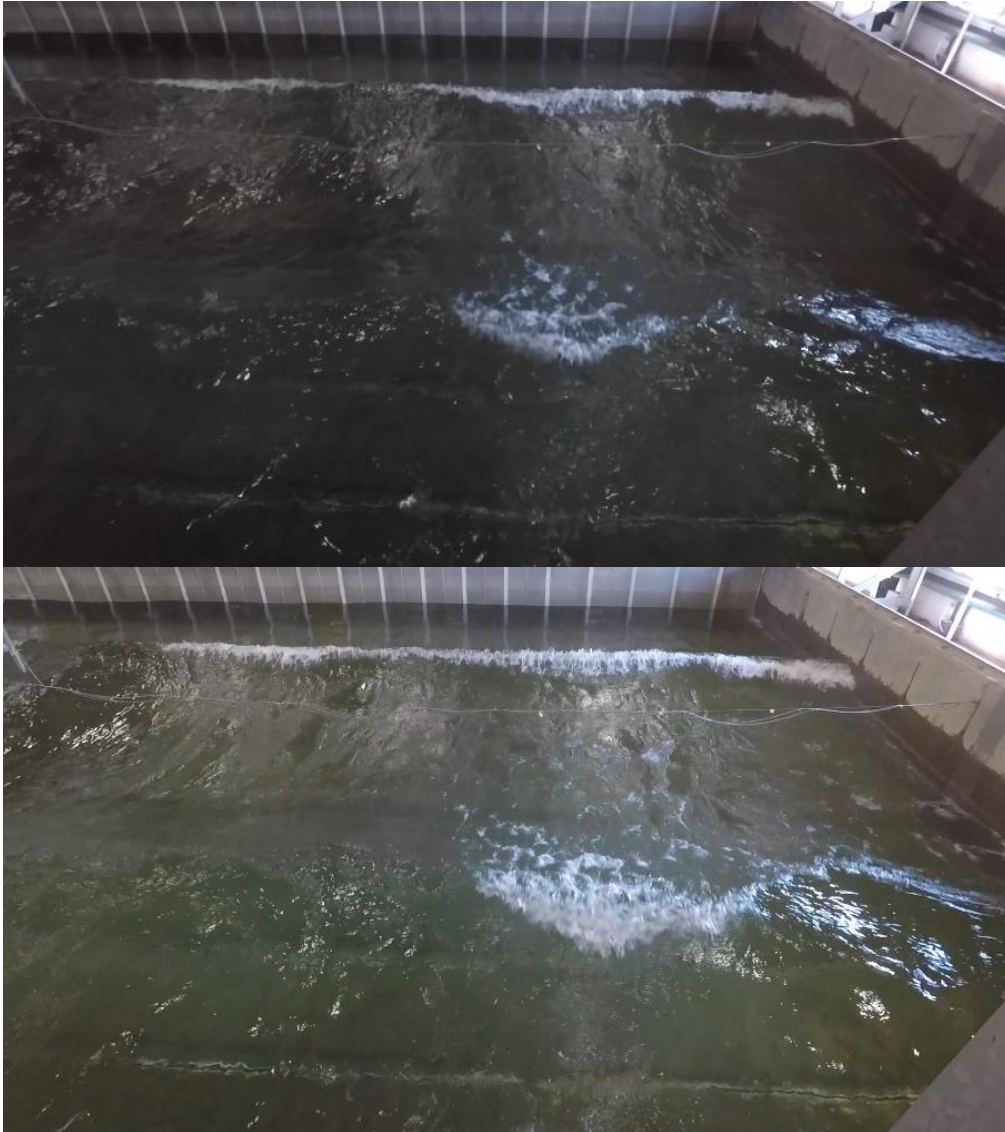


Figure 5.2: Screenshot of the output video from Basin Views experiment during regular waves viewed from the beach center (position 7).

### 5.1.2 Camera Settings

For each camera position, two camera settings were tested in an attempt to reduce water surface glare and blur in each video frame. The GoPros<sup>®</sup> used for this study have the capability of manually controlling camera settings such as shutter speed, ISO, and exposure with an on-camera feature called Protune. With Protune turned on, the user can adjust camera settings as desired, but when turned off the camera automatically adjusts settings according to the scene being captured. To reduce image noise and glare a lower ISO of 400 and faster shutter speed of 1/60 were selected and then compared to the automatic setting. Figure 5.3 shows two screenshots taken from the same camera position on the instrumentation bridge facing towards the wavemaker with Protune either on or off. Camera settings adjustment slightly reduced surface reflections and decreased the blur of the breaking wave crest, but overall the scene was much darker and the free surface was less distinguishable. This created a higher failure rate within WASS and in some cases the videos were not able to be reconstructed at all, so Protune was turned off for the remainder of the study. From a photography perspective, this is a minimal amount of camera settings adjustment and further optimization is most likely possible, but this is outside of the scope of this project.



*Figure 5.3: Screenshots of GoPro® videos with Protune on and off from the Basin Views experiment from the instrumentation bridge facing the wavemaker. Top shows GoPro® with Protune on with an ISO of 400 and a shutter speed of 1/60. Bottom shows GoPro® with Protune off in Auto setting.*

### 5.1.3 Lighting

Numerous lighting settings were tested to investigate whether reducing surface reflections or thoroughly lighting the scene had a higher impact on the success of WASS' reconstruction. The four diffuse lighting fixtures mounted on the instrumentation frame were either turned on or off for each video taken from the instrumentation bridge. When cameras were placed much further from these lighting fixtures and their surface reflections were inconsequential, the fixtures were left on and the overhead lights in the HWRL were then switched on and off. It was found that when the GoPros® were filming a smaller area, such as under the instrumentation frame, the

diffuse lighting became important to WASS' success and should be left on regardless of the reflections they produced. When the cameras were attempting to film a larger area, such as the entire basin, the sunlight coming from the windows of the HWRL had a higher impact and turning the overhead lights off did not affect WASS' success. It is therefore suggested for future trials to be run during times with reduced sunlight and to thoroughly light the scene with diffuse lighting fixtures strategically placed to decrease surface reflections.

## 5.2 *Airy Validation*

With the ideal camera positioning, camera settings, and lighting established in the Basin Views experiment, longer two to three-minute videos were recorded in the Airy Validation experiment to validate the reconstructed camera data. GoPro® cameras were placed on the bridge facing onshore and slightly to the North or South of the basin in order to focus on different wave gauges on either side of the instrumentation frame. Two regular wave conditions were tested, one with un-broken waves and the other with semi-broken waves where only certain sections of the wave crests were breaking. These waves were generated using Airy wave theory which aims to output a sinusoidal wave profile, but once generated the waves may not always remain this shape. Output videos, similar to the process in the Basin Views experiment, were generated to visualize where WASS was able to reconstruct the water surface. Screenshots of these videos can also be seen in Appendix B. It was noted that for both wave conditions, WASS consistently failed at the start of each trial when the water surface was smooth and untextured. Then, once several waves had propagated through the cameras' fields of view, WASS began to recognize the water surface approximately 30 seconds after wavemaker start-up.

### 5.2.1 *Un-broken Waves*

Two camera angles were tested for the un-broken wave cases, both for which WASS performed significantly worse than the broken wave trials. All video frames from one of the unbroken wave trials failed to be reconstructed by WASS while on the other it failed in 1700 out of the 4200 frames. Upon examining the output video from the more successful trial, it could be concluded that the majority of the data was noise and no further analysis was completed for the unbroken wave cases. Without significant foam and bubble accumulation on the water surface from wave breaking, the surface was not easily recognized by WASS.

### 5.2.2 Broken Waves

The same camera angles were used for the broken wave trials. Output videos from either angle showed that the majority of data came from areas where a broken wave had left a trail of foam on the water surface, which is showcased in Figure 5.4. This is likely due to the bubbles created from wave breaking making the water surface more recognizable and decreasing the cameras' ability to see through the water. It can also be seen in Figure 5.4 that WASS was generally unable to recognize the water surface in the darker areas occurring behind un-broken sections of the crest. This meant that if waves were not breaking directly in-line with the wave gauges there was often no data in these locations, preventing any data comparison between the gauge and camera measurements.

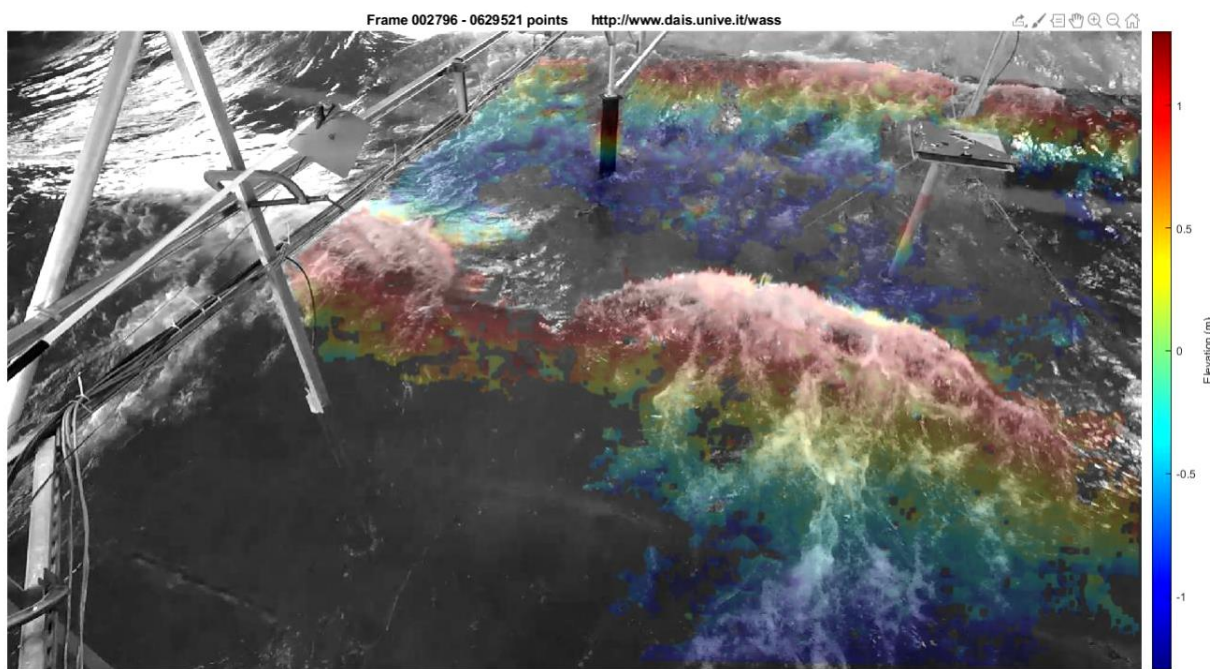


*Figure 5.4: Screenshot of an output video highlighting WASS' ability to reconstruct the foamy trail left by a broken wave crest in the Airy Validation experiment.*

For trials where the surface reconstruction was deemed valid after inspection of the output video, interpolated spatial data from the trial's NetCDF file (Section 4.1.4) was compared to the recorded free surface elevation data from each wave gauge in view of the cameras. A two-dimensional timeseries was extracted from within the camera dataset at the location of each wave gauge and plotted against the recorded gauge data in Wavelab. The wave amplitude and shape recorded could then be visually compared. The WASS data contained high frequency noise with

numerous gaps, but the wave amplitude and shape generally followed that of the wave gauges. The quality of the camera data also seemed to depend on the wave gauge location within the video frame. For the trial shown in Figure 5.4, WASS had difficulty recognizing the troughs of the waves closer to the camera (WG 11). Figure 5.5 shows the comparison of what was recorded by the wave gauge and WASS in the same location. WASS inaccurately reconstructed the wave troughs with a flatter shape and higher elevation. There was consistently an absence of data being each wave crest as well for this particular location. Figure 5.6 shows the same comparison for a wave gauge further from the camera position (WG 13). WASS more accurately captured the shape and magnitude of each wave in this location, but significant noise was present. It is noted that the sharp vertical decreases in the signal from WASS (blue line) are due to the absence of data at that time that had to be replaced by -99 to be recognized by Wavelab's software.

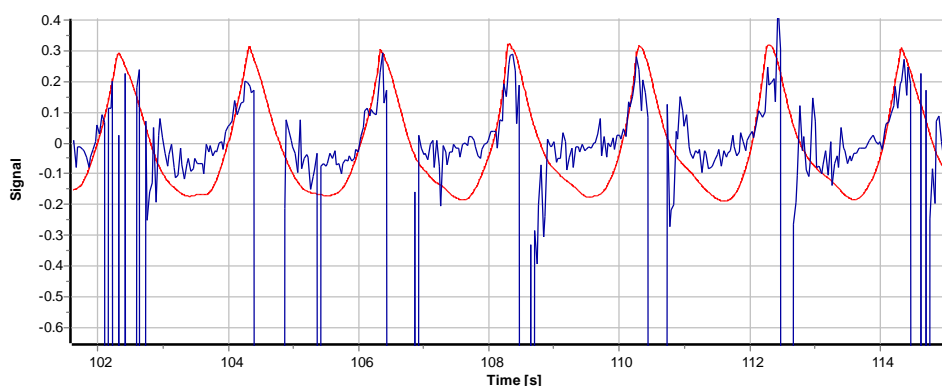


*Figure 5.5: Signal comparison of WG 11 (red) and WASS (blue) during the trial shown in Figure 5.4. Areas with sharp downward spikes within the WASS data signify an absence of data.*

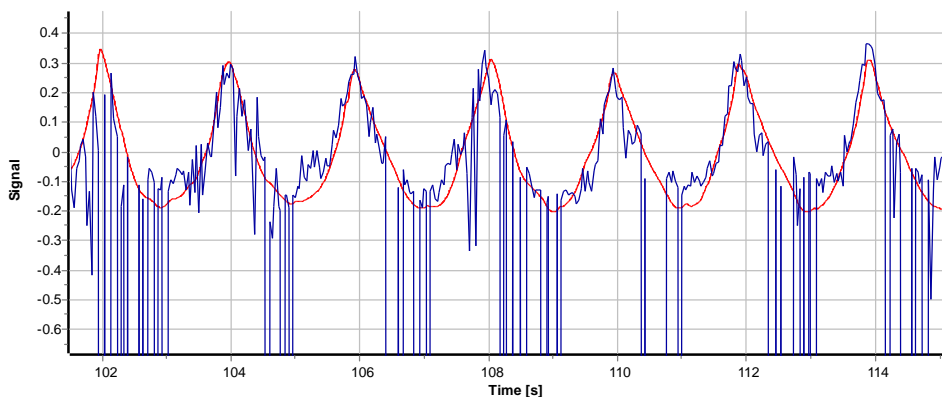


*Figure 5.6: Signal comparison of WG 13 (red) and WASS (blue) during the trial shown in Figure 5.4. Areas with sharp downward spikes within the WASS data signify an absence of data.*

The other broken wave trials were analyzed to determine if there was any correlation between wave gauge location and data quality. Due to the limited amount of data collected, no conclusions could be made, but this was reconsidered in future experiments.

Water surface elevation data from both the camera and wave gauges were plotted against one another to visualize any discernable trends in WASS' surface reconstruction. With wave gauge measurements on the x-axis and camera measurements on the y-axis, linear regression was used to fit a model to this data. Figure 5.7 shows all data points for each WG location during the broken wave trials in the Airy Validation experiment. The linear regression model shows that WASS tended to underestimate the water surface elevation recorded by the wave gauges. It can also be seen that there are many data points in areas where the wave gauges were measuring wave crests (positive) or troughs (negative) and WASS recognized them as the opposite (data points in the second and fourth x-y quadrants). This is clearly an unrealistic representation of the water surface elevation at that time and can be categorized as noise.

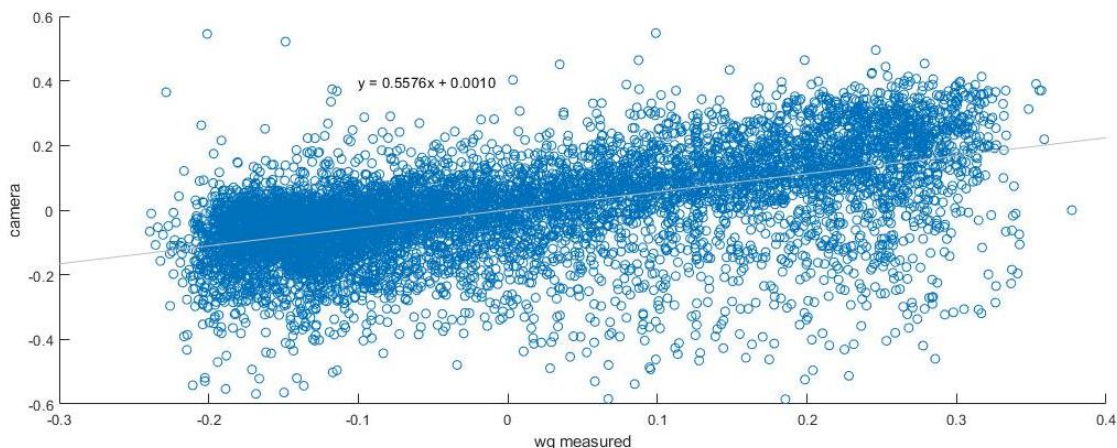


*Figure 5.7: Measured wave gauge data vs. camera data from all broken wave trials in Airy Validation. Linear regression model (grey line) equation shown.*

### 5.3 CPL Filter

Adequate lighting was needed to improve stereo reconstruction, but water surface reflections were decreasing WASS' ability to recognize the water surface. To counteract this, polarized lenses were attached to the GoPros<sup>®</sup> in the CPL Filter experiment. The GoPro<sup>®</sup> cameras were centered on the bridge under the instrumentation frame at a higher elevation so that the majority of the wave gauges were in view. The water surface was either completely lit by turning on all

diffuse lighting fixtures or backlit by turning off the lights facing toward the cameras. Three different wave conditions were tested during this experiment: two breaking wave conditions (focusing waves and regular waves) and one unbroken wave condition (regular waves). Focusing waves were selected so that wave breaking occurred directly under the instrumentation frame without the water level being adjusted.

Data visualization videos, similar to those of the previous experiments, were used to examine the data output from WASS. Output videos showed that although WASS successfully reconstructed the unbroken wave case, the data was not accurate and contained mostly noise. The data quality in the broken wave cases, however, increased greatly and a larger area was able to be reconstructed. The lighting of the scene only affected the beginning of each trial run before waves began breaking in view of the cameras. Once wave breaking occurred, the reflections from the lights onshore of the cameras were insignificant so backlighting was unnecessary.

Upon examining the two-dimensional data at each wave gauge location, it was found that WASS was reconstructing the water surface much more consistently with fewer gaps in the data. Noise was still present throughout each trial but greatly decreased from the Airy Validation experiment. At the beginning of each trial before waves had broken, WASS still had difficulty recognizing the water surface but this seemed to stabilize once a sufficient amount of foam and texture was present. Figure 5.8 shows the signal comparison of WG 13 and the camera data from this location at the beginning of the focusing wave trial. Initially there is a lot of noise when the waves are smaller and not breaking, then once the waves reach a certain size the noise decreases.

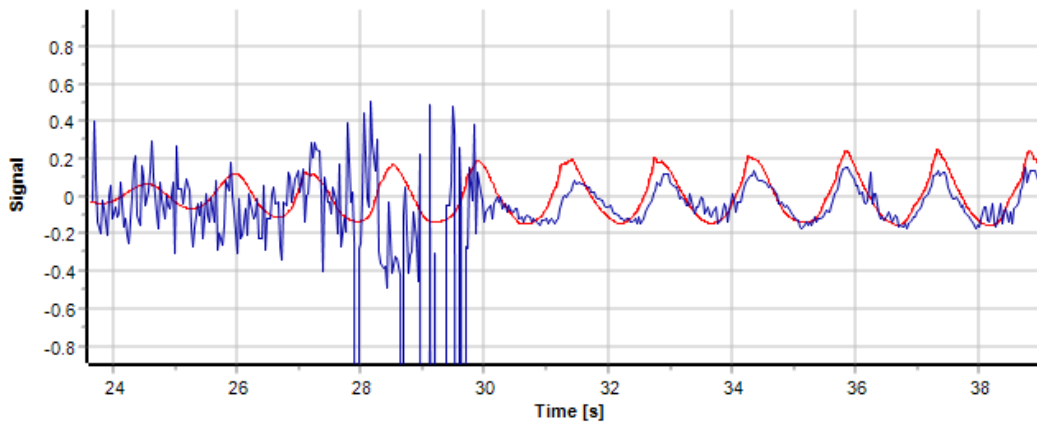


*Figure 5.8: Wavelab signal comparison of wave gauge 13 (red) and WASS data (blue) from this location during the beginning of a focusing wave trial.*

To understand how WASS was handling the two different breaking wave cases, focusing and regular waves, data from WG 13 was compared to the camera data for both trials. Figure 5.9 shows both data comparisons along with the linear regression fit and associated  $R^2$  value for each. The amplitude of the regular wave case was captured more accurately but had more noise present while wave heights from the focusing wave case were generally underestimated. This is reflected in the slope and  $R^2$  values for each case. Both trials were more accurately measured than cases from the previous experiments and noise was greatly reduced so the polarized lenses were considered a valuable addition and used for the final experiments.

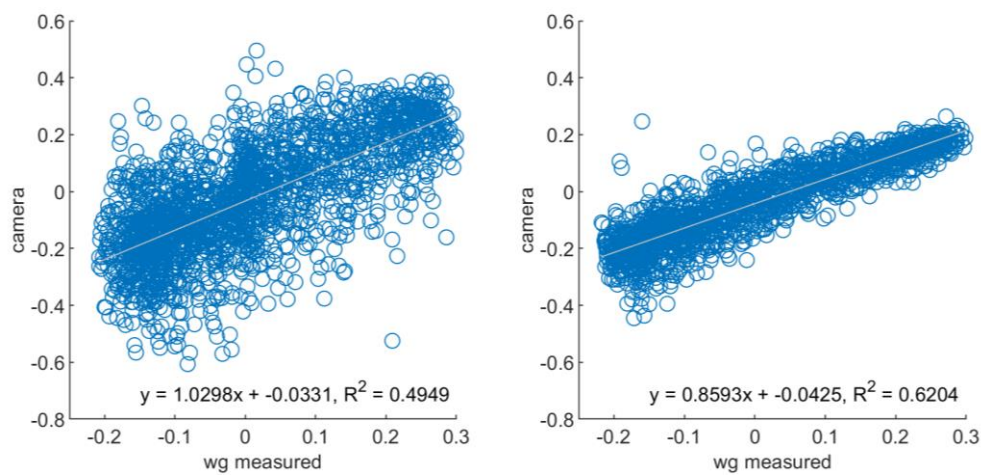


Figure 5.9: Camera vs. WG 13 data for regular (left) and focusing (right) wave cases and their associated linear regression fit and  $R^2$  values.

#### 5.4 Two WASS Stereo Pairs and Intel® Camera

The primary objectives of the final experiments were to test the Intel® camera system and compare its performance to WASS while increasing the data quality and measurement area of WASS. Two experiments were designed to achieve these goals: the first focusing on measuring waves under the instrumentation frame and the second attempting to increase the measurement area by relocating the cameras to the basin beach. An additional set of GoPros® was added to the western side of the instrumentation frame facing offshore, which gave an additional perspective of waves passing under the instrumentation frame allowing them to be measured from both sides. The cameras facing onshore were removed for the second experiment and repositioned on to the beach with an increased stereo baseline in an attempt to reconstruct the entire basin's water



surface. Both camera systems were tested in a variety of wave conditions and their post-processing methodologies were finalized.

First, videos from both GoPro<sup>®</sup> camera sets were separately processed through WASS and NetCDF files were generated for each trial. For the first experiment with both camera sets attached to the instrumentation frame, only the cases with significant wave breaking were able to be processed without numerous frame failures within WASS. The data collected from the beach was unable to be processed by WASS and was not analyzed any further. This was likely due to the lower elevation of their positioning on the beach, creating a highly oblique perspective of the water surface and increasing the shadowing effect of oncoming waves.

A grid sensitivity study was performed on the focusing wave case in order to optimize NetCDF generation. When the raw point cloud data is being interpolated into a regular grid layout, the grid spacing (dxy) can be selected by the user. This spacing affects how the data is interpolated which could significantly alter results. The focusing wave case was selected due to its success in previous experiments within WASS. Two different grid spacings, 0.1 m and 0.5 m, were selected so that they were significantly smaller than the measured 3 m wavelength of the focusing waves but large enough to minimize computational time. This is common practice within numerical wave modeling [48]. NetCDF's for both camera sets were then generated with this grid spacing and compared with each wave gauge in view. Figure 5.10 shows the measurements from the cameras vs. the wave gauges. The smaller 0.1 m grid spacing proved to be slightly more accurate, but more analysis is needed before making further conclusions.

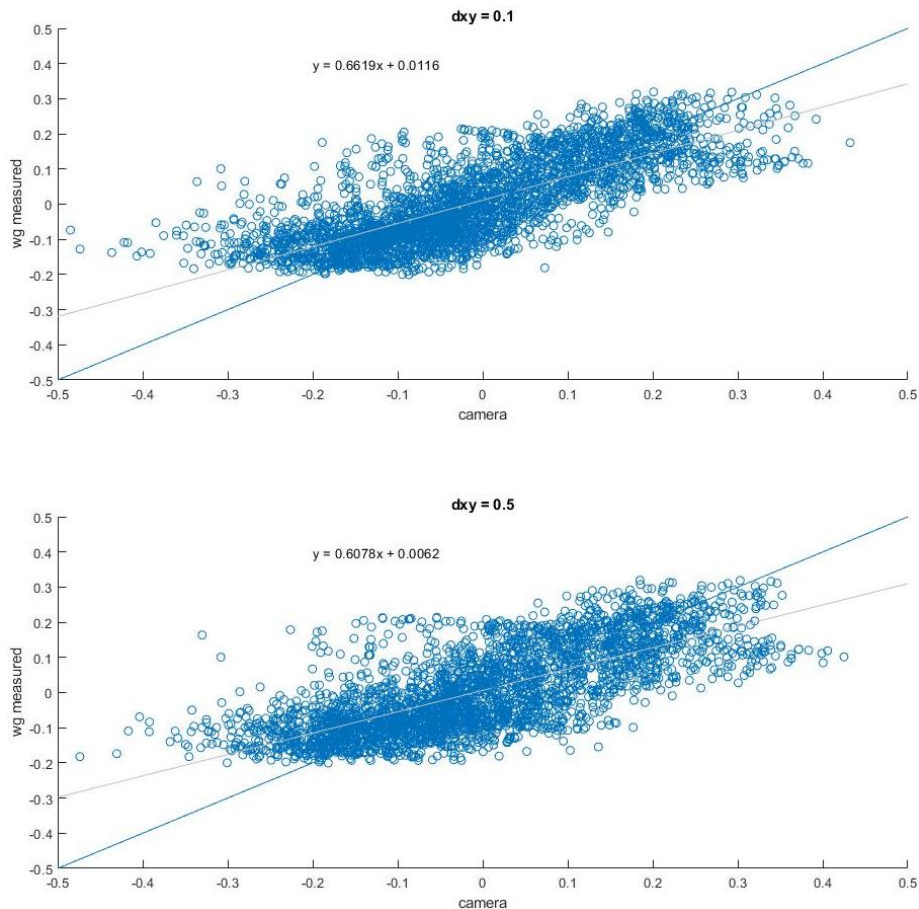


Figure 5.10: Wave gauge measurements vs. WASS measurements for two different NetCDF grid sizes:  $dxy = 0.1$  m and  $0.5$  m for focusing waves.

Other factors that could be affecting the accuracy of the WASS system were also explored. The effect of the direction each camera set was facing, both onshore and offshore, was analyzed as well as if accuracy was increased when both datasets were combined. The camera's ability to recognize the water surface seemed to vary depending on the location within the video frame, so each wave gauge was analyzed separately to determine if there were any spatial trends in accuracy. Figure 5.11 shows the linear regression fit along with its associated  $R^2$  value for each wave gauge for the focusing waves trial. The figure is displayed in a plan view of the instrumentation frame with waves propagating in from the left-hand side and each camera icon and wave gauge box in their corresponding real-world location. The color of each equation determines the camera pair it is associated with and the  $dxy$  value is the NetCDF grid spacing. The red and green equations are from the onshore and offshore facing camera sets respectively. A linear regression slope of 1, a y-intercept of 0, and an  $R^2$  of 1 is desired ( $y = 1x + 0$ ,  $R^2 = 1$ ).

The offshore facing camera set and the smaller grid spacing consistently performed better, but there was no discernable trend in the data quality when it came to the location of the wave gauge in the camera's view. This is most likely case specific, dependent upon lighting, water surface texture, and camera position so it would be difficult to determine from any number of cases. It could also be dependent on the calibration quality of each camera set. The 0.1 m grid spacing was used for the remainder of the study, but further analysis should be completed to determine an optimal grid spacing for each wave case. This was not completed in this study due to time constraints but should be considered for future work. For more information on the spatial study see Appendix C.

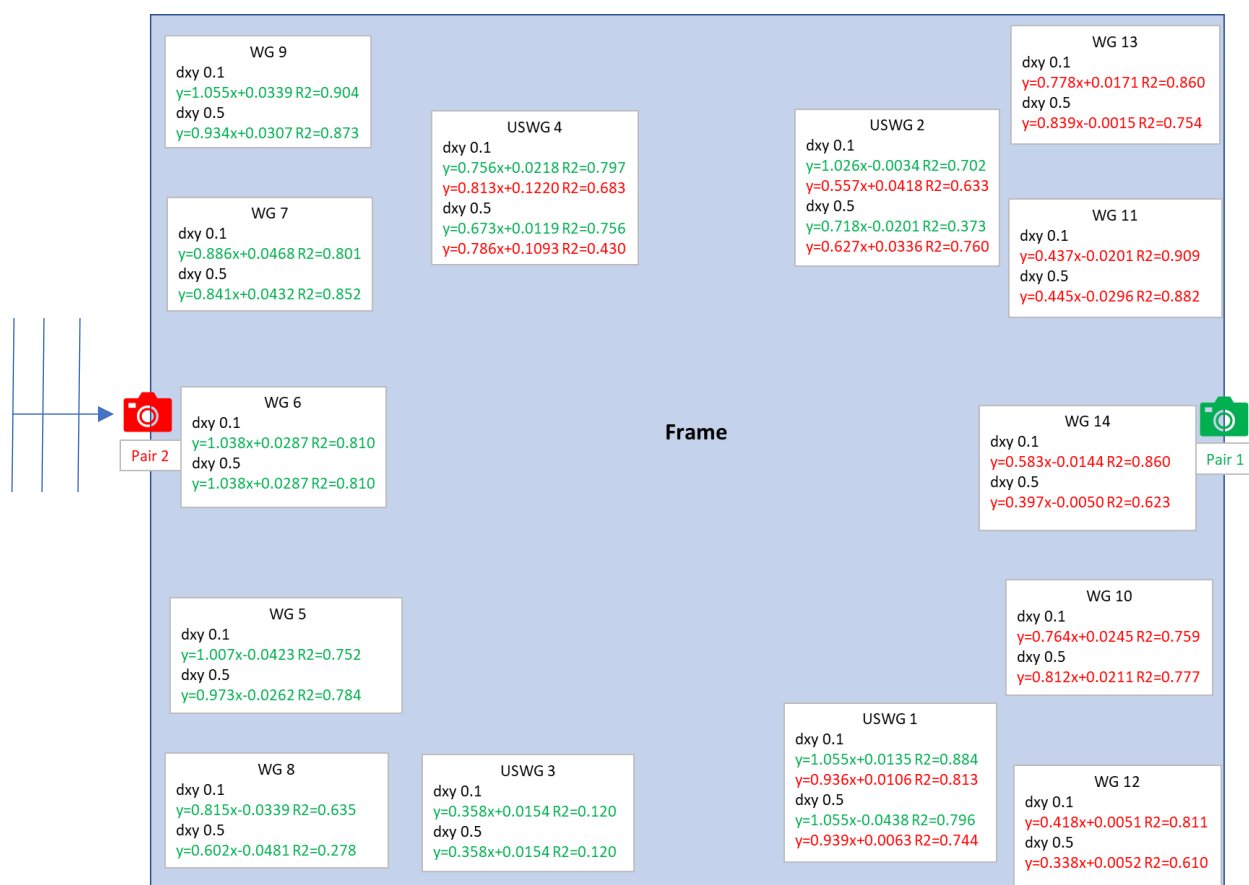


Figure 5.11: Linear regression fits and associated  $R^2$  values for WASS vs. wave gauge measurements for each gauge locations comparing two different NetCDF grid sizes ( $dxy = 0.1m$  and  $0.5m$ ) and the onshore (red) and offshore (green) facing camera sets.

Raw spatial data from both WASS camera sets were combined using a translation matrix derived from their measured distances. This data was then interpolated into a gridded NetCDF

file and analyzed. Due to incorrect spatial reconstruction or errors in the real-world measurement of camera locations, the datasets did not align well and the interpolated data was highly inaccurate. The datasets were then manually aligned and combined but an increase in accuracy was still not seen. Further work would need to be done to create a methodology to combine two WASS datasets but was not able to be completed within this project due to time constraints.

The offshore and onshore WASS datasets with a grid spacing of 0.1 m were compared to measurements from the Intel<sup>®</sup> camera. The time series analysis function in Wavelab was utilized to output frequency and time domain wave height statistics from both datasets. For more information on these analyses, see Sections 5.4.2 and 5.4.3. Figure 5.12 compares wave height statistics from both camera systems to the wave gauge values during the focusing waves trial. The Intel<sup>®</sup> camera was consistently more accurate for both the time and frequency domain analyses. It was also confirmed that the offshore facing WASS cameras were more accurate than the onshore. Figure 5.13 shows a similar comparison but for wave periods. The Intel<sup>®</sup> camera has a perfect correlation for this wave case while the WASS datasets were less accurate.

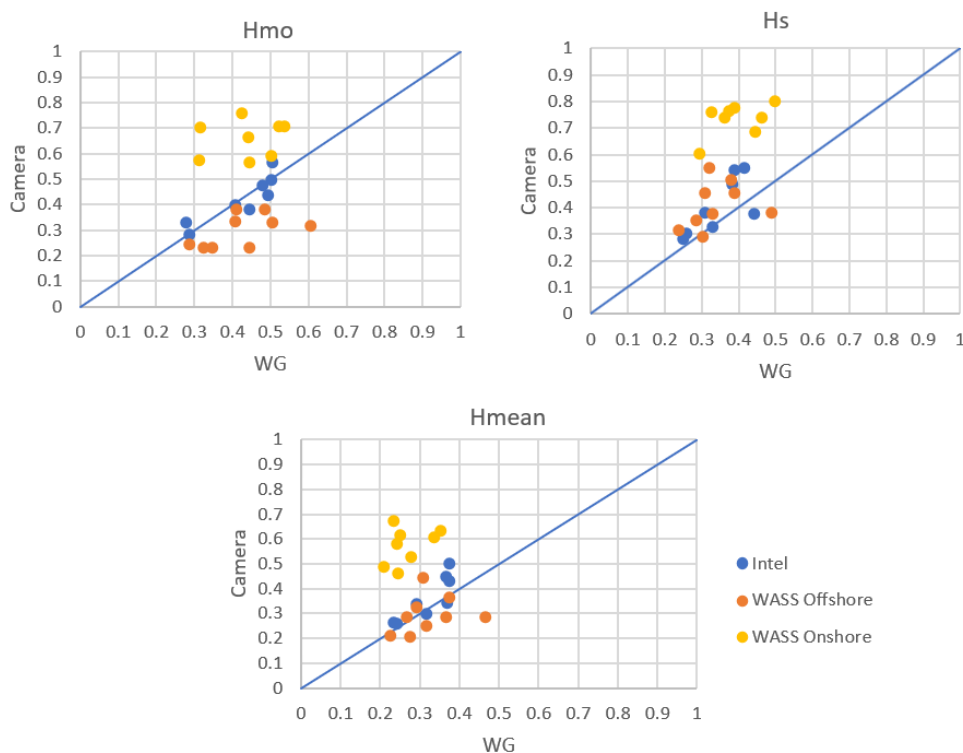


Figure 5.12: Spectral ( $H_{mo}$ ), significant ( $H_s$ ), and mean ( $H_{mean}$ ) wave height values for WASS and Intel<sup>®</sup> vs. wave gauge for the focusing wave case. The blue lines signify a perfect correlation.

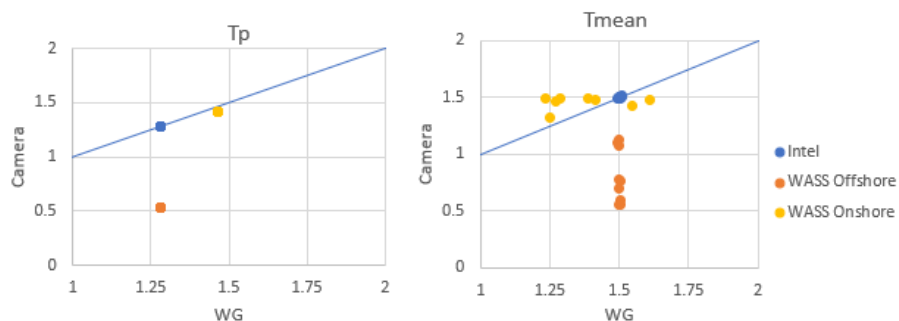


Figure 5.13: Peak ( $T_p$ ) and mean ( $T_{mean}$ ) wave periods for WASS and Intel<sup>®</sup> vs. wave gauge for focusing wave case. The blue lines signify a perfect correlation.

The regular wave case was then analyzed where WASS failed on reconstructing 40% of the video frames. This wave condition had significantly less wave breaking under the instrumentation frame, so WASS had more difficulty recognizing the water surface. Figure 5.14 shows the time series comparisons of both the Intel<sup>®</sup> and WASS camera systems to the gauge measurements from WG 13, a location in which no wave breaking occurred. WASS registered the water surface in this location as wave crests passed but failed to recognize it during wave troughs. The Intel<sup>®</sup> camera was able to collect data for the entire trial, but both systems had significant high frequency noise.

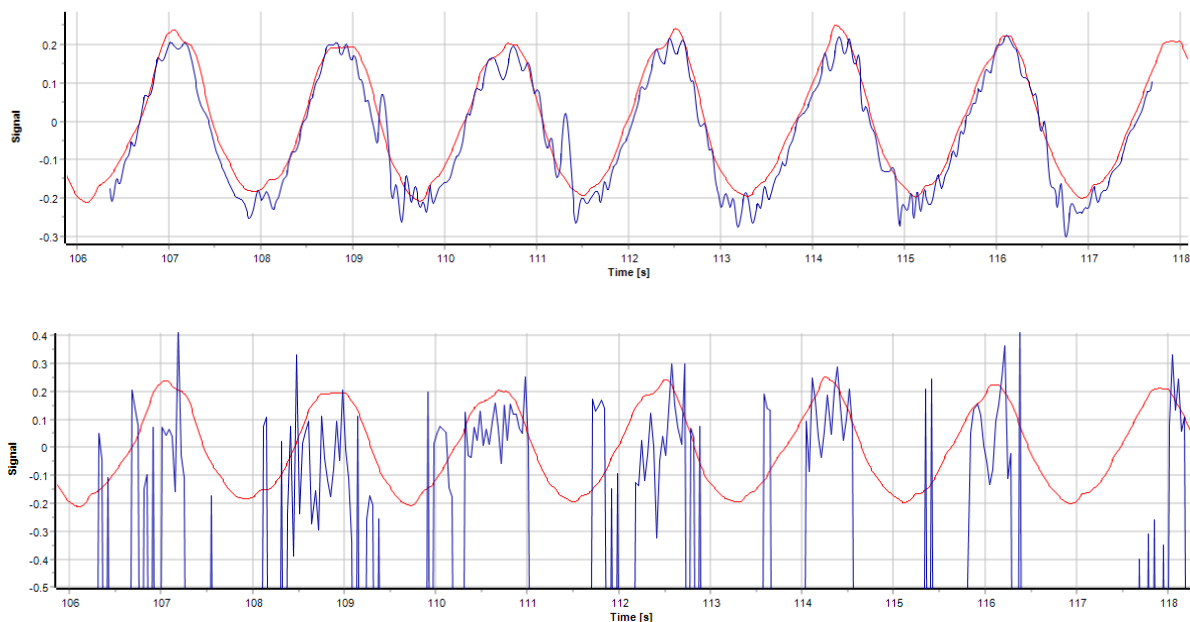


Figure 5.14: Intel<sup>®</sup> (top) and WASS (bottom) timeseries vs. WG 13 for regular wave case.

For the longer duration irregular wave case, containing 5 minutes of both breaking and non-breaking waves, the Intel<sup>®</sup> camera was able to resolve each wave regardless of if there was foam present on the water surface. Figure 5.15 shows the time series comparison of the Intel<sup>®</sup> and wave gauge data for the irregular wave case showing that the camera was able to resolve both the larger and smaller wave amplitudes. Figure 5.16 is the data comparison for USWG 1 for this trial along with the linear regression fit and  $R^2$  value, showing the Intel<sup>®</sup> camera was generally underestimating wave amplitudes in this location. For this trial, WASS was only able to resolve 30% of the video frames, which were all during larger amplitude breaking waves. Due to lack of data availability, no analyses were completed on the WASS dataset for this wave case.

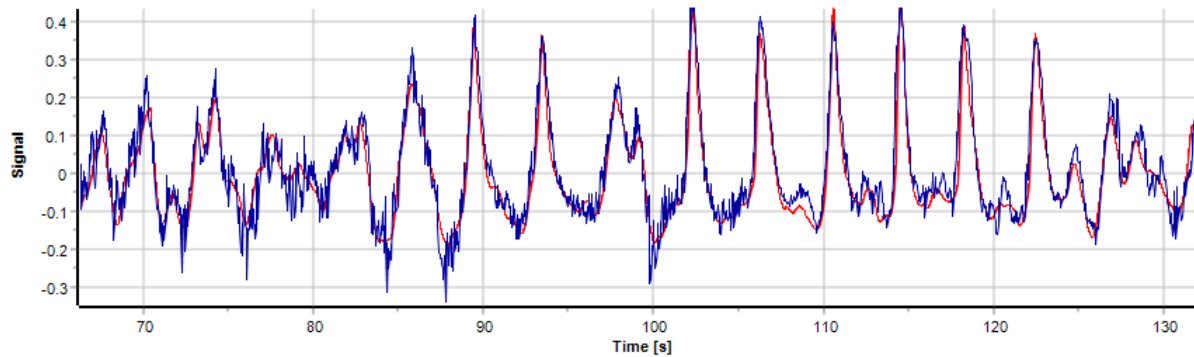


Figure 5.15: Time series comparison of Intel<sup>®</sup> (blue) vs wave gauge (red) data for an irregular wave case.

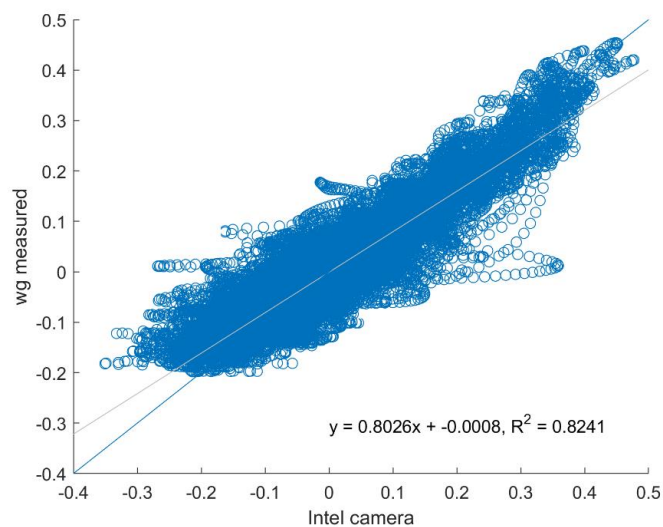


Figure 5.16: Wave gauge vs. Intel<sup>®</sup> data with linear regression fit and  $R^2$  value for USWG 1 during an irregular wave case.

For these three wave cases, focusing, regular, and irregular waves, the Intel<sup>®</sup> camera consistently performed more accurately than WASS. WASS heavily relied on wave breaking for it to recognize the water surface while the Intel<sup>®</sup> camera was also able to collect data regardless. The variety of wave conditions present in this experiment combined with the specific conditions required for WASS to successfully collect data made much of the WASS data unusable for this experiment. Due to these reasons, the remainder of the data analysis in this study focuses on the Intel<sup>®</sup> camera's data. Any data shown from this point forward will be related to the Intel<sup>®</sup> system. A more in-depth spatial analysis is applied to these datasets using the methods described in the following sub-sections.

#### 5.4.1 Data Filtering

Before further analyzing the Intel<sup>®</sup> dataset, a time domain filter was used to correct any high frequency noise that occurred throughout the data. The HWRL commonly uses the Tukey 53H method described in Goring and Nikora [24] during its post-processing routines to filter data from any USWG's used in the experiment. For consistency, the same filtering technique was used for the Intel<sup>®</sup> dataset. Figure 5.17 shows an example of Intel<sup>®</sup> surface elevation data compared to WG data before and after applying the filter. High frequency spikes can be seen throughout the unfiltered data, particularly during wave crests and troughs, but are corrected by the filter.

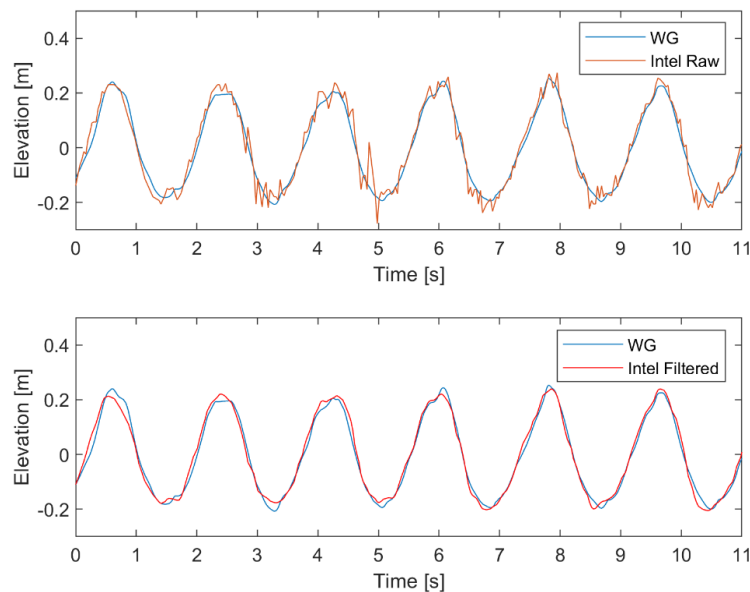


Figure 5.17: Intel<sup>®</sup> vs. WG data before (top) and after (bottom) filtering.

Once this filter was applied to the Intel<sup>®</sup> dataset, time and frequency domain analysis methods were used to calculate statistical wave height values such as mean, significant, and spectral significant wave height ( $H_{\text{mean}}$ ,  $H_s$ , and  $H_{\text{mo}}$  respectively), and wave period values such as mean, and spectral wave period ( $T_{\text{mean}}$  and  $T_{01}$  respectively). Directional analyses were also used to calculate the instantaneous direction of wave propagation across each crest line and the mean directional energy distribution of waves throughout the entire trial. These analysis methods are described in the following sub-sections.

#### 5.4.2 Time Domain Analysis

Analyzing data in the time domain entails separating individual waves within a timeseries and statistically analyzing certain characteristics such as wave height and wave period. For this project, a zero up-crossing technique was used to isolate individual waves by identifying when the water surface elevation crosses upwards (from negative to positive) about the time series' average value or zero and defining this point as the beginning or end of a wave. Once each wave is separated in the time series, their amplitude and period can be measured. Then the entire timeseries can be represented statistically by calculating the average wave height or period ( $H_{\text{mean}}$  and  $T_{\text{mean}}$ ), a common practice for regular waves, or averaging the largest one third of the waves (significant wave height or  $H_s$ ), a common practice for irregular waves. Figure 5.18 shows an example of a water surface elevation timeseries for an irregular wave case. Three waves are separated using their up-crossings (\*) and individual wave heights ( $H_n$ ) and periods ( $T_n$ ) are measured.

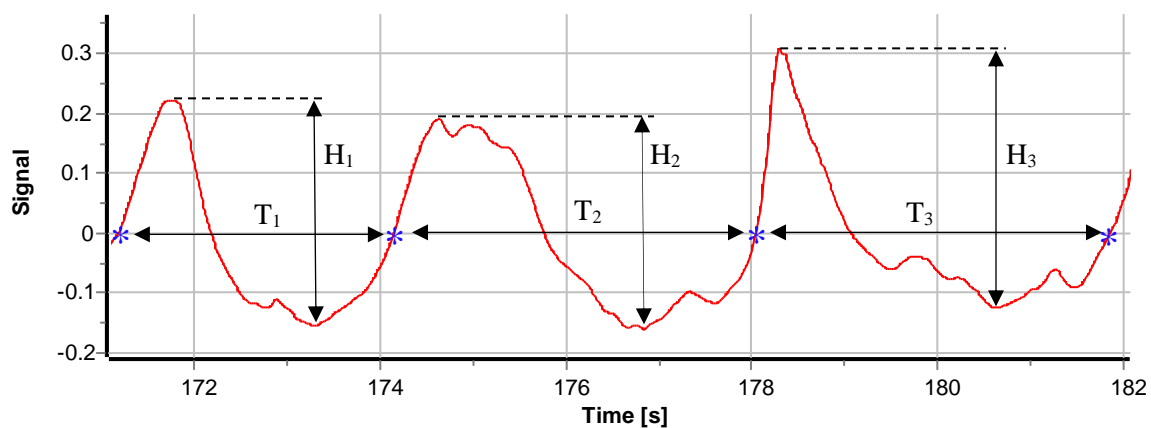


Figure 5.18: Irregular wave surface elevation time series with individual wave heights ( $H_n$ ) and periods ( $T_n$ ) labeled.



This technique was applied to individual grid nodes within the camera dataset. Due to the spatial extent of the camera measurements, a tool was created in Matlab that performed this analysis for every node location and determined statistical wave values across the entirety of the space measured for each trial.

#### 5.4.3 Frequency Domain Analysis

While a time domain analysis focuses on individual wave characteristics and how they vary over time, a frequency domain analysis uses mathematical techniques to represent the entire wave signal as a series of regular sine or cosine wave components with different frequencies. A Fast Fourier Transform is applied to the time series to separate it into different sine or cosine waves. The result is an energy distribution of the wave field dependent on frequency called the spectral distribution or wave spectrum ( $S(\omega)$ ). Figure 5.19 shows a graphical representation of the relationship between the time domain and frequency domain with the wave spectrum arising vertically from the left-hand axis.

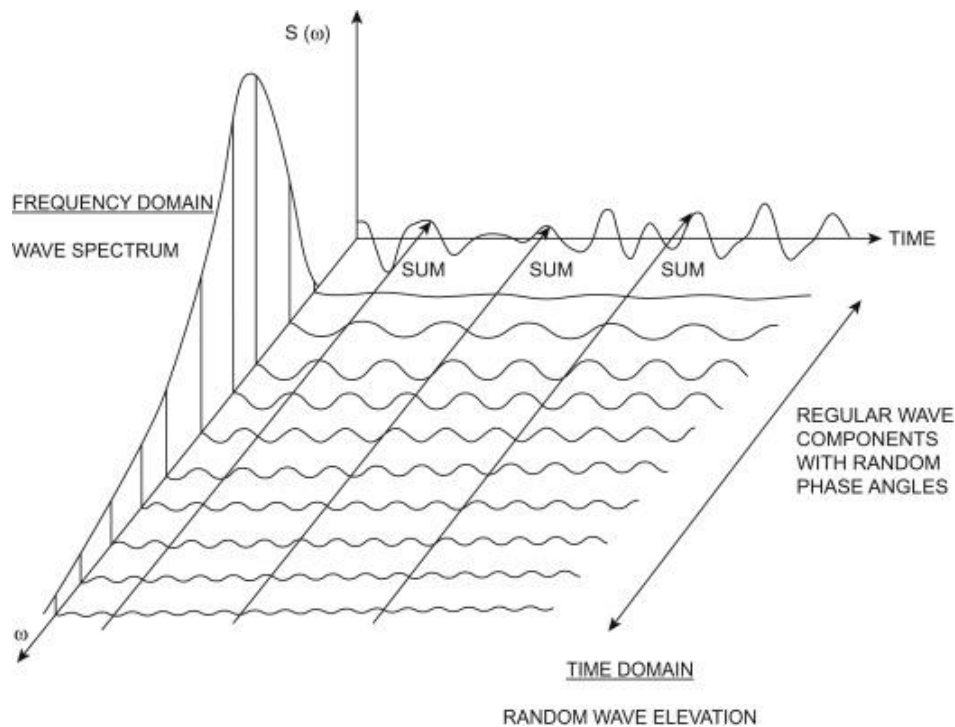


Figure 5.19: Relationship between frequency and time domain of an irregular wave time series. Source:[21].

Once an energy distribution is obtained, useful representative wave heights and periods can be derived from the shape of this wave spectra. This method is more commonly used for irregular

waves due to the high variety of wave frequencies present. It is often difficult for a time domain analysis to differentiate these frequencies so a frequency domain analysis is used instead. The spectral significant wave height ( $H_{m0}$ ) and period ( $T_{01}$ ) are often used to characterize the wave field, which can be derived from the “moments” of the wave spectra’s shape.  $H_{m0}$  and  $T_{01}$  can then be related to  $H_s$  and  $T_{mean}$  [16]. Similar to the methods used for the time domain analysis, each grid node in the camera dataset was analyzed individually in the frequency domain so a spatial variability in spectral wave height and period could be output.

#### 5.4.4 *Directional Analysis*

The direction of wave propagation is another important wave characteristic to investigate in laboratory studies. Similar to wave height analyses, there are several methods for determining and defining wave direction but understanding the directional aspect of a wave field requires more information than simply a stationary two-dimensional surface elevation time series. Generally multiple wave gauges are deployed in a layout that allows for the estimation of a directional wave spectrum from simultaneous surface elevation measurements in different known locations. This analysis is limited by the number of wave gauges and the difficulty related to changing instrumentation layouts. With the camera’s ability to measure the water surface over a significant spatial extent, this problem is simplified because multiple wave gauges do not need to be deployed. The same analysis techniques can be used by strategically selecting nodes from the camera dataset to create “optical gauge” arrays with specific geometries.

Directional analyses of wave data generally output the energy distribution of the wave field, similar to a frequency domain analysis only with the added element of directionality. This results in a directional wave spectrum showing the amount of energy present from each frequency in each direction. Although this is the most common way to represent wave direction, three-dimensional data allows one to investigate the instantaneous wave direction of individual waves along the entire measured crest line. For this project, two approaches were used toward wave direction: a traditional directional spectrum approach that averages wave direction over time, and an instantaneous approach that calculates each waves propagation direction during a snapshot in time.

First, the more traditional method was considered where specific grid nodes were extracted from the camera dataset and input into the directional analysis tool within Wavelab. This software

uses the Bayesian Directional Method (BDM) [30] to calculate the directional wave spectra from the input wave gauge measurements and location. Multiple wave gauges must be placed in an array whose geometry eliminates the chance of ambiguous solutions to wave direction. Several gauge array geometries have been optimized for the field and laboratory for point wave gauges [6], but with the spatial extent of the camera eliminating the need to deploy multiple wave gauges, further options could be explored. The wave gauges seen within the field of view of the camera were first input into Wavelab for directional analysis then camera data from these locations was analyzed in the same way for a direct comparison. Then different grid array geometries were tested by selecting specific points from the camera dataset and inputting their locations and time series into Wavelab. Initially, the entire camera dataset was input, but computational power and time involved were far too great. To more adequately utilize the spatial extent of the camera data, a 6 m by 6 m area outline was used and regular grid arrays with different resolutions were selected within this area. A 100, 36, and 15-gauge grid arrays were tested for the directional regular wave case in order to optimize this array geometry. These arrays were either regular or checkered for a total of six different array geometries, shown in Figure 5.21. A trapezoidal, five-gauge array commonly used for directional wave analysis, called the CERC array [47], was also tested. The ideal spacing of a CERC array is dependent on the wavelength of the waves being measured, so its size varied depending on the trial. The CERC array for the irregular wave case can be seen in Figure 5.20. The output from the BDM analysis within Wavelab for each geometry was then analyzed graphically.

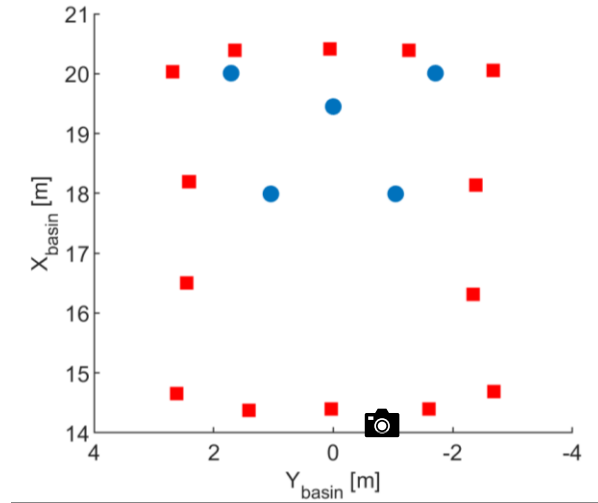


Figure 5.20: WG (red) and extracted Intel® data node (blue) locations for the irregular wave CERC array. Intel® camera location denoted by the camera icon. Both camera and wave propagation direction in the positive  $x$  direction.

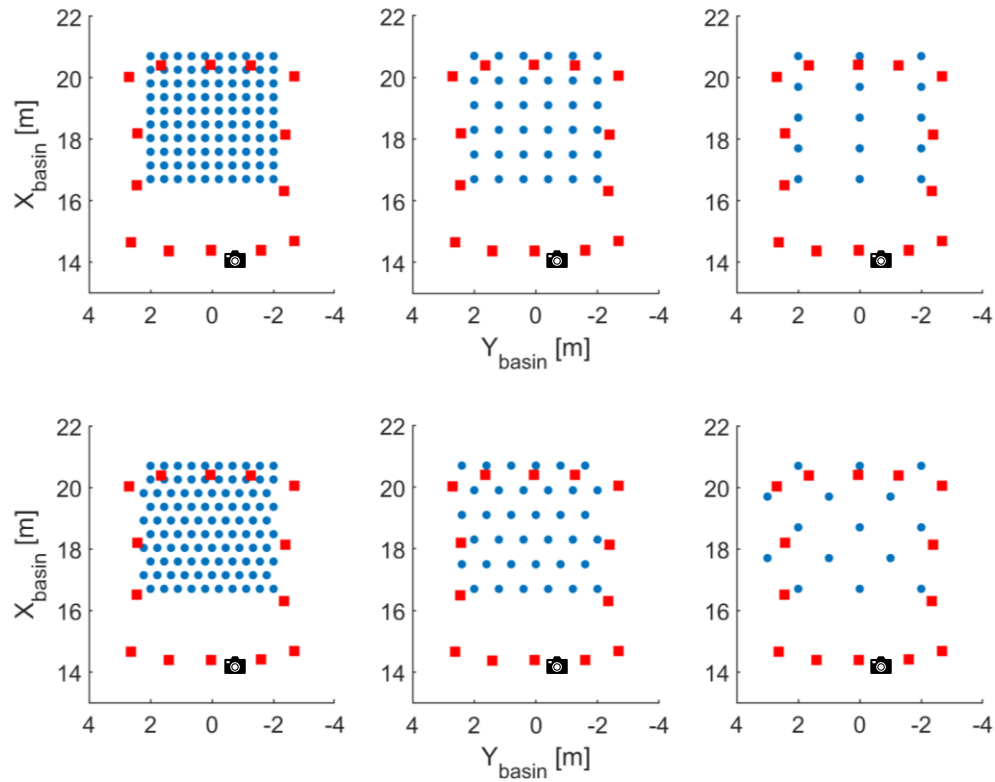


Figure 5.21: WG (red) and extracted Intel® data node (blue) locations for regular (top) and checkered (bottom) directional analysis grid arrays. Intel® camera location denoted by the camera icon. Both camera and wave propagation direction in the positive  $x$  direction.

Next, an analytical tool was developed in Matlab to extract crest lines from each frame of the camera dataset. Ideally, the gradient of these surfaces could be taken and areas of higher elevation with a gradient of zero (no slope) would be identified as the top of each wave crest, but due to the presence of high frequency spatial noise this technique was not feasible. The top of each wave crest contained numerous spikes and small peaks, so the Matlab function *islocalmax* was used to identify these local maxima. This output an x-y scatter of points located about the top of each wave crest, from which a polynomial curve could be fit to using the Matlab function *polyfit*. This polynomial line could be used to represent each wave's crest line. The tangential normal at any point on this line could then be assumed to be that part of the wave crest's propagation direction. A graphical representation from the focusing wave case is shown in Figure 5.22. Although this method gave a good general estimation of each wave crest, its accuracy was not validated and therefore is not recommended for use in future research. This tool was used to produce visual representations of instantaneous wave directionality, rather than extensive directionality quantification.

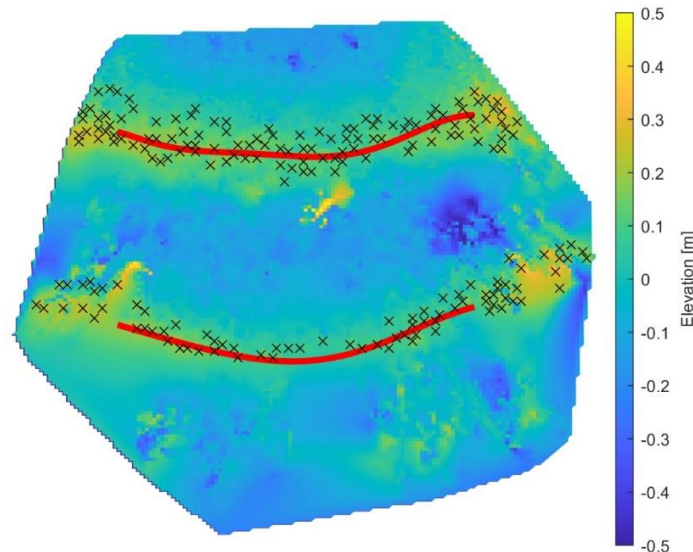


Figure 5.22: Crest detection tool output for focusing wave case with measured surface elevation, local crest maxima (black), and wave crest lines (red) represented by polynomial curve fits.

## 5.5 Chapter Conclusions

Chapter 5 discussed the methods of data analysis used within this study and the important information revealed from each experiment. The majority of conclusions made from the

preliminary experiments were based on data visualization techniques that were not analytically intensive, but rather gave an idea of the ideal conditions for each camera systems. This allowed for optimization of the experimental setup and wave conditions selection for the final experiment that would best validate the cameras' abilities to perform similar tasks to the deployed wave gauges. It was found that WASS was heavily reliant on wave breaking to successfully recognize the water surface. Although the addition of polarized lenses to the GoPros<sup>®</sup> and the optimization of their positioning and lighting greatly improved data quality in the preliminary experiments, they failed to measure many of the trials in the final experiment deeming much of the data unusable. The Intel<sup>®</sup> camera, however, was consistently able to recognize the water surface regardless of if there was wave breaking present, and therefore will be the main focus of the remainder of this study. Chapter 6 discusses the results of a more extensive spatial analysis of each wave case from the final experiments. Details on these analyses were described at the end of Chapter 5. Each trial was examined, and wave height spatial variability is observed. These measurements are validated using the wave gauge and video data. Wave height was calculated in the time and frequency domain and errors are compared. Wave directionality was calculated using the BDM method and the aforementioned crest detection tool. The results are then discussed, and several concluding remarks are made.

## Chapter 6 Results

The object of this research study was to test multiple stereo-video measurement systems for use in the HWRL in an attempt to spatially reconstruct the water surface. The DWB was used to test and compare an open-source stereo image processing pipeline, WASS, paired with of multiple sets of calibrated GoPro<sup>®</sup> cameras, and an Intel<sup>®</sup> RealSense<sup>™</sup> D455 Depth Camera. Several experiments were completed and it was found that the Intel<sup>®</sup> system successfully measured the surface elevation in a variety of wave conditions while the WASS system heavily relied on wave breaking to recognize the water surface. Chapter 5 discussed both the analytical and graphical analyses used to make these conclusions, and this chapter discusses the results of a more extensive spatial analysis on the Intel<sup>®</sup> data from the final experiments.

Each wave condition is examined separately and the results are discussed. The same analyses were completed on the wave gauge data present from each trial and used to validate the camera measurements. The Intel<sup>®</sup> camera was often recording only a portion of each trial, so gauge data was cropped to this particular time period for a more direct comparison. In locations where reliable surface elevation data is not present, visual aids, predominately recorded GoPro<sup>®</sup> video, was used to ground truth camera measurements. The water surface area measured by the camera generally began in the center of the instrumentation frame due to field of view limitations, but the wave gauge data located outside of the camera measurement area is still displayed. These values can be used as another mechanism of ground truthing the camera outputs by visually extending the wave field. Although this is a rudimentary validation method, when it is combined with validating results with relevant gauge data as well as available visual media, proper validation can be achieved.

The error ( $\epsilon$ ) calculated at each wave gauge is the relative error between the nearest interpolated grid node from the camera dataset ( $H_{\text{camera}}$ ) and the respective wave gauge ( $H_{\text{WG}}$ ), as shown in Equation 6.1. The exact location of the wave gauge often did not lie directly on a grid node within the camera dataset, so the nearest node was used and defined as  $H_{\text{camera}}$ . A number of different spatial averaging techniques could also be applied to define  $H_{\text{camera}}$ , but interference from the adjacent wave gauge caused high noise within the dataset in these locations so any averaging technique would most likely have resulted in incorrect values.

$$\epsilon = \frac{H_{camera} - H_{WG}}{H_{WG}} \quad (6.1)$$

### 6.1 Regular Waves

Although generating monochromatic waves of equal amplitude intuitively seems to be a straightforward application for any wavemaker, it is in fact extremely difficult. A number of hydrodynamic disruptions can occur that create wave height variability, underlying currents, and other processes that hinder the creation of a uniform wave field. Regular waves are often desired for lab experiments involving a specimen such as a wave energy converter, so measuring the degree of this nonuniformity is an important research objective of this study. Also, knowing the wave height at the location of the specimen is typically required, but this may be difficult or impossible to measure without significant disruption. For this reason, measurements are often taken directly surrounding the specimen and interpolated to the point of interest. If the variability in the wave field is drastic enough, this assumption may be incorrect. Hence, the main interest with the regular wave cases in this study was to utilize the camera's capability of measuring a large spatial area without any hydrodynamic disruption.

$$H_{WG_{AVG}} = \frac{\sum H_{WG}}{N_{WG}} \quad (6.2)$$

$$k_{WG} = \frac{H_{WG}}{H_{WG_{AVG}}} \quad (6.3)$$

$$k_{camera} = \frac{H_{camera}}{H_{WG_{AVG}}} \quad (6.4)$$

Wave heights calculated using time and frequency domain analyses were normalized by the average gauge measurement ( $H_{WG_{AVG}}$ , Equation 6.2) in order to highlight the variability around this value. When measuring surface elevations around a research specimen, a similar technique would be applied to characterize the effective wave height in this area. To observe the percent variability in wave height around this particular value, both the gauge and camera measurements are normalized by  $H_{WG_{AVG}}$  and labeled  $k_{WG}$  and  $k_{camera}$  respectively (Equations 6.3 and 6.4). A table of the average wave gauge values ( $H_{WG_{AVG}}$ ) for each trial can be found in Appendix E for reference. These values were calculated with the time and frequency domain analysis described



in Section 5.4.2 and 5.4.3, but a wave profile averaging technique needed to be applied to the directional regular wave case. Wave directionality was also explored for this case by extracting specific gauge array geometries from the camera dataset. BDM analyses (Section 5.4.4) were completed within Wavelab and pertinent results are discussed.

#### *6.1.1 Shore Normal ( $H = 0.5\text{ m}$ , $T = 1.8\text{ s}$ , $\theta = 0\text{ deg}$ , $h = 1\text{ m}$ )*

The shore normal regular wave case consisted of breaking waves with a wave height of 0.5 m, period of 1.8 s, in a water depth of 1 m. From visual inspection during testing and of the GoPro<sup>®</sup> videos, there seemed to be wave height variability due to the fact that only certain sections of the wave crests were breaking. The duration of this trial was approximately 2.5 minutes including the wavemaker ramp-up and ramp-down, but partial wave crest breaking began only after wavemaker ramp-up was complete and waves reached their desired amplitude. Wave breaking was forced to occur by increasing the wave height and using a sinusoidal wavemaker motion. Waves of this amplitude do not wish to maintain a sinusoidal profile and are therefore unstable and break, introducing a series of harmonics that interact with the generated waves and contours of the basin. Variability in the wave field is introduced by these harmonics as well as other factors such as resonant excitation within the basin, in which an alongshore standing wave is created and disrupts the wave amplitude, or hydrodynamic disruptions from the instrumentation frame. Although shore normal regular waves are generally intended to be uniform, the non-homogeneities in the basin were desired to verify whether the camera was able to capture them.

Figure 6.1 shows the normalized mean wave height from the shore normal regular wave case calculated for both the camera and gauge data using the time domain analysis discussed in Section 5.4.2. This trial was one of the first tests of the Intel<sup>®</sup> camera, so only short videos were recorded in an attempt to understand the camera's capabilities and test multiple camera angles. Figure 6.1 was calculated from a short 16 s video and is not a good representation of the trial as a whole. The short video duration increases the chances of error within a time domain analysis due to the limited number of waves being analyzed, in this case 8 waves in total. That being said, the Intel<sup>®</sup> camera performed relatively well, with errors on the order of 1-16% with an average error of 7.5%.

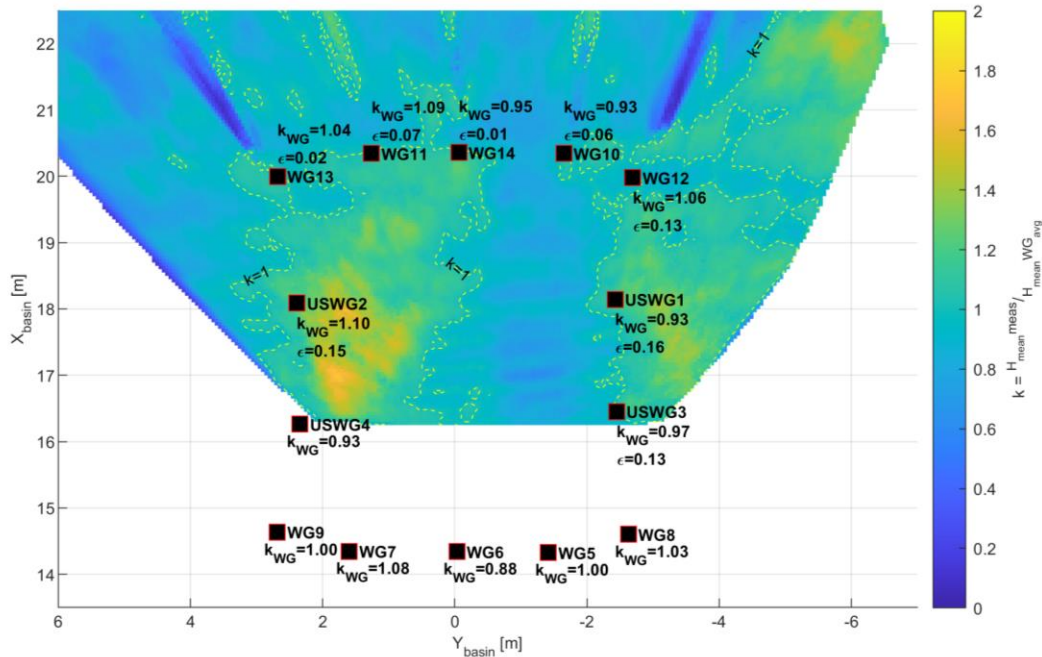


Figure 6.1: Normalized mean wave height ( $k$ ) for the shore normal regular wave case in the basin coordinate system with direction of wave propagation in the positive  $x$  direction. WG and USWG measurements normalized and relative error ( $\epsilon$ ) between the camera and gauge measurement are also displayed for each wave gauge.

Figure 6.2 shows a similar result for the normalized spectral significant wave height calculated using the frequency domain analysis discussed in Section 5.4.3. This rendered similar errors to the time domain analysis, ranging from 0-17% with an average error of 5.6%. It is noted that the regions beginning behind the row of gauges along  $x = 20$  with a sudden increase or decrease in wave height are due to the optical disruption the frame supports and wave gauges provide, and should be ignored. There is also a sinusoidal variation in wave height and its frequency decreases as the distance from the camera increases, denoted by horizontal stripes throughout both figures. This could potentially be a hydrodynamic phenomenon, but is more likely an artifact of the camera's spatial reconstruction. At this time no conclusions were made, but it is revisited in the following wave cases.

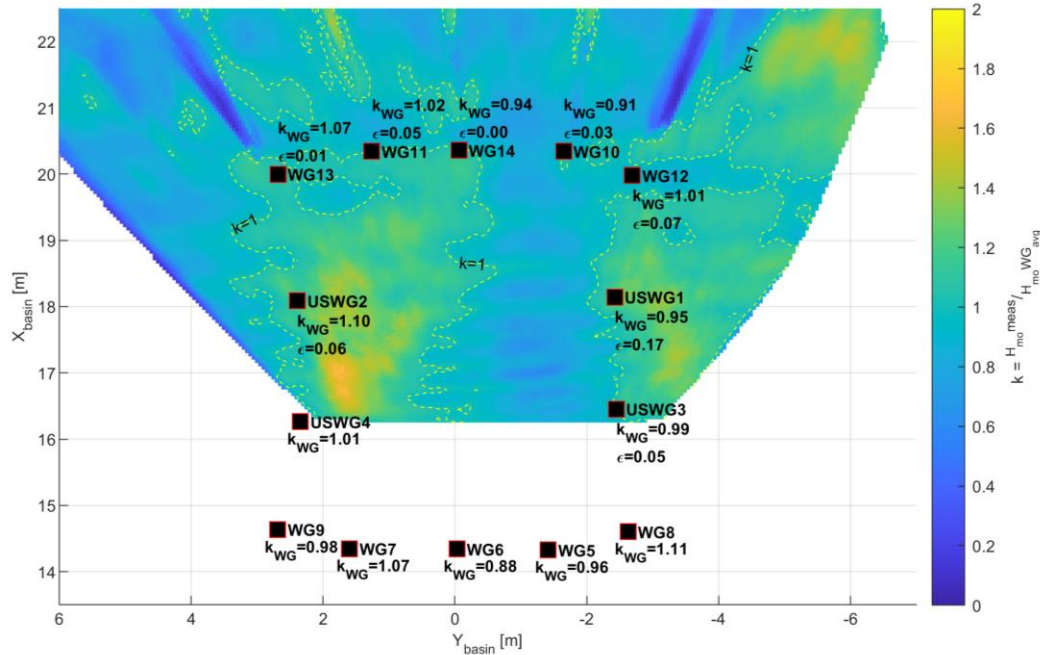
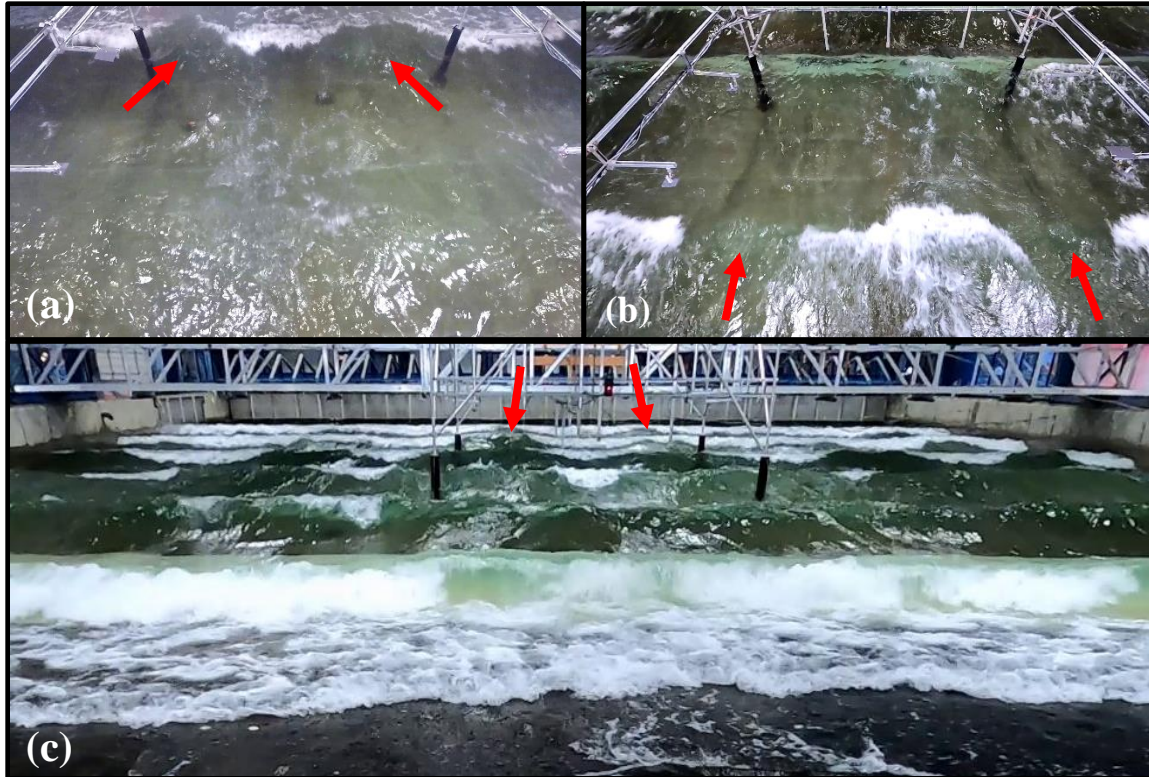


Figure 6.2: Normalized spectral significant wave height ( $k$ ) for the shore normal regular wave case in the basin coordinate system with direction of wave propagation in the positive  $x$  direction. WG and USWG measurements normalized and relative error ( $\epsilon$ ) between the camera and gauge measurement are also displayed for each wave gauge.

These results confirm the spatial variability in wave height seen during testing. In both figures, an area of larger wave height can be seen along USWG 2 and 4 where the wave heights reached up to twice the average for the area under the instrumentation frame. This is validated by the gauge measurements from WG 7, 11, and 13 as well as USWG 2. Directly to the right of this region, there is an area of smaller wave height that borders the center of the instrumentation frame. This is validated by the lower wave heights measured from WG 6, 10, and 14. There is a steep gradient in wave amplitude between these two adjacent regions in a linear distance of approximately 2-3 m. This gradient is confirmed by the difference between WG 11 and 14 as well as WG 7 and 6, where a difference of up to 20% is seen in a space of less than 2 m.

For further validation of these results, snapshots were taken from GoPro<sup>®</sup> videos of this trial. From these images it is apparent that the area of smaller wave height to the right side of the instrumentation frame was caused by wave dissipation due to breaking. In view (a) looking offshore from the frame as well as in view (c) looking offshore from the beach, the variation in the wave height along each crest can be well seen, with an increase in amplitude on either side of the wave breaking.



*Figure 6.3: GoPro<sup>®</sup> screenshots of shore normal regular wave case from (a) instrumentation frame looking offshore (b) instrumentation frame looking onshore (c) basin beach looking offshore. Red arrows indicate areas with larger wave crests.*

Wave period was also investigated through the time domain analysis. Figure 6.4 shows the normalized mean wave period. As expected, there is very little variation in the mean wave period and camera errors range from 0-2% with an average of 1.1%. Shadows are still seen behind each instrument location and can be ignored.

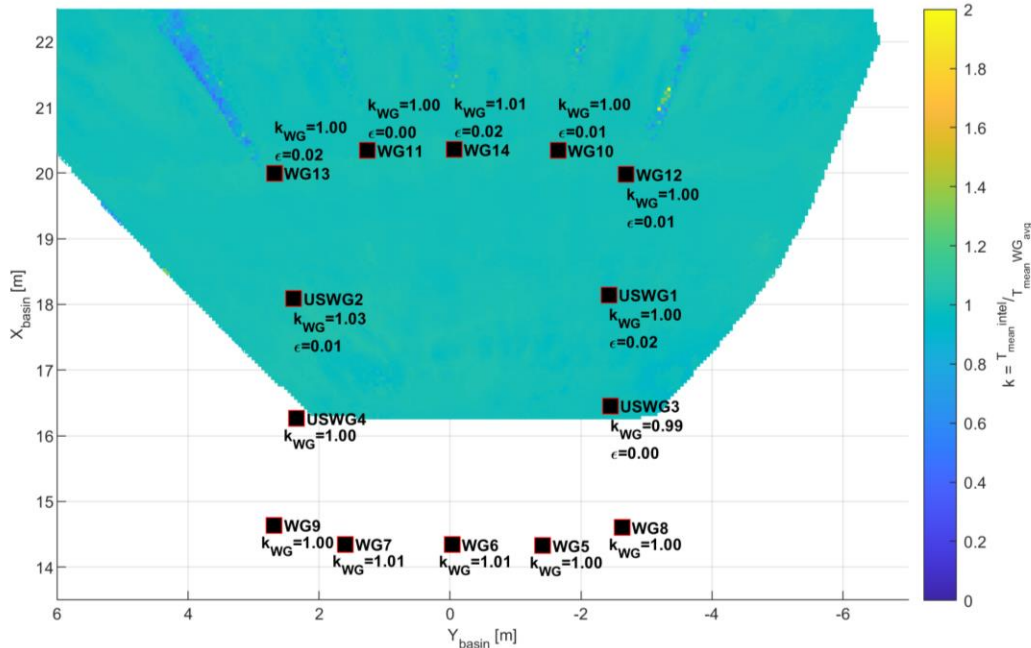


Figure 6.4: Normalized mean wave period ( $k$ ) for the shore normal regular wave case in the basin coordinate system with direction of wave propagation in the positive  $x$  direction. WG and USWG measurements normalized and relative error ( $\epsilon$ ) between the camera and gauge measurement are also displayed for each wave gauge.

### 6.1.2 Directional ( $H = 0.56$ m, $T = 5$ s, $\theta = 15$ deg, $h = 1$ m)

The directional wave case had larger, longer waves with a desired wave height of 0.56 m, period of 5 s, and direction of 15 degrees (angled southward) in a water depth of 1 m. These waves broke 1-2 m from the wavemaker starting in the center of the basin and extending to the wall towards the South. The diffraction zone of the wavemaker to the North (see Figure 3.10) created a region where the waves were too small to break. By the time the waves had reached the instrumentation frame, the crest was broken across the entire width of the basin minus the wavemaker's diffraction zone. The size and length of these waves suggest that their equilibrium shape would be purely nonlinear, but the sinusoidal wavemaker motion was attempting to force them into an unnatural linear shape. This introduced bound and free harmonic waves, similar to those causing the variability in the shore normal waves, which increased the wave height and induced early wave breaking. The result was a combination of non-linear wave processes that transferred energy into higher harmonics of the fundamental wave at an integer fraction of the frequency, which is referred to as a superharmonic. These superharmonic waves had a slower celerity (wave speed) than the longer 5 s waves, causing them to pass through one another at

regular intervals. When a time domain analysis was run on the data from this trial, high errors in wave height were seen due to the up-crossing method's inability to differentiate between the smaller superharmonic waves and the fundamental wave profile. This was a problem in the analysis technique rather than a wave generation problem.

The analysis technique was therefore modified to appropriately calculate wave height for this trial by phase averaging each timeseries. To consider both the spatial and temporal variability in wave profile, phase averaging separates each timeseries into multiple sections containing individual waves of the desired wave period (5 s). Then they were overlaid on to one another, and averaged over time to calculate the average wave profile. The maximum (crest) and minimum (trough) values of this profile were subtracted to calculate the average wave height ( $H_{avg}$ ). This technique was applied to both the gauge and camera data and then compared. Figure 6.5 shows the average wave profiles at WG 10 and 13 measured by the wave gauge and camera. Although these locations have approximately the same x location within the basin, the directionality of the waves caused wave crests to reach WG 10 before WG 13 and the average wave profiles were drastically different. The smaller, high frequency wave is easily identified in the wave profile for WG 13, while WG 10 has a flat trough in between two main wave crests. This is likely due to the location of the main wave crest relative to the shorter superharmonic, where they are passing through one another at WG 10 and completely separated at WG 13. The wave profiles measured by the gauges and camera compared well, and the results were spatially plotted to further investigate.

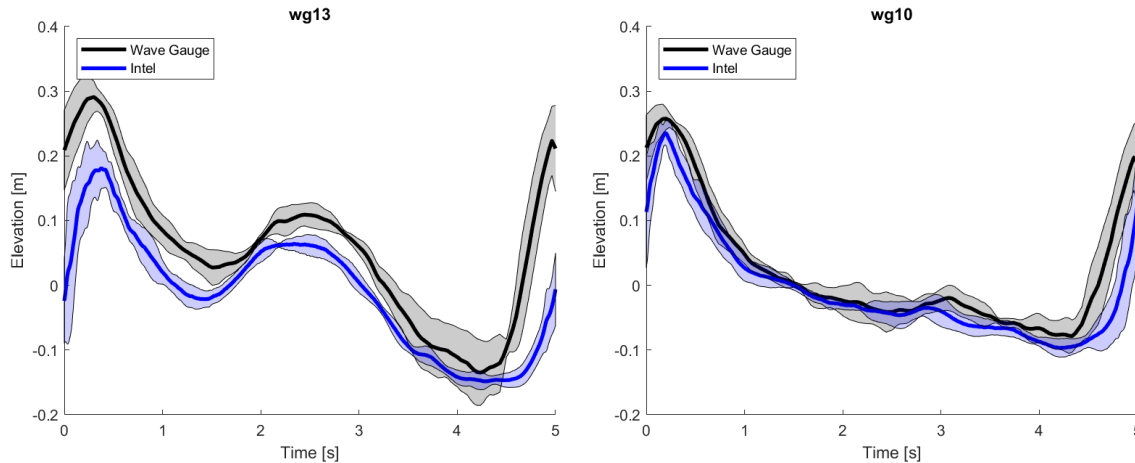


Figure 6.5: Average wave profiles for the wave gauges (black) and Intel<sup>®</sup> camera (blue) at WG 13 (left) and WG 10 (right). Shaded regions indicate the standard deviation in wave profiles.

Figure 6.6 shows the average wave profile's height for each gauge and location measured by the camera. The data from the camera was taken from the Northeast corner of the instrumentation frame, around basin coordinates  $x = 14$  m,  $y = -3$  m, so the data had to be rotated into basin coordinates, hence the tilted nature of the camera measurement area. Similar to previous results, effects from the instrumentation frame supports can be seen in the upper region of the camera's measurement area and can be disregarded. A strong gradient in wave height can be seen in WG 5-9 from left to right. The waves also slowly dissipated through breaking processes and a decline in gauge measured wave height is generally seen as  $x$  increases. The camera shows a region of larger wave height to the right of the figure, but this is difficult to validate even though the USWGs generally show a similar trend as  $y$  decreases. Ultrasonic gauges often become erroneous with high amounts of wave breaking, which may explain the higher wave height measured by USWG 2 compared to its surrounding gauges.

This data analysis technique rendered higher error values, with errors ranging from 1-29% with an average value of 12.4%. The duration of this recording was slightly longer (26 s) than the shore normal regular waves, but because the wave period was also greater the total number of waves recorded was lower (6 waves). The small number of recorded waves in this dataset may have increased the error in addition to the higher complexity in the wave field. During testing it was noted that strong circulation patterns were formed towards the end of the trial, creating alongshore currents that may have spatially affected the wave height too.

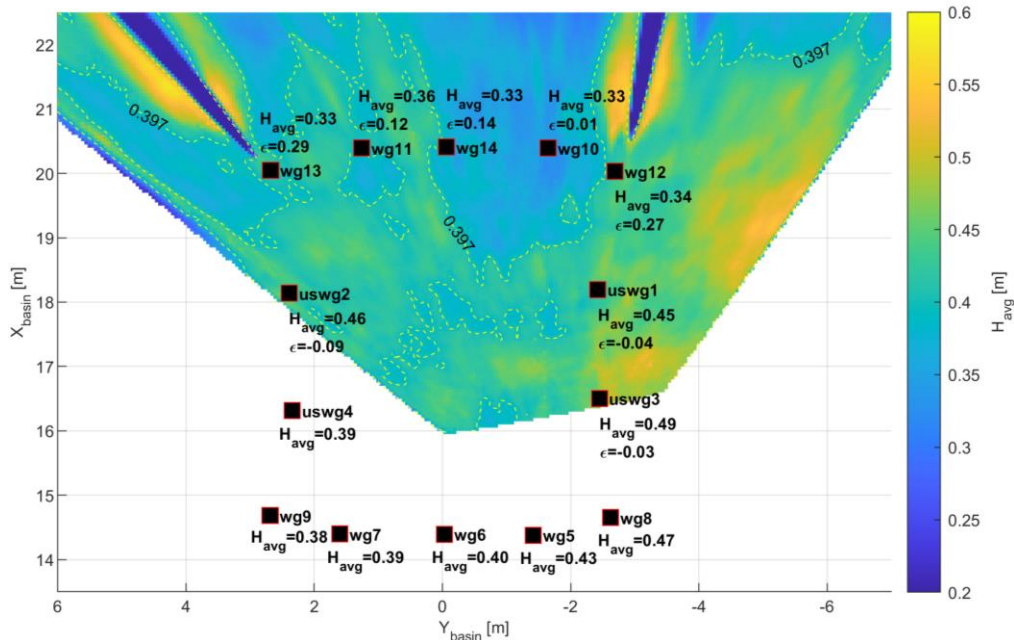


Figure 6.6: Average wave profile height ( $H_{avg}$ ) for the directional regular wave case in the basin coordinate system. WG and USWG measurements are displayed along with relative error ( $\epsilon$ ) between the camera and gauge.

Directionality was analyzed using the BDM method described in Section 5.4.4. Although the wave gauge layout was not designed to measure directionality, the gauge data was first analyzed using this technique. Grid nodes from the camera data were then extracted to form arrays with different geometries, which are also described in Section 5.4.4. Six different grid arrays were tested and it was found that the 3 by 5 node array produced the most realistic results. A CERC array specifically designed for this wave case was also tested. Figure 6.7 shows the directional analysis results from three different array geometries (a) the Intel<sup>®</sup> CERC array, (b) the Intel<sup>®</sup> 3 by 5 grid array, and (c) the WGs. The WG timeseries were shortened so that they only included the length of data during which the Intel<sup>®</sup> was recording. Due to the duration of the video recorded for this trial, the BDM technique had difficulty producing reliable results regardless of the array geometry.



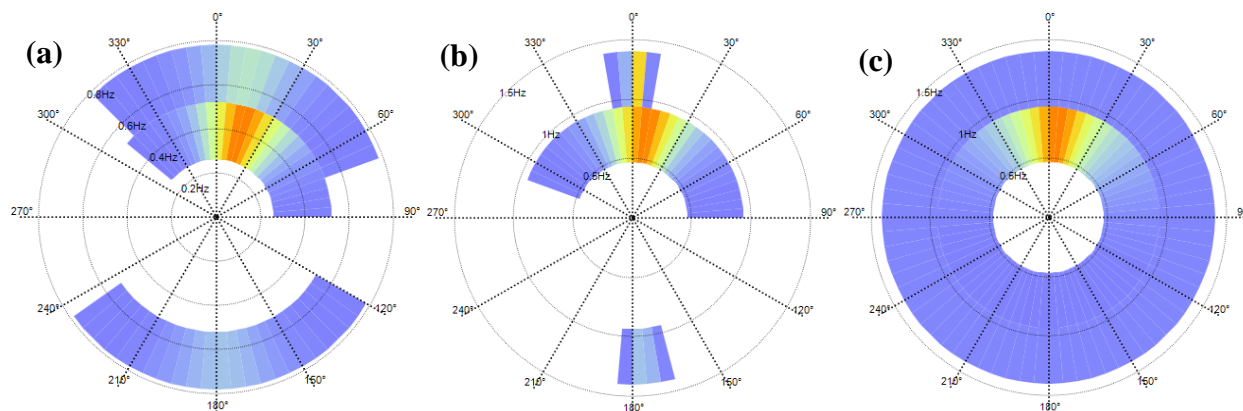


Figure 6.7: Directional wave spectra output from BDM analysis using data from: (a) shortened WG timeseries, (b) Intel<sup>®</sup> 3 by 5 grid array, and (c) Intel<sup>®</sup> CERC array from the directional regular wave case.

To counteract the camera timeseries' shorter length, it was extended by repeating each timeseries a total of 10 times and concatenating them together. This created timeseries with 60 measured waves instead of 6. The data was reanalyzed for the CERC array geometry and WG's and the results are shown in Figure 6.8. A more realistic result was output for both cases, with the majority of the energy distributed near the correct frequency (0.2 Hz) and direction (15 deg.). A secondary peak of energy, most likely associated with the superharmonic waves, was located at twice the frequency and half of the direction. The CERC array results also detected energy propagating towards the wavemaker, which can be identified as reflectional effects from the basin wall and beach.

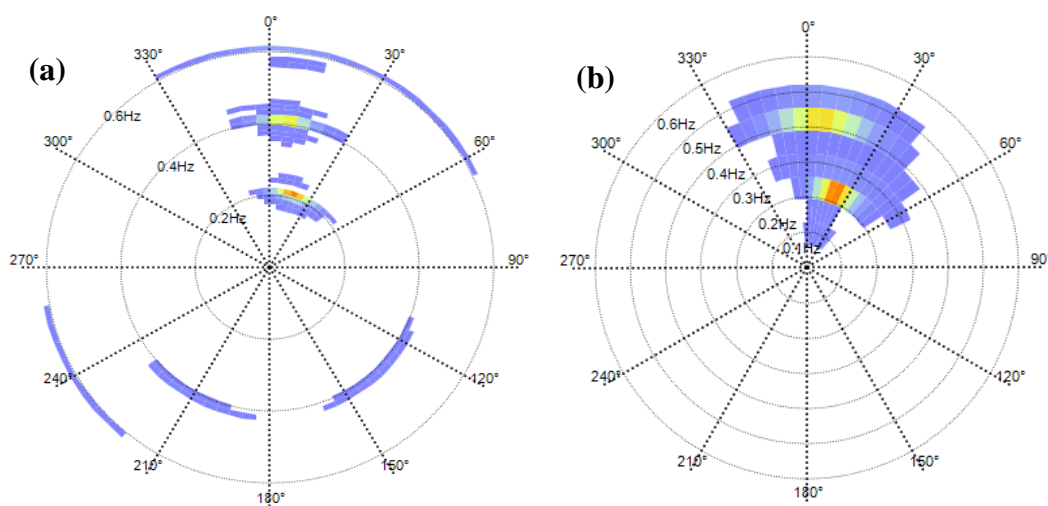


Figure 6.8: Directional wave spectrum output from BDM analysis calculated using: (a) extended Intel<sup>®</sup> CERC array timeseries and (b) complete WG timeseries.

### 6.1.3 Bidirectional ( $H = 0.3 \text{ m}$ , $0.3 \text{ m}$ , $T = 2 \text{ s}$ , $2 \text{ s}$ , $\theta = 15 \text{ deg}$ , $-15 \text{ deg}$ , $h = 1 \text{ m}$ )

The bidirectional regular wave case consisted of two superimposed regular wave cases, each with a desired wave height of 0.3 m, wave period of 2 s, and wave directions of 15 and -15 degrees in a water depth of 1 m. Theoretically, the regularity in the wave field would cause the intersection of each wave crest to occur in the same location throughout the trial, creating a noticeable pattern of wave heights across the basin. This is ideal for comparing gauge and camera measurements and observing spatial variability.

Figure 6.9 shows normalized mean wave height for this trial. The locations of wave crest intersection can be seen in the two vertical stripes of larger mean wave height where the superposition of both crests nearly doubled the amplitude. This amplification is captured by the gauge measurements, as seen in USWG 1-3 and WG 8, 12, and 13 which all measured a wave height that was about one third above average. A sharp decrease in wave height was measured by the gauges along the center of the basin, with WG 6 and 14 measuring wave heights approximately one third below average. This aligned well with the camera measurements, and errors ranged from 2-24% overestimations by the camera, with an average error of 8.25%. USWG 4 was malfunctioning during this trial which is why it is not present on this figure.

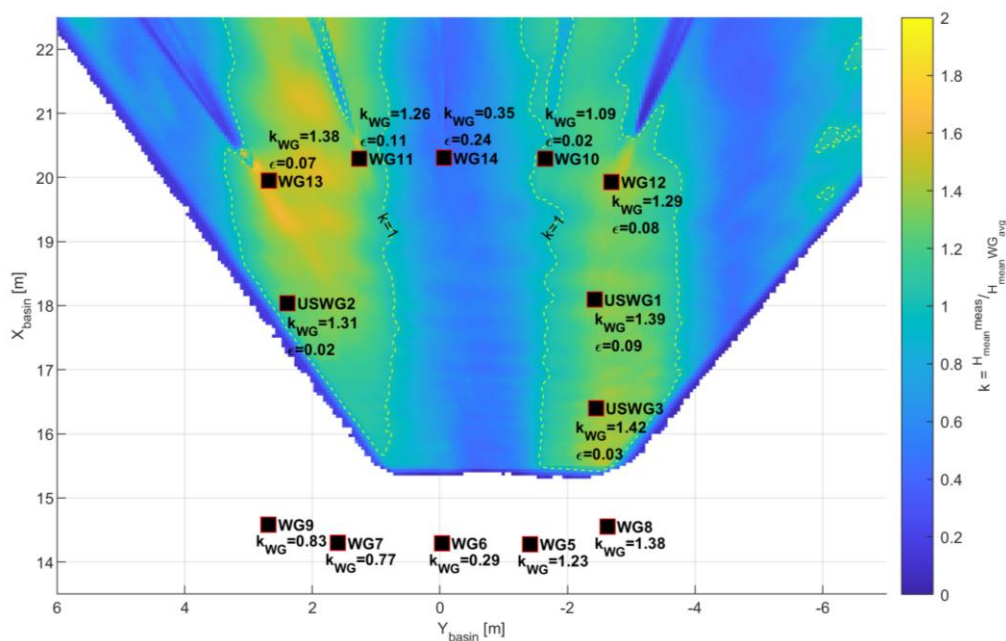


Figure 6.9: Normalized mean wave height ( $H_{mean}$ ) for the bidirectional regular wave case in the basin coordinate system. WG and USWG measurements are displayed along with relative error ( $\epsilon$ ) between the camera and gauge.

Figure 6.10 shows the normalized spectral significant wave height for the bidirectional wave case. A similar pattern from the previous figure is seen by the camera and gauge measurements, with slightly better agreement between the two. Errors ranged from 2-11% with an average error of 6%. The frequency domain analysis for the shore normal regular wave case also produced less error, which is noted and revisited once further wave cases are analyzed.

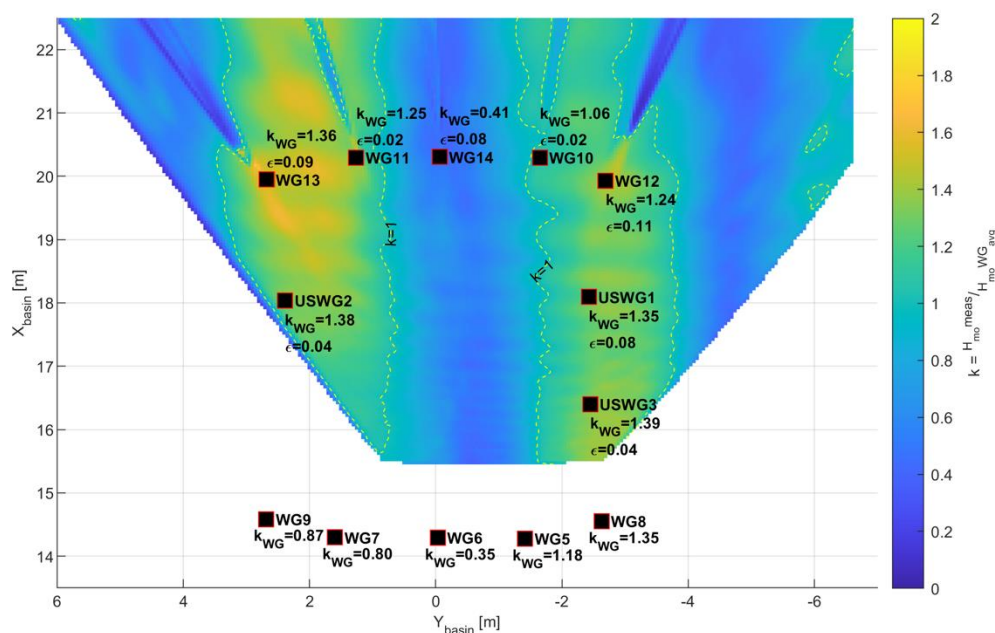


Figure 6.10: Normalized spectral significant wave height ( $H_{mo}$ ) for the bidirectional regular wave case in the basin coordinate system. WG and USWG measurements are displayed along with relative error ( $\epsilon$ ) between the camera and gauge.

As predicted, a pattern in wave height was seen in the gauge and camera measurements for this case. This variability was the greatest seen thus far in the study, with average wave height varying from twice the average to about 40% in a matter of 2 m in space. The present gauge layout was capable of capturing this well in the y direction, but a coarser gauge resolution in the x direction and the lack of gauges in the center of the instrumentation frame makes it difficult to accurately infer wave height in these areas. The camera, however, was able to capture this variability without the need to deploy more gauges. Snapshots of GoPro<sup>®</sup> video taken from the basin beach, as seen in Figure 6.11, validate the camera measurements by displaying wave crest intersection and breaking along the line of the frame supports.



Figure 6.11: GoPro<sup>®</sup> snapshot of waves under the instrumentation frame taken from basin beach during the bidirectional regular wave case.

6.2 Irregular Waves (JONSWAP spectra,  $H_s = 0.51$  m,  $T_p = 4$  s,  $\theta = 0$  deg, spreading =  $\pm 20$  deg,  $h = 1$  m)

This section focuses on the directionally spread, short-crested irregular wave case that was generated using a JONSWAP model spectra with a peak enhancement factor ( $\gamma$ ) of 6, significant wave height of 0.51 m, peak period of 4 s, and directional spreading of  $\pm 20$  degrees in a water depth of 1 m. For completeness, the duration of this trial was extended to 340 s to allow for the generation of over 100 waves. Breaking and non-breaking waves with different frequencies and directions were present in the basin at any given moment. The Intel<sup>®</sup> camera recorded the entirety of the trial excluding the wavemaker ramp down process.

Figure 6.12 shows the results from the time domain analysis of this irregular wave case, more specifically the normalized significant wave height calculated for the gauge and camera data. The majority of the water surface area measured by the camera was approximately equal to the average gauge significant wave height ( $k=1$ ) without much variability besides the region closest to the camera. As seen in the figure, the larger wave height region extends from the start of the camera measurement area in the positive x direction along  $y=0$  m. Very little wave height variability was expected with an irregular wave case with this extended duration, so this region with almost twice the wave height needed to be further investigated. Upon extracting the timeseries of a data point within this region, it was found that during extended periods of little to no wave action, the camera was detecting a Unistrut supporting mount and a surrounding rusted area on the basin floor. This created sharp decreases in the surface elevation as the camera

measured the bottom of the basin instead of the water surface. The noise generated by this measurement significantly increased wave heights in this region due to the large troughs it created which was not corrected by data filtering. During the regular wave cases there was constant wave action during camera recording, so this issue did not arise. This is noted for future use of the camera and the region is to be ignored for the present trial. Similar to previous wave cases, the shadows created by the instrumentation can also be ignored.

Examining the wave gauge measurements, a similar trend of low wave height variability can be seen. USWG 3 shows the greatest deviation from the average gauge measurement at +8%, which after further examination of the timeseries was due to error with the ultrasonic when measuring broken waves. Besides this exception, the gauges are all within approximately  $\pm 5\%$  of the average wave height. Error between the camera and gauge measurements ranged from -12-2% with an average error of -6.1%. As opposed to the regular wave cases, the camera tended to underestimate the wave height for the irregular wave case in the time domain.

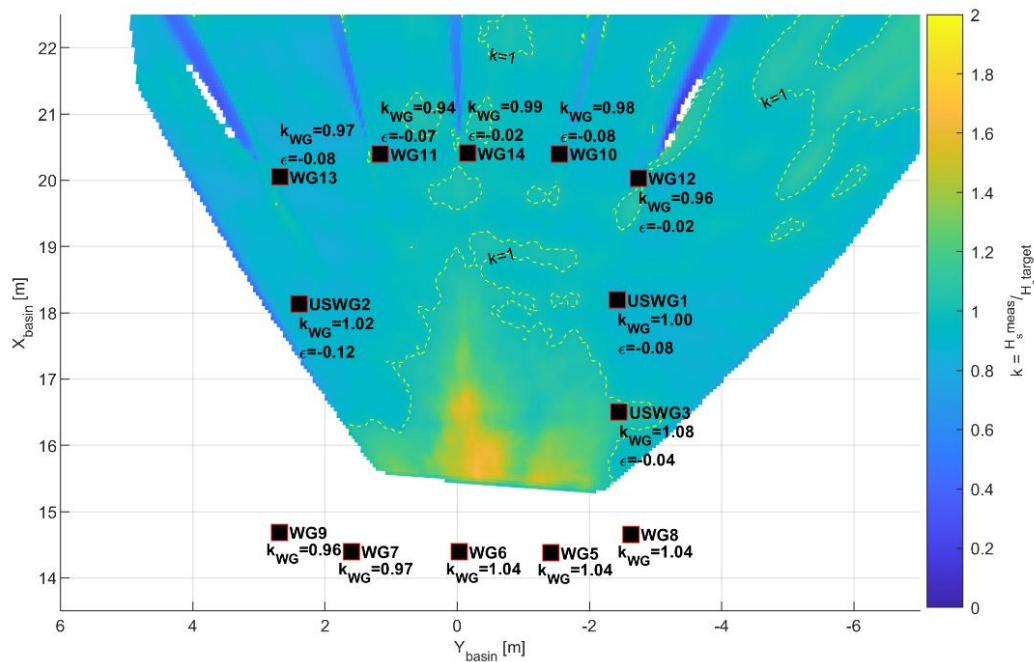


Figure 6.12: Normalized significant wave height ( $H_s$ ) for the directionally spread irregular wave case in the basin coordinate system. WG and USWG measurements are displayed along with relative error ( $\epsilon$ ) between the camera and gauge.

Figure 6.13 shows the normalized spectral significant wave height calculated through frequency domain analysis for the irregular wave case. The same erroneous region of larger wave height in

the time domain analysis is seen in this figure as well. Once again, this region can be ignored along with the instrumentation shadows. With that being said, there seems to be even less wave height variability for both the camera and gauge data when analyzed in the frequency domain. A slight decrease in spectral wave height is seen in the gauge measurements as  $x$  increases too, which is most likely due to wave dissipation through breaking. This was captured by the cameras but it is difficult to see graphically because of how subtle the decrease is. Errors for this trial were the lowest seen by any wave case and ranged from 0-6% with an average of 3%. As opposed to the time domain analysis results, the camera tended to overestimate the spectral wave height when compared to the gauges.

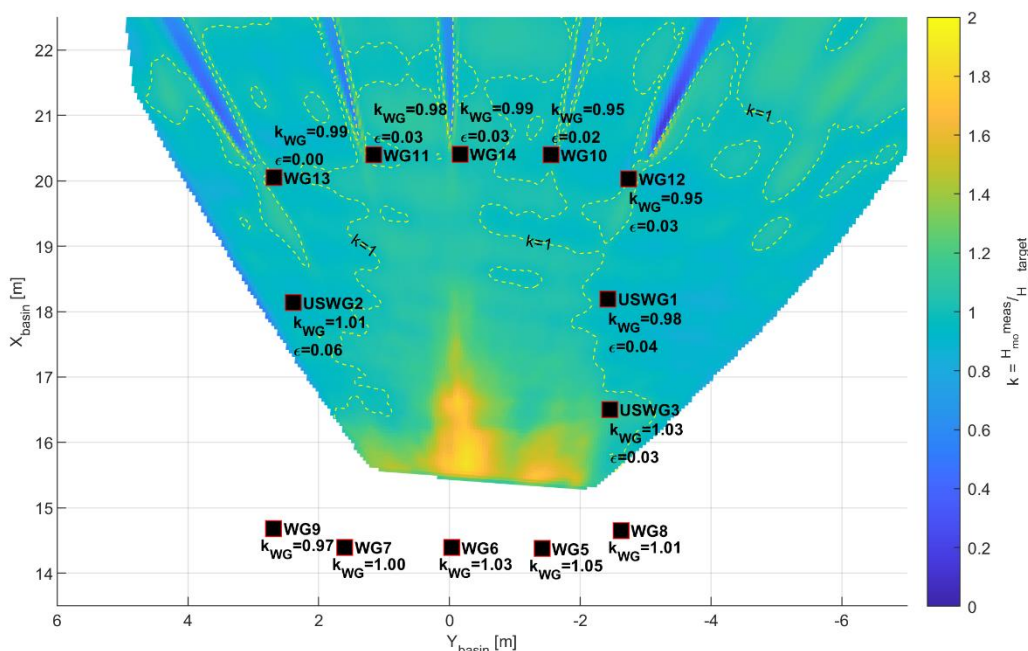


Figure 6.13: Normalized spectral significant wave height ( $H_{mo}$ ) for the directionally spread irregular wave case in the basin coordinate system. WG and USWG measurements are displayed along with relative error ( $\epsilon$ ) between the camera and gauge.

Figure 6.14 shows the output directional wave spectra from BDM analyses on (a) the wave gauges, (b) a CERC array of Intel<sup>®</sup> data points, and (c) a 3 by 5 grid array of Intel<sup>®</sup> data points. The results show higher frequency (0.8 Hz) energy from all directions for the gauge data while the Intel<sup>®</sup> cases show this at a lower frequency (0.3 Hz). This may be an artifact of the BDM analysis, as often this method requires tuning for accurate results [6], or there could be significant wave reflection effects present in the basin causing this energy output. Regardless, all

three cases show the most significant amount of energy at approximately 0.25 Hz, which is equal to the desired peak period of 4 s. The gauge and Intel<sup>®</sup> grid array output the center of this peak 5 and 10 degrees away from shore normal (0 degrees) respectively while the CERC array output a shore normal energy peak. The directional spreading of these measurements is portrayed by the width of each primary energy peak. An exact quantification of spreading is difficult to establish from this particular figure, but each seem relatively accurate based on visual inspection. Another feature to note is the secondary peak occurring at twice the peak frequency (0.5 Hz) for each case. There was significant wave breaking occurring for the larger waves throughout this trial, which may have caused a similar non-linear process to the directional regular wave case (Section 6.1.2) where energy was transferred to a superharmonic frequency of the breaking waves.

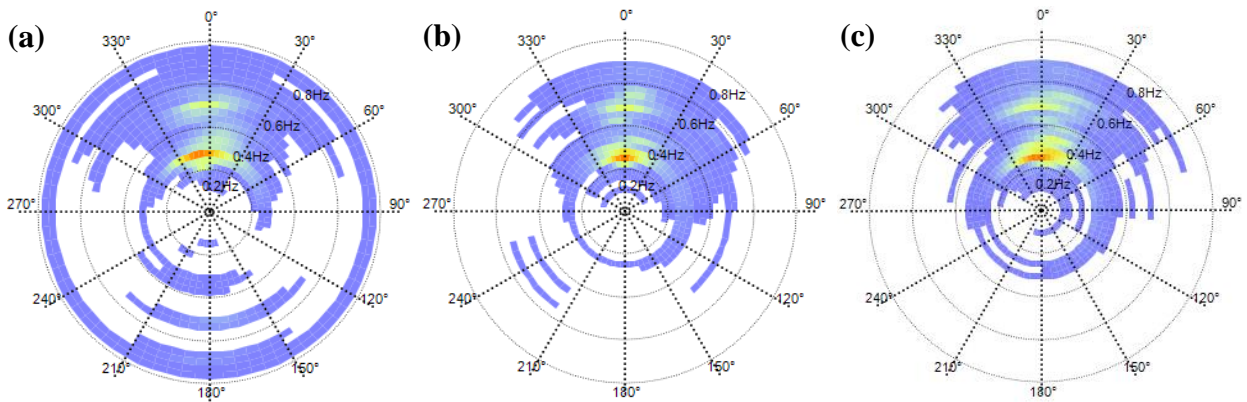


Figure 6.14: Directional wave spectra output from BDM analysis using data from: (a) WGs, (b) Intel<sup>®</sup> CERC array, and (c) Intel<sup>®</sup> 3 by 5 grid array from the directionally spread irregular wave case.

Figure 6.15 shows a three-dimensional reconstruction of the plot for Figure 6.14(b). This allows one to graphically visualize the significance of each peak's energy distribution. Although Figure 6.14 indicates that there is energy present in every direction, this plot emphasizes how insignificant this energy is relative to the primary and secondary peaks. It also gives a good comparison of the differing amplitudes of these two peaks.

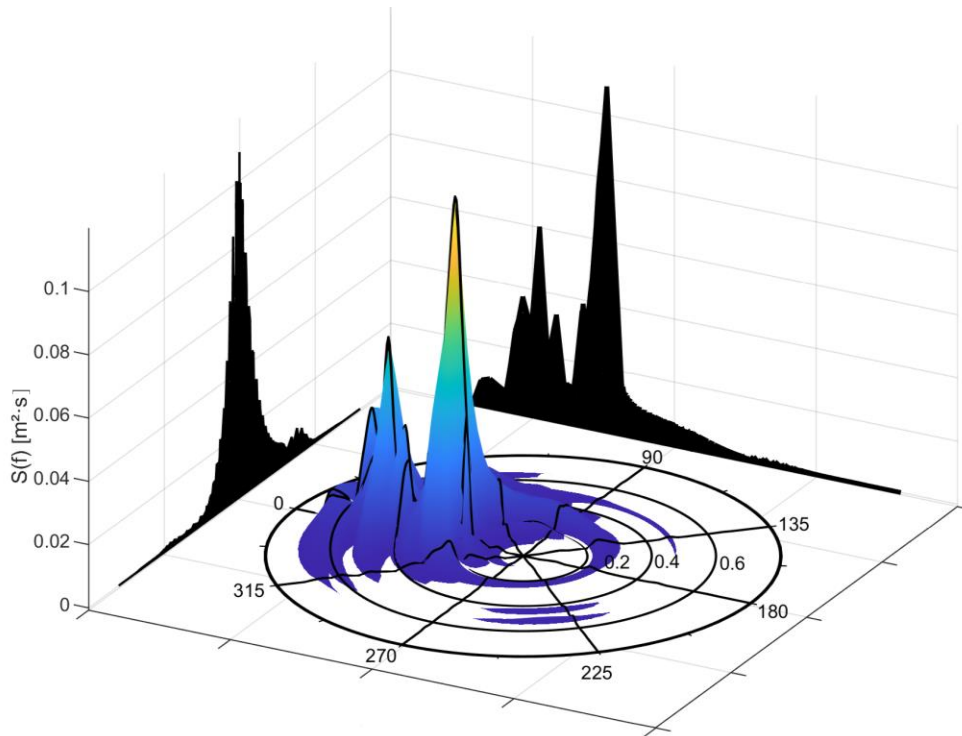


Figure 6.15: 3D polar directional wave spectra from BDM analysis for the Intel® CERC array. The radial axis is the frequency [Hz], azimuthal axis is the wave direction [deg], and z axis is the spectral density ( $S(f(\theta))$ ).

### 6.3 Focusing Waves

The final wave condition examined in this study are the focusing wave cases. The initial focusing wave trial was the first attempt at using the Intel® camera, so only short recordings were taken in order to test multiple camera positions. Once camera positioning was optimized, this wave condition was repeated in another trial at the end of the experiment so that a longer recording could be taken. This ensured a more thorough analysis and gave the opportunity to compare wave height variability patterns measured from different camera perspectives. The results from both trials were rotated into the basin coordinate system to facilitate visual comparison.



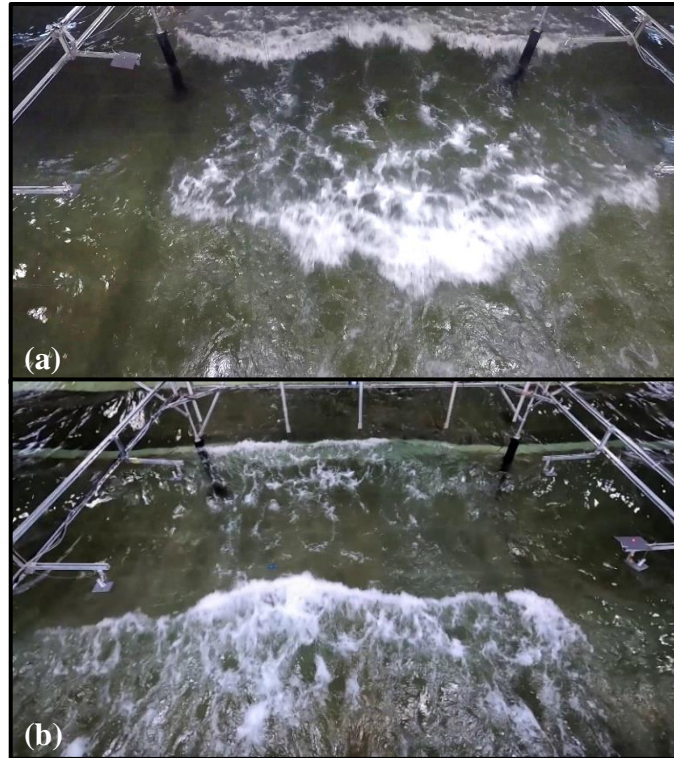


Figure 6.16: Snapshot from a GoPro<sup>®</sup> video of the focusing wave case viewed the instrumentation frame looking (a) offshore and (b) onshore.

The nature of the focusing waves created high variability under the instrumentation frame. Wave crests peaked slightly South of the frame's centerline and began breaking several meters before reaching the offshore frame supports. While propagating through the frame, the waves dissipated significantly and ceased to break directly after coming into contact with the onshore line of wave gauges (WG 10-14). Figure 6.16 shows these characteristics from two snapshots of GoPro<sup>®</sup> videos looking under the instrumentation frame in both the offshore and onshore direction. Looking offshore in the figure (a), two wave crests are breaking before and under the frame with the maximum wave height slightly South of center. The onshore view (b) shows another two wave crests, the further of which has significantly dissipated, and very little breaking is occurring.

These wave characteristics were then compared to the data collected from the Intel<sup>®</sup> camera in both trials. Figure 6.17 shows the normalized mean wave height from the first (top) and second (bottom) focusing wave trial. The data from the first trial was collected from a location near WG 8 in the Northeast corner of the instrumentation frame. The second trial was recorded from the

centerline of the frame near  $y=0$ . Both perspectives show a similar pattern, with the peaking wave crest path clearly visible in the form of a triangle of larger wave height aimed directly toward WG 11. This is where the energy of the focusing wave crest was concentrating, breaking before the frame, then dissipating and ceasing to break just after WG 11. The region is accompanied by a surrounding area of smaller wave height approximately 1 m in width that forms the shape of an upside down “V”. Finally, another region of larger wave height was present on either side of this depressed region. Both sets of camera and wave gauge data confirm this pattern for either test.

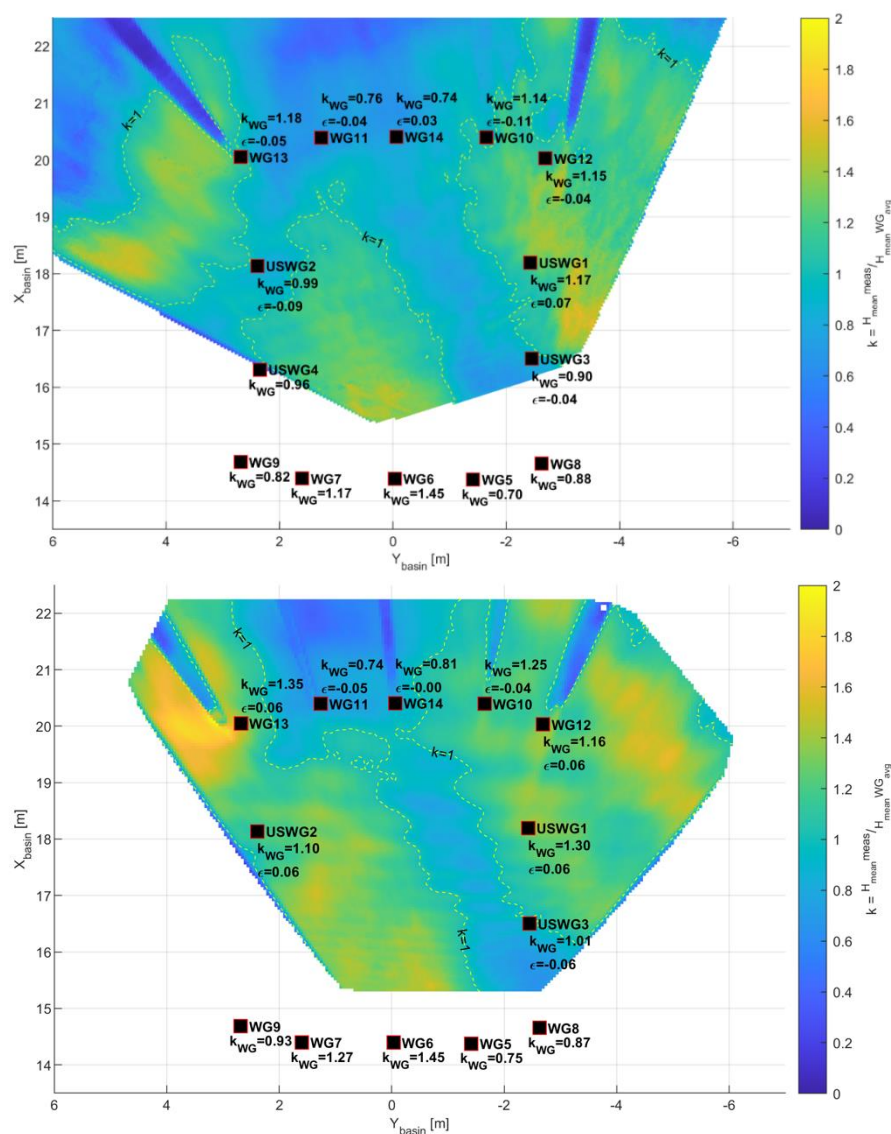


Figure 6.17: Normalized mean wave height ( $H_{\text{mean}}$ ) for the focusing wave cases in the basin coordinate system. The top shows results for a shorter duration video (15 s) taken from a location near WG 8 and the

*bottom shows a longer duration video (80 s) taken between WG 5 and 6. WG and USWG measurements are displayed along with relative error ( $\epsilon$ ) between the camera and gauge.*

In both trials the camera over and underestimated gauge measurements dependent on the location. Error from either trial ranged from an underestimation of -11% and an overestimation of 9%. The initial, shorter duration dataset had a higher average error of 5.9% while the longer duration dataset was 4.9% on average. As previously mentioned, having lesser waves in a dataset can often generate higher error from a time domain analysis, but the difference in error between trials is not significant enough for concern.

Figure 6.18 shows the normalized spectral significant wave height for both trials. A similar pattern is seen in wave height variability, but as opposed to the time domain analysis results, the shorter duration dataset had less associated error. Wave height was once again both over and underestimated by the camera, with errors ranging from an underestimation of -11% to an overestimation of 12%. The initial trial had an average error of 5.4% while the second trial averaged 7.1%.

This was the first and only trial where two separate camera datasets were able to be compared for the same wave conditions. The difference in views of these datasets gave an unambiguous validation to the wave height variability measured by the camera. As seen in both Figure 6.17 and Figure 6.18, the pattern in wave height variability matches for either view giving a good confirmation that these measurements are at least spatially realistic even if the magnitude is not completely accurate.

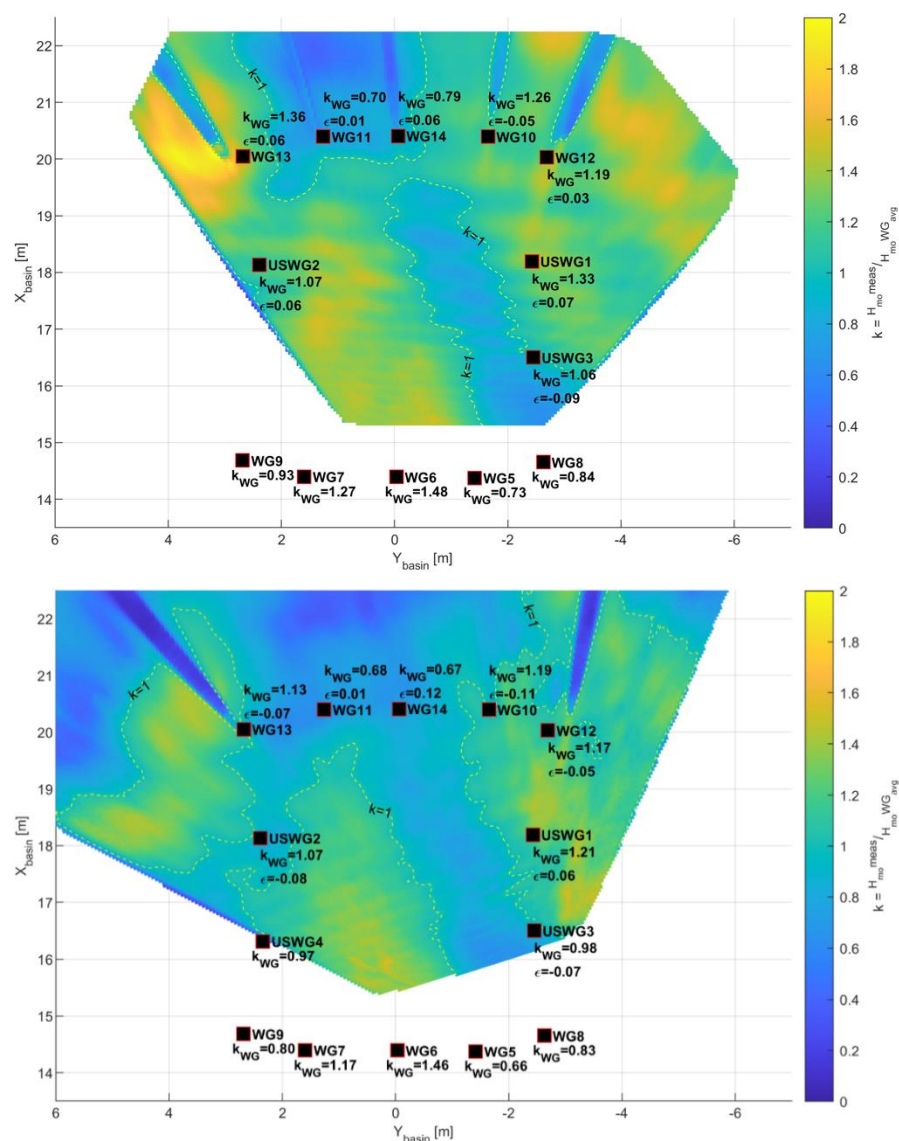


Figure 6.18: Normalized spectral significant wave height ( $H_{mo}$ ) for the focusing wave cases in the basin coordinate system. The top shows results for a shorter duration video (15 s) taken from a location near WG 8 and the bottom shows a longer duration video (80 s) taken between WG 5 and 6. WG and USWG measurements are displayed along with relative error ( $\epsilon$ ) between the camera and gauge.

#### 6.4 Discussion

Chapter 6 presented the results of detailed wave analyses for each wave condition recorded by the Intel® camera and compared them to wave gauge measurements and visual observations for validation. Several wave height analysis methods were used, predominantly time and frequency domain analysis to calculate statistical wave height values. A wave profile averaging method was used in place of the time and frequency domain analysis for the directional regular wave case.

Each interpolated data node within the camera datasets was analyzed with these techniques in order to output a spatial map of wave heights. The same analysis was used on each wave gauge timeseries and then overlaid onto the plots. The value from the closest camera node to each wave gauge was used to calculate the relative error at that location. Table 6.1 shows the average errors for each wave type for both time and frequency domain analysis as well as the average overall error for both analysis methods. Generally, the frequency domain analysis rendered smaller errors except for during the focusing wave case. This is most likely due to this method's ability to filter the high frequency noise that was present in much of the camera data.

*Table 6.1: Average relative camera error for each wave type and statistical analysis method.*

<b>Wave Type</b>	<b>Time Domain</b>	<b>Frequency Domain</b>
Regular Shore Normal	7.50%	5.60%
Regular Bidirectional	8.25%	6.00%
Irregular Directionally Spread	6.10%	3.00%
Focusing	5.40%	6.25%
<b>Average</b>	<b>6.81%</b>	<b>5.21%</b>

Overall, the camera performed well in breaking and non-breaking wave conditions and was able to reliably measure wave height variability in an area approximately 8 m by 8 m. Areas of the water surface beyond this, up to 15 m away, were also measured by the camera but no gauge data was present and its accuracy could not be validated. Wave heights ranging from 8-70 cm were able to be measured with periods ranging from 1.8-5 s. During the irregular wave case, it was found that the camera began recognizing objects at the bottom of the basin during periods of low wave energy. This occurred directly in front of the camera's location to approximately 3 m away, but this distance is most likely dependent on the obliquity of the camera's view to the water surface. High frequency noise was also present throughout much of the surface elevation measurements. This was partially compensated for using data filtering, but not well enough to justify replacing traditional wave gauges with the camera. It did, however, successfully quantify relative wave height variability when compared to measurements and observations. This can be particularly useful for the mapping of average wave heights over a large spatial extent without having to rely on the deployment of an array of traditional wave gauges.

The results shown proved that it may not always be accurate to rely on traditional point gauges to characterize the entire wave field, as even for the regular shore normal case wave height variability can occur in relatively small areas in between gauge locations. The spatial resolution in surface elevation measurement required is generally not feasible for a gauge array because of the difficulty of deployment and the potential for significant hydrodynamic disruptions. It is for these applications where the camera is more suitable than traditional wave gauges. In cases with higher wave height variability such as the bidirectional regular waves, a 100% increase in wave height was seen in a space of just 2 m. Although this wave field was designed for high variability, it further shows the inaccuracy in representing any particular wave field with a single value.

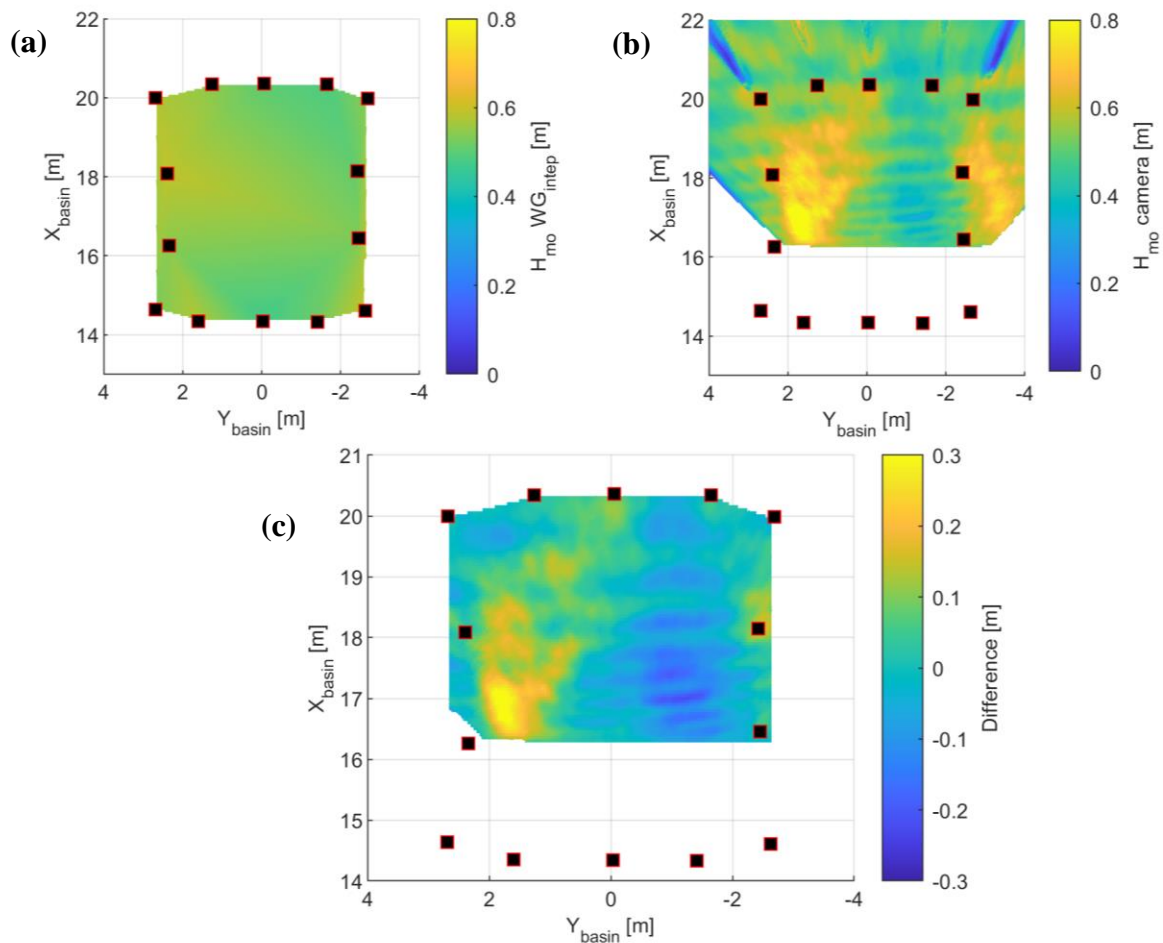


Figure 6.19: Comparison of (a) predicted spectral significant wave height ( $H_{mo} WG_{interp}$ ) interpolated from wave gauge measurements and (b) Intel® measured spectral significant wave height ( $H_{mo} camera$ ) from the regular shore normal wave case. (c) Difference between each ( $H_{mo} camera - H_{mo} WG_{interp}$ ) also displayed. WG and USWG locations labelled on each plot as black squares.

To further exemplify this conclusion, the regular shore normal wave case is revisited. It is common for a non-directional regular wave case such as this to only require surface elevation measurements along the length of the basin to quantify amplitude changes as the waves propagate into a shallower depth. The camera and gauge measurements for this trial, however, show an alongshore variability in the wave height that demonstrate the need for spatial measurement. Even with the instrumentation layout used for this study, which was designed to measure wave heights over a large space, much of the variation was not able to be captured. Figure 6.19(a) shows a spatial wave height plot interpolated from the gauge measurements in this trial. This is a representation of what the predicted wave field would look like based on solely wave gauge measurements. The Intel<sup>®</sup> camera measurements from this trial (b) along with the difference between the two plots (c) are also displayed. The difference plot exhibits what was not captured by the gauge measurement interpolation. Areas with positive values correspond to where the interpolation underestimated wave height and negative values correspond to an overestimation. The significant areas of larger and smaller wave height within the center of the instrumentation frame were clearly not captured by the gauge array. This would be problematic in an instance where uniform loading is expected on a research specimen. If it were located directly between these regions an alongshore gradient in hydrodynamic force would be created and an unanticipated loading would be put on the specimen. It is in scenarios such as this where it is unacceptable to characterize the wave field with a single value and spatial measurements are more appropriate.

Wave directionality was also able to be measured using the camera data. Traditional wave gauge array geometries were extracted from the dataset and analyzed using the BDM method to calculate the directional wave spectra. Although the instrumentation layout was not designed for this application, the gauge data was also analyzed with the BDM method for comparison. The camera and gauge results were comparable for both regular and irregular waves. For simplicity, this was the only method used to calculate wave directionality, but much further analysis could be done with a three-dimensional spatial dataset such as this. Instead of only analyzing two-dimensional byproducts of the overall dataset, the entire three-dimensional surface could be analyzed on a per wave basis to extract instantaneous and average directionality. This could be done for each particular location within the camera measurement area. A crest detection algorithm, described in Section 5.4.4, was formulated and attempted this with some success but

further testing would be required to validate this method. Other studies applied a 3D Fast Fourier Transform method to similar surface elevation datasets [39][57], which could be a useful technique for future research utilizing the Intel® camera. Regardless, the camera's capability of quantifying directionality without the need for rigorous wave gauge array deployment was proved. It could be feasibly applied in research studies that require directionality measurements without hydrodynamic disruption. It could also be integrated into a traditional CERC array system for measurement validation.

That concludes the main body of this study. The following chapter summarizes the methodology and findings of this project. Future research and applications are suggested for the camera systems. Unused data recorded during these experiments and other concurrent projects at the HWRL is described along with its potential use.



## Chapter 7 Conclusion

The objective of this study was to implement and analyze an instrumentation system that can three dimensionally measure the water surface elevation in a laboratory setting, allowing a higher spatial understanding of wave height variability than with traditional point measurement wave gauges. Two stereoscopic camera measurement systems were selected to test in a variety of wave conditions in the DWB at the HWRL. Stereo systems were deemed the most feasible for this application due to their low cost, ease of deployment, and past research success in measuring wave height in dynamic lab and field environments [5][28]. Multiple preliminary experiments were designed to understand the cameras' abilities and optimize camera positioning, lighting, and wave conditions. A methodology to post process data from both systems was developed. A final set of experiments compared the cameras and traditional wave gauge measurements in directional, non-directional, regular, and irregular waves. Several wave data analysis techniques were used on the camera and gauge data to statistically compare wave height values in both the time and frequency domain. Directionality was analyzed using the BDM method and a new technique was developed for analyzing instantaneous wave crest directionality. This chapter summarizes the two camera systems' functionalities, the methodologies used for post processing their data, and the important findings for each. Future research considerations are discussed and potential applications are suggested.

### 7.1 WASS Findings

The first stereo camera system selected for testing was WASS, an open-source stereo image processing pipeline developed by Filippo Bergamasco [7] to analyze open ocean waves in field applications. It is a software-based system in which the user provides image data from a calibrated and synchronized camera set and an estimation of the three-dimensional pixel reconstruction is output. GoPro<sup>®</sup> cameras were selected due to their low cost and availability and calibrated using the Camera Calibration Toolbox for Matlab [9]. The cameras' high lens distortion characteristics made them difficult to accurately calibrate with no previous calibration experience, but nonetheless an accurate calibration was achieved. Camera sets were mounted approximately 0.5 m apart on a custom built Unistrut mount that allowed for both system and individual camera pan and tilt. The stereo baseline was increased when a larger area of the basin was being measured. Several different camera positions and lighting were tested. A

synchronization method was developed using a randomly blinking LED in view of both cameras that allowed the video frames to be aligned with one another and gauge measurements after recording. Once a point cloud of the stereo reconstruction was output, the data was interpolated into gridded format to be further analyzed.

In preliminary testing, it was found that the success of this system was highly dependent on the texture of the water surface. WASS was specifically designed for open-ocean applications where the water is generally very texturized and opaque. Conversely, the water surface in a laboratory setting is generally smoother and translucent, which can make it difficult for the cameras to recognize. Past research studies have counteracted this issue by seeding the water with floating particles or opaque dye [3][18][28][55], but this study aimed to analyze WASS for future use in a variety of research projects and this method may not always be feasible so it was not implemented. Instead, diffuse lighting fixtures and circular polarized lenses were used to increase the cameras' ability to capture the water surface while decreasing glare and reflections. An oblique view from an elevation of 2 m or more was found optimal. Instrumentation, support structures, and passing wave crests that obstructed the cameras' views greatly affected the data quality so two sets of cameras were used in the final experiments in attempt to increase both data quality and measurement area.

The final experiments were designed to record surface elevation data in the center of the basin under an instrumentation frame that supported the stereo camera systems, lighting fixtures, and 14 traditional wave gauges. A variety of wave conditions were selected to test the cameras' abilities to reliably measure breaking and non-breaking waves and compare the data to the gauge measurements. The cameras were then repositioned on to the basin beach in attempt to reconstruct the entire water surface and analyze both camera systems' ability to measure the nearshore surf zone. After processing the videos from the final experiments through WASS, it was found that the system had extreme difficulty recognizing the water surface unless there were waves breaking within the field of view of the cameras. WASS only had success in cases where waves were breaking directly under the instrumentation frame for the duration of the trial. The wave breaking left a trail of bubbles and foam behind each wave crest which had the same effect as seeding the water with floating material or dye. During these instances, WASS intermittently measured an area approximately 6 by 6 m. Combining datasets from two separate stereo pairs

proved difficult and did not increase the data quality within this area. Some success was seen measuring a larger area of the basin in preliminary trials, but the data recorded from the beach in the final experiments could not be processed. This seemed to be due to the positioning of the cameras which was at too low of an elevation. Camera positions could be adjusted in the future to potentially measure the entire wave basin, but more research needs to be completed to validate this conclusion.

The focusing and shore-normal regular wave cases showed that the WASS data had high frequency noise present across the entire measurement area. Often only the breaking wave crests were recognized, creating spatial and temporal gaps throughout the data. Depending on the size of the gap, it could be smoothed over with interpolation, but this introduced error into the dataset. The data quality was also dependent on its location within the camera frame, but this was specific to the camera positioning and ambient lighting during the time of the trial and no consistent spatial trends were found. In cases where wave breaking occurred directly in line with wave gauges, the amplitude and shape of the wave profiles measured by both the camera and gauges would match relatively well but the high frequency noise present often created large spikes at the wave crests and troughs. The instrumentation would also create large elevation spikes in the camera data surrounding the location of the wave gauges, so it was difficult to directly compare the camera and gauge measurements. The data output by this system and computational time required proved to be cumbersome as well. Due to these reasons, much of the data collected in the final experiments through WASS was left unused.

In conclusion, WASS was successfully able to reconstruct a 6 by 6 m area within the basin with no seeding to the water but was limited to measuring breaking waves. The measurements were noisy and inconsistent but relative accuracies were found in certain wave cases. This system is much more involved and requires careful selection, calibration, and placement of the cameras and lighting during experimentation, but the ability to customize the stereo baseline between both cameras gives it a higher potential for measuring larger surface areas. Any obstructions within the measurement area greatly affected the data quality, which could hinder its applicability for projects with any specimen or large instrumentation frame. High computational power and data storage space are required for post processing, but once video data is processed it can be deleted to decrease data size. Although WASS was capable of measuring the water

surface within the lab, it was clearly intended for field use and its limitations within the lab are apparent. Future applications of WASS within the HWRL are most likely limited, but the scenario may arise where a large spatial extent of the water surface must be measured and WASS could be applied.

## 7.2 *Intel® Findings*

The Intel® RealSense™ D455 Depth Camera was the second stereo system selected for testing in this study. Unlike WASS, this system provides the sensors and hardware which consists of an off-the-shelf consumer grade depth camera module with two depth cameras, an RGB camera, an infrared structured light projector, and an IMU. The camera also has on-board processing hardware that internally synchronizes and processes each sensor to output a fully reconstructed point cloud from the camera pixels. Intel® provides a Software Developer Kit and data viewer desktop application that displays the two and three-dimensional data in real-time, allowing the user to visually inspect data during testing and optimize camera positioning and lighting. This system was introduced in the final experiments, where it was thoroughly analyzed and compared to WASS. The randomly blinking LED was also used to synchronize the data recorded from the Intel® camera to the wave gauge data recorded from the DAQ. Point cloud data required coordinate system rotation, and then it was interpolated into gridded format for further analysis.

Although the testing of this system was limited to the final set of experiments, it was apparent that it out-performed WASS in a laboratory setting. All wave conditions were able to be measured, regardless of wave breaking. Texture was still required for the camera to recognize the water surface, but significantly less than WASS. The camera generally began accurate measurement once one or two small amplitude waves propagated through the camera's field of view. During periods of low wave energy in the irregular wave cases, the camera recognized underwater objects in the basin which significantly affected data quality. This only occurred directly in front of the camera where there was less obliquity in the view of the water surface, which may potentially be solved by adjusting the camera angle. The ambient lighting also seemed to be less important to this system's success, likely due to its use of an IR projector to assist the depth cameras in stereo reconstruction. This enabled the system to measure the water surface regardless of its position relative to the lighting fixtures. The fixed stereo baseline of the camera module, which was much smaller than that used for the WASS cameras (0.095 m vs. 0.5

m), limited the distance at which it was able to measure objects. This created a smaller potential measurement area on the water surface when compared to WASS, but because it was more consistent and accurate a larger area was in fact measured. An approximately 8 by 8 m area of the water surface was generally able to be measured. The optimal camera position was much closer to the water surface than for the WASS cameras, but both preferred an oblique view. Objects obstructing the view of the camera also affected the surrounding data quality, but this system was able to decipher between these objects and the water surface much more reliably than WASS. The stereo matching algorithm built for the Intel<sup>®</sup> system was designed to spatially reconstruct the entire video frame while WASS' was designed to crop out any objects it detects that are blocking the water surface. This created fewer spatial gaps in the Intel<sup>®</sup> data and allowed the water surface to be analyzed directly adjacent to objects such as the instrumentation frame supports. Objects were able to be filtered out of the final point cloud during post-processing with some success, but this method should be further improved for future research.

After a preliminary data comparison of the two camera systems, it was concluded that the Intel<sup>®</sup> system performed better overall and further investigation focused solely on its dataset. Each wave case was analyzed in the time and frequency domain and mean, significant, and spectral significant wave height values were calculated for the camera and wave gauges. The average relative error between the camera and gauge values were 6.81% and 5.21% for the time and frequency domain analyses respectively. Wave heights ranging from 8-70 cm with periods of 1.8-5 s were able to be measured, but further testing is required to quantify the camera's limitations. The camera performed best during the irregular directionally spread wave case which was also the longest duration trial. Relative wave height variability was successfully measured and validated for all cases, but the two-dimensional time series extracted from the camera dataset still contained high frequency noise, deeming it invalid as a full replacement for traditional point measurement wave gauges. Wave height tended to be underestimated by the camera.

Directionality was measured by extracting nodes from the camera dataset that created specific array geometries and inputting them into Wavelab's BDM analysis. The instrumentation layout for the final experiments was not designed to measure directionality so results could not be properly validated. A technique was developed to measure instantaneous wave directionality using the entire three-dimensional water surface reconstruction, but this requires further testing.

In conclusion, the Intel<sup>®</sup> system performed more accurately and consistently than the WASS system. It measured an 8 by 8 m area of the water surface in a variety of wave conditions with an average relative accuracy of ~6% when compared to traditional wave gauges. The entire measurement area was able to be analyzed with traditional methods in both the time and frequency domain to statistically determine wave heights, periods, and directionality. No camera calibration was required, and optimization could be completed on the lab floor while viewing the spatial data in real-time. High frequency noise was present throughout the dataset and several optical errors occurred deeming the Intel<sup>®</sup> infeasible as a substitute for traditional point measurement gauges, but the resolution of spatial data that it was capable of measuring revealed the limitations of point measurements. For each wave case investigated, including the regular shore normal waves, a level of nonuniformity was captured by the camera that could not be measured by the gauge array. It was capable of showing gradients in wave height variability across the entire water surface through the use of a single instrument, which could only be inferred when using traditional point measurements. Therefore, the application of the Intel<sup>®</sup> system is not in replacing point wave measurements, rather working in parallel with them in order to better understand the spatial variability surrounding the gauges. This will prove valuable in future research when general areas of larger or smaller wave heights need to be known. The camera can measure the area of interest and provide a general “road map” of the wave heights so that researchers can understand hot spots of wave amplification and adjust their instrumentation layout as necessary.

### 7.3 *Future Considerations*

This study laid the groundwork for what is possible in free surface measurement with an off-the-shelf, consumer grade stereo camera such as the Intel<sup>®</sup> camera, but many different research avenues were not explored. Further investigation on directional analysis techniques is required to determine the most appropriate method for analyzing a three-dimensional dataset. Rather than utilizing the two-dimensional aspects of the dataset and inputting them into traditional directional analyses such as the BDM method, an approach that considers the entire reconstructed water surface should be considered. These methods have been successfully applied to similar datasets in previous research [39][57].

In order to increase both data quality and measurement area, multiple cameras could be added to the system. Unlike the WASS system, Intel<sup>®</sup> cameras have the capability of being hardware synchronized by connecting each camera to one another and designating a single camera as the master [26]. This could be utilized in a similar fashion to the multiple GoPro<sup>®</sup> camera sets without the added difficulty of system synchronization. Multiple Intel<sup>®</sup> sensor types can also be connected which may be useful for other applications that require LiDAR or object tracking by using the Intel<sup>®</sup> L515 and T265 cameras.

Many physical modelling research projects that occur within a wave lab incorporate a single or multiple specimen that include but are not limited to wave energy converters, model coastal infrastructure, vessels, and nature-based engineering features. Measurements are typically made around these specimens, but it can often be difficult to place instrumentation in areas without disrupting either the surrounding hydrodynamics, motion of the specimen, or the functionality of the instrument. The Intel<sup>®</sup> system could be useful in applications where wave height needs to be measured near an object and traditional wave gauge cannot be used. Figure 7.1 shows an example of a situation where the Intel<sup>®</sup> camera measured the water surface around a series of specimens. Model mangrove trees were built to study their wave attenuation and coastal protection characteristics, so wave height measurements were required along the length of the flume. Traditional wave gauges, including wire and ultra-sonic gauges, were used but in many areas within the mangrove forest it was difficult to place instrumentation without the possibility of the specimen into contact with the gauge and corrupting its data. The Intel<sup>®</sup> camera was able to record surface elevation data from a distance without physically disrupting the specimen. The measurements were not validated however, and further work needs to be completed before implementing this method in future research.

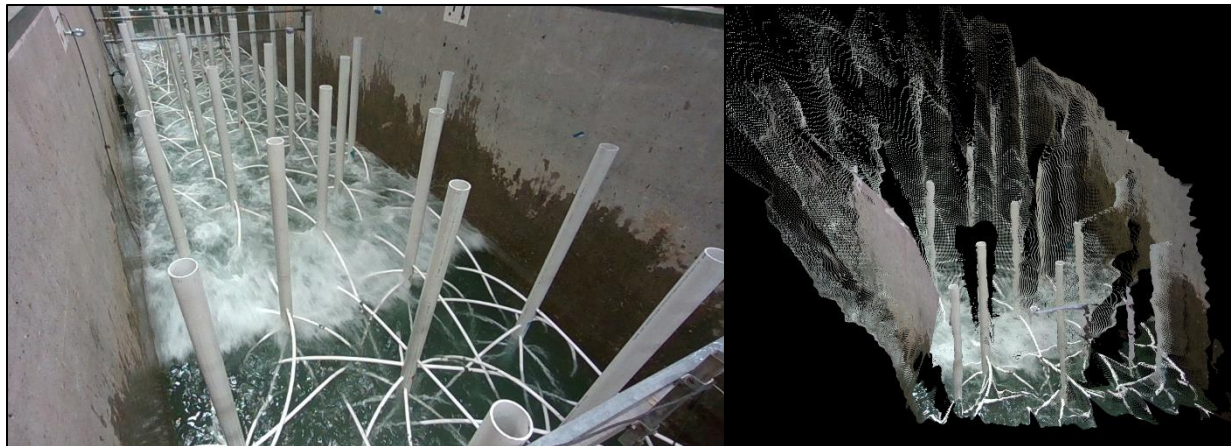


*Figure 7.1: Example of both RGB (left) and point cloud (right) data collected by the Intel<sup>®</sup> camera of a model mangrove forest. Traditional wave gauges could not be placed in many areas of the flume where they could potentially collide with the lower “root” section of the model trees.*

Another possible laboratory application of this camera system is object tracking. One of the largest users of this product line is the robotics community and tracking objects such as cars and people is a common application. Many techniques have been developed for this using spatial data from the Intel<sup>®</sup> camera [12], and these could potentially be applied to research projects that require the measurement of an object’s position and orientation.

During the final experiment of this study, the Intel<sup>®</sup> camera successfully recorded the water surface in the surf zone of the basin. An example of the image and spatial data is shown in Figure 7.2. No analysis was completed on these datasets so the accuracy cannot be validated, but upon visual inspection one can see the water surface was reconstructed. The nearshore environment is a nonuniform dynamic area with many open research questions that have yet to be answered. It is often difficult to place instrumentation here and the Intel<sup>®</sup> camera could prove valuable. Topics such as rip currents, runup, and nearshore circulation could be explored.

Having the ability to spatially measure the free surface within a wave research laboratory in a reliable, versatile manner is a powerful tool that can be used in many research applications. Although this system is unable to substitute traditional point measurements, it can provide researchers with other important information that will assist in the understanding, design, and implementation of ocean and coastal research in the future.



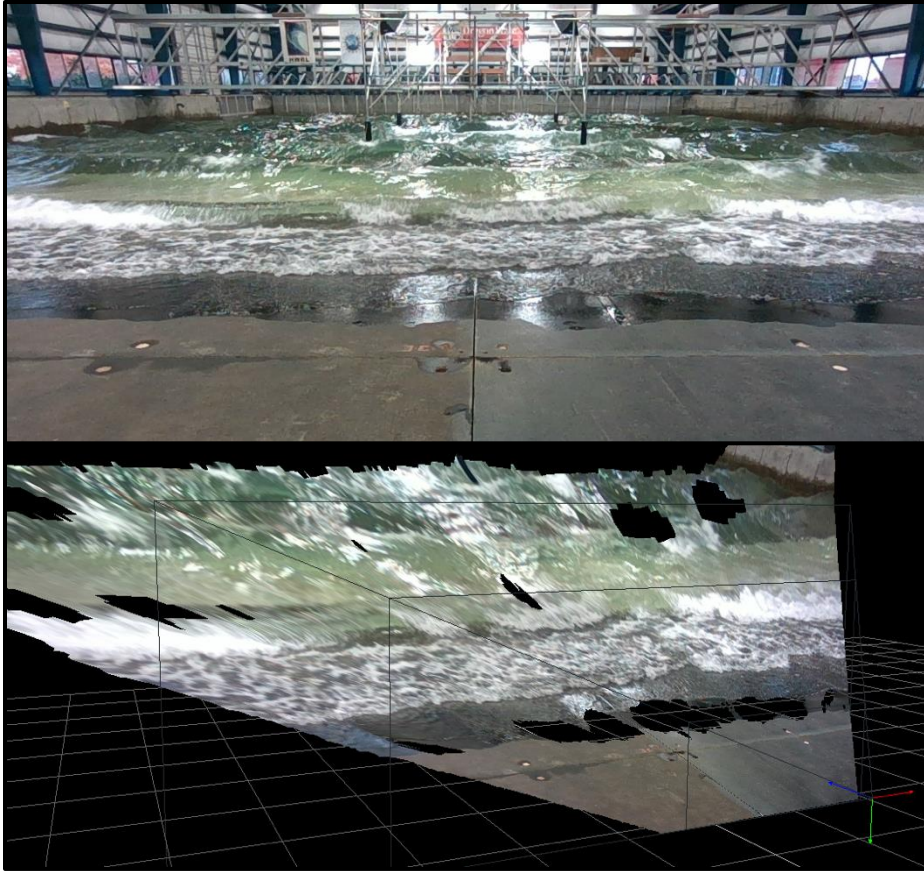


*Figure 7.2: Example of RGB (top) and point cloud (bottom) data collected by the Intel<sup>®</sup> camera of the nearshore environment in the DWB.*

## References

- [1] Albarelli, A., Rodolà, E., & Torsello, A. (2012). Imposing semi-local geometric constraints for accurate correspondences selection in structure from motion: A game-theoretic perspective. *International journal of computer vision*, 97(1), 36-53.
- [2] Anil, Kıvanç & Danışman, Devrim & Sarıöz, Kadir. (2017). Simulation-Based Analysis of Ship Motions in Short-Crested Irregular Seas. *Journal of ETA Maritime Science*, 5(1), 19-38.
- [3] Baker, C. M., Moulton, M., Palmsten, M. L., Brodie, K. L., & Kumar, N. (2020, February). Remote sensing of transient rip currents and surface waves in a laboratory wave basin. In *Ocean Sciences Meeting 2020*. AGU.
- [4] Benetazzo, A. (2006). Measurements of short water waves using stereo matched image sequences. *Coastal engineering*, 53(12), 1013-1032.
- [5] Benetazzo, A., Fedele, F., Gallego, G., Shih, P. C., & Yezzi, A. (2012). Offshore stereo measurements of gravity waves. *Coastal Engineering*, 64, 127-138.
- [6] Benoit, M. (1993, July). Extensive comparison of directional wave analysis methods from gauge array data. In *Proc. 2nd Int. Symp. on Ocean Wave Measurement and Analysis (ASCE)* (pp. 740-754).
- [7] Bergamasco, F., Torsello, A., Sclavo, M., Barbariol, F., & Benetazzo, A. (2017). WASS: An open-source pipeline for 3D stereo reconstruction of ocean waves. *Computers & Geosciences*, 107, 28-36.
- [8] Bergamasco, F. Personal communication, August 28<sup>th</sup>, 2020.
- [9] Bouguet, J. Y. (2004). Camera calibration toolbox for matlab. [http://www.vision.caltech.edu/bouguetj/calib\\_doc/index.html](http://www.vision.caltech.edu/bouguetj/calib_doc/index.html).
- [10] Bung, D. B., Crookston, B. M., & Valero, D. (2020). Turbulent free-surface monitoring with an RGB-D sensor: the hydraulic jump case. *Journal of Hydraulic Research*, 1-12.
- [11] Chen, Y., & Yeh, H. (2014). Laboratory experiments on counter-propagating collisions of solitary waves. Part 1. Wave interactions. *Journal of fluid mechanics*, 749, 577-596.
- [12] Chen, Y. C., Weng, W. C., & Lin, S. W. (2019, October). A High Reliability 3D Object Tracking Method for Robot Teaching Application. In *IOP Conference Series: Materials Science and Engineering* (Vol. 644, No. 1, p. 012010). IOP Publishing.
- [13] Coe, R. G., Bacelli, G., Forbush, D., Spencer, S. J., Dullea, K. J., Bosma, B., & Lomónaco, P. (2020). *FOSWEC dynamics and controls test report* (No. SAND2020-11695). Sandia National Lab.(SNL-NM), Albuquerque, NM (United States).

- [14] Dabiri, D., Zhang, X., & Gharib, M. (1995). A real-time free surface slope mapping technique.
- [15] De Vries, S., Hill, D. F., De Schipper, M. A., & Stive, M. J. F. (2011). Remote sensing of surf zone waves using stereo imaging. *Coastal Engineering*, 58(3), 239-250.
- [16] Dean, R. G., & Dalrymple, R. A. (1991). *Water wave mechanics for engineers and scientists* (Vol. 2). World Scientific Publishing Company.
- [17] Deetjen, M. E., Biewener, A. A., & Lentink, D. (2017). High-speed surface reconstruction of a flying bird using structured light. *Journal of Experimental Biology*, 220(11), 1956-1961.
- [18] Douxchamps, D., Devriendt, D., Capart, H., Craeye, C., Macq, B., & Zech, Y. (2005). Stereoscopic and velocimetric reconstructions of the free surface topography of antidune flows. *Experiments in Fluids*, 39(3), 535-553.
- [19] Emec, K. D., Luh, H. F., Pu, G. L., & Uedin, J. B. R. (2014). Non-intrusive wave field measurement.
- [20] Engineering, C.o. Directional Wave Basin.  
<https://wave.oregonstate.edu/directional-wave-basin>.
- [21] Faltinsen, O. (1993). *Sea loads on ships and offshore structures* (Vol. 1). Cambridge university press.
- [22] Gerig, G. (2012). Image Rectification (Stereo). *CS 6320*.
- [23] Gomit, G., Chatellier, L., Calluau, D., & David, L. (2013). Free surface measurement by stereo-refraction. *Experiments in fluids*, 54(6), 1-11.
- [24] Goring, D. G., & Nikora, V. I. (2002). Despiking acoustic Doppler velocimeter data. *Journal of hydraulic engineering*, 128(1), 117-126.
- [25] Grant, I., Zhao, Y., Smith, G. H., & Stewart, J. N. (1995). Split-screen, single-camera, laser-matrix, stereogrammetry instrument for topographical water wave measurements. *Applied optics*, 34(19), 3806-3809.
- [26] Grunnet-Jepsen, A., Winer, P., Takagi, A., Sweetser, J., Zhao, K., Khuong, T., ... & Woodfill, J. (2018). Using the RealSense D4xx depth sensors in multi-camera configurations. *Intel Corp., Santa Monica, CA, USA, Tech. Rep. Rev 0.4*.
- [27] Guimarães, P. V., Ardhuin, F., Bergamasco, F., Leckler, F., Filipot, J. F., Shim, J. S., ... & Benetazzo, A. (2020). A data set of sea surface stereo images to resolve space-time wave fields. *Scientific data*, 7(1), 1-12.
- [28] Harry, M., Zhang, H., Lemckert, C., Colleter, G., & Blenkinsopp, C. (2011, January). Remote sensing of water waves: wave flume experiments on regular and irregular waves. In *20th Australasian Coastal and Ocean Engineering Conference 2011 and the 13th Australasian Port and Harbour Conference* (pp. 138-143).

- [29] Hasselmann, K., Sell, W., Ross, D. B., & Müller, P. (1976). A parametric wave prediction model. *Journal of Physical Oceanography*, 6(2), 200-228.
- [30] Helm-Petersen, J. (1996). Directional Wave Analysis using BDM Method: Manual and Software. *Aalborg Universitetsforlag*.
- [31] Higgins, C., Cox, D., & Lomónaco, P. (2017). NHERI experimental facility for coastal waves/surge and tsunamis at Oregon State University. In *Proc., 16th World Conf. on Earthquake Engineering* (pp. 1-8). Belgrade, Serbia: Institute of Theoretical and Applied Mechanics.
- [32] Hilsenstein, V. (2005). Surface reconstruction of water waves using thermographic stereo imaging. In *Image and Vision Computing New Zealand* (Vol. 2). Citeseer.
- [33] Hirschmuller, H. (2007). Stereo processing by semiglobal matching and mutual information. *IEEE Transactions on pattern analysis and machine intelligence*, 30(2), 328-341.
- [34] Holland, K. T., Puleo, J. A., & Kooney, T. N. (2001). Quantification of swash flows using video-based particle image velocimetry. *Coastal Engineering*, 44(2), 65-77.
- [35] Holthuijsen, L. H. (1983). Stereophotography of ocean waves. *Applied ocean research*, 5(4), 204-209.
- [36] Iglesias, G., Ibáñez, O., Castro, A., Rabuñal, J. R., & Dorado, J. (2009). Computer vision applied to wave flume measurements. *Ocean engineering*, 36(14), 1073-1079.
- [37] Intel Corporation. (2020). Intel RealSense Product Family D400 Series Datasheet. <https://www.intelrealsense.com/wp-content/uploads/2020/06/Intel-RealSense-D400-Series-Datasheet-June-2020.pdf>.
- [38] Keselman, L., Iselin Woodfill, J., Grunnet-Jepsen, A., & Bhowmik, A. (2017). Intel realsense stereoscopic depth cameras. In *Proceedings of the IEEE Conference on Computer Vision and Pattern Recognition Workshops* (pp. 1-10).
- [39] Leckler, F., Ardhuin, F., Peureux, C., Benetazzo, A., Bergamasco, F., & Dulov, V. (2015). Analysis and interpretation of frequency–wavenumber spectra of young wind waves. *Journal of Physical Oceanography*, 45(10), 2484-2496.
- [40] Lee, Y., Haroutunian, M., & Trodden, D. G. (2017). 3D Wave Reconstruction Through Image Processing. In *5th International Conference on Advanced Model Measurement Technology for The Maritime Industry (AMT'17)*. Newcastle University.
- [41] Li, C., Pickup, D., Saunders, T., Cosker, D., Marshall, D., Hall, P., & Willis, P. (2012). Water surface modeling from a single viewpoint video. *IEEE Transactions on Visualization and Computer Graphics*, 19(7), 1242-1251.

- [42] Liu, C., Ma, S., Ma, Q., & Zeng, X. (2011, November). Stereo vision system based on the laser dot matrix projection. In *2011 International Conference on Optical Instruments and Technology: Optical Systems and Modern Optoelectronic Instruments* (Vol. 8197, p. 819704). International Society for Optics and Photonics.
- [43] Liu, H. T., Katsaros, K. B., & Weissman, M. A. (1982). Dynamic response of thin-wire wave gauges. *Journal of Geophysical Research: Oceans*, 87(C8), 5686-5698.
- [44] McGraw-Hill Companies, Inc. (2003). Free surface. *McGraw-Hill Dictionary of Scientific and Technical Terms*.
- [45] Meinert, P., Andersen, T. L., & Frigaard, P. (2011). AwaSys 6 user manual.
- [46] Meyer, Harald. (2020). Multi Camera Control for GoPro (1.0.4) [Mobile app]. *App Store*. <https://apps.apple.com/us/app/multi-camera-control-for-gopro/id1449808197>.
- [47] Panicker, N. N., & Borgman, L. E. (1970). Directional spectra from wave-gage arrays. In *Coastal Engineering 1970* (pp. 117-136).
- [48] Park, J. C., Kim, M. H., & Miyata, H. (2001). Three-dimensional numerical wave tank simulations on fully nonlinear wave–current–body interactions. *Journal of Marine Science and Technology*, 6(2), 70-82.
- [49] Perelman O., Wu C.H., Boucheron R., Fréchou D. (2011). 3D wave fields measurements techniques in model basin: application on ship wave measurement. In: *The 2nd International Conference on Advanced Model Measurement Technology for EU Maritime Industry*.
- [50] Piepmeier, J. A., & Waters, J. (2004, September). Analysis of stereo vision-based measurements of laboratory water waves. In *IGARSS 2004. 2004 IEEE International Geoscience and Remote Sensing Symposium* (Vol. 5, pp. 3588-3591). IEEE.
- [51] Santel, F., Linder, W., & Heipke, C. (2004, July). Stereoscopic 3D-image sequence analysis of sea surfaces. In *Proceedings of the ISPRS Commission V Symposium* (Vol. 35, No. part 5, pp. 708-712).
- [52] Savelyev, I., & Fuchs, J. (2018). Stereo thermal marking velocimetry. *Frontiers in Mechanical Engineering*, 4, 1.
- [53] Schwendeman, M. S., & Thomson, J. (2017). Sharp-crested breaking surface waves observed from a ship-based stereo video system. *Journal of Physical Oceanography*, 47(4), 775-792.
- [54] Sun, H., Qiu, D., Shen, Y., & Wang, Y. (2004). Wave measurement based on light refraction. *Acta oceanologica sinica*, 23(2), 359-366.

- [55] Sutherland, P., & Melville, W. K. (2013). Field measurements and scaling of ocean surface wave-breaking statistics. *Geophysical Research Letters*, *40*(12), 3074-3079.
- [56] Tsubaki, R., & Fujita, I. (2005). Stereoscopic measurement of a fluctuating free surface with discontinuities. *Measurement Science and Technology*, *16*(10), 1894.
- [57] Veras Guimarães, P., Ardhuin, F., Sutherland, P., Accensi, M., Hamon, M., Pérignon, Y., ... & Ferrant, P. (2018). A surface kinematics buoy (SKIB) for wave-current interaction studies. *Ocean Science*, *14*(6), 1449-1460.
- [58] Vieira, M., Guimarães, P. V., Violante-Carvalho, N., Benetazzo, A., Bergamasco, F., & Pereira, H. (2020). A Low-Cost Stereo Video System for Measuring Directional Wind Waves. *Journal of Marine Science and Engineering*, *8*(11), 831.
- [59] Viriyakijja, K., & Chinnarasri, C. (2015). Wave flume measurement using image analysis. *Aquatic Procedia*, *4*, 522-531.
- [60] Wang, T. M., & Shih, Z. C. (2021). Measurement and Analysis of Depth Resolution Using Active Stereo Cameras. *IEEE Sensors Journal*, *21*(7), 9218-9230.
- [61] Yoo, J., Kim, M., Son, D., & Shin, S. (2020, February). 3D observation of water surface in the nearshore using stereo camera. In *Ocean Science Meeting 2020* (pp. CP42A-01). AGU.
- [62] Zavadsky, A., Benetazzo, A., & Shemer, L. (2017). On the two-dimensional structure of short gravity waves in a wind wave tank. *Physics of Fluids*, *29*(1), 016601.

## Appendix A: Test Sheets

Table A.1: Basin Views experiment test sheet

Experiment: Basin Views 8/11/2020					
Test #	Waves	Camera Position	Camera Settings	Lighting	Notes
1	Focus5 – 100%	Frame Elevation 2m from SWL	Auto, Protune ISO 400 Shutter 1/60	Diffuse lights on/off	4 videos: Auto lights on/off, Protune lights on/off
2	Focus5 – 100%	Frame Elevation 3m from SWL	Auto, Protune ISO 400 Shutter 1/60	Diffuse lights on/off	4 videos: Auto lights on/off, Protune lights on/off
3	Focus5 – 100%	Bridge towards beach	Auto, Protune ISO 400 Shutter 1/60	Diffuse lights on	2 videos: Auto, Protune
4	Focus5 – 100%	Bridge towards wavemaker	Auto, Protune ISO 400 Shutter 1/60	Diffuse lights on	2 videos: Auto, Protune
5	Focus5 – 100%	Side of basin	Auto, Protune ISO 400 Shutter Auto	Diffuse lights on	2 videos: Auto, Protune
6	Focus5 – 100%	Beach corner	Auto, Protune ISO 400 Shutter Auto	Diffuse lights on	2 videos: Auto, Protune
7	Focus5 – 100%	Beach center	Auto, Protune ISO 400 Shutter Auto, EV -1.0	Diffuse lights on	2 videos: Auto, Protune
8	Airy – 0.5m 2s	Beach center	Auto, Protune ISO 400 Shutter Auto	Diffuse lights on	2 videos: Auto, Protune
9	Airy – 0.5m 2s	Beach corner	Auto, Protune ISO 400 Shutter Auto	Diffuse lights on	2 videos: Auto, Protune
10	Airy – 0.5m 2s	Side of basin	Auto, Protune ISO 400 Shutter Auto	Diffuse lights on	2 videos: Auto, Protune
11	Airy – 0.5m 2s	Bridge towards wavemaker	Auto, Protune ISO 400 Shutter 1/60	Diffuse lights on	2 videos: Auto, Protune
12	Airy – 0.5m 2s	Bridge towards beach	Auto	Diffuse lights on	1 video: Auto
13	Airy – 0.5m 2s	Frame Elevation 2m from SWL	Auto, Protune ISO 400 Shutter Auto	Diffuse lights on/off	4 videos: Auto lights on/off, Protune lights on/off
14	Airy – 0.5m 2s	Frame Elevation 3m from SWL	Auto, Protune ISO 400 Shutter Auto	Diffuse lights on/off	4 videos: Auto lights on/off, Protune lights on/off

**Notes:** Run each wave case continuously until all camera positions have been recorded, then turn off wavemaker and let basin settle before running next wave case

Table A.2: Airy Validation experiment test sheet

Experiment: Airy Validation 8/18/2020				
Trial #	Trial Description	Trial Conditions	Duration	WASS notes
1	Validation of semi-breaking waves, cameras at WG 10/12	Airy Waves H = 0.5 m T = 2 s h= 1m	3 min	500 fails first video, 600 fails second video
2	Validation of un-broken waves, cameras at WG 10/12	Airy Waves H = 0.4 m T = 2 s h= 1m	4 min	1700 fails, most in beginning
3	Validation of semi-breaking waves, cameras at WG 11/13	Airy Waves H = 0.5 m T = 2 s h= 1m	4 min	1900 fails at beginning/end
4	Validation of un-broken waves, cameras at WG 11/13	Airy Waves H = 0.4 m T = 2 s h= 1m	4 min	All failed

**Notes:** Cameras on tripod placed on instrumentation bridge facing toward beach. When noted that cameras are facing WG 10/12, tripod North of center of instrumentation frame. When noted that cameras are facing WG 11/13, tripod South of center of instrumentation frame.

Table A.3: CPL Filter experiment test sheet.

Experiment: CPL Filter					
Trial #	Trial Description	Trial Conditions	Time	Notes	WASS Notes
1	Semi-breaking waves, backlit, cameras on bridge facing WG 12,13,14	Airy Waves H = 0.5 m T = 2 s h= 1.08 m	11:40	Waves too small/not breaking fully	4 "ransac" failures
2	Semi-breaking waves, backlit, cameras on bridge facing WG 12,13,14	Airy Waves H = 0.54 m T = 2 s h= 1.08 m	12:04	Some reflections from overhead lab lights	4 "ransac" failures
3	Semi-breaking waves, fully-lit, cameras on bridge facing WG 12,13,14	Airy Waves H = 0.54 m T = 2 s h= 1.08 m	12:22		27 "ransac" failures
4	3D focusing waves, backlit, cameras on bridge facing WG 12,13,14	focus5 100% h = 1.08 m	12:40		
5	3D focusing waves, fully-lit, cameras on bridge facing WG 12,13,14	focus5 100% h = 1.08 m	12:58		
6	Semi-breaking waves, fully-lit, cameras on North side of basin facing WG 8,10,12	Airy Waves H = 0.54 m T = 2 s h= 1.08 m	13:20		42 "ransac" failures

**Notes:** Run waves for 1 minute per Trial, running DAQ for 3.5 min, 21,000 samples to collect



Table A.4: Two Stereo Pairs, Intel® Cam, Frame experiment test sheet.

Experiment: TwoStereoPairs_IntelCam_Frame						
Trial	Trial Description	Trial Conditions	Date	Time	Notes	WASS Notes
1	Breaking focusing waves, GoPros® on frame, Intel® camera on bridge	focus5 100%, duration = 120 s	6-Nov	15:48	Intel® cam on NE corner of frame	Pair 1: No fails Pair 2: 17 fails
2	Regular breaking waves, GoPros® on frame, Intel® camera on bridge	Airy Waves H = 0.50 m, T = 1.8 s, Theta = 0 deg, durations = 120 s	6-Nov	16:07	Intel® cam under GoPro® mount on same Unistrut, less breaking under frame, height was recorded wrong in DAQ (entered H=0.05 instead of 0.50)	Pair 1: 1518 fails Pair 2: 846 fails
3	Regular breaking directional waves, GoPros® on frame, Intel® camera on bridge	Airy Waves H = 0.55 m, T = 3.0 s, Theta = 15 deg, duration = 120 s	6-Nov	16:26	Intel® cam on GoPro® Unistrut but lower than before	Pair 1: No fails Pair 2: 129 fails
4	Regular breaking directional waves, GoPros® on frame, Intel® camera on bridge	Airy Waves H = 0.56 m, T = 5.0 s, Theta = 15 deg, duration = 120 s	6-Nov	16:45	Intel® cam low on NE corner of frame	Pair 1: No fails Pair 2: 61 fails
5	Irregular multi-directional waves, GoPros® on frame, Intel® camera on bridge	File: JS_H0.51_T4.0_h1.0_20deg_gm6_disp.bin	12-Nov	10:40	File length: 5:40, DAQ runtime: 8 min, recorded Intel® on frame for 5 min = 8 GB .bag file, 5 ft below GoPros®	Pair 1: 7031 fails Pair 2: 5576 fails
6	Breaking cross waves with wave height variability under frame, GoPros® on frame, Intel® camera on bridge	File: H0p3_T2_15deg_cf_180outofphase.bin	12-Nov	11:02	File length: 1:40, DAQ runtime: 5 min, 8 GB .bag file	Pair 1: No fails Pair 2: 470 fails
7	Non-breaking smaller cross waves, GoPros® on frame, Intel® camera on bridge	File: H0p15_T2_25_0deg_inphase.bin	12-Nov	11:22	File length: 1:40, DAQ runtime: 5 min	Pair 1: 1384 fails Pair 2: 2537 fails
8	Breaking focusing waves, 1 to1 Intel® GoPro® comparison	focus5 100%, duration = 60 s	12-Nov	11:39	DAQ runtime: 5 min	Pair 1: 149 fails Pair 2: 278 fails

Notes: Pair 1 offshore facing, Pair 2 onshore facing. Both mounted on instrumentation frame

Table A.5: Two Stereo Pairs, Intel® Cam, Beach experiment test sheet.

Experiment: TwoStereoPairs_IntelCam_Beach						
Trial	Trial Description	Trial Conditions	Date	Time	Notes	WASS Notes
1	Breaking focusing waves, GoPros® on beach, Intel® camera on beach	focus5 100%, duration = 120 s	12-Nov	16:25	Intel® between GoPros®, picking up some of nearshore zone but not further	Pair 1: No fails Pair 2: All failed
2	Regular semi-breaking waves, GoPros® on beach, Intel® camera on beach	Airy Waves H = 0.50 m, T = 1.8 s, Theta = 0 deg, durations = 120 s	12-Nov	16:44	Moved lights facing onshore from frame to the beach to light up nearshore better, Intel® cam in between GoPros®	Pair 1: 2488 fails Pair 2: All failed
3	Regular semi-breaking directional waves, GoPros® on beach, Intel® camera on beach	Airy Waves H = 0.55 m, T = 3.0 s, Theta = 15 deg, duration = 120 s	12-Nov	17:02	Intel® on SW corner of beach, looked at runup	Pair 1: 48 fails Pair 2: All failed
4	Breaking cross waves with wave height variability under frame, GoPros® on beach, Intel® camera on beach	File: H0p3_T2_15deg_cf_180outofphase.bin	13-Nov	15:24	Wave shadows from Intel® (cam too low), middle of beach	Pair 1: 1681 fails Pair 2: All failed
5	Regular semi-breaking directional waves, GoPros® on beach, Intel® camera on beach, move cameras back (more runup)	Airy Waves H = 0.56 m, T = 5.0 s, Theta = 15 deg, duration = 120 s	13-Nov	15:41	GoPros® raised to 1.34m above beach slope/moved back 4.8m from SWL	Pair 1: 699 fails Pair 2: All failed
6	Irregular uni-directional waves, GoPros® on beach, Intel® camera on beach	File: JS_H0.50_T4.0_h1.0_disp.bin	13-Nov	16:00	Intel® cam raised higher in center (1.75m off beach)	Pair 1: All fails Pair 2: All failed
7	Irregular multi-directional waves, GoPros® on beach, Intel® camera on beach	File: JS_H0.51_T4.0_h1.0_20deg_gm6_disp.bin	13-Nov	16:21	Intel® on side	Pair 1: All fails Pair 2: All failed

**Notes:** Pair 1 offshore facing mounted on instrumentation frame, Pair 2 onshore facing on the beach

## Appendix B: Output Video Screenshots

### B.1 Basin Views Experiment

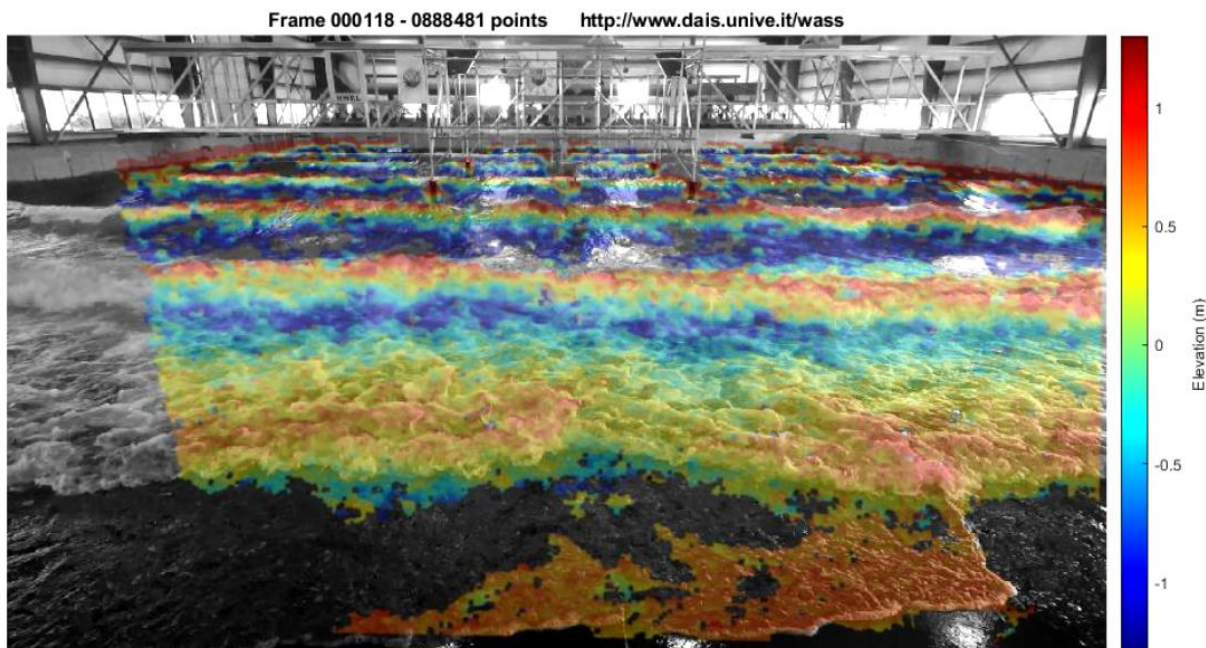


Figure B.1: Basin Views WASS auto snapshot for regular wave case from beach center.

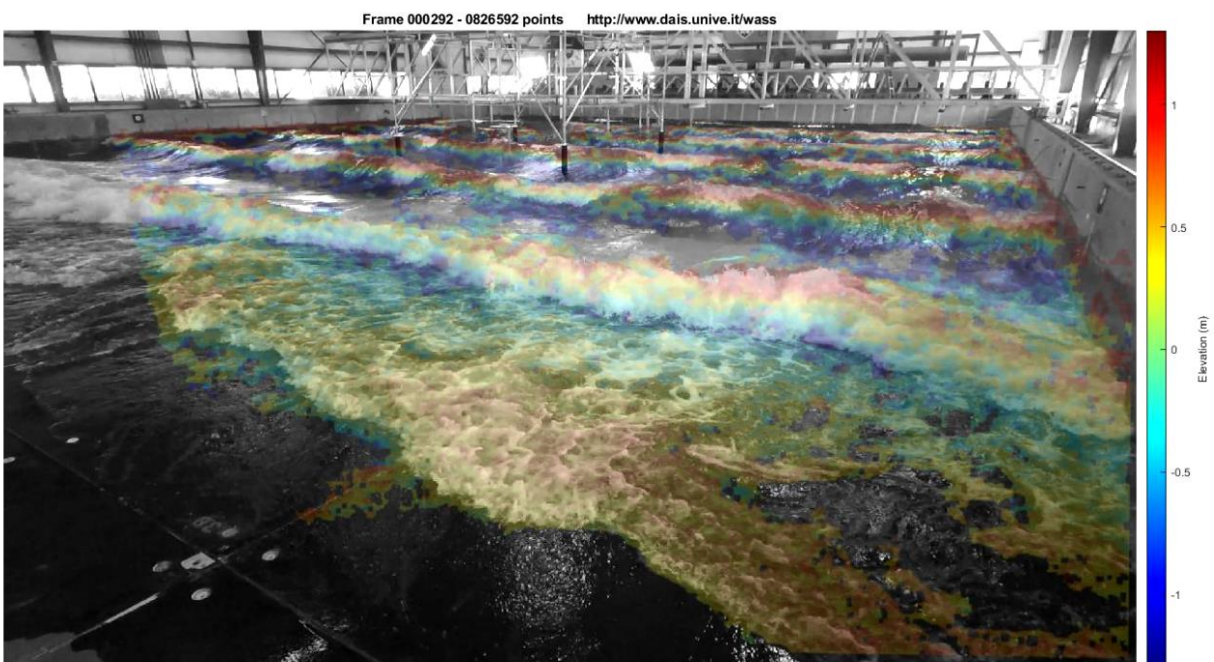
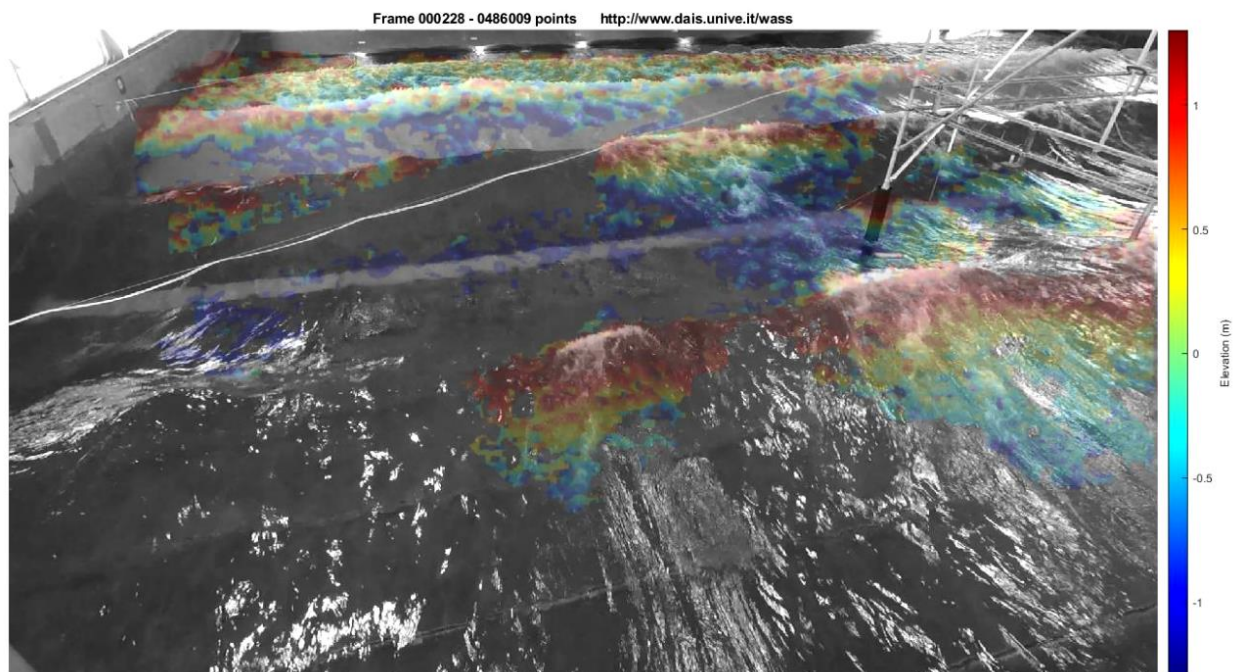
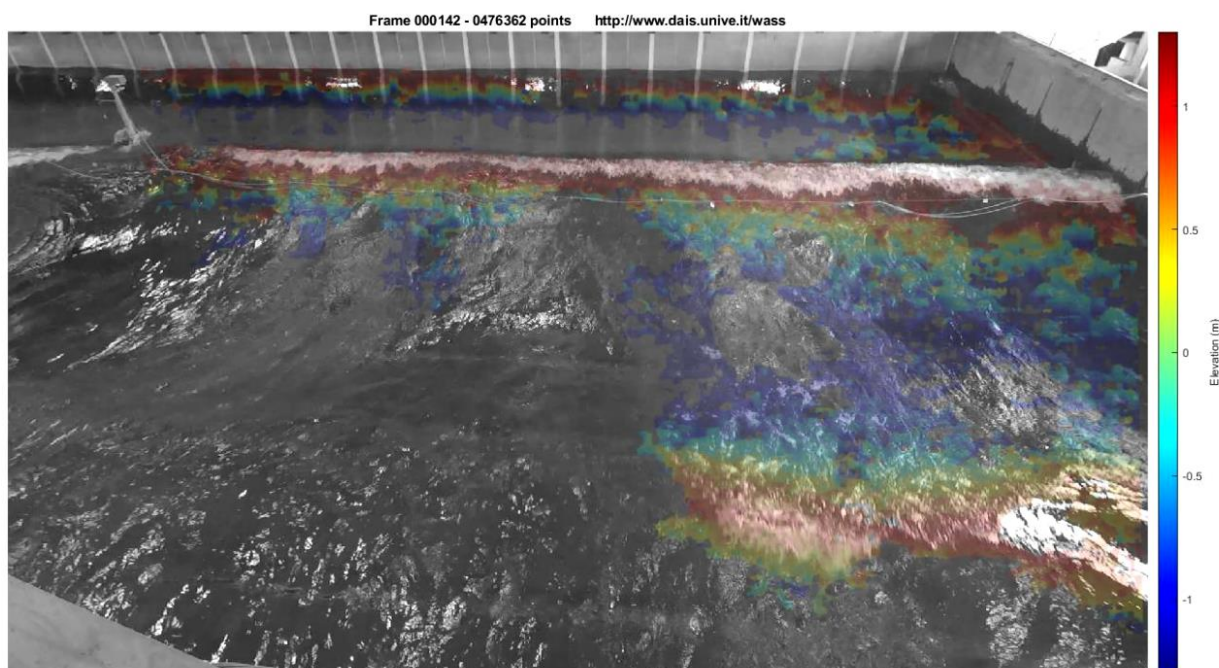


Figure B.2: Basin Views WASS auto snapshot for regular wave case from beach side.



*Figure B.3: Basin Views WASS auto snapshot for regular wave case from instrumentation bridge side toward beach.*



*Figure B.4: Basin Views WASS auto snapshot for regular wave case from instrumentation bridge side toward wavemaker.*

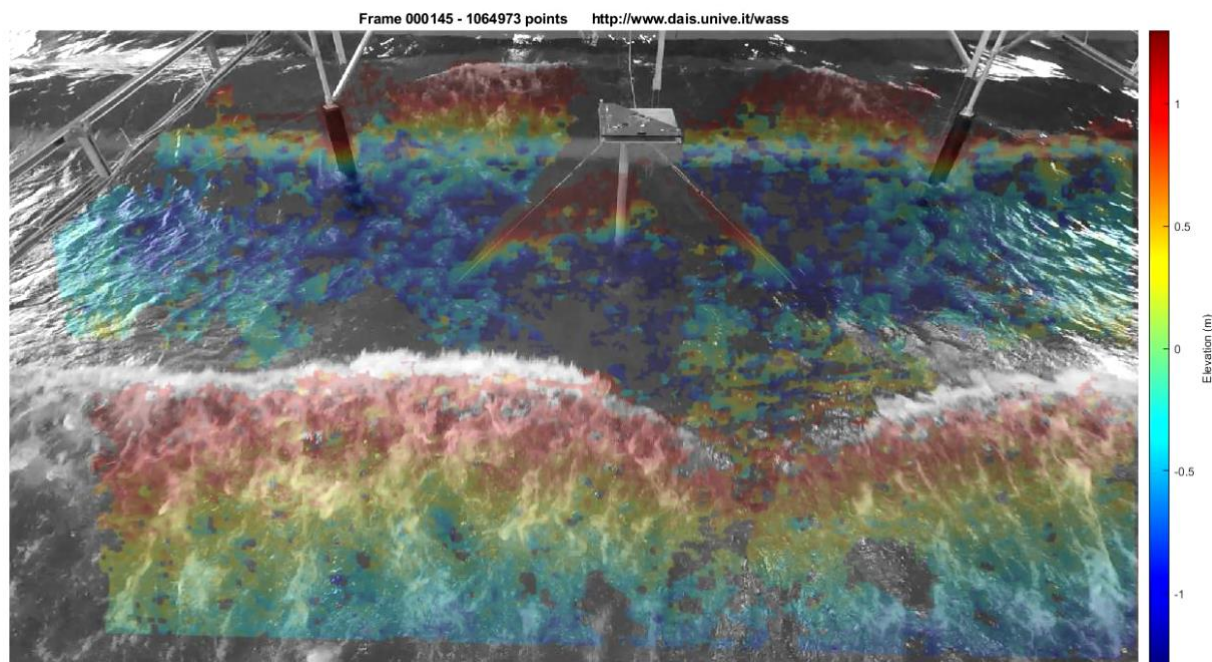


Figure B.5: Basin Views WASS auto lights on snapshot for regular wave case from instrumentation frame high.

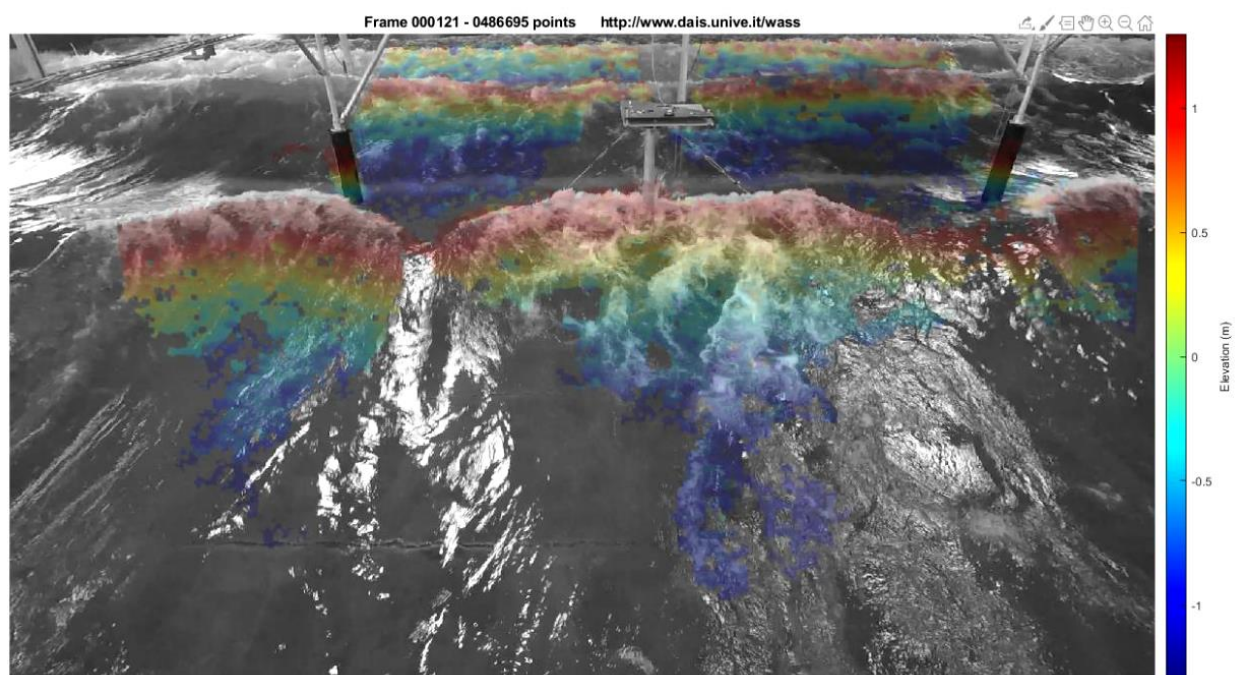


Figure B.6: Basin Views WASS auto lights on snapshot for regular wave case from instrumentation frame low.

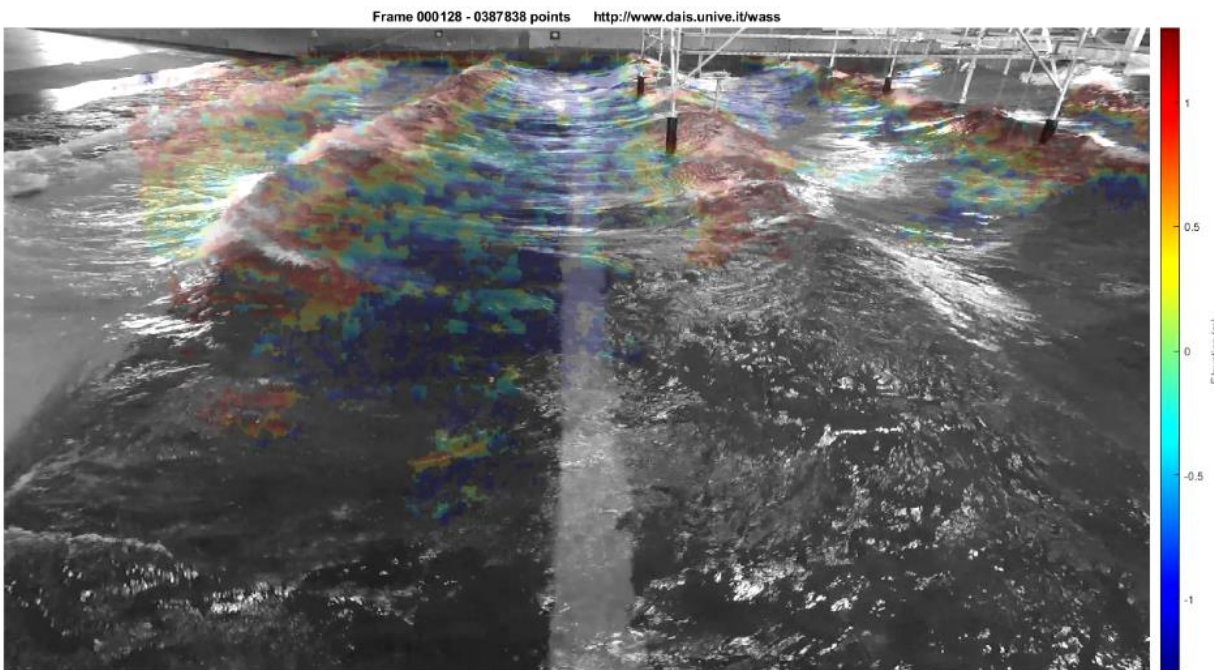


Figure B.7: Basin Views WASS auto snapshot for regular wave case from basin side.

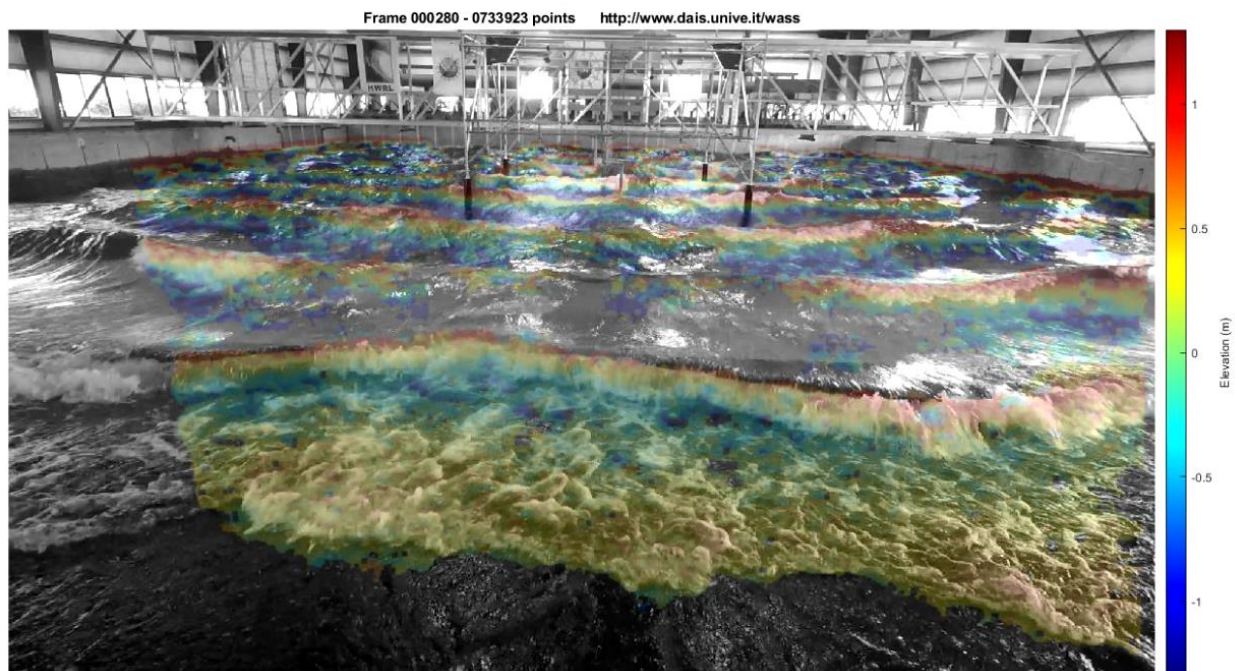
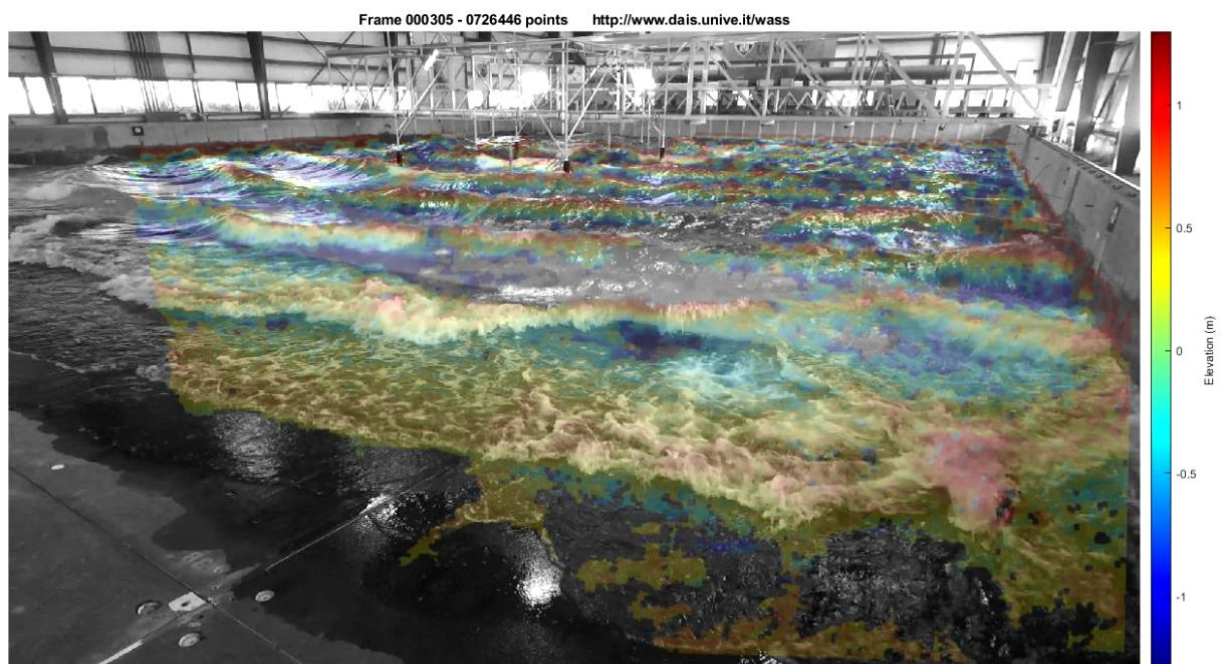
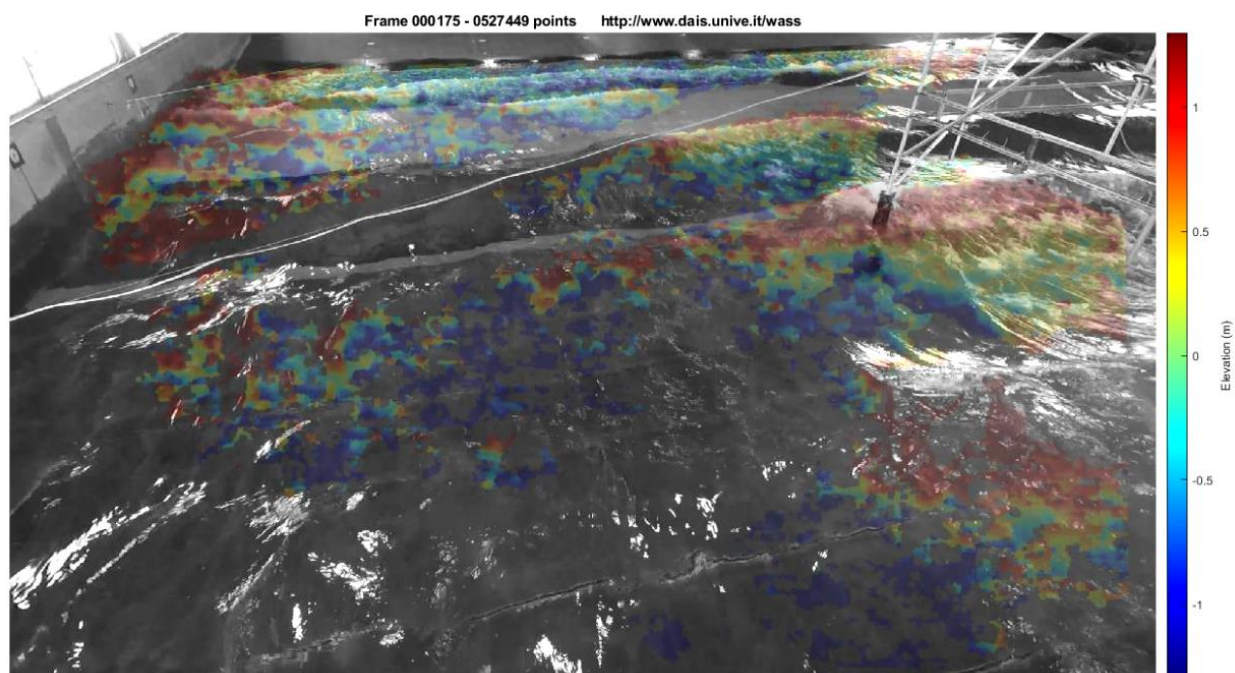


Figure B.8: Basin Views WASS auto snapshot for focusing wave case from basin beach center.



*Figure B.9: Basin Views WASS auto snapshot for focusing wave case from basin beach side.*



*Figure B.10: Basin Views WASS auto snapshot for focusing wave case from instrumentation bridge side toward beach.*

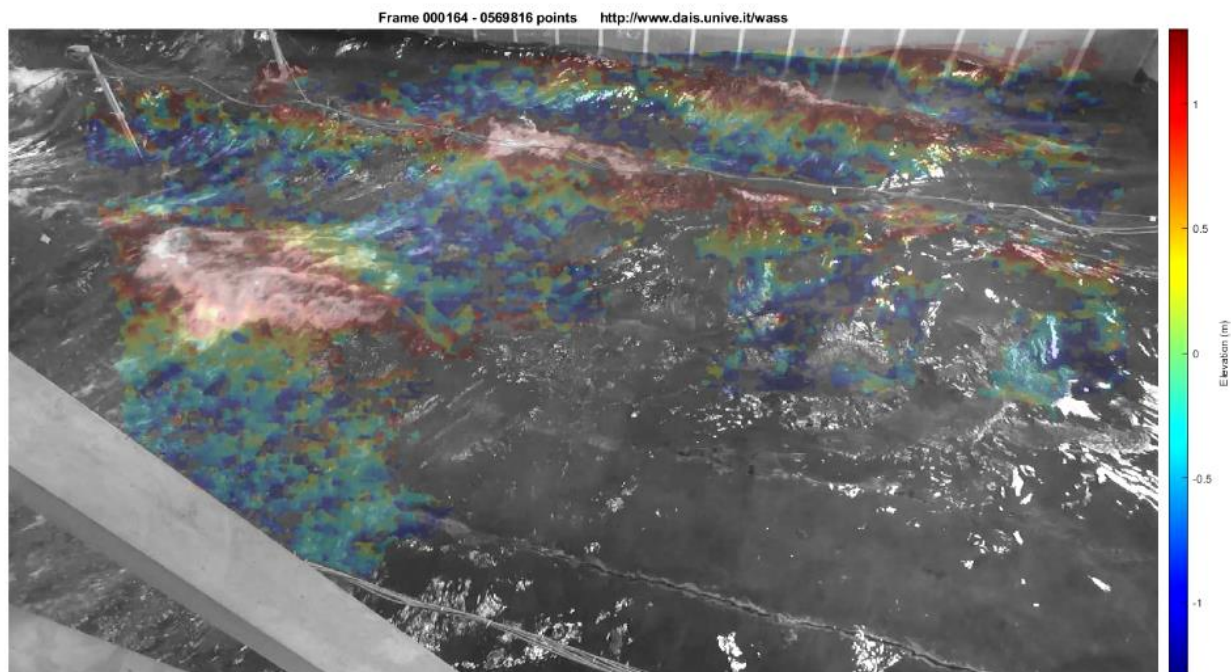


*Figure B.11: Basin Views WASS auto snapshot for focusing wave case from instrumentation bridge side toward wavemaker.*

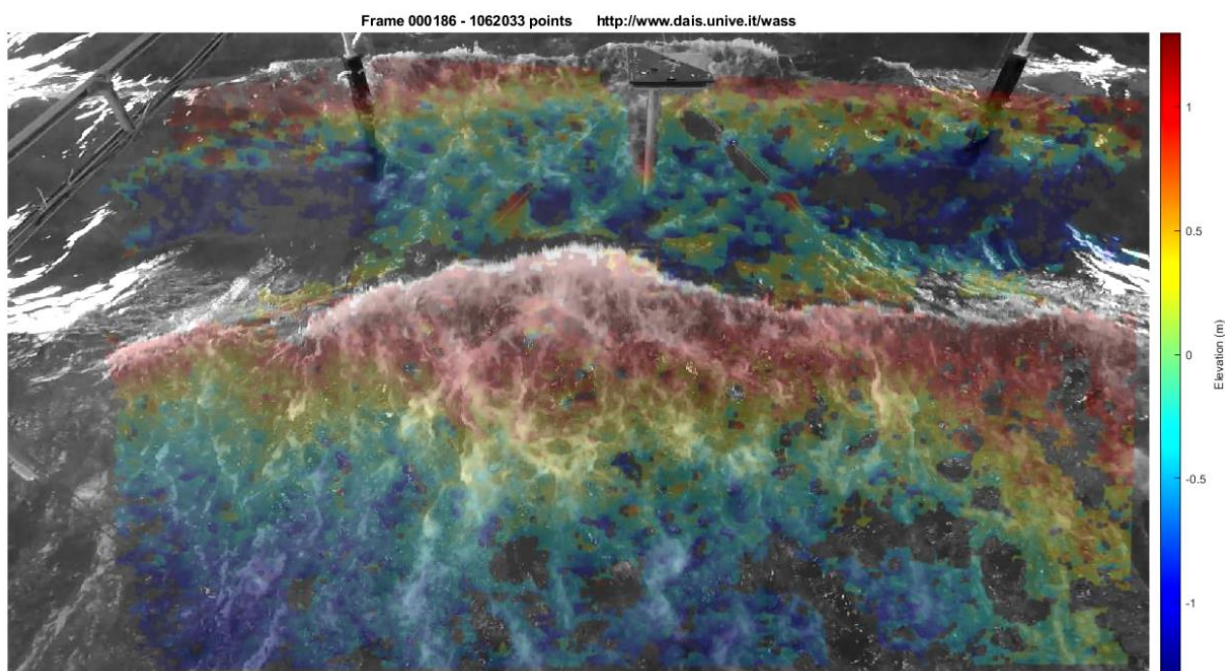


*Figure B.12: Basin Views WASS auto lights off snapshot for focusing wave case from instrumentation frame high.*



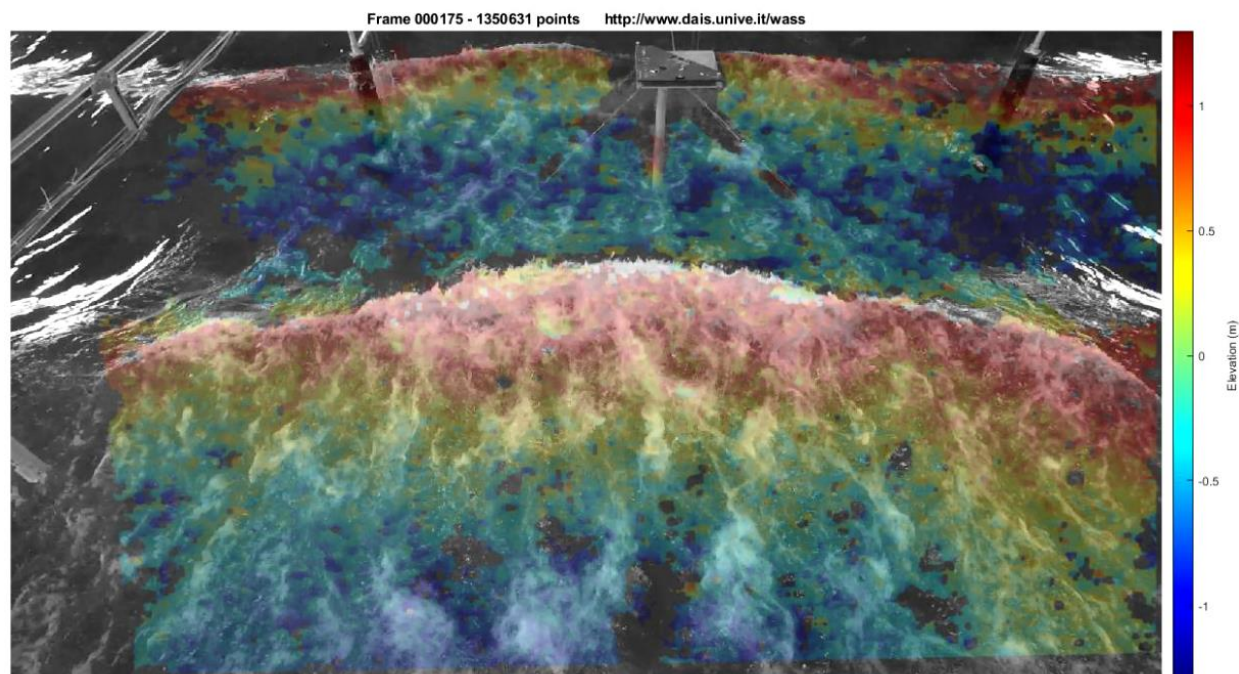


*Figure B.13: Basin Views WASS auto lights on snapshot for focusing wave case from instrumentation frame high.*

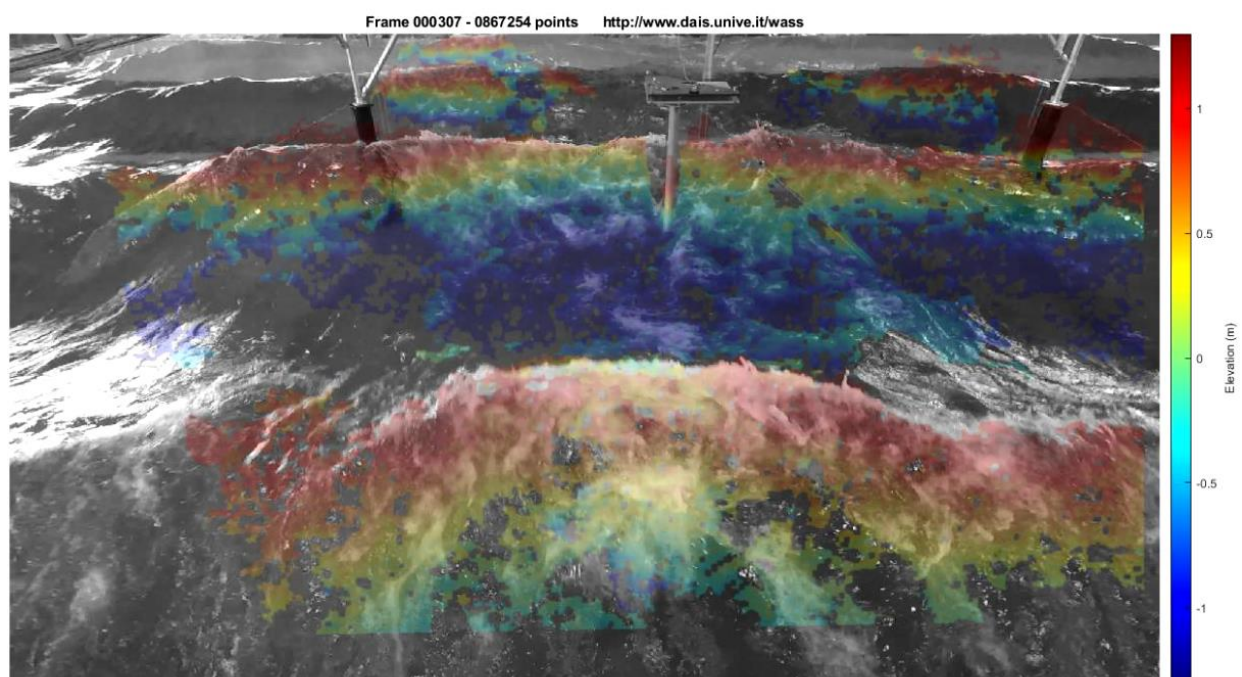


*Figure B.14: Basin Views WASS auto lights off snapshot for focusing wave case from instrumentation frame low.*

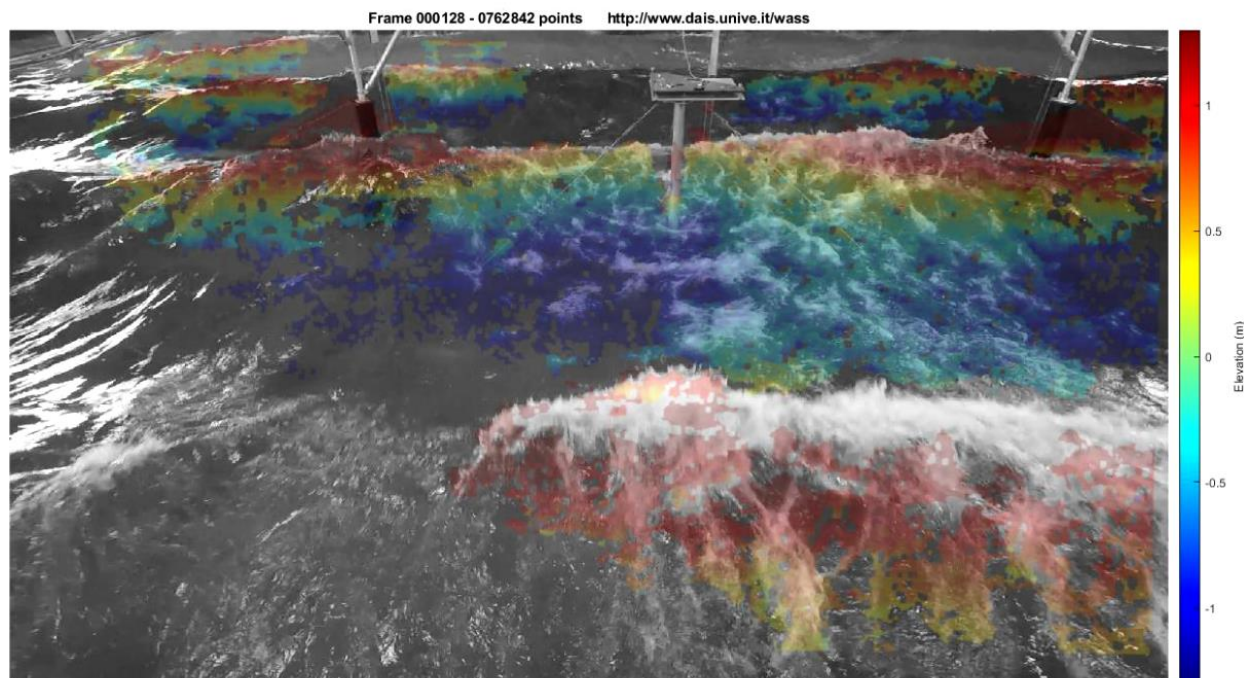


*Figure B.15: Basin Views WASS auto lights on snapshot for focusing wave case from instrumentation frame low.*

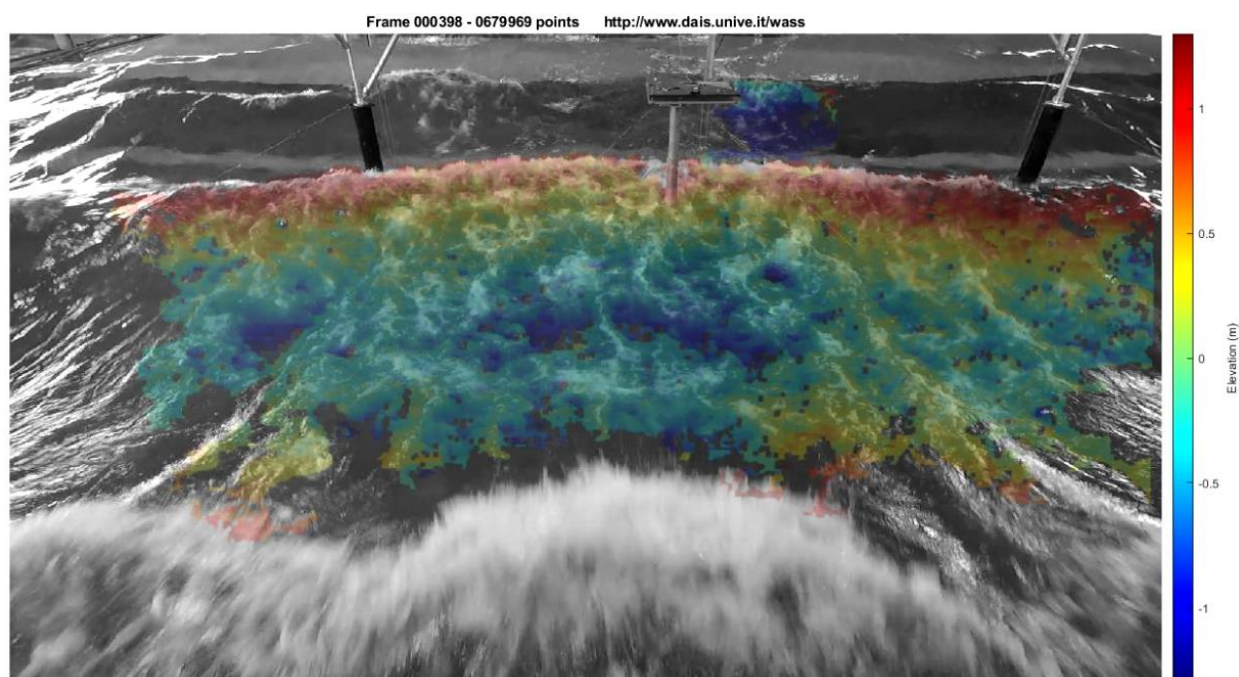


*Figure B.16: Basin Views WASS protune lights off snapshot for focusing wave case from instrumentation frame low.*

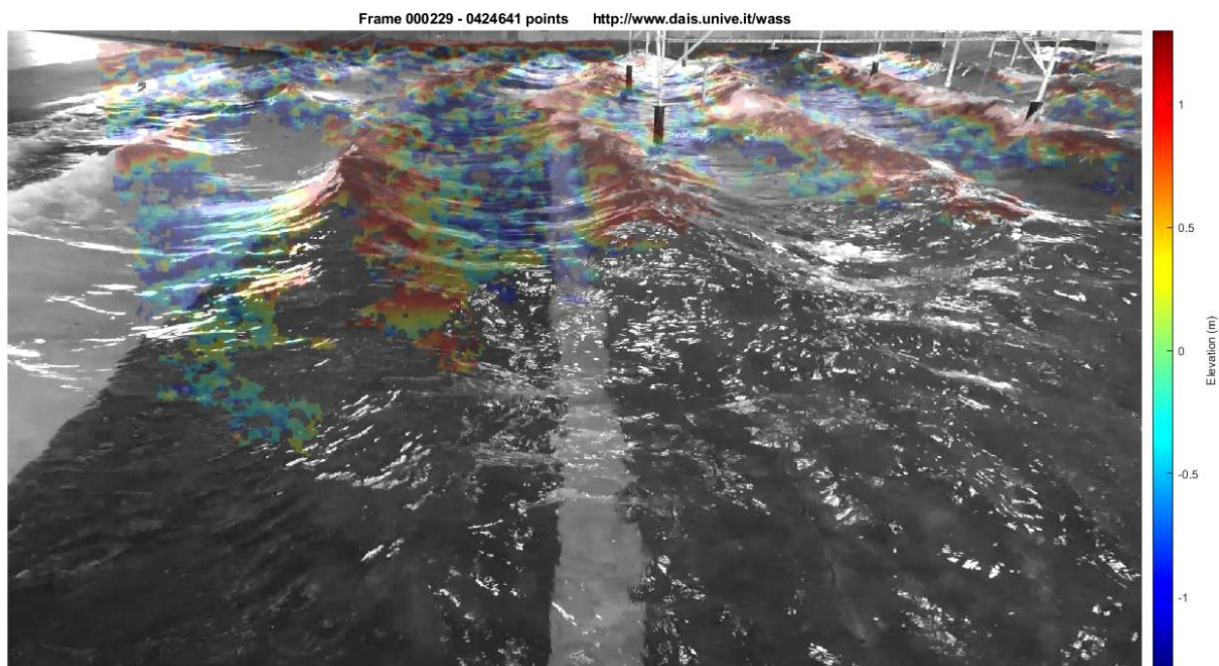


Figure B.17: Basin Views WASS auto snapshot for focusing wave case from basin side.

## B.2 Airy Validation Experiment

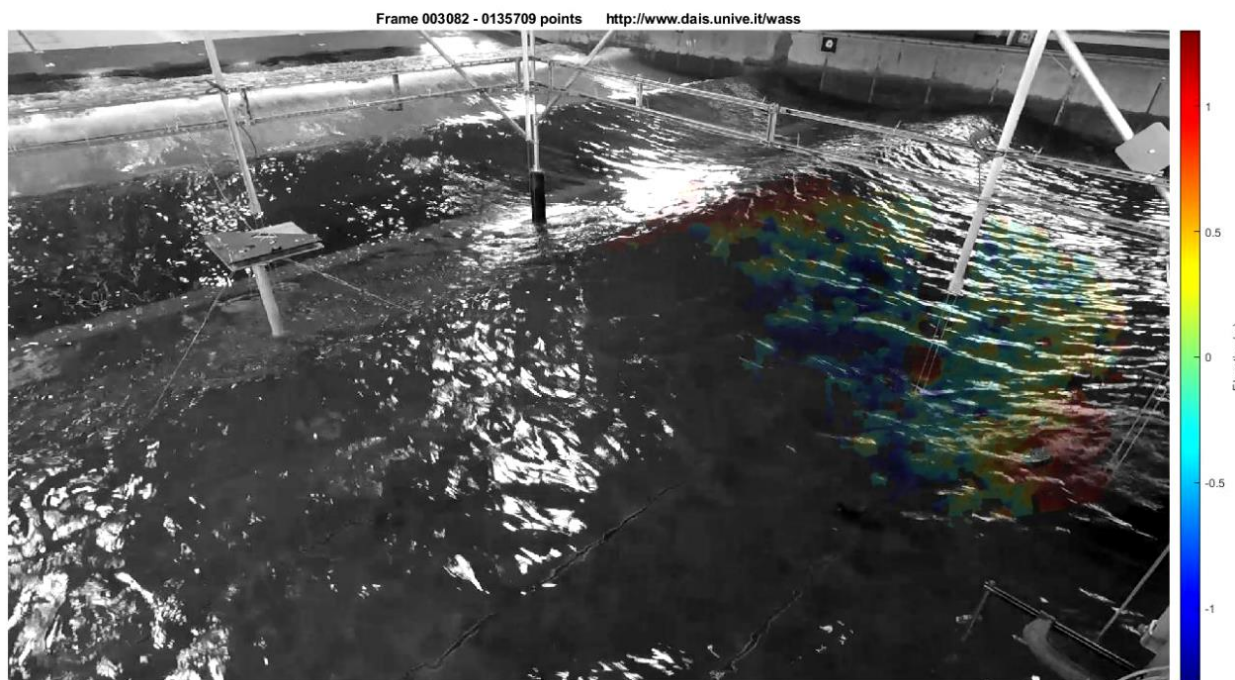


Figure B.18: Airy Validation WASS snapshot non-breaking regular wave case instrumentation frame toward North.

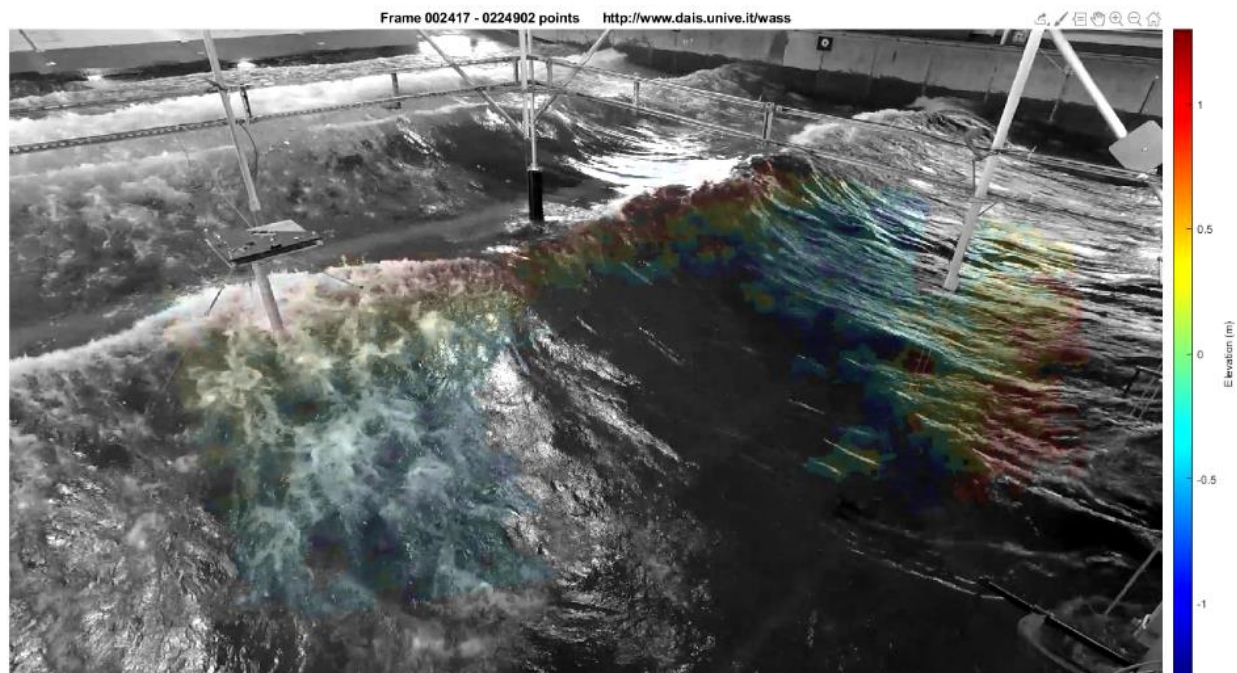


Figure B.19: Airy Validation WASS snapshot breaking regular wave case instrumentation frame toward North.

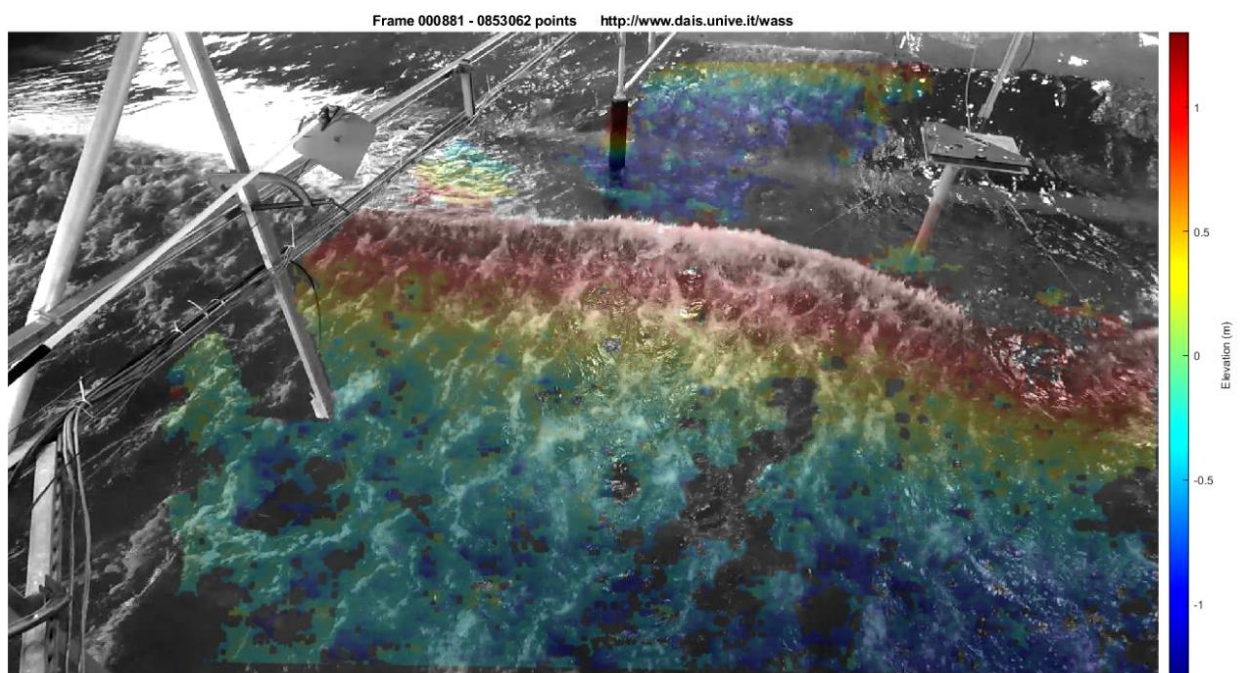


Figure B.20: Airy Validation WASS snapshot breaking regular wave case instrumentation frame toward South.

### B.3 CPL Filter Experiment

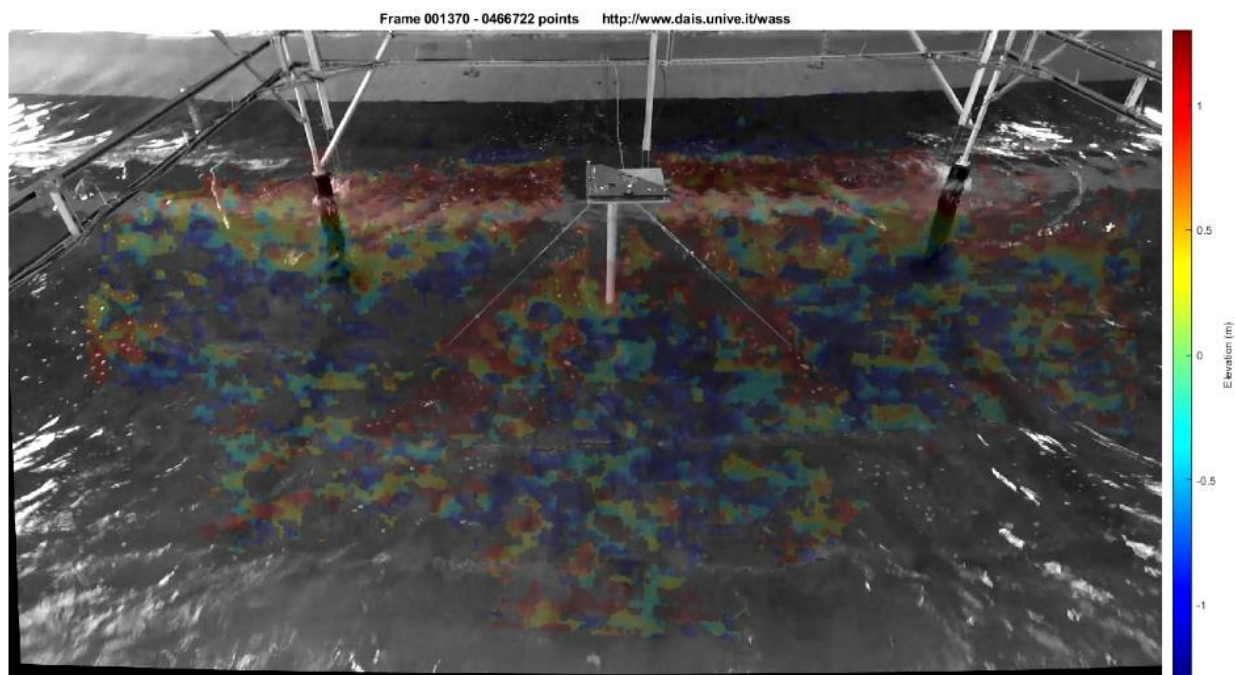


Figure B.21: CPL Filter WASS backlit snapshot non-breaking regular wave case instrumentation frame center.

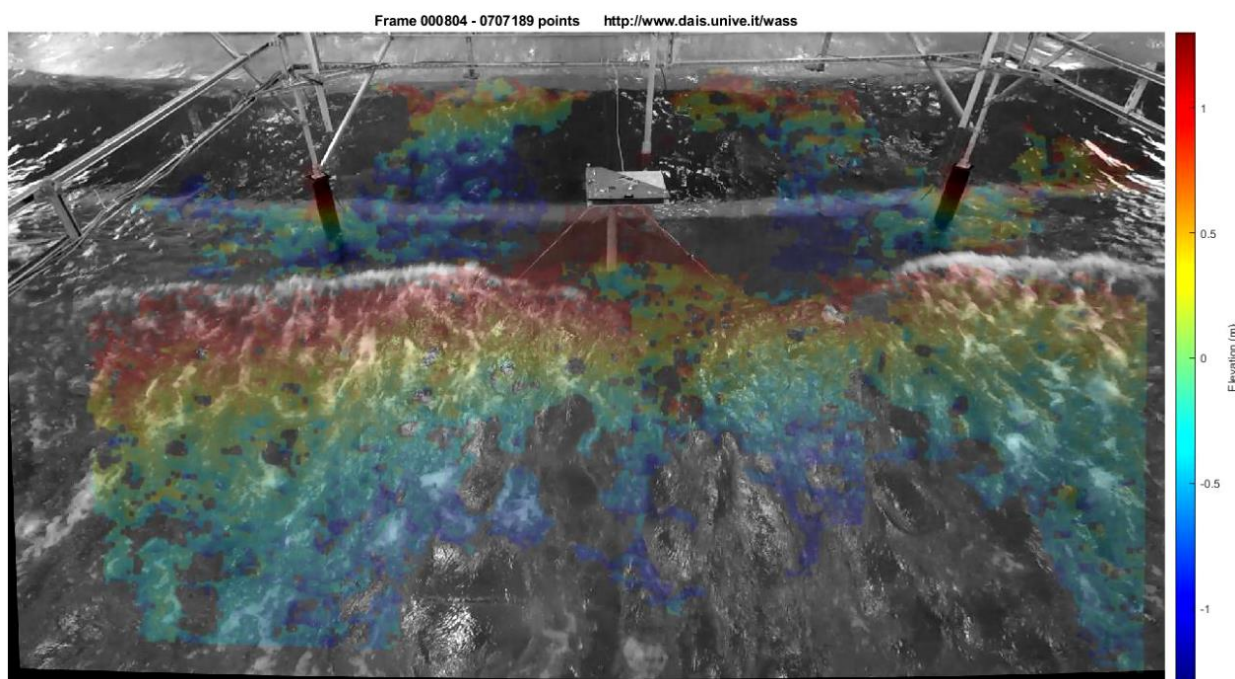
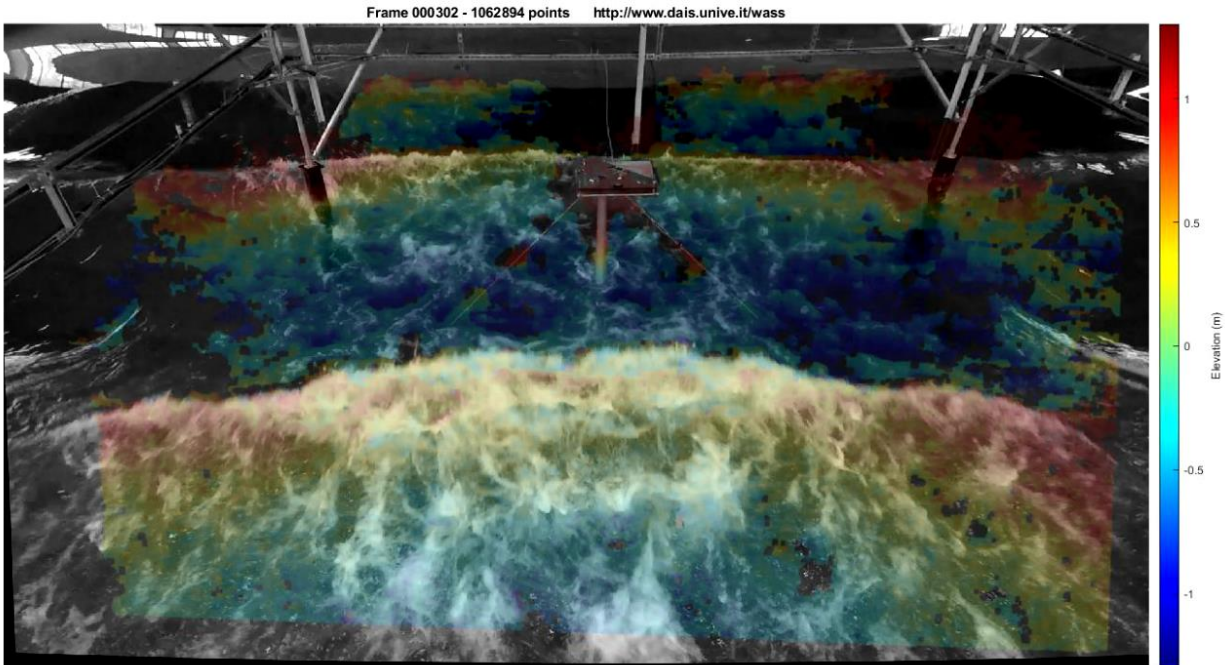


Figure B.22: CPL Filter WASS fully-lit snapshot breaking regular wave case instrumentation frame center.



*Figure B.23: CPL Filter WASS backlit snapshot focusing wave case instrumentation frame center.*

### Appendix C: WASS Camera Pairs Comparisons

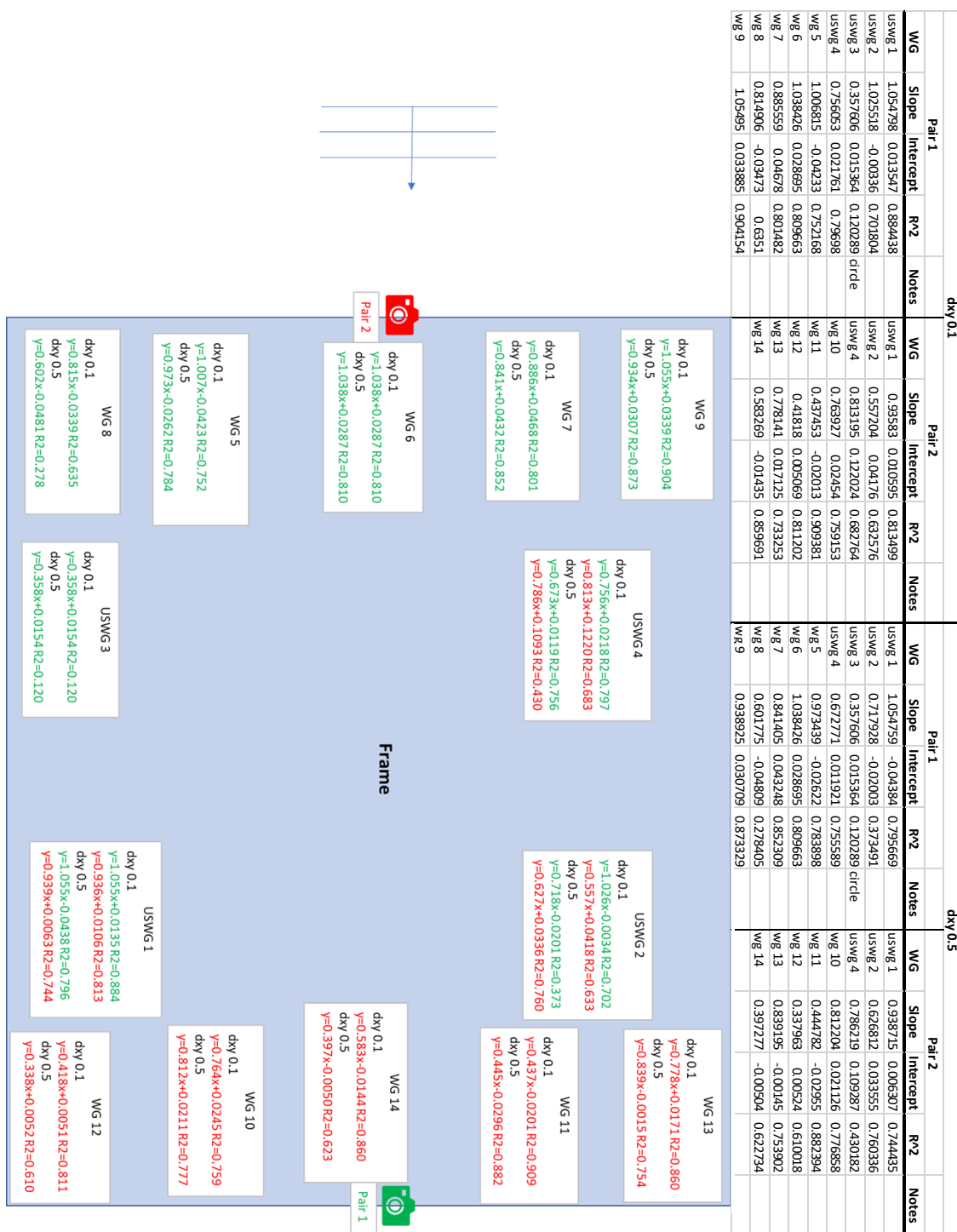


Figure C.1: WASS spatial/grid spacing study. Wave propagation direction and gauge/camera locations labelled. Linear regression fit equations  $R^2$  values shown at each wave gauge locations with red associated with onshore facing camera (Pair 2) and green associated with offshore facing (Pair 1). Table containing linear regression slope, intercept, and  $R^2$  values for each grid spacing, wave gauge, and camera pair.

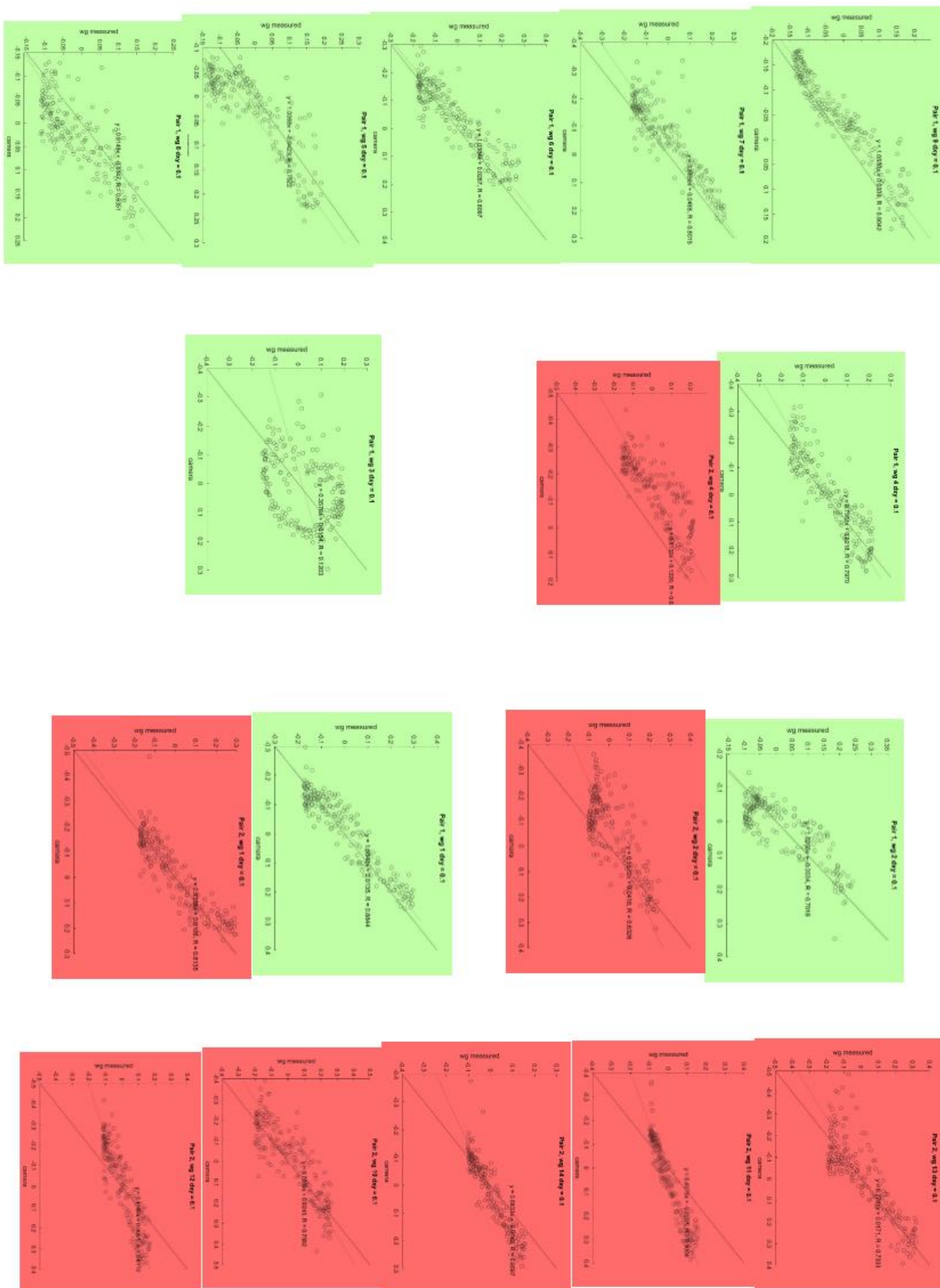


Figure C.2: WG vs. WASS data comparison plots in plan view of gauge locations for 0.1 m grid spacing with green plots for offshore facing camera pair and red plots for onshore camera pair.



## Appendix D: Camera Distortion Models

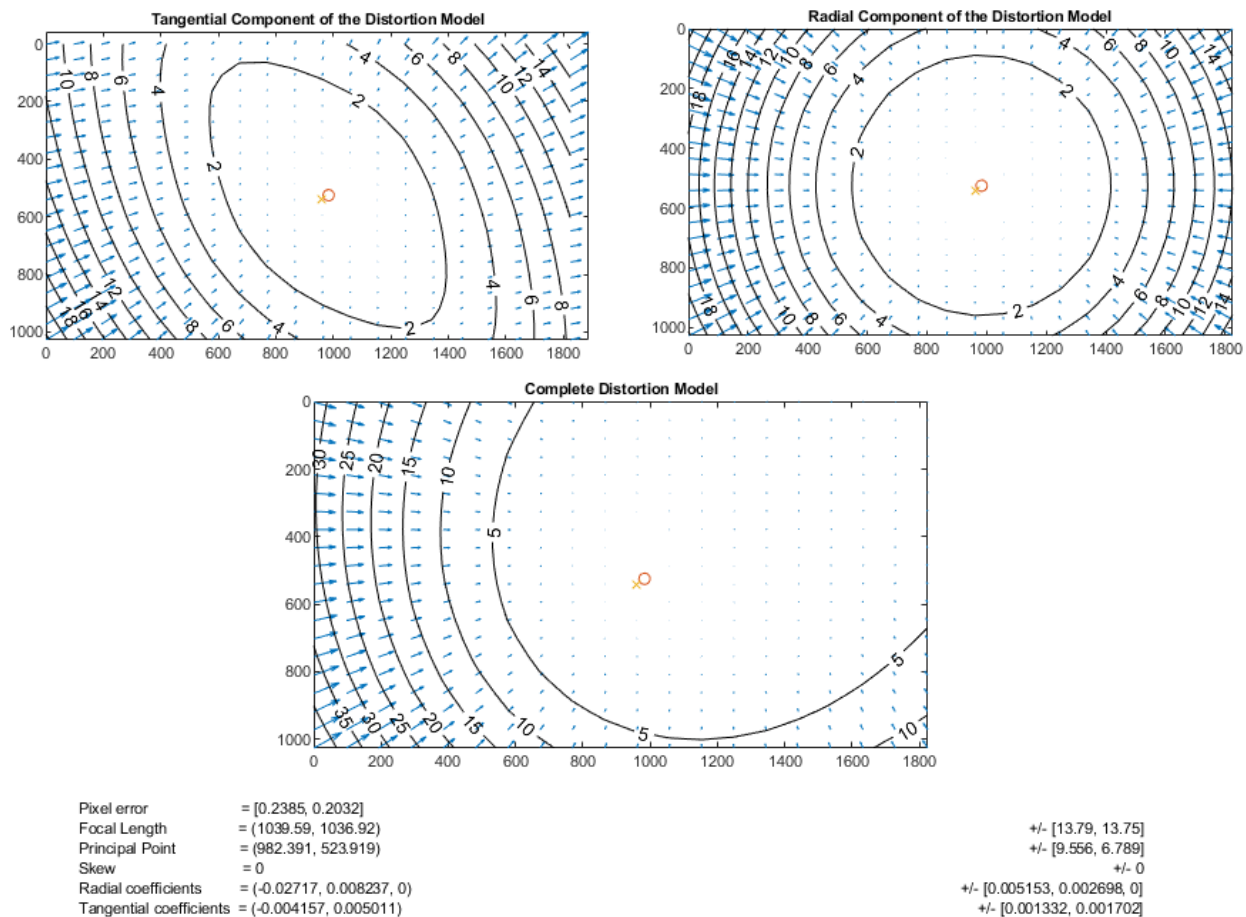
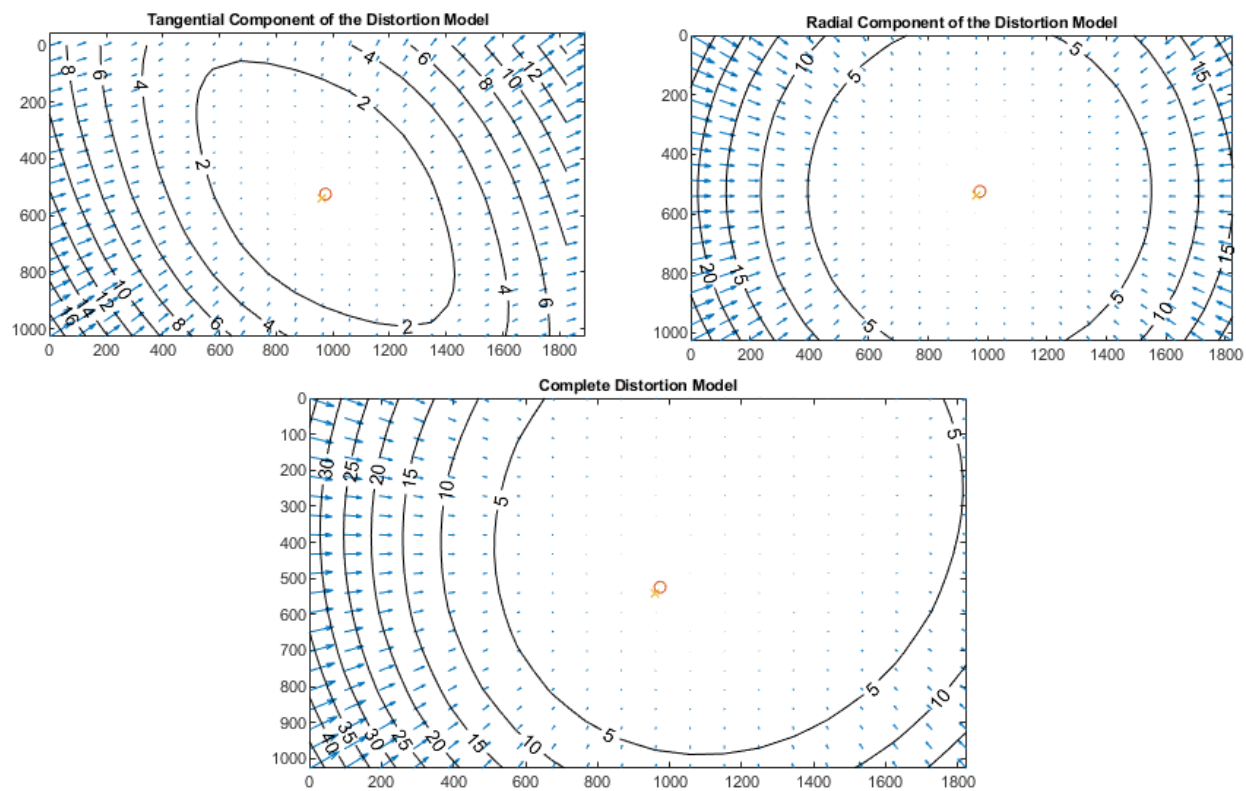
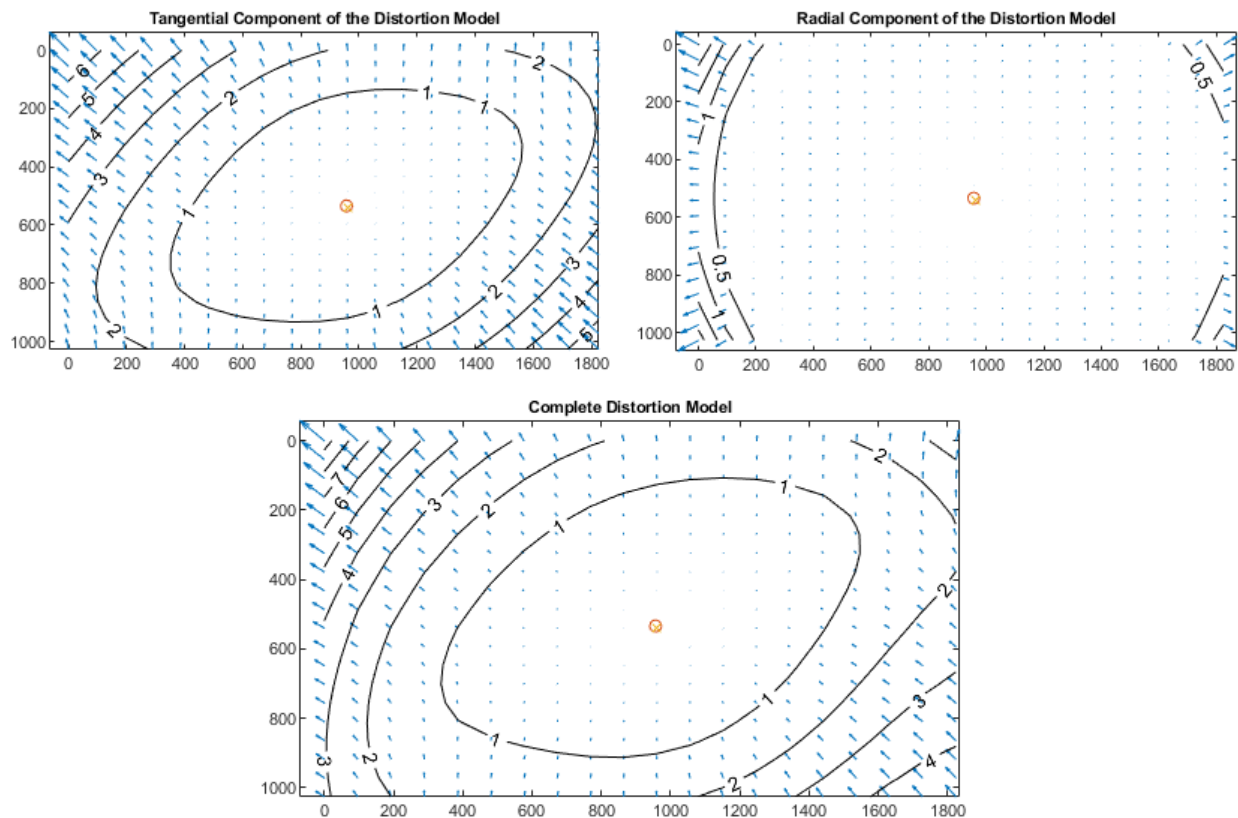


Figure D.1: GoPro® Hero 6 R25 (Pair 1) distortion models.



Pixel error	= [0.2425, 0.197]	
Focal Length	= (1028.52, 1026.38)	+/- [12.31, 12.22]
Principal Point	= (972.762, 523.493)	+/- [8.471, 8.12]
Skew	= 0	+/- 0
Radial coefficients	= (-0.02846, 0.004457, 0)	+/- [0.004924, 0.003042, 0]
Tangential coefficients	= (-0.004026, 0.004179)	+/- [0.001508, 0.001543]

Figure D.2: GoPro<sup>®</sup> Hero 6 L48 (Pair 1) distortion models.



Pixel error	= [0.2503, 0.2186]	
Focal Length	= (1040.63, 1036.12)	+/- [0.9496, 0.9287]
Principal Point	= (955.862, 533.098)	+/- [1.182, 1.125]
Skew	= 0	+/- 0
Radial coefficients	= (-0.002266, 0.003918, 0)	+/- [0.001154, 0.001075, 0]
Tangential coefficients	= (-0.002279, -0.0009645)	+/- [0.0003008, 0.0003166]

Figure D.3: GoPro<sup>®</sup> Hero 6 3433 (Pair 2) distortion models.

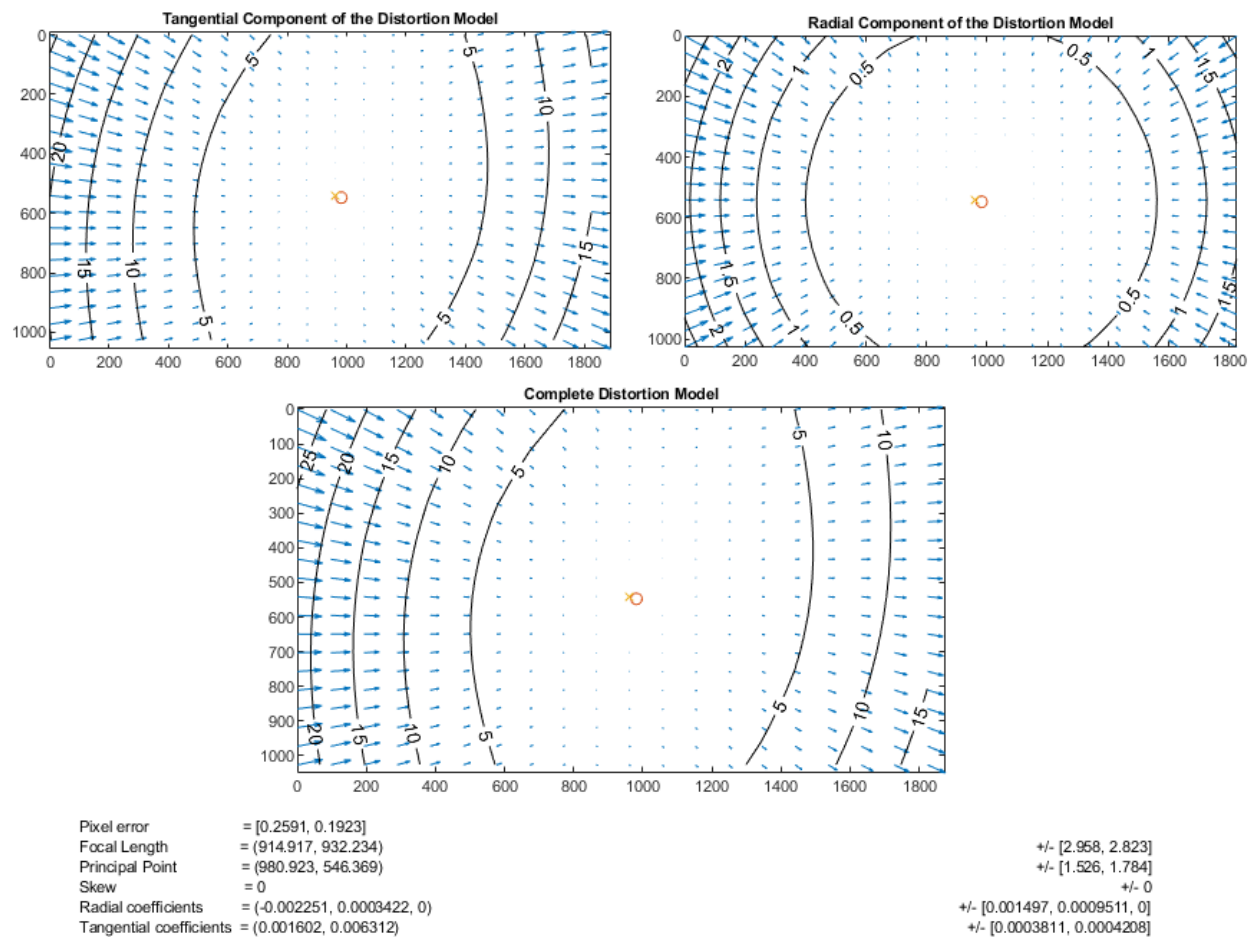


Figure D.4: GoPro® Hero 8 1885 (Pair 2) distortion models.

## Appendix E: Average Wave Gauge Values

Table E.1: Average measured wave gauge values for trials discussed in Chapter 6.

Trial #	Waves	Time Domain			Frequency Domain	
		$H_{\text{mean}}$ [m]	$H_s$ [m]	$T_{\text{mean}}$ [s]	$H_{\text{mo}}$ [m]	$T_{\text{mo}}$ [s]
1	Focusing	0.319	0.342	1.502	0.418	1.185
2	Regular Shore Normal	0.402	0.420	1.771	0.499	1.216
4	Regular Directional	0.327	0.449	3.602	0.381	2.111
5	Irregular Directionally Spread	0.307	0.459	3.108	0.423	2.924
6	Regular Bidirectional	0.246	0.418	1.428	0.434	1.580
8	Focusing	0.269	0.346	1.461	0.384	1.410

Appendix F: Intel® RealSense™ D455 Depth Camera Mechanical Drawing

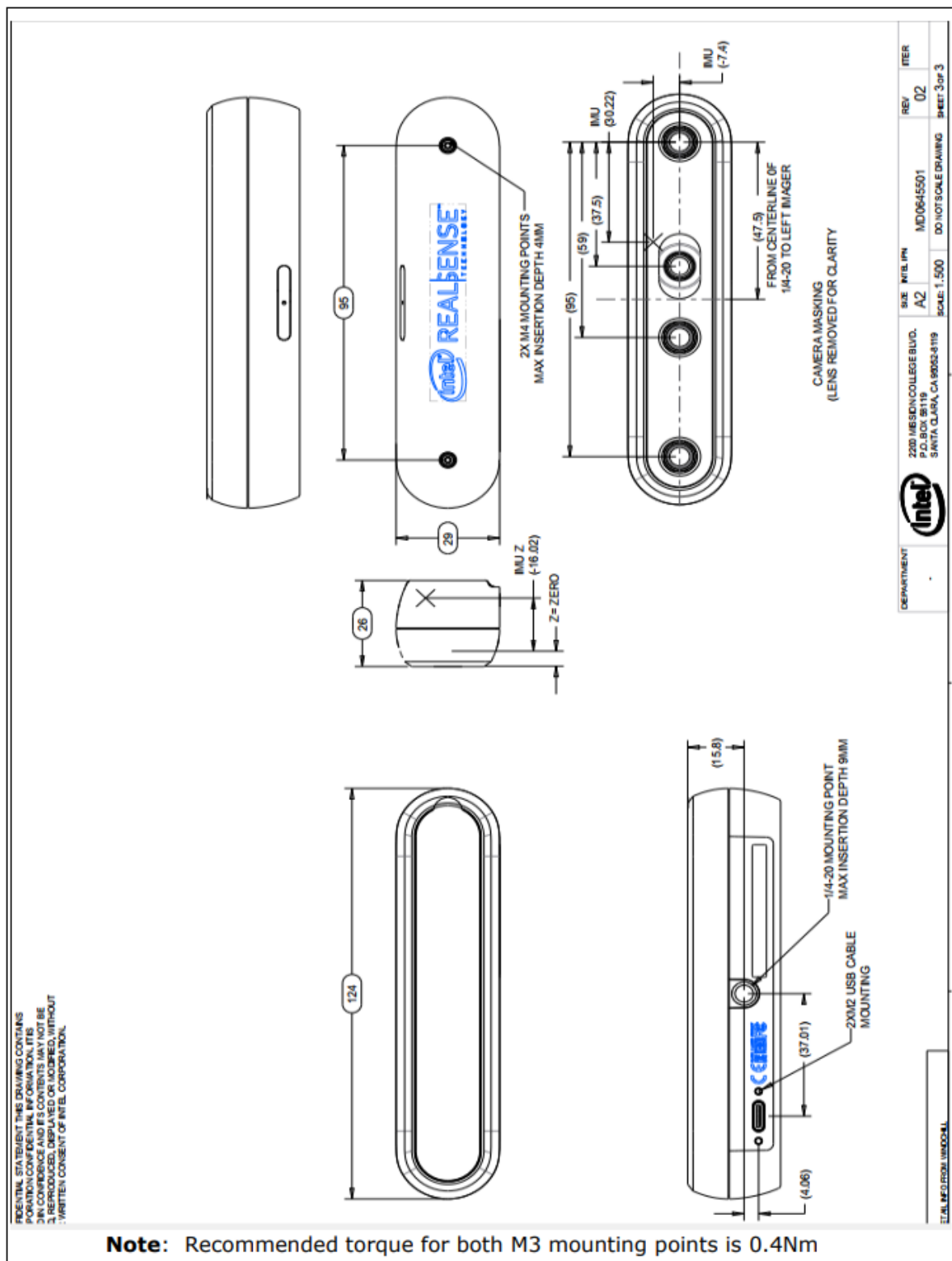


Figure F.1: Mechanical drawing of Intel® RealSense™ D455 external housing. Source: [37].

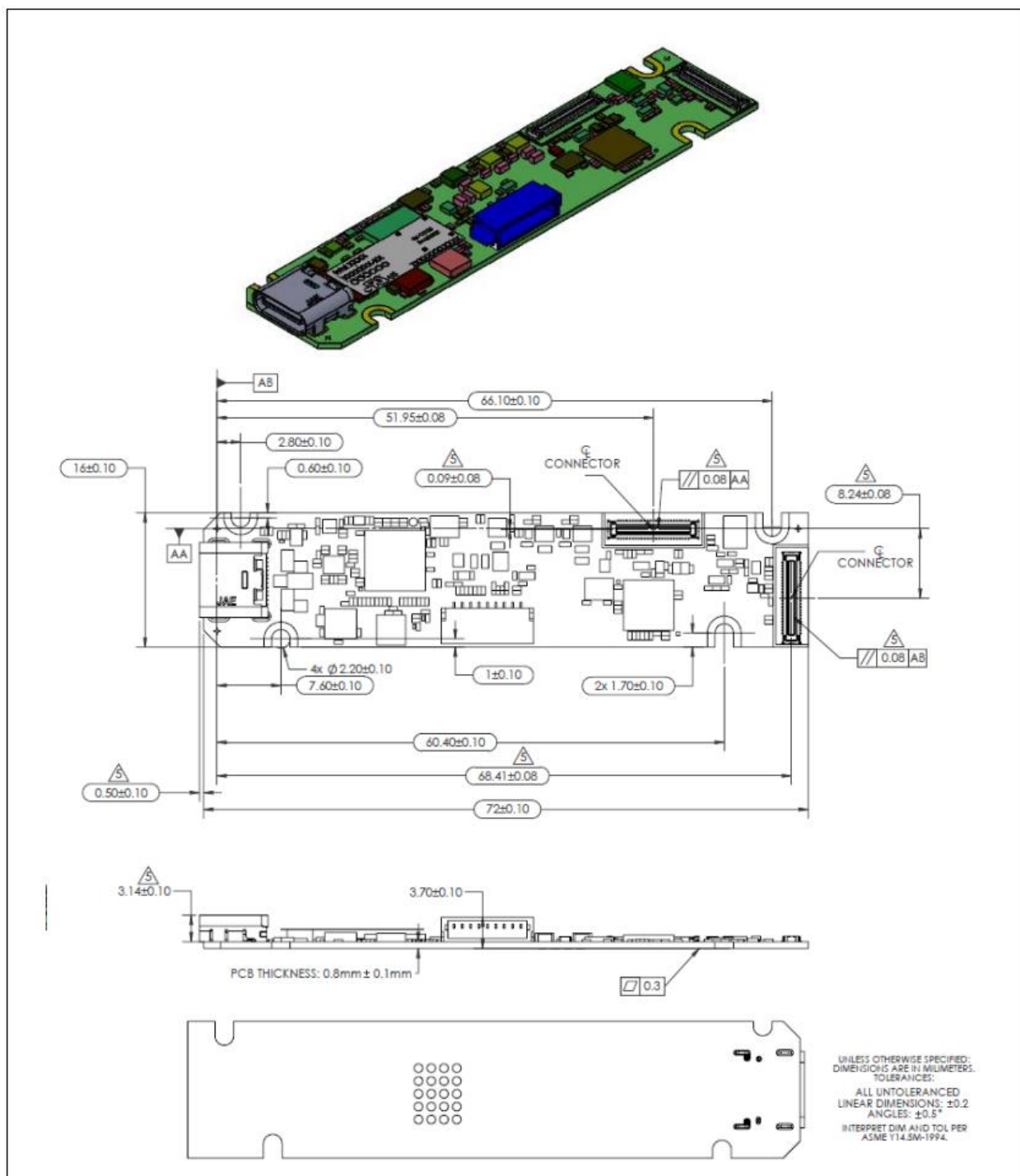


Figure F.2: Mechanical drawing of D4Vision Processor board. Source: [37].